

**BIOLOGICAL ACTIVITY OF RHODIUM METALLOINSERTORS AND
THE DESIGN OF BIFUNCTIONAL CONJUGATES**

Thesis by

Alyson G. Weidmann

In Partial Fulfillment of the Requirements

for the Degree of

Doctor of Philosophy in Chemistry

California Institute of Technology

Pasadena, CA

2015

(Defended May 28, 2015)

© 2015

Alyson G. Weidmann

All Rights Reserved

Acknowledgments

First and foremost, I would like to thank my advisor, Professor Jacqueline Barton. You have been an endless source of wisdom, optimism, enthusiasm, and support. My growth as a scientist has been in no small part due to your guidance and example. Your faith in me continued even when I did not have faith in myself, and for that I will always be grateful. It has truly been a privilege to be a member of this lab.

I am deeply thankful to my dissertation committee for being a tremendous source of insight, inspiration, and perspective. To Professor Harry Gray, you have been the most wonderful committee chair; I thank you for all of your advice and guidance. To Professor Brian Stoltz, I am grateful for all of your support and encouragement. I would also like to thank Professor Jonas Peters for your enthusiasm, collegiality, and approachability. I have been so fortunate to have a committee comprised of incredibly creative and knowledgeable faculty who are committed to academic excellence, yet at the same time are down to earth and accessible. Thank you.

I have also had the privilege of working as a teaching assistant for Chem 10. I thank Professor Peter Dervan, whose unparalleled commitment to undergraduate research has served as an example in mentorship. I also thank Professor Andre Hoelz, for your dedication to academic rigor as well as your unmatched sense of humor. It has been great fun TA-ing this class for you both these past four years.

I would also like to thank the people who make the Caltech Chemistry Department run like a well-oiled machine: Agnes Tong, you have been a fantastic Option Administrator as well as an amazing friend. Our Ath lunches hold a special place in my heart. To Mo Renta, thank you for keeping the lab in tip top shape. Thank you to Joe

Drew, Memo, and the rest of the stockroom crew for all that you do, as well as always being down for a good football conversation (thank you for not making too much fun of my beloved New York Giants). Thank you also to Silva Virgil, Amy Woodall-Ojeda, Anne Penney, Steve Gould, and Elisa Brink for always being willing to lend a helping hand. I am also grateful to Mona Shahgholi and Dave VanderVelde – no chemistry would get done without you. Thank you Larry Henling, for diffracting my crystals even though they were crappy. And thank you Felicia Hunt, for always being a friendly face willing to listen.

I am deeply indebted to Nathan Dalleska and the Environmental Analysis Center, without whom half the data in my thesis would simply not exist. Nathan, your endless patience with the ICP-MS instruments has been admirable and invaluable. Thank you for teaching me analytical chemistry (which has, to my delight, involved boiling cancerous human flesh in concentrated acid) as well as how to not take the little things (such as a malfunctioning ball of plasma at 20,000 °C) too seriously.

Thank you to our amazing collaborators for helping to bring our metalloinsertor complexes ever closer to the clinic. Julie Bailis, you have been absolutely wonderful in your diligence and passion for these complexes. Thank you also to Professor Jeremy Stark for your openness to collaboration and creative ideas. I am deeply grateful to Diana Yanez for patiently teaching me immunofluorescence staining and collecting microscopy images. It has been a delight to work with you and I wish you all the best in your M.D.-Ph.D. program. Thank you also to the rest of the Stark Lab, who have welcomed me from Day 1 and have always been a friendly, supportive bunch. I wish your lab all the success in the world.

I must also thank the people from my undergraduate institutions who have played a huge role in my decision to go to grad school: to Columbia University Dean Jim Valentini (Deantini), who got me my first summer research position back when he was head of the Chemistry Department, which changed the course of my life. Thank you also to Professors Koji Nakanishi and Nina Berova of Columbia University, who welcomed me into their lab and taught me magic tricks in addition to chemistry. I am incredibly grateful to Professor JoAnne Stubbe of MIT; your incredible research and group solidified my decision to pursue a Ph.D and inspired me to study bioinorganic chemistry. Thank you also to Joey Cotruvo for your amazing mentorship, and to the rest of the Stubbe lab, for being wonderful co-workers and friends. I am also grateful to the professors who provided guidance and advice to me as an undergraduate: Professor Cathy Drennan, Professor Brent Stockwell (who talked me out of grad school), and Professor Jon Owen (who talked me back into it).

I am incredibly grateful also to my labmates in the Barton laboratory, especially those who took the time to train and teach me. Russ Ernst, you took me under your wing from the very beginning. Your good-naturedness and scientific rigor have been an example to me throughout my graduate career. Thank you also to Curtis Schneider, for teaching me everything I know about synthesis, inorganic chemistry, and beer. And to Alexis Komor, who has been both a great friend as well as an example for me to look up to in lab. I always knew that if I was doing an experiment the way you did it, I was doing it right. Thanks to Jessica Yeung, my incredibly talented former SURF, who continues to amaze me with her dedication and passion for research.

Thank you also to the rest of the Barton lab – all of you have made my time at Caltech a special and unique experience. Natalie Muren, you have always floored me with your unending support and willingness to help or just lend an ear. Phil Bartels, you have been a steadfast worker, an outstanding co-TA, and a true friend. Thank you also to Katie Schaefer, Liz O'Brien, and Anna Arnold for being wonderful co-workers and great sources of conversation and animal videos. A special shout-out to everyone in Subgroup 1, for never making me doubt for a second that I joined the right subgroup: Hang Song, for your optimism and friendliness; Anna McConnell, for all of your synthetic knowledge and sunny disposition; Adam Boynton, for filling the South Side with positivity and sick beatz; and Kelsey Boyle for your rigor and eagerness to learn. It has been a pleasure working with you. I have no doubt that I am leaving Team Rhodium/Ruthenium in the best of hands.

Finally, I must thank the people who truly kept me sane throughout my Ph.D: my amazing friends and family. I would not have gotten through this without your support. Special thanks in particular to Breanne Siegel, Julianna Parapugna, Albert Lee, Andrew Wang, Myles Herbert, Jeremy Kallick, Alex Goldberg, Guy Edouard, Brad Hulse, Mike Post, Jeff Holder, Tim Aarons, Seth Tallob, Ethan van Arnam, Judy Lattimer, Michael van Vliet, Megan McDuffie, and Lina Schatz. Thank you especially to Tim Mui, who *everybody knows* is a fabulous co-worker (as well as a great friend!).

And to Ariel Furst, my partner in crime, my common-law spouse, my roommate and best friend: without you, I literally would have gone insane. I would have gone batshit, Michael-Jackson-baby-dangling, Britney-Spears-head-shaving, let's-make-a-Star-Wars-prequel, communism-works-in-theory c-r-a-z-y. From our wine nights and

bad TV to all the amazing trips we've taken, it's been a blast. So thank you for being there for me always, and for keeping me out of the looney bin, and for being the type of friend who would visit me in the looney bin and bring me cheese and contraband. It has been a long road that we've crab-walked, but we've finally made it and now we can adopt a bunch of cats and drink our way through San Francisco. You are a true gem and an incredibly talented chemist, and I am so grateful to have such an amazing friend in my life.

And thank you, truly, to my family, who have unquestioningly supported me throughout this entire process. Mom, Dad, and Danielle, I am so thankful to have you in my life and so honored to have made you proud. I would not be the person that I am, and would not have achieved the success that I have without you. Thank you. I love you.

Abstract

The Barton laboratory has established that octahedral rhodium complexes bearing the sterically expansive 5,6-chrysene diimine ligand can target thermodynamically destabilized sites, such as base pair mismatches, in DNA with high affinity and selectivity. These complexes approach DNA from the minor groove, ejecting the mismatched base pairs from the duplex in a binding mode termed metalloinsertion. In recent years, we have shown that these metalloinsertor complexes also exhibit cytotoxicity preferentially in cancer cells that are deficient in the mismatch repair (MMR) machinery.

Here, we present evidence to support the notion that mismatches in genomic DNA are the primary biological target of rhodium metalloinsertors and the source of their cell-selectivity. A structure-activity study on a family of ten metalloinsertor complexes revealed a highly sensitive relationship between the lipophilicity of the non-inserting ancillary ligands and the biological activity of the complex. Complexes with hydrophilic ligands were found to be highly cell selective, exhibiting preferential cytotoxicity in MMR-deficient cells at low concentrations and short incubation periods, whereas complexes with lipophilic ligands displayed poor cell-selectivity. ICP-MS studies were carried out to determine the cellular uptake and localization patterns of the ten compounds. The lipophilic complexes displayed enhanced cellular uptake compared to the more polar compounds, and their uptake patterns were indicative of a passive diffusion mechanism. Curiously, there was no correlation between cellular uptake of rhodium and selectivity for MMR-deficient cells. In fact, the complexes with the most selective activity exhibited low cellular accumulation overall. It was also discovered that

all of the complexes localized to the nucleus in concentrations sufficient for mismatch binding; however, highly lipophilic complexes also exhibited high mitochondrial uptake, consistent with the previous study. This relationship between subcellular localization and cell-selective biological activity confirms that mitochondrial DNA is not the desired target of metalloinsertor complexes; rather, these complexes recognize mismatches in genomic DNA.

We have also explored the potential for metalloinsertors to be developed into more complex structures with multiple functionalities that could either enhance their overall potency or impart mismatch selectivity onto other therapeutic cargo. We have constructed a family of bifunctional metalloinsertor conjugates incorporating *cis*-platinum, each unique in its chemical structure, DNA binding interactions, and biological activity. Attachment of a potent oxaliplatin derivative to a metalloinsertor through the leaving group ligand afforded an intrinsically metastable complex with high cytotoxicity in MMR-deficient cancer cells as well as enhanced cellular uptake properties. Additionally, we developed a bimetallic complex derived from a new family of potent and selective metalloinsertors containing an unusual Rh—O axial coordination. This complex also incorporates a platinum center containing only one labile site for coordination of DNA, rather than two, which leads to nonclassical platinum adduct formation selectively at mismatched DNA. Finally, we synthesized a mixed metal dinuclear Rh(III)/Pt(II) complex, wherein both the rhodium and platinum centers are coordinated to a bridging aromatic ligand capable of interaction with the DNA base stack through either intercalation or insertion. These complexes bind DNA mismatches from

the minor groove through metalloinsertion, situating the reactive platinum metal center directly at the mismatched site.

In the development of metalloinsertor-*cis*-platinum conjugates, we have acquired a diverse repertoire of bifunctional complexes with mismatch recognition capability as well as the ability to form covalent adducts. Although we have yet to achieve cell-selective toxicity in MMR-deficient cells, we almost universally observe potency surpassing that of the FDA-approved chemotherapeutic cisplatin in a variety of human cancer cell lines. Moreover, a significant finding in our study of these conjugates has been the discovery that these complexes induce apoptotic cell death, rather than the necrotic pathway typically triggered by rhodium metalloinsertors. It appears that rerouting to the apoptotic pathway is incongruous with the uniquely selective biological activity observed for metalloinsertors. This result suggests that there is a critical response to mismatch recognition in a cellular environment that leads to cell-selective activity.

We further explored the underlying mechanisms surrounding the biological response to mismatch recognition by metalloinsertors in the genome. Immunofluorescence assays of MMR-deficient and MMR-proficient cells revealed that a critical biomarker for DNA damage, phosphorylation of histone H2AX (γ H2AX) rapidly accumulates in response to metalloinsertor treatment, signifying the induction of double strand breaks in the genome. Significantly, we have discovered that our metalloinsertor complexes selectively inhibit transcription in MMR-deficient cells, which may be a crucial checkpoint in the eventual breakdown of the cell via necrosis. Additionally, preliminary *in vivo* studies have revealed the capability of these compounds to traverse the complex environments of multicellular organisms and accumulate in MMR-deficient

tumors. Our ever-increasing understanding of metalloinsertors, as well as the development of new generations of complexes both monofunctional and bifunctional, enables their continued progress into the clinic as promising new chemotherapeutic agents.

Table of Contents

Chapter 1: Introduction	1
1.1 Overview: Inorganic Complexes as Chemotherapeutic Agents.....	1
1.2 Platinum-Based Chemotherapeutics.....	3
1.2.1 Mechanism of <i>Cis</i> -platinum (II) Activity.....	3
1.2.2 Cisplatin Derivatives and Analogues.....	6
1.3 Targeted Chemotherapy with Metal Complexes.....	8
1.3.1 Proteins as Targets.....	10
1.3.2 Organelles as Targets.....	12
1.4 DNA as a Target: Noncovalent Binding.....	12
1.4.1 Metallointercalators.....	14
1.4.2 Metallointercalators for Selective DNA Recognition.....	19
1.4.3 Metalloinsertors.....	22
1.4.4 Metalloinsertors as Targeted Chemotherapeutics.....	25
1.5 Expanding the Reactivity of Metalloinsertors: Bifunctional Conjugates..	32
1.5.1 Metalloinsertor-Alkylator Conjugate.....	34
1.5.2 Metalloinsertor Conjugate for DNA Cleavage.....	36
1.5.3 Metalloinsertor-Cisplatin Conjugate.....	36
1.5.4 Metalloinsertors Conjugated to Cell-Penetrating Peptides.....	37
1.5.5 Outlook for Bifunctional Metalloinsertor Conjugates.....	38
1.6 Conclusions.....	41
1.7 References.....	43

Chapter 2: Cell-Selective Biological Activity of Rhodium

Metalloinsertors Correlates with Subcellular Localization.....50

2.1	Introduction.....	50
2.2	Experimental Protocols.....	54
2.2.1	Materials.....	54
2.2.2	Ligand Synthesis.....	54
2.2.2.1	Tert-butyl 2-(di(pyridine-2-yl)amino)acetate.....	54
2.2.2.2	2-(di(pyridine-2-yl)amino)ethanol.....	55
2.2.2.3	N-propyl-N-(pyridin-2-yl)pyridin-2-amine.....	55
2.2.3	Metal Complexes.....	57
2.2.3.1	$\text{Rh}(\text{NH}_3)_4\text{chrysi}^{3+}$	57
2.2.3.2	<i>rac</i> - $\text{Rh}(\text{DPAE})_2\text{chrysi}^{3+}$	57
2.2.3.3	<i>rac</i> - $\text{Rh}(\text{PrDPA})_2\text{chrysi}^{3+}$	59
2.2.4	Octanol/Water Partition Coefficient (log P).....	59
2.2.5	Cell Culture.....	60
2.2.6	Cellular Proliferation ELISA.....	60
2.2.7	Cellular Proliferation MTT.....	60
2.2.8	Binding Competition Titrations.....	61
2.2.9	Whole-Cell Rhodium Accumulation.....	63
2.2.10	Mitochondrial Rhodium Accumulation.....	63
2.2.11	Nuclear Rhodium Accumulation.....	64
2.3	Results.....	65

2.3.1	Synthesis and Characterization of $[\text{Rh}(\text{DPAE})_2\text{chrysi}]^{3+}$ and $[\text{Rh}(\text{PrDPA})_2\text{chrysi}]^{3+}$	65
2.3.2	DNA Binding Affinity.....	66
2.3.3	Cellular Proliferation ELISA.....	68
2.3.4	MTT Cytotoxicity Assay.....	73
2.3.5	Cellular Uptake of Metal Complexes.....	76
2.3.7	ICP-MS Assay for Nuclear Rhodium Levels.....	80
2.3.8	ICP-MS Assay for Mitochondrial Rhodium Levels.....	82
2.4	Discussion.....	83
2.4.1	Biological Activity of Rhodium Metalloinsertors.....	83
2.4.2	Biological Effects of Simple Changes in Functionality on Rhodium Metalloinsertors.....	85
2.4.3	Metalloinsertor Uptake and Nuclear Accumulation.....	87
2.4.4	Mitochondrial Accumulation of Rhodium Metalloinsertors.....	90
2.4.5	General Implications for Design.....	92
2.5	Conclusions.....	94
2.6	References.....	95

Chapter 3: Construction and Application of a Rh-Pt DNA

	Metalloinsertor Conjugate.....	98
3.1	Introduction.....	98
3.2	Experimental Protocols.....	99
3.2.1	Materials.....	99

3.2.2	Synthesis of Rhodium Scaffold Precursor.....	100
3.2.2.1	[Rh(HDPA)Cl ₄]HDPA.....	100
3.2.2.2	[Rh(HDPA)(OTf) ₄]HDPA.....	101
3.2.2.3	[Rh(HDPA)(NH ₃) ₄](OTf) ₃	101
3.2.2.4	[Rh(HDPA)(chrysi)(NH ₃) ₂](TFA) ₃	103
3.2.2.5	[Rh(HDPA)(chrysi)(dpa-AcOH)](TFA) ₃	103
3.2.3	Synthesis of Rh(Amal) and RhPt.....	104
3.2.3.1	[Rh(HDPA)(chrysi)(diethyl-2-(2-(di(pyridin-2-yl)amino)acetamido)malonate)] (TFA) ₃	104
3.2.3.2	[Rh(HDPA)(chrysi)(2-(2-(di(pyridin-2-yl)amino)acetamido)-3-ethoxy-3-oxopropanoic acid)] (TFA) ₃	105
3.2.3.3	RhPt.....	105
3.2.4	[Pt(DACH)(aminomalonate)].....	107
3.2.5	Photocleavage Competition Titrations.....	109
3.2.6	Binding Constant Determination.....	110
3.2.7	Dimethyl Sulfate Footprinting of Platinated DNA.....	111
3.2.8	Cell Culture.....	111
3.2.8.1	HCT116N/O.....	111
3.2.8.2	A2780cis.....	112
3.2.9	Cellular Proliferation ELISA.....	112
3.2.10	ICP-MS Assay for Whole-Cell Rh and Pt Levels.....	112
3.2.11	ICP-MS Assay for Nuclear Rh and Pt Levels.....	113
3.2.12	ICP-MS Assay for Mitochondrial Rh and Pt Levels.....	114

3.2.13	MTT Cytotoxicity Assay.....	114
3.2.14	Preparation of Cell Extracts for <i>In Vitro</i> DNA Replication Assay.....	114
3.2.15	<i>In Vitro</i> SV40 DNA Replication Assay.....	116
3.3	Results	
3.3.1	Complexes Synthesized.....	116
3.3.2	DNA Binding Studies.....	118
3.3.2.1	Binding Affinity of Rhodium at a CC Mismatch.....	118
3.3.2.2	Platinum Binding to DNA.....	120
3.3.2.3	Dimethyl Sulfate Footprinting of Pt-DNA Crosslinks.....	120
3.3.3	Quantitation of Inhibition of Cellular Proliferation Using an Enzyme-Linked Immunosorbent Assay (ELISA).....	123
3.3.4	Cell-Free SV40 DNA Replication Assay.....	128
3.3.5	MTT Cytotoxicity.....	129
3.3.6	ICP-MS Assay for Whole-Cell Rhodium and Platinum Levels.....	132
3.3.7	ICP-MS Assay for Nuclear Rhodium and Platinum Levels.....	136
3.3.8	ICP-MS Assay for Mitochondrial Rhodium and Platinum Levels.....	138
3.3.9	Caspase and PARP Inhibition Assays.....	141
3.4	Discussion.....	144
3.4.1	DNA Binding Behavior.....	144
3.4.2	Antiproliferative and Cytotoxic Activity in MMR-Deficient Cells.....	145
3.4.3	Cellular Uptake and Subcellular Localization of Metal Complexes.....	147

3.4.4	Mechanism of Cell Death.....	148
3.5	Conclusions.....	149
3.6	References.....	150

Chapter 4: Targeting Platinum to DNA Mismatches via Conjugation to a Metalloinsertor Containing a Rh—O Bond.....153

4.1	Introduction.....	153
4.2	Experimental.....	159
4.2.1	Materials.....	159
4.2.2	Synthesis of $[\text{Rh}(\text{chrysi})(\text{phen})(\text{DPE-Pt}(\text{NH}_3)_2\text{Cl})]^{3+}$	159
4.2.3	Photocleavage Competition Titrations.....	160
4.2.4	Binding Constant Determination.....	163
4.2.5	Platinum Binding to Mismatched and Well-Matched Duplex DNA.....	164
4.2.6	Dimethyl Sulfate Footprinting of Platinated DNA.....	165
4.2.7	Cell Culture.....	166
4.2.7.1	HCT116N/O.....	166
4.2.7.2	A2780cis.....	166
4.2.8	MTT Cytotoxicity Assay.....	166
4.2.9	MTT Caspase and PARP Inhibition Assays.....	167
4.3	Results.....	167
4.3.1	DNA Binding Studies.....	168
4.3.1.1	Binding Affinity of Rhodium at a CC Mismatch.....	168
4.3.1.2	Platination of Mismatched and Well-Matched DNA.....	170

4.3.1.3	Dimethyl Sulfate Footprinting of Pt-DNA Crosslinks.....	177
4.3.2	MTT Cytotoxicity Assay.....	178
4.3.3	Caspase and PARP Inhibition Assays.....	182
4.4	Discussion.....	187
4.4.1	Synthesis of $[\text{Rh}(\text{chrysi})(\text{phen})(\text{DPE-Pt}(\text{NH}_3)_2\text{Cl})]^{3+}$	187
4.4.2	DNA Binding Behavior.....	189
4.4.3	Characterization in Cell Tissue Culture.....	193
4.5	Conclusions.....	194
4.6	References.....	196

Chapter 5: Synthesis and Characterization of Bimetallic Rh(III)-Pt(II) DNA Mismatch Binding Complexes with Bridging Intercalator Ligands.....200

5.1	Introduction.....	200
5.2	Experimental Protocols.....	206
5.2.1	Materials.....	206
5.2.2	Ligand Synthesis.....	207
5.2.2.1	Synthesis of 5,6-dihydrobenzo[<i>b</i>][1,10]phenanthroline..	207
5.2.2.2	Synthesis of benzo[<i>b</i>][1,10]phenanthroline-5,6-dione....	207
5.2.3	Synthesis of Metal Complexes.....	210
5.2.3.1	$[\text{PtCl}_2(\text{phendione})]$	210

5.2.3.2	$[(bpy)_2Rh(\mu\text{-phendione})PtCl_2]^{3+}$	210
5.2.3.3	$[Rh(bpy)_2bzp]^{3+}$	213
5.2.3.4	$[(bpy)_2Rh(\mu\text{-bzip})PtCl_2]^{3+}$	213
5.2.4	DNA Binding Behavior.....	217
5.2.4.1	Photocleavage Competition Titration of $[Rh(bpy)_2chrysi]^{3+}$ with $[(bpy)_2Rh(\text{phendione})PtCl_2]^{3+}$	217
5.2.4.2	Photocleavage Titration of $[(bpy)_2Rh(\mu\text{-bzip})PtCl_2]^{3+}$	220
5.2.4.3	Analysis of DNA Binding.....	221
5.3	Results.....	222
5.3.1	Complexes Synthesized.....	222
5.3.2	DNA Binding of $[(bpy)_2Rh(\text{phendione})PtCl_2]^{3+}$	222
5.3.2.1	Binding of $[(bpy)_2Rh(\text{phendione})PtCl_2]^{3+}$ to a CC Mismatch.....	223
5.3.2.2	Covalent Platinum Binding of $[(bpy)_2Rh(\text{phendione})PtCl_2]^{3+}$ to Mismatched and Well-Matched DNA.....	226
5.3.3	DNA Binding of $[(bpy)_2Rh(\mu\text{-bzip})PtCl_2]^{3+}$	228
5.3.3.1	Binding of $[(bpy)_2Rh(\mu\text{-bzip})PtCl_2]^{3+}$ to a CC Mismatch.....	228
5.3.3.2	Binding of $[(bpy)_2Rh(\mu\text{-bzip})PtCl_2]^{3+}$ to a GA Mismatch.....	234
5.3.3.3	Binding of $[(bpy)_2Rh(\mu\text{-bzip})PtCl_2]^{3+}$ to Mismatched and Well- Matched DNA Hairpins.....	236
5.4	Discussion.....	238

5.5	Conclusions.....	244
5.6	References.....	247

Chapter 6: Cellular Processing of Rhodium Metalloinsertors:

Investigations into the Underlying Biological Mechanisms Involved in Response to Mismatch

Recognition.....250

6.1	Introduction.....	251
6.2	Experimental Protocols.....	254
6.2.1	Materials.....	254
6.2.2	Cell Culture.....	254
6.2.3	Immunofluorescence Staining of Fixed Cells.....	255
6.2.3.1	Cell Treatment and Fixation.....	255
6.2.3.2	Immunofluorescence Staining.....	255
6.2.3.3	Quantification and Analysis of Fluorescence Images.....	256
6.2.4	MTT Cytotoxicity Assay.....	258
6.2.5	Comet Assay for Damage of Cellular DNA.....	258
6.2.6	Assay for <i>In Cellulo</i> RNA Synthesis in HCT116N and O Cells.....	259
6.2.7	Animals.....	260
6.2.8	Analysis of Tumor Samples for Rhodium Content by ICP-MS.....	261
6.3	Results.....	261
6.3.1	Immunofluorescence Staining of HCT116 Cells.....	261

6.3.1.1	Induction of γ H2AX in HCT116 Cells.....	263
6.3.1.2	Induction of 53BP1 in HCT116 Cells.....	271
6.3.2	MTT Cytotoxicity Assay.....	274
6.3.3	Metalloinsertors Induce Double Strand Breaks in the Genome of MMR-deficient Cells: Comet Assay.....	277
6.3.4	Fluorescence Detection of Nascent RNA Synthesis <i>in Cellulo</i>	281
6.3.5	Rhodium Accumulation in Tumors.....	282
6.4	Discussion.....	288
6.4.1	Metalloinsertors Damage Genomic DNA.....	288
6.4.2	Metalloinsertors Inhibit Transcription in MMR-Deficient Cells.....	291
6.4.3	Effects of Rhodium Metalloinsertors <i>in Vivo</i>	292
6.5	Conclusions.....	293
6.6	References.....	295
	Chapter 7: Summary and Outlook.....	299

List of Figures, Tables, and Schemes

Figure 1.1	Chemical structures of classical, FDA-approved platinum-based chemotherapeutics.....	2
Figure 1.2	Chemical structures of targeted chemotherapeutics.....	9
Figure 1.3	Design of Octasporine complexes as inhibitors of protein kinases.....	11
Figure 1.4	Chemical structures of octahedral ruthenium (II) tris(phenanthroline) complexes.....	15
Figure 1.5	Chemical structures of Δ -[Rh(bpy) ₂ phi] ³⁺ and Δ -[Ru(bpy) ₂ dppz] ²⁺	16
Figure 1.6	Rhodium (III) intercalators.....	18
Figure 1.7	Structure of Δ - α -[Rh[(R,R)-Me ₂ trien]phi] ³⁺	21
Figure 1.8	Comparison of the width of intercalating ligand phi and inserting ligand chrysi.....	23
Figure 1.9	Chemical structures of Δ -[Rh(bpy) ₂ chrysi] ³⁺ and Δ -[Rh(bpy) ₂ phzi] ³⁺	26
Figure 1.10	Metalloinsertor DNA binding and cytotoxicity.....	28
Figure 1.11	Effects of the non-inserting ancillary ligands on the biological activity of rhodium metalloinsertors.....	30
Figure 1.12	Inhibitory effects of [Rh(DPAE) ₂ chrysi] ³⁺ and [Rh(PrDPA) ₂ chrysi] ³⁺ on cellular proliferation and subcellular localization.....	31
Figure 1.13	NCI-H23 subclones treated with cisplatin and [Rh(chrysi)(phen)(DPE)] ²⁺	33
Figure 1.14	Chemical structures of bifunctional, mismatch-specific metalloinsertor conjugates.....	35
Figure 1.15	Structure of a metalloinsertor-peptide conjugate.....	39

Figure 1.16	Chemical structures and binding affinities for a CC mismatch of a new family of metalloinsertor complexes bearing Rh—O ligand coordination.....	40
Figure 2.1	Rh(L) ₂ chrysi ³⁺ metalloinsertors. [Rh(DPAE) ₂ chrysi] ³⁺ and [Rh(PrDPA) ₂ chrysi] ³⁺	53
Figure 2.2	Binding affinities determined through DNA photocleavage.....	62
Figure 2.3	Sigmoidal curves for competition titrations with Rh(DPAE) ₂ chrysi ³⁺ and Rh(PrDPA) ₂ chrysi ³⁺	67
Figure 2.4	Chemical structures, binding affinities for CC mismatches, and approximated nuclear concentration of all compounds studied.....	69
Figure 2.5	Inhibitory effects of [Rh(DPAE) ₂ chry] ³⁺ and [Rh(PrDPA) ₂ chrysi] ³⁺ as a function of incubation time on cellular proliferation.....	70
Figure 2.6	Inhibitory effects of rhodium metalloinsertors as a function of metalloinsertor identity.....	72
Figure 2.7	Cell viability of HCT116O cells treated with either [Rh(DPAE) ₂ chrysi] ³⁺ or [Rh(PrDPA) ₂ chrysi] ³⁺ over a 24 h period, as determined by MTT assay.....	74
Figure 2.8	Differential cytotoxicities of rhodium metalloinsertors [Rh(DPAE) ₂ chrysi] ³⁺ and [Rh(PrDPA) ₂ chrysi] ³⁺	75
Figure 2.9	ICP-MS assay for rhodium uptake in whole cell extracts.....	77
Figure 2.10	ICP-MS assay for whole-cell rhodium accumulation.....	79
Figure 2.11	ICP-MS assay for nuclear and mitochondrial rhodium accumulation.....	81
Figure 2.12	ICP-MS assay for rhodium uptake in nuclear and mitochondrial fractions.....	86

Figure 2.13	Model for the requirements for cell-selective targeting of MMR-deficient cells by rhodium metalloinsertors.....	93
Figure 3.1	Chemical structures of RhPt and control complexes studied.....	117
Figure 3.2	Competition titration of of RhPt.....	119
Figure 3.3	Representative sigmoidal curve of photocleavage competition titrations of RhPt for binding constant determination at the CC mismatch.....	121
Figure 3.4	Representative sigmoidal curve fit of DNA platination by the platinum subunit of RhPt.....	122
Figure 3.5	Dimethyl sulfate (DMS) footprinting of RhPt.....	124
Figure 3.6	Inhibitory effects of RhPt, oxaliplatin, and cisplatin on cellular proliferation.....	126
Figure 3.7	Inhibitory effects of all complexes on cellular proliferation in HCT116O cells after 24 h treatment with 2 μ M of each complex.....	127
Figure 3.8	Cell-free <i>in vitro</i> SV40 replication assay with HCT116O extract.....	130
Figure 3.9	Cell-free <i>in vitro</i> SV40 replication assay with Hela cell extract.....	131
Figure 3.10	Dose-response cytotoxicity curves of HCT116O cells treated with RhPt, oxaliplatin, Rh(Amal), Pt(Amal), and cisplatin.....	133
Figure 3.11	Dose-response cytotoxicity curves of cisplatin-resistant A2780cis cells.....	134
Figure 3.12	Cellular accumulation of metal complexes in HCT116O cells.....	137
Figure 3.13	Subcellular localization of metal complexes.....	139

Figure 3.14	Cell viability in HCT116O cells after 72h with PARP and caspase inhibitors.....	143
Figure 3.15	The bifunctional DNA metalloinsertor conjugate (“RhPt”).....	146
Figure 4.1	Chemical structures of $[\text{Rh}(\text{chrysi})(\text{phen})(\text{DPE-Pt}(\text{NH}_3)_2\text{Cl})]^{3+}$, $[\text{Rh}(\text{chrysi})(\text{phen})(\text{DPE})]^{2+}$, and cisplatin.....	158
Figure 4.2	ESI-MS spectrum of $[\text{Rh}(\text{chrysi})(\text{phen})(\text{DPE-Pt}(\text{NH}_3)_2\text{Cl})]^{3+}$	162
Figure 4.3	Competition titration of $[\text{Rh}(\text{chrysi})(\text{phen})(\text{DPE-Pt}(\text{NH}_3)_2\text{Cl})]^{3+}$ at a DNA mismatch.....	169
Figure 4.4	Representative sigmoidal curve of photocleavage competition titrations of $[\text{Rh}(\text{chrysi})(\text{phen})(\text{DPE-Pt}(\text{NH}_3)_2\text{Cl})]^{3+}$ for binding constant determination at the CC mismatch.....	172
Figure 4.5	Autoradiogram depicting the formation of covalent platinum adducts with mismatched and well-matched DNA duplexes as a function of time.....	173
Figure 4.6	Quantification of platination of mismatched and well-matched duplex DNA by $[\text{Rh}(\text{chrysi})(\text{phen})(\text{DPE-Pt}(\text{NH}_3)_2\text{Cl})]^{3+}$	174
Figure 4.7	Autoradiogram depicting the formation of covalent platinum adducts with mismatched and well-matched DNA duplexes as a function of metalloinsertor concentration.....	175
Figure 4.8	Quantification of platination of mismatched and well-matched duplex DNA (by $[\text{Rh}(\text{chrysi})(\text{phen})(\text{DPE-Pt}(\text{NH}_3)_2\text{Cl})]^{3+}$ as a function of concentration.....	176
Figure 4.9	Dimethyl sulfate (DMS) footprinting of 5'-end radiolabeled duplex DNA containing a CC mismatch.....	179

Figure 4.10	MTT cytotoxicity assay of HCT116N (MMR-proficient) and HCT116O (MMR-deficient) cells treated with $[\text{Rh}(\text{chrysi})(\text{phen})(\text{DPE-Pt}(\text{NH}_3)_2\text{Cl})]^{3+}$, cisplatin, and $[\text{Rh}(\text{chrysi})(\text{phen})(\text{DPE})]^{2+}$	181
Figure 4.11	MTT cytotoxicity assay of cisplatin-resistant A2780cis cells treated with $[\text{Rh}(\text{chrysi})(\text{phen})(\text{DPE})]^{2+}$	182
Figure 4.12	Cell viability in HCT116N and HCT116O cells after treatment with PARP inhibitor DPQ.....	184
Figure 4.13	Cell viability in HCT116N and HCT116O cells after treatment with caspase inhibitor Z-VAD-FMK.....	186
Figure 5.1	General structures of two distinct families of Rh-Pt metalloinsertor conjugates.....	204
Figure 5.2	Chemical structures of two mixed-metal Rh(III)/Pt(II) metalloinsertor complexes, wherein both metal centers are coordinated to the bridging aromatic ligand that interacts with the DNA base stack.....	205
Figure 5.3	UV-visible spectrum of $[(\text{bpy})_2\text{Rh}(\mu\text{-phenidione})\text{PtCl}_2]^{3+}$	214
Figure 5.4	UV-visible spectrum of $[\text{Rh}(\text{bpy})_2\text{bzp}]^{3+}$	216
Figure 5.5	UV-visible spectrum of $[(\text{bpy})_2\text{Rh}(\mu\text{-bzp})\text{PtCl}_2]^{3+}$	219
Figure 5.6	Photocleavage titration of $[(\text{bpy})_2\text{Rh}(\mu\text{-phenidione})\text{PtCl}_2]^{3+}$	224
Figure 5.7	Competition titration of $[(\text{bpy})_2\text{Rh}(\mu\text{-phenidione})\text{PtCl}_2]^{3+}$	225
Figure 5.8	Representative plot of photocleavage competition titrations of $[(\text{bpy})_2\text{Rh}(\mu\text{-phenidione})\text{PtCl}_2]^{3+}$	227

Figure 5.9 Representative sigmoidal curve fit of DNA platination by the platinum subunit of $[(bpy)_2Rh(phendione)PtCl_2]^{3+}$	229
Figure 5.10 Representative exponential curve fit of DNA platination by the platinum subunit of $[(bpy)_2Rh(phendione)PtCl_2]^3$ after 2h incubation.....	230
Figure 5.11 Photocleavage titration of $[(bpy)_2Rh(\mu-bzp)PtCl_2]^{3+}$ at a CC mismatch.....	232
Figure 5.12 Quantification of the percentage of DNA containing a CC mismatch that is photocleaved and platinated by $[(bpy)_2Rh(\mu-bzp)PtCl_2]^{3+}$	233
Figure 5.13 Photocleavage titration of $[(bpy)_2Rh(\mu-bzp)PtCl_2]^{3+}$ at a GA mismatch.....	235
Figure 5.14 Photocleavage titration of $[(bpy)_2Rh(\mu-bzp)PtCl_2]^{3+}$ with mismatched and well-matched DNA.....	237
Figure 5.15 Quantification of the percentage of hairpin DNA containing a CC mismatch or is fully matched that is platinated by $[(bpy)_2Rh(\mu-bzp)PtCl_2]^{3+}$ as a function of complex concentration.....	239
Figure 5.16 Quantification of the percentage of platinated CC-mismatched and well-matched DNA by $[(bpy)_2Rh(\mu-bzp)PtCl_2]^{3+}$ (50 μ M) either in the absence of irradiation or after 15 min irradiation.....	240
Figure 5.17 Schematic of hypothesized binding interactions of $[(bpy)_2Rh(\mu-bzp)PtCl_2]^{3+}$ in the presence of mismatched DNA versus well-matched DNA.....	245

Figure 6.1	Chemical structures of $[\text{Rh}(\text{chrysi})(\text{phen})(\text{PPO})]^{2+}$, $[\text{Rh}(\text{chrysi})(\text{phen})(\text{PPE})]^{2+}$, $[\text{Rh}(\text{HDP A})_2\text{chrysi}]^{3+}$, (<i>S</i>)-(+)-Camptothecin, and cisplatin.....	262
Figure 6.2	Confocal microscopy of immunofluorescence for γH2AX	264
Figure 6.3	Confocal microscopy of dose-dependent immunofluorescence for γH2AX as a function of rhodium concentration.....	265
Figure 6.4	Confocal microscopy of dose-dependent immunofluorescence for γH2AX as a function of time.....	267
Figure 6.5	Quantitation of γH2AX foci in rhodium-treated HCT116N and HCT116O cells over time.....	268
Figure 6.6	Quantitation of γH2AX -positive HCT116N and HCT116O cells over time treated with rhodium or camptothecin over time.....	270
Figure 6.7	Quantitation of γH2AX foci in untreated or camptothecin-treated HCT116N and HCT116O cells over time.....	272
Figure 6.8	Confocal microscopy of immunofluorescence for 53BP1.....	273
Figure 6.9	Quantitation of 53BP1 foci in untreated, rhodium treated, or camptothecin-treated HCT116N and HCT116O cells over time.....	275
Figure 6.10	Quantitation of 53BP1-positive HCT116N and HCT116O cells over time treated with rhodium or camptothecin over time.....	276
Figure 6.11	MTT cytotoxicity assay of HCT116N and HCT116O cells treated with $[\text{Rh}(\text{chrysi})(\text{phen})(\text{PPO})]^{2+}$ and camptothecin.....	278
Figure 6.12	Single cell gel electrophoresis of HCT116N and HCT116O cells.....	280

Figure 6.13	Analysis of RNA synthesis in HCT116N and HCT116O cells as a function of $[\text{Rh}(\text{chrysi})(\text{phen})(\text{PPO})]^{2+}$ or cisplatin concentration.....	283
Figure 6.14	Rhodium accumulation in human HCT116 tumors harvested from nude mice.....	285
Table 2.1	Qualitative nuclear ^a and mitochondrial ^b uptake properties, as well as the presence or absence of cell-selective biological activity ^c for metalloinsertors.....	88
Table 3.1	LC ₅₀ Values ^a of Metal Complexes in HCT116O and A2780cis Cells.....	135
Table 3.2	Subcellular Distribution of Metal Complexes in HCT116O Cells.....	140
Table 6.1	Antibodies for Immunofluorescence Staining.....	257
Table 6.2	Rhodium Accumulation in HCT116 Tumors.....	287
Scheme 1.1	Thermal activation of cisplatin via associative ligand substitution of the labile chloride ligands with water molecules.....	5
Scheme 2.1	Synthesis of ancillary ligands 2-(di(pyridine-2-yl)amino)ethanol (DPAE) and N-propyl-N-(pyridin-2-yl)pyridin-2-amine (PrDPA).....	56
Scheme 2.2	Synthesis of <i>rac</i> - $[\text{Rh}(\text{L})_2\text{chrysi}]^{3+}$	58
Scheme 3.1	Synthesis of rhodium metalloinsertor scaffold for conjugation, $[\text{Rh}(\text{chrysi})(\text{HDPA})(\text{dpa-AcOH})]^{3+}$	102
Scheme 3.2	Synthesis of conjugate RhPt and its immediate precursor Rh(Amal).....	106
Scheme 3.3	Synthesis of platinum subunit, Pt(Amal).....	108
Scheme 4.1	Synthesis of $[\text{Rh}(\text{chrysi})(\text{phen})(\text{DPE-Pt}(\text{NH}_3)_2\text{Cl})]^{3+}$	161
Scheme 5.1	Synthesis of 5,6-dihydrobenzo[<i>b</i>][1,10]phenanthroline.....	208

Scheme 5.2	Synthesis of benzo[<i>b</i>][1,10]phenanthroline-5,6-dione.....	209
Scheme 5.3	Synthesis of [PtCl ₂ (phendione)].....	211
Scheme 5.4	Synthesis of [(bpy) ₂ Rh(μ-phendione)PtCl ₂] ³⁺	212
Scheme 5.5	Synthesis of [Rh(bpy) ₂ bzp] ³⁺	215
Scheme 5.6	Synthesis of [(bpy) ₂ Rh(μ-bzp)PtCl ₂] ³⁺	218

Chapter 1: Introduction*

1.1 Overview: Inorganic Complexes as Chemotherapeutic Agents

The serendipitous discovery of the anticancer properties of *cis*-dichlorodiammineplatinum (II) (cisplatin) in 1965 played an integral role in the birth of medicinal inorganic chemistry as a field.¹⁻⁵ Metal complexes, previously considered to be simply toxic, could now be applied strategically to inhibit the rapid cell division of malignant cancers. For many years, the field focused on the development of more potent analogues, mainly in the form of second and third generation derivatives of cisplatin, leading to the FDA approval of two additional *cis*-platinum(II) complexes, carboplatin and oxaliplatin (**Figure 1.1**).^{2,3} Cisplatin and carboplatin, in particular, have been highly successful in the treatment of a variety of cancers, including testicular, ovarian, cervical, and non-small cell lung cancers.⁴ However, these treatments are often associated with severe side effects and a build-up of resistance. These issues have led researchers to focus more recently on the development of novel non-platinum chemotherapeutics.

The rich photophysical and photochemical properties of metal complexes, in addition to their basic coordination chemistry, make them ideal scaffolds for a wide variety of biological applications. Though the pharmaceutical industry in general has shied away from “heavy metal” therapeutics, with the exception of cisplatin and its derivatives, there are in fact real opportunities in the development of transition metal pharmaceuticals, given their high modularity, ease of synthesis in preparing molecules of complex shapes and

*Adapted from Weidmann, A. G.; Komor, A. C.; Barton, J. K. Targeted Chemotherapy with Metal Complexes. *Comments in Inorg. Chem.* **2014**, *34*, 114-123. DOI: 10.1080/02603594.2014.890099.

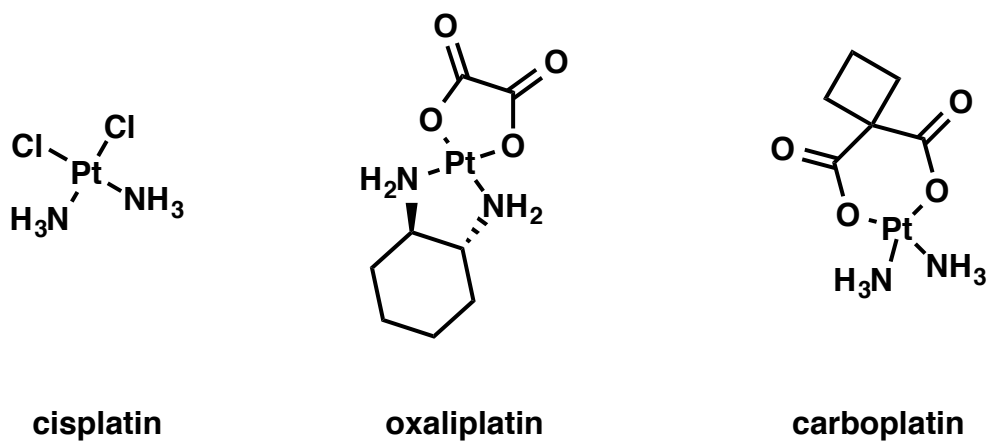


Figure 1.1 Chemical structures of classical, FDA-approved platinum-based chemotherapeutics.

symmetries, and the ability to monitor their fate within the cell using a variety of spectroscopies.

The traditional focus of many laboratories has been in the development of more potent metal complexes that function like cisplatin in coordinating to DNA but are more effective, either because of more optimum uptake characteristics, or the inability of lesions formed to be easily detected and repaired. Much time and attention have been spent in this arena. However, the goal has moved also to the design of complexes with a new strategy based upon selectivity, with the preparation of transition metal complexes that are more selective than cisplatin owing to a design strategy where the complex interacts with a specific biological target found prominently in cancer cells.

1.2 Platinum-Based Chemotherapeutics

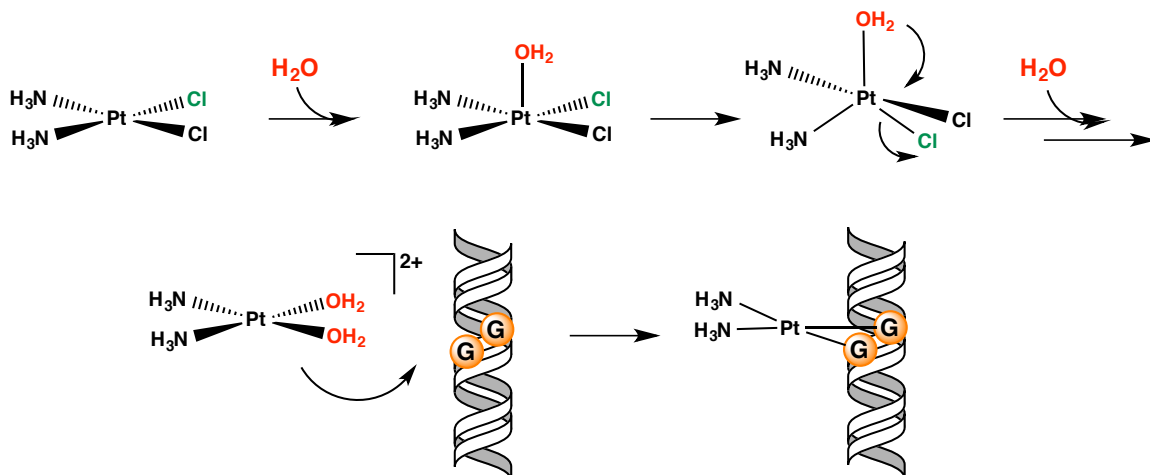
1.2.1 Mechanism of *Cis*-platinum (II) Activity

The anticancer properties of cisplatin and its analogues arise primarily from their ability to covalently bind DNA. In the case of cisplatin, the *cis*-chloride ligands remain largely inert in an extracellular environment, where the salt concentration is high ($[Cl^-] = 100 \text{ mM}$). Once inside the cell, the chloride concentration decreases approximately 25 fold.^{5,6} Cisplatin then becomes aquated via a reversible associative ligand substitution mechanism, driven forward by the reduced intracellular chloride concentration.⁵ The subtle hydrolysis kinetics of cisplatin are critical to its efficacy and distinguish it from its clinically ineffective stereoisomer, transplatin. The *trans* effect labilizes the chloride ligands of transplatin, deactivating the complex before it can achieve potency.⁷ In contrast, the resulting *cis*- $[Pt(NH_3)_2(OH_2)_2]^{2+}$ is a potent electrophile that readily reacts with various biological ligands, but its primary therapeutic target is DNA. In particular, cisplatin

forms crosslinks at the *N7* position of guanine residues, which is the most nucleophilic site on DNA (**Scheme 1.1**). Due to the presence of two *cis*-labile ligands, *cis*-platinum complexes generally form 1,2- and 1,3-intrastrand crosslinks – known as “bifunctional” adducts – with guanine residues in the major groove, which account for more than 90% of *cis*-platinum-DNA adducts in the cell.⁴

Platinum adducts severely distort DNA through helical unwinding and bending; in the case of cisplatin, 1,2-intrastrand crosslinks bend the duplex up to 60° toward the major groove, exposing a wide and shallow minor groove. Several classes of proteins, including those involved in DNA repair, recognize this lesion, triggering a variety of biological responses.⁵ For example, proteins involved in the correction of DNA base pair mismatches, known as the mismatch repair (MMR) pathway, bind cisplatin-DNA adducts and attempt, unsuccessfully, to initiate repair. The inability of repair enzymes to fix the damaged DNA leads to inhibition of transcription and DNA synthesis, as platinated residues cannot be properly replicated.^{4,5} This in turn causes cell-cycle arrest and, ultimately, cell death by apoptosis.⁸ As a result, *cis*-platinum (II) activity is most potent in rapidly dividing cells, such as those involved in carcinogenesis.

In some cases, platinum adducts are recognized by proteins that are able to excise the lesion and thus repair the DNA. For instance, nucleotide excision repair (NER) proteins, which recognize and repair DNA damage that distorts the helix, are able to successfully restore crosslinked DNA to its original state, leading to cisplatin resistance.⁹⁻¹¹ In cisplatin-sensitive cells, platinum adducts are often recognized first by alternative proteins, such as high mobility group (HMG)-domain proteins, which shield the lesions from binding and repair by the NER pathway.^{12,13}



Scheme 1.1 Thermal activation of cisplatin via associative substitution of the labile chloride ligands with water molecules. The resulting cisplatin di-aqua complex is a potent electrophile that reacts readily with DNA, preferentially forming 1,2-intrastrand cross-links with nucleophilic guanine residues (represented by “G” in the orange circles) at the *N7* position.

Cisplatin resistance can arise through recognition and repair of Pt-DNA lesions, as is the case with NER, or through the absence of proteins that process these adducts and induce cell death. Cancers that are deficient in the MMR pathway are generally resistant to cisplatin;^{14,15} the futile cycle of recognition and attempted repair of platinum adducts by MMR proteins is postulated to trigger a signaling cascade that initiates apoptosis.⁴ In cancers that are MMR-deficient, these signaling events do not occur or do so improperly, and thus cells evade cisplatin-induced apoptosis and continue to proliferate. Indeed, loss of MMR proficiency increases the rate of development of resistance to cisplatin 1.8 fold, and MMR-deficiencies are found in 80% of hereditary nonpolyposis colorectal carcinomas and 16% of all solid tumors.^{14,16} Treatment of MMR-deficient cancers with cisplatin can be potentially devastating, in fact, as the preferential targeting of healthy MMR-proficient cells selects for and enables the continued proliferation of the malignant phenotype.

1.2.2 Cisplatin Derivatives and Analogues

In addition to the previous examples, there are many classes of proteins that bind and process cisplatin adducts in DNA and, as a result, many sources of inherent and acquired resistance. Cisplatin resistance can also arise from cellular efflux or deactivation of the drug through off-target binding.¹⁷ Furthermore, cisplatin causes notoriously severe side effects, including kidney failure (nephrotoxicity), nervous system damage (neurotoxicity), hearing loss (ototoxicity), and bone marrow suppression (myelotoxicity).¹⁸ Much effort has been focused on the development of derivatives to overcome the clinical limitations of cisplatin.

To date, thousands of platinum-based anticancer complexes have been synthesized and studied; however, only two have passed clinical trials and been approved for use by the FDA: carboplatin and oxaliplatin (**Figure 1.1**).¹⁸ Despite the limited success of platinum derivatives, a strict structure activity relationship (SAR) had evolved, claiming that *cis*-coordination of two monodentate or one bidentate labile ligand(s) to a platinum (II) center in a square planar geometry was essential for anticancer activity.¹⁹

The FDA-approved therapeutics carboplatin and oxaliplatin follow this classical SAR pattern. Carboplatin contains a bidentate cyclobutanedicarboxylato leaving group ligand and two *cis*-ammine non-leaving group ligands. The dicarboxylate ligand alters the activation kinetics of aquation, reducing side effects and off-target toxicity. The active form of carboplatin, *cis*-[Pt(NH₃)₂(OH)₂]²⁺, is identical to that of cisplatin, however, and forms the same DNA adducts. As a result, carboplatin mitigates the side effects of cisplatin but does not offset resistance.^{19,20}

Oxaliplatin also contains a bidentate oxalate leaving group ligand, but has a bidentate *trans*-(R,R)-1,2-diaminocyclohexane non-leaving group ligand in lieu of free amines.² The covalent adducts formed by oxaliplatin are chemically distinct from that of cisplatin and carboplatin, although it still preferentially binds at d(GpG) sites to form 1,2-intrastrand crosslinks. The distortions to the DNA duplex as a result of oxaliplatin binding are less severe than those of cisplatin, and the hydrogen bonding contacts between the inert amine ligand and the DNA backbone are altered.²¹ As a result, the oxaliplatin-DNA adduct is not recognized by the same proteins that process cisplatin-DNA, including those involved in MMR, and is instead processed by orthogonal biological

pathways.²² Consequently, oxaliplatin displays little cross-resistance with cisplatin and is typically a first-line therapy for MMR-deficient cancers.²³

Over the years, syntheses of platinum complexes have strayed from the restrictive SAR rules to afford octahedral Pt(IV) centers,²⁴ monofunctional Pt(II) complexes containing *N*-heterocyclic ligands,²⁵ *trans*-platinum (II) complexes,²⁶ and many others. Variations in the leaving and non-leaving ligand sets, geometries, and oxidation states have allowed for tunable platinum therapeutics that are highly potent and often exhibit little cross-resistance with cisplatin in many cancerous cell lines. However, the primary mechanism by which these complexes function remains fundamentally the same – that is, they form covalent crosslinks with genomic DNA to interfere with replication, transcription, and mitotic processes to trigger cell death by apoptosis. In this way, cisplatin and its analogues are known as “classical” chemotherapeutics: they achieve potency by damaging cancer cells *more* than healthy cells, yet possess no real mechanism for avoiding healthy cells entirely. For these reasons, research efforts in recent years have shifted towards the development of targeted chemotherapy.

1.3 Targeted Chemotherapy with Metal Complexes

In “targeted” therapy, a drug is developed to target a specific cellular signaling pathway on which cancer cells depend for growth, metastasis, or angiogenesis.²⁷ These types of compounds aim to damage cancer cells *instead* of healthy cells. Targeted therapy focuses on the development of selective therapeutics, whereas classical therapy has focused on the development of increasingly cytotoxic compounds. The next generation of chemotherapeutics has focused on targeting biomolecules, including proteins, organelles, and specific DNA lesions (**Figure 1.2**).

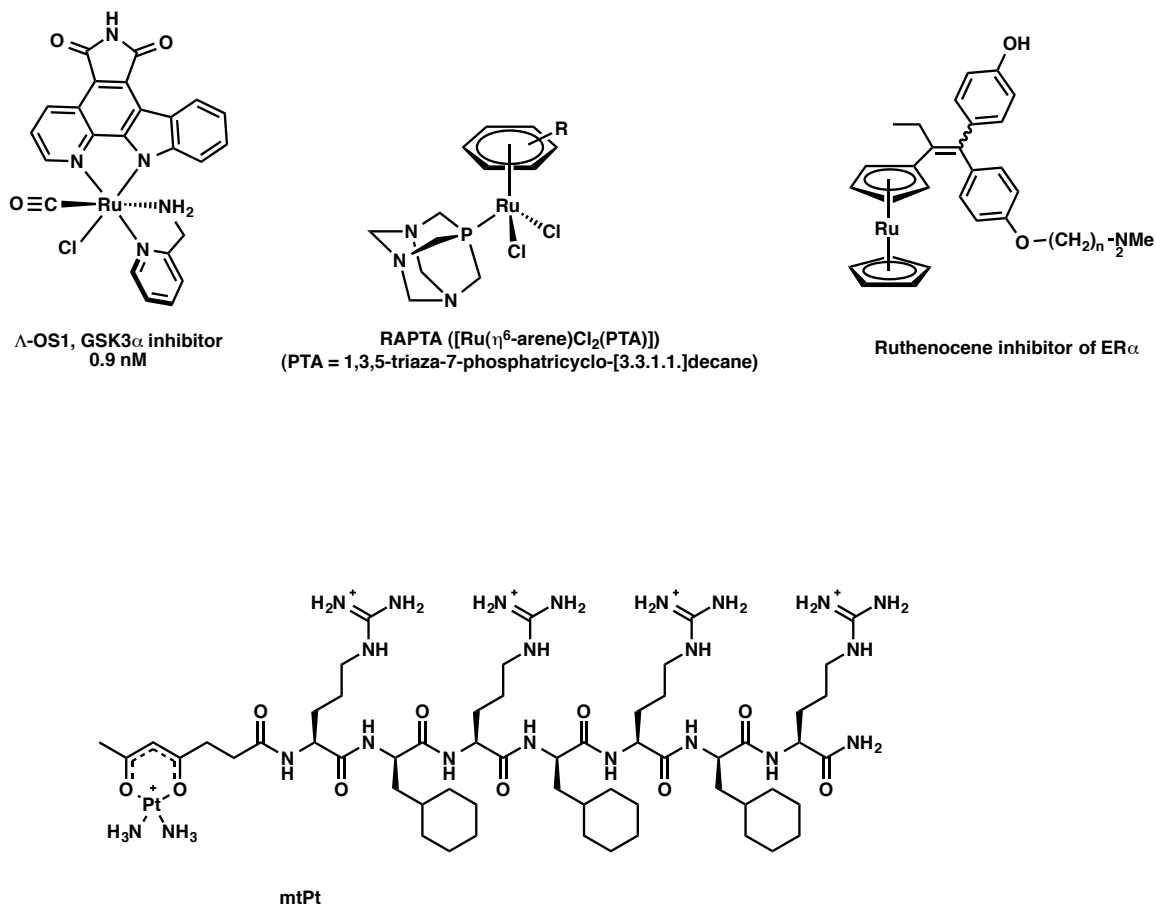


Figure 1.2 Chemical structures of targeted chemotherapeutics discussed in this Chapter: (top, left to right) The octasporine complex OS1, a potent inhibitor of the protein kinase GSK3a; General architecture of RAPTA cathepsin B inhibitors; Ruthenocene analogues of tamoxifen for the selective targeting of ER α ; (bottom, left to right) The first generation rhodium metalloinsertor, [Rh(bpy)₂(chrysi)]³⁺, selectively binds to mismatched and abasic sites in duplex DNA; Structure of mtPt, a cisplatin analogue designed to localize to the mitochondria.

1.3.1 Proteins as Targets

As an illustration, the high levels of mutagenesis in cancerous cells often lead to upregulation and overexpression of proteins, making them attractive candidates for targeting. Metal complexes, due to their modular nature and inherent chirality, are uniquely able to target selectively these chiral biomolecules. In particular, this approach has been applied toward the selective inhibition of kinase activity. Phosphorylation of proteins by kinases is a highly important regulatory activity. However, over-phosphorylation of proteins is common in many types of cancer.²⁸ In a recent study by Meggers et al., inert metal complexes, inspired by the natural product staurosporine and termed octasporines, were designed as highly selective kinase inhibitors (**Figure 1.2**).^{29,30} Six complexes were synthesized, all containing a ruthenium or iridium center and a bidentate pyridocarbazole ligand designed to bind the hinge region of the ATP-binding pocket of the kinase. However, the remaining ligands on each complex were designed to make up a unique set of hydrogen-bonding interactions with the glycine-rich loop of the ATP-binding pockets of six distinct kinases (**Figure 1.3**).²⁹ *In vivo* studies have revealed the anti-angiogenic properties of one of these types of compounds in zebrafish embryos, exemplifying their potential.³⁰

Whereas the previous example utilized the structural complexity of inert metal complexes, the reactive nature of certain metal centers can also be exploited in targeted therapy. Proteases play a crucial role in tumorigenesis by suppressing cell-death pathways and promoting cell-survival pathways.³¹ One such protease, cathepsin B, has been targeted by ruthenium arene RAPTA compounds (**Figure 1.2**).^{32,33} These compounds were found to inhibit cathepsin B protease activity and exhibited selective anti-metastatic

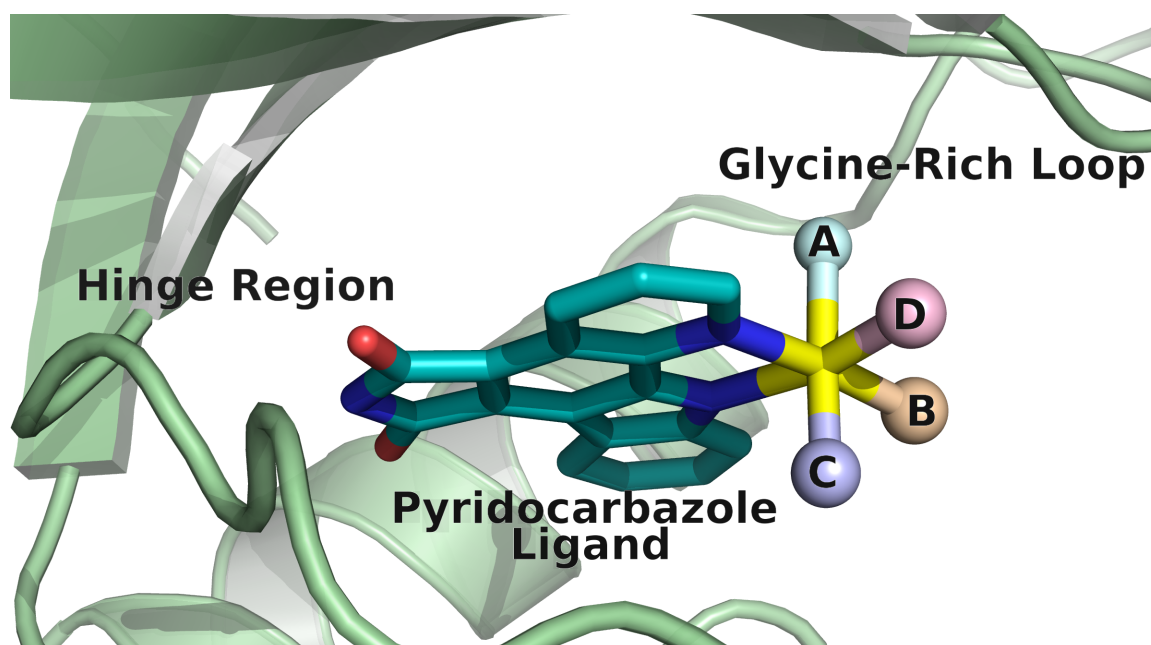


Figure 1.3 Design of Octasporine complexes as inhibitors of protein kinases (adapted from reference 32). The pyridocarbazole ligand, common to all complexes, binds to the hinge region (where the adenine portion of ATP binds) of the ATP-binding pocket. The remaining A, B, C, and D ligands make up a set of hydrogen-bonding interactions with the glycine-rich loop (where the ribose triphosphate portion of ATP binds) of the ATP binding pocket, each unique to a particular kinase.

activity *in vivo*.^{33,34} Estrogen receptors such as estrogen receptor α (ER α), which is over-expressed in several types of breast cancer, have also been the subject of targeted therapy studies.³⁵ Several organometallic analogues of tamoxifen, an antagonist of estrogen receptors, have been developed to selectively target ER α (Figure 1.2).^{36,37} These complexes have demonstrated cytotoxic activity selectively in ER α -positive breast cancer cell lines.³⁶

1.3.2 Organelles as Targets

In addition to protein targeting, the mitochondria can also serve as a valuable target for drug design. Mitochondria produce reactive oxygen species as a byproduct of metabolism, and they also play a crucial role in the regulation of cell death pathways.³⁸ Targeting mitochondria and mitochondrial DNA can induce apoptosis in tumorigenic cells, as was recently demonstrated by Lippard and Kelley.³⁹ They constructed a *cis*-platinum(II) complex tethered to a mitochondrial penetrating peptide, which contained alternating cationic and lipophilic residues to enhance mitochondrial uptake (**Figure 1.2**). This complex was shown to localize almost exclusively to mitochondria in several cancer cell lines. Moreover, the complex was able to induce apoptosis in cisplatin-resistant ovarian cancer cells by damaging mitochondrial DNA.

1.4 DNA as a Target: Noncovalent Binding

It has been established that DNA is the primary therapeutic target of cisplatin and its derivatives. The mechanism of action of classical platinum-based chemotherapeutics is the formation of covalent DNA adducts, followed by cellular processing of these lesions.⁴ The synthesis of new generations of classical therapeutics with enhanced DNA binding properties in order to increase cytotoxicity have been extensively explored. How-

ever, the design and synthesis of therapeutics that bind specific DNA lesions that are more prevalent in cancer cells than normal cells may represent a targeted strategy for new chemotherapy.

A major deviation from classical inorganic chemotherapeutics like *cis*-platinum is the development of metal complexes that do not form covalent crosslinks with DNA, but rather bind noncovalently and, therefore, reversibly. Here, the metal center remains substitutionally and oxidatively inert and instead acts as a scaffold for the ligands to interact with DNA. These complexes typically contain low spin, d^6 metal centers with octahedral geometry, such as Rh (III), Ru (II), Ir (III), Os (II), and Re (I), that are coordinatively saturated, usually with aromatic bidentate ligands.⁴⁰

The inert metal center anchors its ligands in chiral, three-dimensional geometries that can be modulated for specific interactions with DNA. In some of the earliest work on complexes of this nature, performed with tris(phenanthroline) complexes of ruthenium (II) and other metals, two distinct DNA binding modes were observed. One binding interaction was characterized by hydrophobic interactions between the ligands and the minor groove of DNA, as is the case for Λ -[Rh(phen)₃]²⁺ (phen = 1,10-phenanthroline).⁴¹ A well known groove binder is [Cu(phen)₂]²⁺,⁴² which can also cleave the DNA backbone upon binding in the presence of oxidants.⁴³

The other binding mode was identified as partial intercalation of one of the phenanthroline ligands into the DNA duplex from the major groove, resulting in a π -stacking interaction between the ligand and the flanking base pairs. The metallointercalative DNA binding mode can be observed with the Δ -enantiomer of [Rh(phen)₃]²⁺ but not with the groove-binding Λ -enantiomer, highlighting the significance of chirality in the binding of

octahedral metal complexes to DNA, itself a chiral molecule.⁴¹ Indeed, the right-handed B-form DNA can only accommodate intercalation from similarly right-handed Δ -enantiomers of octahedral metal complexes (**Figure 1.4**).⁴⁴

1.4.1 Metallointercalators

Metallointercalators, like their organic intercalator counterparts, unwind the DNA helix to π -stack between two consecutive base pairs. Metallointercalation is thus generally best achieved with planar, aromatic ligands that protrude away from the metal center, facilitating interactions with the base stack. Intercalating ligands phi (9,10-phenanthroline diimine) and dppz (dipyrido[3,2-*a*:2'.3'-*c*]phenazine) have been extensively studied by the Barton laboratory and others. In metallointercalators $[\text{Ru}(\text{bpy})_2(\text{phi})]^{2+}$ and $[\text{Ru}(\text{bpy})_2(\text{dppz})]^{2+}$, both intercalating ligands contain aromatic groups that extend away from the site of coordination to the metal center (**Figure 1.5**). These complexes also bind DNA from the major groove and are highly enantiospecific.⁴⁵

Metallointercalative binding has significant physical and chemical implications for the DNA to which it is bound. To accommodate the incoming intercalating ligand, the helical rise (i.e., the vertical distance between consecutive base pairs) doubles, and the major groove widens at the binding site.^{45,46} This lengthening of the duplex is accompanied by an increase in the viscosity of the DNA in solution.⁴⁷ Intercalation also enhances the thermodynamic stability of the duplex, increasing the melting temperature.⁴⁸ Interestingly, while metallointercalation induces local distortions to the duplex at the site of binding, the long-range structural effects are minimal. Unlike *cis*-platinum binding, metallointercalation does not bend the duplex, and the sugars and bases maintain their C_2' -endo and *anti* conformations, respectively.^{46,48}

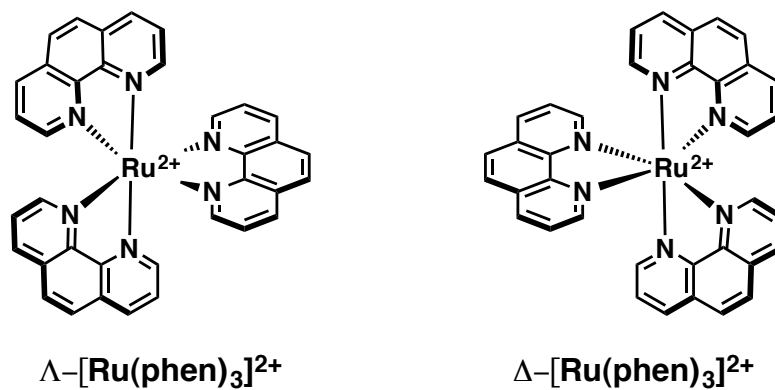


Figure 1.4 Chemical structures of octahedral ruthenium (II) tris(phenanthroline) complexes. Left: Λ -[Ru(phen)₃]²⁺, which interacts with DNA via minor groove binding interactions. Right: Δ -[Ru(phen)₃]²⁺, which interacts with DNA via partial intercalation of a phen (1,10-phenanthroline) ligand from the major groove.

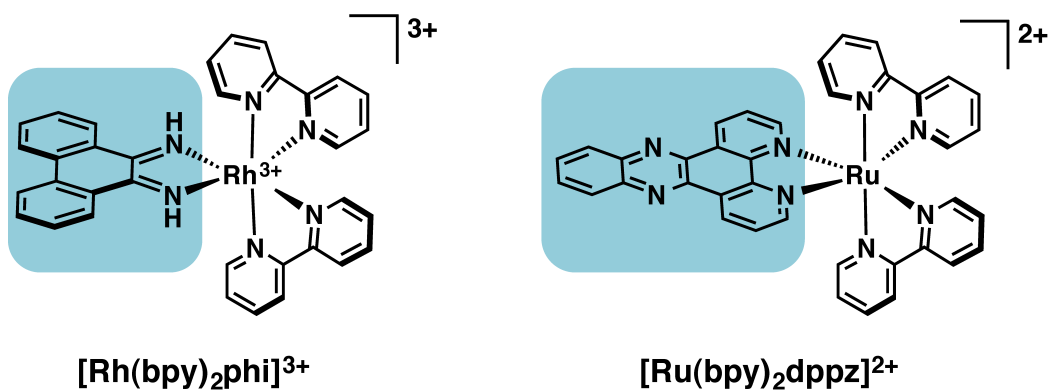


Figure 1.5 Chemical structures of Δ -[Rh(bpy)₂phi]³⁺ (left) and Δ -[Ru(bpy)₂dppz]²⁺ (right). Intercalating ligands phi (9,10-phenanthroline diimine) and dppz (dipyrido[3,2-*a*:2'.3'-*c*]phenazine) are highlighted in blue. These planar, aromatic ligands extend away from the metal center and π -stack between two adjacent base pairs in the DNA duplex, acting essentially as another base pair. [Rh(bpy)₂phi]³⁺ cleaves the DNA upon irradiation with UV light; [Ru(bpy)₂dppz]²⁺ is a DNA “light switch;” the complex is non-emissive in aqueous solvent but luminesces upon binding to DNA via intercalation. These complexes are also highly enantiospecific in their binding – the Λ -enantiomers do not readily bind to B-form DNA.

The applications of metallointercalation extend beyond altering the physical properties of DNA. Despite the substitutional inertness of the coordinatively saturated, low-spin heavy metal centers, the electronic configurations of these transition metals enable rich photochemistry and luminescence properties generally not afforded to organic intercalators. In one of the most well-studied examples of metallointercalation, the complex $[\text{Ru}(\text{bpy})_2\text{dppz}]^{2+}$ (bpy = 2,2'-bipyridine, **Figure 1.5**) exhibits solvatochromatic luminescence in organic solvents at ambient temperature, yet this luminescence is quenched in aqueous solution due to hydrogen bonding interactions between water and the phenazine nitrogen atoms of dppz. Upon intercalative binding to DNA, however, luminescence is restored as the π -stacking interactions within the duplex protect the ligand from solvation, thus becoming, famously, a “light switch” for DNA.⁴⁹

DNA light switch complexes of ruthenium and other metals have been extensively reported. Derivatives of $[\text{Ru}(\text{bpy})_2\text{dppz}]^{2+}$ have been developed wherein the luminescence properties are tuned via variation of the non-intercalating ancillary ligands – such as $[\text{Ru}(\text{phen})_2\text{dppz}]^{2+}$ and $[\text{Ru}(\text{DIP})_2\text{dppz}]^{2+}$ (DIP = 4,7-diphenyl-1,10-phenanthroline) – in addition to complexes containing altogether new intercalating ligands. The luminescence properties of DNA-binding transition metal complexes have been heavily investigated as potentially powerful diagnostic tools and imaging agents for cellular studies.⁵⁰⁻⁵³

In addition to robust luminescence, octahedral metallointercalators can also mediate photochemical reactions upon binding to DNA. Rhodium-based intercalators, such as $[\text{Rh}(\text{bpy})_2\text{phi}]^{3+}$ and $[\text{Rh}(\text{phen})_2\text{phi}]^{3+}$ (**Figure 1.6**), have been shown to induce single strand scission of the DNA backbone upon irradiation with short-wave ultraviolet (UV) light (313-325 nm).⁵⁴ Photoactivation of these complexes intercalated into

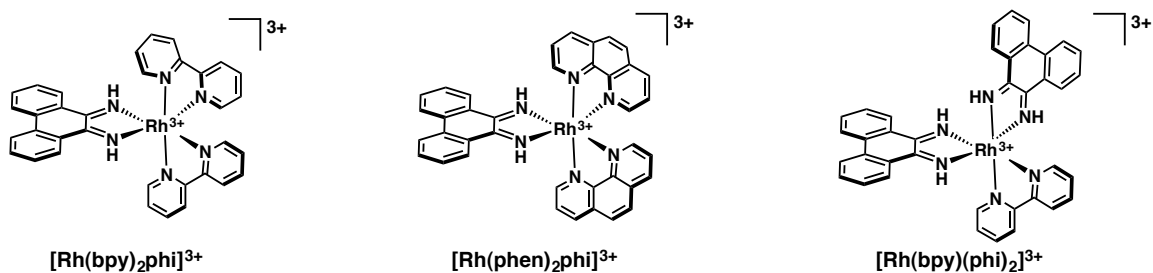


Figure 1.6 Rhodium (III) intercalators: Δ - $[\text{Rh}(\text{bpy})_2\text{phi}]^{3+}$ (left); Δ - $[\text{Rh}(\text{phen})_2\text{phi}]^{3+}$ (center); Δ - $[\text{Rh}(\text{phi})_2\text{bpy}]^{3+}$ (right). These complexes photocleave the DNA on one strand at the site of binding upon irradiation with UV-light.

DNA triggers the formation of a ligand-based radical that abstracts a hydrogen atom from the deoxyribose ring of a neighboring nucleotide.⁵⁵ It is the subsequent degradation of the sugar radical that prompts DNA cleavage at that site. For complexes intercalated from the major groove, it is proposed that this initial hydrogen atom abstraction occurs at the C2' of the adjacent sugar, and hydrogen migration to form the observable C3' radical occurs prior to degradation of the ribose ring.

The photochemistry of metallointercalators usefully enables facile visualization and quantification of DNA binding events by electrophoretic mobility shift assay (EMSA); the migratory differences of cleaved (i.e., complex bound) and non-cleaved (no complex bound) DNA can be observed with radiolabeled oligonucleotides on a denaturing polyacrylamide gel. This provides information regarding the site of binding as well as the amount of complex bound, allowing for the determination of equilibrium binding constants. Potential therapeutic applications of photocleaving intercalator complexes have been explored, as light-induced DNA strand scission is often accompanied by the generation of reactive oxygen species (ROS), which are toxic to the cell.⁵⁶ Photoactive rhodium intercalators have also been employed as redox probes to monitor the migration of electrons and holes through the DNA π -stack – a remarkable phenomenon known as DNA charge transport.⁵⁷

1.4.2 Metallointercalators for Selective DNA Recognition

Overall, metallointercalators are a highly diverse class of inorganic complexes with versatile applications for DNA recognition. However, the nature of the metallointercalative binding mode is by definition nonspecific: the intercalating ligand is accepted into the base stack, acting essentially as a new base pair. This interaction can occur any-

where in the DNA sequence with little discrimination, thereby limiting the application of metallointercalators for targeted therapy.

Efforts to tune the specificity of metallointercalators have exploited the three-dimensional architecture of octahedral metal complexes as well as their modular synthesis. By exchanging ligand sets, it is possible to alter the shape of the complex and, consequently, the nature of its interactions with DNA. The notion of shape-selective DNA recognition stems in part from the highly enantiospecific nature of metallointercalation. Intercalation of a protruding aromatic ligand, such as dppz or phi, into the base stack situates the metal center with its non-intercalating ancillary ligands in the major groove. Thus, the source of the enantiospecificity in intercalative binding stems from steric interactions between the ancillary ligands and the sugar-phosphate backbone of DNA. When the Δ -enantiomer of a metallointercalator binds DNA, the ancillary ligands fit in the major groove, but substantial steric clashing would be encountered if the Λ -enantiomer were bound. As a result, increasing the size of the ancillary ligands can further enhance chiral discrimination.⁴⁴ The geometry and symmetry of metallointercalators, too, can also be advantageous for selective DNA recognition. Bis(heteroleptic) intercalator complexes such as $[\text{Rh}(\text{phen})_2(\text{phi})]^{3+}$ are generally referred to as “octahedral” but in actuality possess C_2 symmetry, affording a propeller twist to these complexes that can be functionalized to preferentially bind specific nucleotide patterns in DNA.⁴⁶

An intricate example of selective recognition can be found in the aforementioned Δ - α - $[\text{Rh}((R,R)\text{-Me}_2\text{trien})(\text{phi})]^{3+}$ complex, shown in **Figure 1.7**. This photocleavage agent was rationally designed to bind and photocleave specifically at 5'-TGCA-3' sites. The selectivity arises from hydrogen bonding contacts between the axial ammine ligands

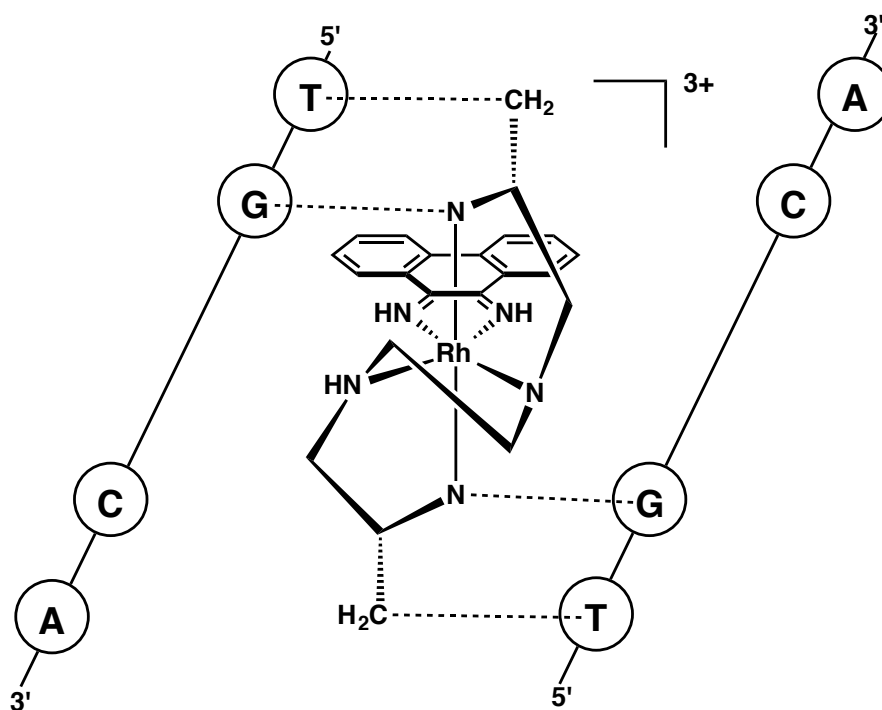


Figure 1.7 Structure of $\Delta\text{-}\alpha\text{-}[\text{Rh}[(\text{R},\text{R})\text{-Me}_2\text{trien}]\text{phi}]^{3+}$ and schematic illustration of the complex binding to its 5'-TGCA-3' recognition sequence. Intercalation of the phi ligand occurs between the GC base pairs. The sequence specificity arises from hydrogen-bonding interactions between the axial NH_2 groups of the ligand and the O_6 -position of the guanines, as well as methyl-methyl interactions between the ligand methyl groups and the methyl groups of the thymine residues.

and the *O6* position of the guanine residues as well as hydrophobic interactions between the methyl groups of the trien ligands and the thymine residues. This complex intercalates with such extraordinary sequence specificity that the first high-resolution crystal structure of a metallointercalator bound to DNA could finally be obtained, revealing a detailed picture of the metallointercalative binding mode.⁵⁸

Many other examples of sequence- and shape-selective metallointercalator complexes have been developed. However, even the most selective complexes have few applications in targeted therapy, as their small, ubiquitous recognition sequences provide little discrimination between healthy and cancerous cells. Additionally, the minimal, localized helical distortions incurred by intercalation often do not create lesions that are critical to cell survival, and thus are not cytotoxic in the absence of UV-damage or oxidative stress. The ultimate goal, then, is the development of metal complexes that can target sites within the DNA that are specific to cancerous cells but are not found in healthy cells.

1.4.3 Metalloinsertors

A major advancement in the development of metal complexes that could specifically target cancerous DNA defects has been the design of octahedral rhodium (III) complexes that bind selectively to base pair mismatches. This class of molecules bears resemblance to rhodium (III) metallointercalators, except the intercalating “phi” ligand – which, at 9.2 Å wide, nonspecifically intercalates into DNA unless guided by ancillary ligands toward specific binding sites – is replaced with a sterically expanded derivative, chrysi (5,6-chrysenequinone, **Figure 1.8**).⁵⁹ Possessing an additional fused benzene ring, the 11.3 Å-wide chrysi ligand is too large to intercalate, as a DNA base pair is only 10.8

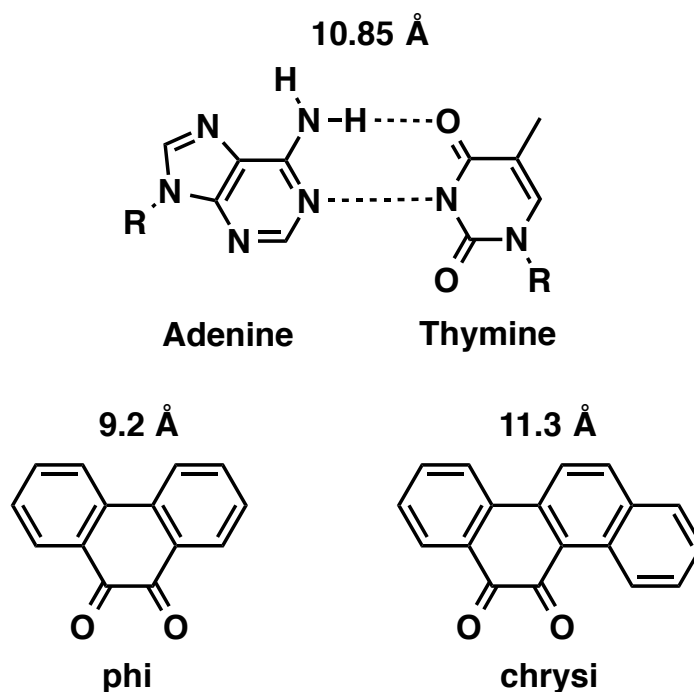


Figure 1.8 Comparison of the width of intercalating ligand phi (9.2 Å across) and inserting ligand chrysi (5,6-chrysenequinone; 11.3 Å across). A standard Watson-Crick base pair is 10.85 Å across; thus, phi is narrow enough to intercalate in the base stack. The chrysi ligand, expanded by an additional fused benzene ring, is too wide for nonspecific intercalation. Thus, this ligand only binds DNA at thermodynamically destabilized sites, such as mismatches, wherein the destabilized base pairs can be ejected from the duplex, leaving enough room for the chrysi ligand to insert into the base stack.

Å across; thus, all nonspecific binding is eliminated. In contrast, single base lesions such as mismatches or abasic sites are thermodynamically destabilized compared to canonical Watson-Crick base pairs, due to imperfect hydrogen bonding between the mismatched bases as well as perturbations in the π -stack. Overall, mismatches in DNA are approximately 3-5 kcal/mol more destabilized than well-matched base pairs, resulting in a dynamic site that is stabilized by the intrusion of the chrysi ligand.^{60,61} In this new binding mode, termed *metalloinsertion*, the chrysi ligand displaces both mismatched base pairs from the helix, inserting fully into the intervening space.^{62,63} Stacking interactions between the expansive chrysi and the flanking base pairs recuperate the energy cost of extruding the mismatch. This metalloinsertive binding mode, which occurs from the minor groove, was predicted by L. S. Lerman in 1961,⁶⁴ nearly 50 years before it would be confirmed crystallographically for the first time by the Barton laboratory.⁶³

The first-generation metalloinsertor complex, $[\text{Rh}(\text{bpy})_2\text{chrysi}]^{3+}$, was synthesized in the Barton laboratory and characterized by *in vitro* DNA binding experiments.^{59,65} Like its rhodium (III) intercalator counterparts, $[\text{Rh}(\text{bpy})_2\text{chrysi}]^{3+}$ induces single-strand scission at the ribose adjacent to the site of binding upon irradiation (although in this case, hydrogen abstraction occurs at the C1' position of the sugar, due to the positioning of the complex in the minor groove). This photocleavage was shown to occur exclusively at mismatched sites, and the equilibrium binding constants for mismatch recognition correlated directly to the thermodynamic stability of the mismatches themselves. That is, the stability of the base pairs – $\text{C}\cdot\text{G} > \text{A}\cdot\text{T} \gg \text{G}\cdot\text{G} \sim \text{G}\cdot\text{T} \sim \text{A}\cdot\text{G} > \text{T}\cdot\text{T} \sim \text{A}\cdot\text{A} > \text{C}\cdot\text{T} \sim \text{A}\cdot\text{C} > \text{C}\cdot\text{C}$ – corresponds to the ease of recognition by $[\text{Rh}(\text{bpy})_2\text{chrysi}]^{3+}$, with cytosine-containing mismatches being the most destabilized and thus the most easily bound.^{66,67}

For instance, the binding affinity of $[\text{Rh}(\text{bpy})_2\text{chrysi}]^{3+}$ to a CC mismatch is $3 \times 10^7 \text{ M}^{-1}$, compared to $2.9 \times 10^5 \text{ M}^{-1}$ for an AA mismatch.⁶⁶ Guanine-containing mismatches, in contrast, are significantly more stable, and consequently are not recognized by metalloinsertors. Overall, metalloinsertors can bind 80% of all mismatches, regardless of the surrounding sequence context.⁶⁸

The extraordinary selectivity of these complexes for DNA mismatches was revealed through photocleavage experiments with a 2725 base pair linearized plasmid containing a single CC mismatch. Upon irradiation with $[\text{Rh}(\text{bpy})_2\text{chrysi}]^{3+}$, photocleavage was found to occur only at this site, with no evidence of binding in the well-matched control plasmid, corresponding to 1000 fold selectivity for mismatches over Watson-Crick base pairs. The first-generation metalloinsertors also display remarkable enantiospecificity, with only the right-handed Δ - $[\text{Rh}(\text{bpy})_2\text{chrysi}]^{3+}$ and Δ - $[\text{Rh}(\text{bpy})_2\text{phzi}]^{3+}$ (phzi = benzo[*a*]phenazine-5,6-dione) enantiomers (**Figure 1.9**) capable of recognizing mismatches in B-DNA.⁶⁶

1.4.4 Metalloinsertors as Targeted Chemotherapeutics

The metalloinsertion binding mode was structurally characterized by co-crystallization of $[\text{Rh}(\text{bpy})_2\text{chrysi}]^{3+}$ to palindromic DNA duplexes containing CA and AA mismatches, revealing the extrusion of the mismatched base pairs from the π -stack and the insertion of the chrysi ligand from the minor groove (**Figure 1.10**).^{63,69} Additionally, crystal structures of the intercalating DNA light-switch complex $[\text{Ru}(\text{bpy})_2\text{dppz}]^{2+}$ revealed a similar binding mode in the presence of mismatched DNA: the dppz ligand, too, was capable of ejecting mismatched base pairs in an insertive manner, albeit without the selectivity afforded by the expanded chrysi and phzi ligands.⁷⁰ These structural char-

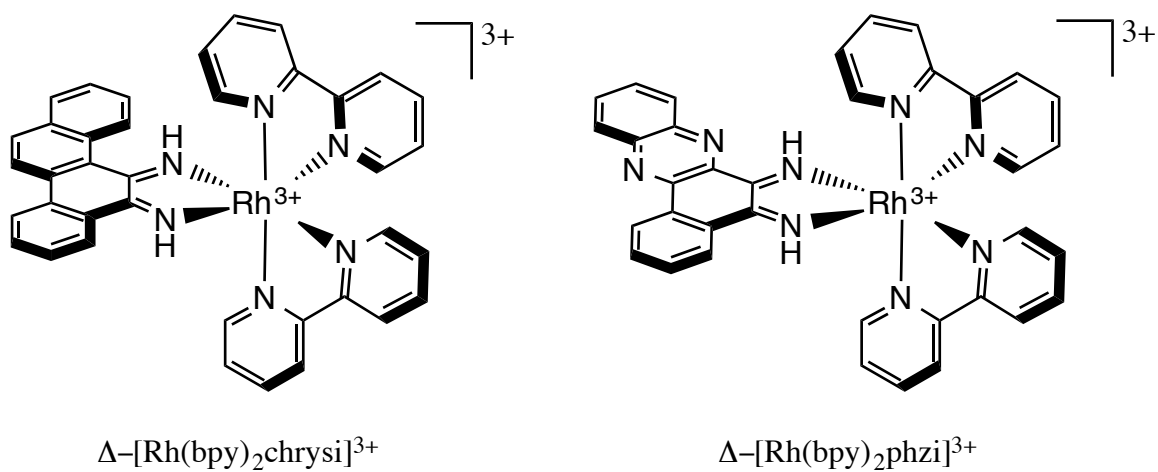


Figure 1.9 Chemical structures of Δ -[Rh(bpy)₂chrysi]³⁺ (left) and Δ -[Rh(bpy)₂phzi]³⁺ (right), the first- and second-generation metalloinsertor complexes, respectively. The sterically expansive inserting ligands, chrysi (5,6-chrysenequinone diimine) and phzi (benzo[*a*]phenazine-5,6-diimine) target thermodynamically destabilized base pair mismatches with over 1000-fold specificity.

acterizations are a testament to the generality of metalloinsertion. Additionally, although metalloinsertion incurs minimal distortions to the duplex with no increase in helical pitch, the ejection of the mismatched bases results in a large lesion that is hypothesized to have the potential to be recognized *in vivo*.

Mismatches in genomic DNA arise naturally as a consequence of replication, but if left uncorrected can lead to mutations.^{71,72} The mismatch repair (MMR) pathway serves as a checkpoint to increase the fidelity of DNA replication ~1000 fold.⁷³ Importantly, deficiencies in the mismatch repair machinery have been associated with several types of cancer, as well, notably, as increased resistance to classical chemotherapeutics such as cisplatin.⁷⁴ Therefore, the development of a targeted therapy for MMR- deficient cancers would be invaluable in the clinic. Due to the unique DNA mismatch-binding properties of rhodium metalloinsertors, we sought to explore their biological properties in MMR-deficient cells. The compounds were initially found to inhibit growth in MMR-deficient colorectal cancer cells over MMR-proficient cells, as measured by antibody assays for DNA synthesis.^{75,76} In a follow-up study, it was discovered that metalloinsertors with accelerated uptake also exhibited preferential cytotoxicity towards MMR-deficient cells (**Figure 1.10**).⁷⁷ Additionally, these complexes were discovered to induce a necrotic mechanism of cell death, rather than the caspase-dependent, programmed apoptotic mode induced by *cis*-platinum therapeutics.

The synthesis of large families of second- and third-generation metalloinsertors enabled the elucidation of structure-activity relationships critical for optimizing biological activity. It had previously been shown that the size of the ancillary ligands directly correlated to the mismatch binding affinity of metalloinsertors; small ligands, such as

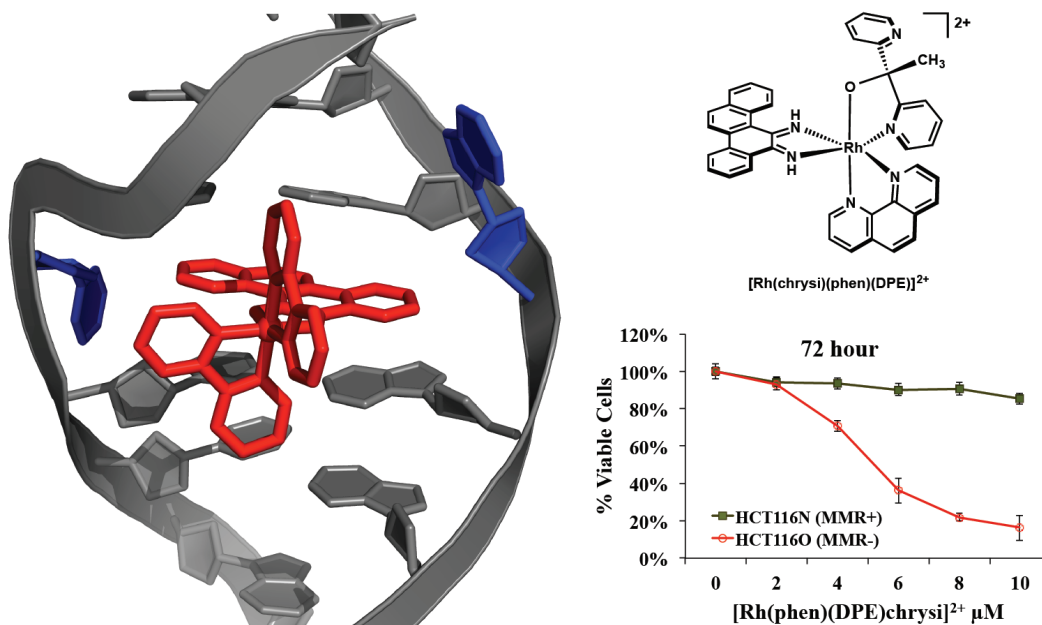


Figure 1.10 (Left) Crystal structure of $[\text{Rh}(\text{bpy})_2(\text{chrysi})]^{3+}$, the first generation metal-loinsertor, bound to an AC mismatch in duplex DNA. (Right, top) Chemical structure of $[\text{Rh}(\text{chrysi})(\text{phen})(\text{DPE})]^{2+}$, a later generation metalloinsertor with enhanced selectivity and potency. (Right, bottom) Cell-selective cytotoxicity of $[\text{Rh}(\text{chrysi})(\text{phen})(\text{DPE})]^{2+}$, the complex selectively kills MMR-deficient (red) cells over MMR-proficient (green) cells.

ammines, allow for tighter binding due to minimal steric interactions with the sugar-phosphate backbone, compared to bulky ligands like DIP, which confer critically weak binding affinities (**Figure 1.11**). It was found that the binding affinity for a mismatch translated to enhanced differential activity – that is, preferential antiproliferative activity in MMR-deficient cells.⁷⁶ Most recently, a structure-function study was conducted by altering the lipophilicities of the non-inserting ligands.^{78,79} This investigation resulted in the synthesis of a family of mismatch-binding complexes with similar binding affinities and selectivities for DNA mismatches, yet drastically different selectivities for MMR-deficient cells. It was discovered that more lipophilic complexes did not exhibit the unique cell-selective activities for which metalloinsertors are distinguished. However, complexes with more hydrophilic ancillary ligands were highly selective for the MMR-deficient cells over MMR-proficient cells. It was discovered that nuclear uptake of all metalloinsertors studied was sufficient for mismatch binding to genomic DNA. However, significant mitochondrial uptake led to an abolishment of their selective targeting of MMR-deficient cells. Most notably, simply substituting a hydroxyl group for a methyl group results in dramatic changes in cell-selective activity due to drastic changes in the subcellular localization (**Figure 1.12**).⁷⁹ This study supports the notion that the unique cell-selective activities of these compounds rises from targeting of mismatches in genomic DNA. In an effort to more directly relate the biological activity of rhodium metalloinsertors to the MMR-deficiency phenotype, our laboratory has now embarked on studies to validate the biological efficacy of these compounds.

All of the cell assay experiments characterizing the *in cellulo* effects of rhodium metalloinsertors had been undertaken on the isogenic cell lines HCT116N and HCT116O.

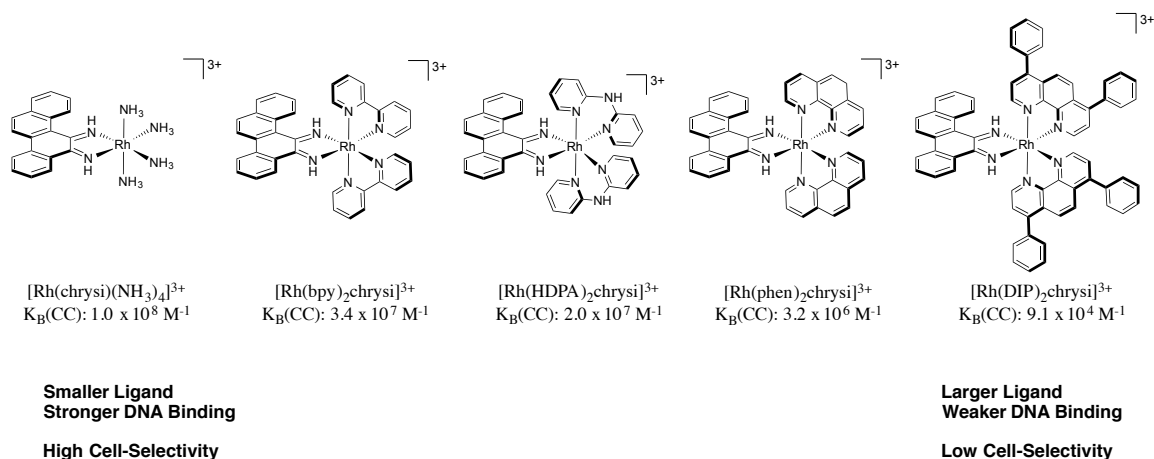


Figure 1.11 Effects of the non-inserting ancillary ligands on the biological activity of rhodium metalloinsertors. Increasing the size of the ancillary ligands imparts steric clashing with the sugar-phosphate backbone upon DNA mismatch recognition; thus, equilibrium binding constants are weaker for complexes with large ligands, as is the case for $[\text{Rh}(\text{DIP})_2\text{chrysi}]^{3+}$. In contrast, complexes with small ligands display tighter binding to DNA mismatches, as is the case with $[\text{Rh}(\text{chrysi})(\text{NH}_3)_3]^{3+}$, due to the lack of steric interference. In a family of five complexes, the *in vitro* DNA binding affinities correlated directly to the differential antiproliferative activity – that is, the preferential inhibition of DNA synthesis in the MMR-deficient HCT116O colorectal cancer cells over the MMR-proficient HCT116N cell line.

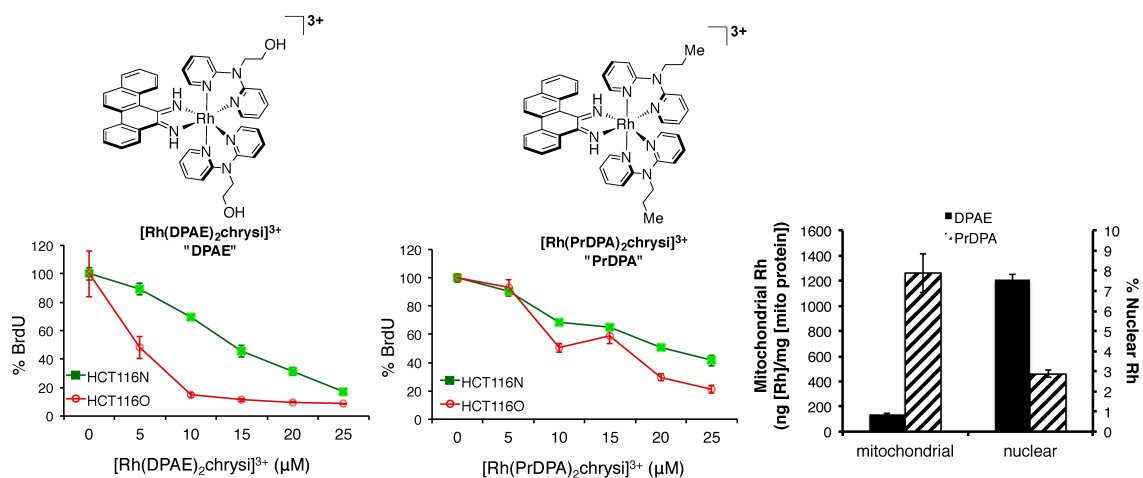


Figure 1.12 Inhibitory effects of $[\text{Rh}(\text{DPAE})_2\text{chrysi}]^{3+}$ (bottom, left) and $[\text{Rh}(\text{PrDPA})_2\text{chrysi}]^{3+}$ (bottom, center) on cellular proliferation in MMR-deficient HCT116O (red) and MMR-proficient HCT116N (green) cells as a function of BrdU incorporation during DNA synthesis (adapted from reference 79). Percent BrdU incorporation is normalized to that of untreated cells. (Bottom, right) Subcellular localization of $[\text{Rh}(\text{DPAE})_2\text{chrysi}]^{3+}$ (black) and $[\text{Rh}(\text{PrDPA})_2\text{chrysi}]^{3+}$ (hashed). Mitochondrial rhodium content (left axis) has been normalized to mitochondrial protein content, and nuclear rhodium content (right axis) is expressed as the percentage of cellular rhodium in the nucleus.

The HCT116 parent cell line is a human colorectal carcinoma line deficient in the *hMLH1* gene. This gene encodes for part of the mismatch repair (MMR) machinery; consequently this cell line is MMR-deficient. The HCT116N cell line has been transfected with human chromosome 3 (ch3), which restores MMR proficiency, while the HCT116O cell line has been transfected with human chromosome 2 (ch2), leaving it MMR-deficient.⁸⁰ In this model system, however, the MMR-proficient cells and MMR-deficient cells are generated as different clones, and are distinct from the parental cell line. These differences can result in changes in chromosome stability or gene expression that are not solely due to MMR deficiency. To this end, we engineered NCI-H23 lung adenocarcinoma cells that contain a doxycycline-inducible short hairpin RNA (shRNA) that suppresses the expression of the mismatch repair gene *MLH1*. This provides an isogenic cell line system that can be used to directly compare MMR-proficient and MMR-deficient cells.⁸¹

It was found that these *MLH1*-deficient cells, which are more resistant to the DNA damaging agents doxorubicin, cisplatin, and etoposide, are indeed more sensitive to rhodium metalloinsertors (**Figure 1.13**).⁸¹ These results further validate the biological activity of rhodium metalloinsertors, as they have now been shown to exhibit selective biological effects across multiple assays and in different systems for comparing MMR deficiency to proficiency. Clearly, the strategy of targeting a specific lesion in DNA is a promising alternative to the classical approach.

1.5 Expanding the Reactivity of Metalloinsertors: Bifunctional Conjugates

Rhodium metalloinsertors are a robust class of complexes that offer a promising alternative for targeting MMR-deficient cancers and circumventing resistance. New generations of metalloinsertors, derived from the first-generation $[\text{Rh}(\text{bpy})_2\text{chrysi}]^{3+}$ and

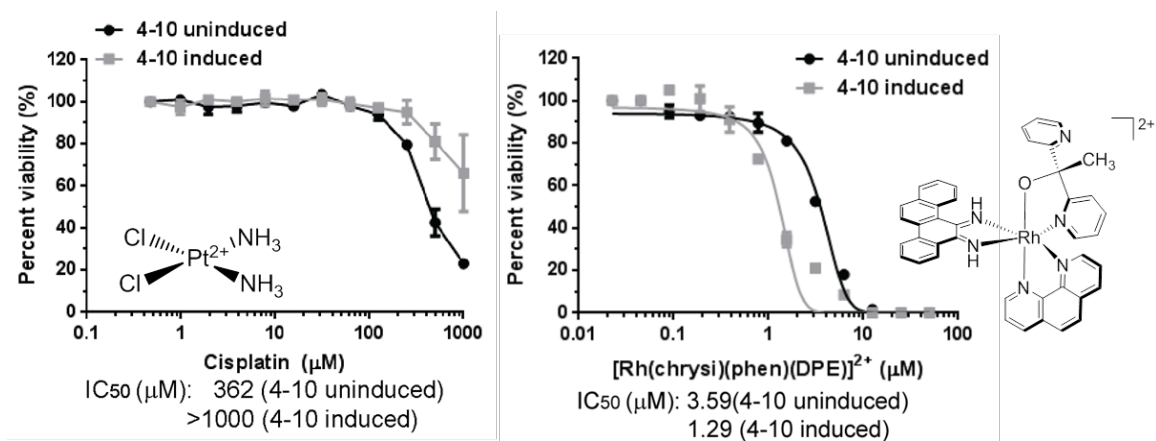


Figure 1.13 NCI-H23 subclones that were uninduced or induced for MLH1 shRNA were treated with either cisplatin (left) or the rhodium metalloinsertor [Rh(chrysi)(phen)(DPE)]²⁺ (right) (adapted from reference 81). Cells were treated at concentrations indicated, and cell viability assessed after 4 days using a Cell Titer-Glo assay. IC₅₀ values are shown below the plots.

$[\text{Rh}(\text{bpy})_2\text{phzi}]^{3+}$ have exhibited increased potency surpassing that of cisplatin, while still maintaining selective targeting to MMR-deficiency.^{78,82} While these compounds are currently being explored as chemotherapeutic agents, they also hold promise as potential adjuvants that could confer their unique selectivity onto other therapeutic cargo.

Several bifunctional metalloinsertor conjugates have been developed for the targeting of therapeutic agents towards mismatched DNA, whereas in their native form they would interact with DNA in a nonspecific manner. In general, metalloinsertor conjugates are constructed as trisheteroleptic (three unique bidentate ligands) complexes, wherein one ancillary ligand is functionalized with the secondary subunit. The metalloinsertor subunit, then, acts as a directing agent that taxis its cargo preferentially towards mismatched sites in DNA.

1.5.1 Metalloinsertor-Alkylator Conjugate

The first bifunctional metalloinsertor conjugate designed in the Barton laboratory consisted of a $[\text{Rh}(\text{chrysi})(\text{phen})(\text{bpy}')]^{3+}$ subunit tethered to an aniline mustard, where bpy' is a 2,2'-bipyridine ligand modified with an amino-alkane tether (**Figure 1.14**). The nitrogen mustard melphalan, which forms covalent adducts with DNA at 5'-GNC-3' sites, was attached to the metalloinsertor via amide bond formation. The complex displayed a bifunctional binding mode involving both metalloinsertion of the rhodium-chrysi moiety at the mismatched site as well as the covalent alkylation of DNA by the melphalan subunit. Additionally, a seven-fold increase in alkylation of mismatched DNA was observed for the conjugate compared to well-matched binding, indicative of metalloinsertor-directed targeting. Furthermore, DNA alkylation proceeds more effectively and with increased site-specificity for the conjugate than with melphalan alone. Remarkably,

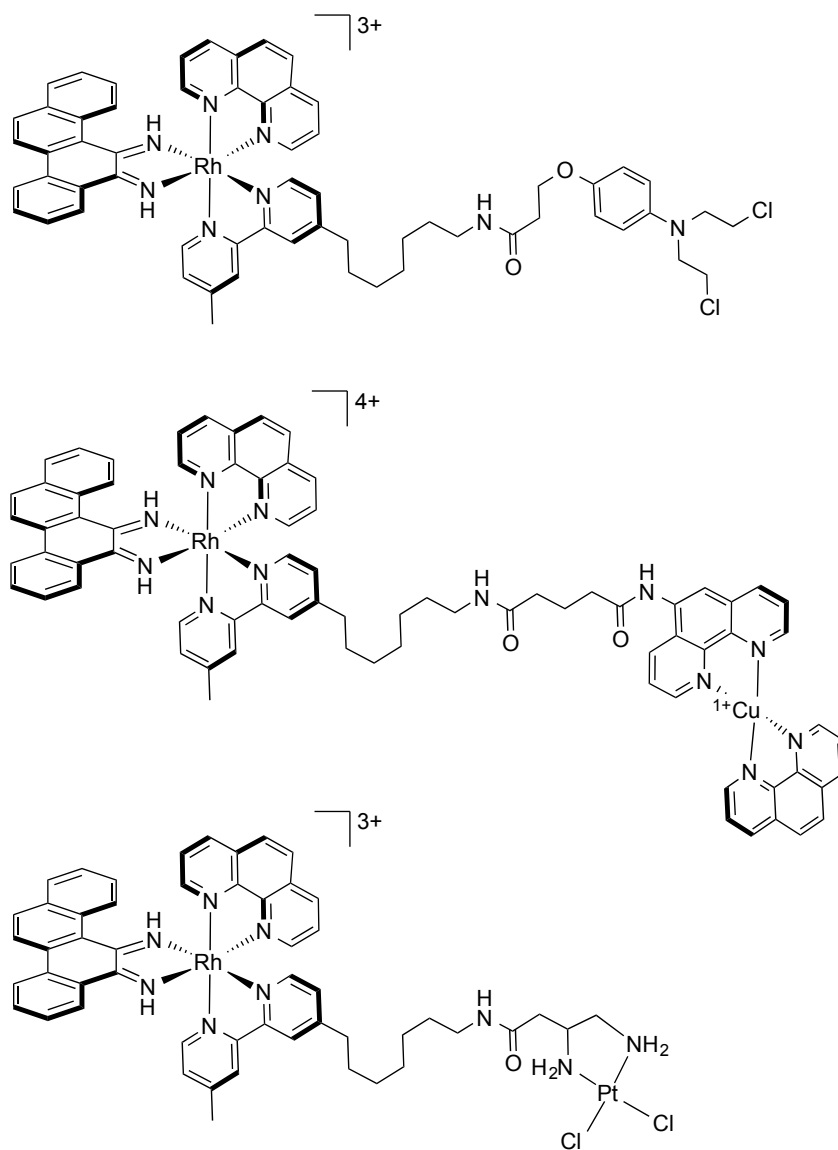


Figure 1.14 Chemical structures of bifunctional, mismatch-specific metalloinsertor conjugates: a metalloinsertor-nitrogen mustard conjugate for mismatch-directed alkylation of DNA (top); a bimetallic Rh(III)-Cu(I) conjugate, which displays selective cleavage of mismatched DNA in the absence of irradiation (middle); and a bimetallic Rh(III)-Pt(II) conjugate, which displays preferential platination of guanine residues on mismatched DNA duplexes (bottom).

the two distinct binding interactions are largely independent of one another, in that alkylation of DNA neither inhibits nor enhances the mismatch binding ability of the metalloinsertor group.⁸³

1.5.2 Metalloinsertor Conjugate for DNA Cleavage

A second example of mismatch-directed conjugate design involves the attachment of the DNA cleavage agent $[\text{Cu}(\text{phen})_2]^{2+}$ to a metalloinsertor (**Figure 1.14**). Again, the $[\text{Rh}(\text{chrysi})(\text{phen})(\text{bpy}')]^{3+}$ scaffold is employed. Here, the rhodium directs copper-induced cleavage of the DNA preferentially towards mismatched DNA. Interestingly, the rhodium induces this potentiating effect even when the two complexes are added as separate subunits. DNA cleavage is enhanced possibly due to the slight opening of the minor groove as a result of metalloinsertion. The therapeutic advantage of this conjugate is that DNA cleavage can be induced near mismatched sites in the absence of UV irradiation, which causes nonspecific damage to the genome.⁸⁴

1.5.3 Metalloinsertor-Cisplatin Conjugate

In recent years, many new strategies in inorganic drug design have been developed for both classical and targeted therapies. Nevertheless, the traditional *cis*-platinum drugs remain the only transition metal complexes approved for therapeutic use worldwide, despite their limitations. Due to the clinical significance of platinum, strategies for tuning its selectivity toward specific lesions in DNA would be invaluable in mitigating both cisplatin resistance as well as side effects arising from off-target toxicity.

A metalloinsertor functionalized with a cisplatin derivative was constructed in an analogous manner to the previous conjugates (**Figure 1.14**). Instead of two monodentate ammine ligands, a bidentate ethylenediamine functionalized with a carboxyl group was

employed for ease of synthesis. Again, the conjugate was shown to successfully target its cargo to mismatched DNA, where the platinum moiety forms both inter- and intrastrand crosslinks with duplex DNA at guanine residues. However, this preferential binding is highly dependent on the presence and location of a d(GpG) site (the preferred binding site of cisplatin); if there is no d(GpG) site, or if it is inaccessible to the platinum center due to limitations in the length and flexibility of the alkyl tether, then minimal platination occurs. Likewise, there was no preference for mismatched DNA in these scenarios. In order to achieve selective platination of mismatched DNA, a d(GpG) site must be present approximately nine base pairs away from the mismatched site, where the six-carbon alkyl tether most favors interactions between the platinum center and the DNA.⁸⁵ Unsurprisingly, this limitation reduces the applications of the conjugate in a biological system; indeed, when characterized in the isogenic HCT116N and HCT116O cell lines, the conjugate displayed no preferential antiproliferative activity in the MMR-deficient line, and in fact exhibited a small preference for the MMR-proficient HCT116N cells.⁸⁶

1.5.4 Metalloinsertors Conjugated to Cell-Penetrating Peptides

The previous examples of metalloinsertor conjugates demonstrate the ability of these complexes to confer their mismatch recognition capabilities onto other chemotherapeutic agents in their interactions with DNA. But some conjugates were designed with the purpose of enhancing the activity of metalloinsertors themselves. One notable example is the development of a rhodium metalloinsertor complex outfitted with a cell-penetrating peptide for enhanced cellular uptake. Highly charged peptide sequences, such as octaarginine tags, facilitate cellular transport of cargo through endocytosis.⁸⁷ When conjugated with a metalloinsertor complex, cellular uptake of rhodium was greatly en-

hanced compared to the typical passive diffusion uptake mechanism exhibited by metal complexes alone (**Figure 1.15**).⁸⁸ The goal of this project was to increase the potency of metalloinsertors through increasing the intracellular concentration of rhodium. However, while the conjugate was able to successfully increase cellular rhodium accumulation with the attachment of a cell-penetrating peptide, the high positive charge of the complex resulted in significant nonspecific, electrostatically-driven DNA binding.

1.5.5 Outlook for Bifunctional Metalloinsertor Conjugates

The current repertoire of bifunctional conjugates comprises a diverse and chemically complex family of metalloinsertors. In many ways, they have been successful in exhibiting dual functionality in their DNA binding behavior and unique chemical reactivities *in vitro*. In a biological context, however, these complexes have critically fallen short in their ability to selectively target MMR-deficiency like their monomeric counterparts. Furthermore, the development and biological characterization of new generations of rhodium metalloinsertors have revealed that cellular uptake, nuclear localization, and increased cell-selective potency could be achieved more simply by altering the chemical environment of the ancillary ligands.^{78,79,82} Most recently, it was found that a new family of rhodium metalloinsertor complexes bearing ligands that coordinate through a Rh—O bond (**Figure 1.16**) exhibit unprecedented selectivity and potency in MMR-deficient cells, with IC₅₀ values in the pharmaceutically significant 200-300 nM range. Remarkably, it was this simple Rh—O coordination that critically altered aspects of the complex, such as the pKa and planarity of the chrysi inserting ligand, leading to its enhanced biological activity and even enabling mismatch recognition by the formerly inactive Λ -enantiomers.⁸²

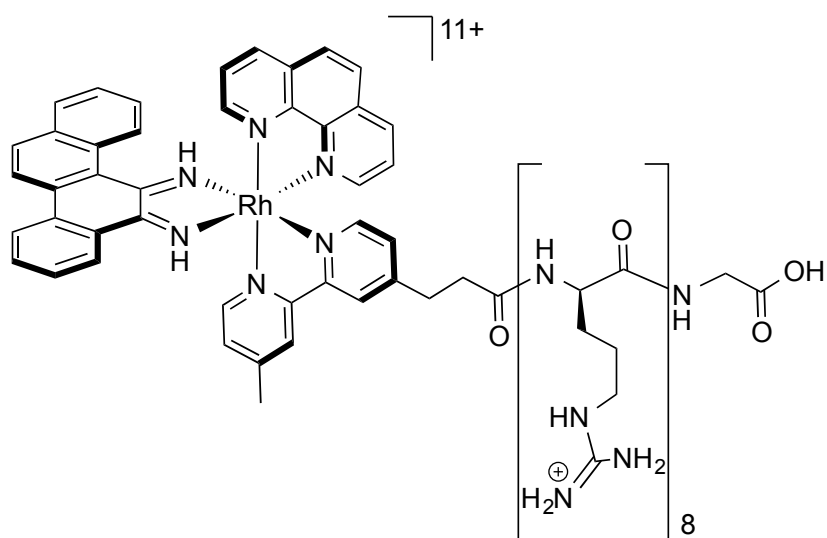


Figure 1.15 Structure of a metalloinsertor-peptide conjugate. A Rh(III) metalloinsertor complex was functionalized with an octaarginine cell-penetrating peptide. The peptide affords enhanced cellular and nuclear uptake of the complex while still enabling mismatch recognition by the rhodium subunit; however, nonspecific DNA binding is increased due to electrostatic interactions arising from the high positive charge of the peptide.

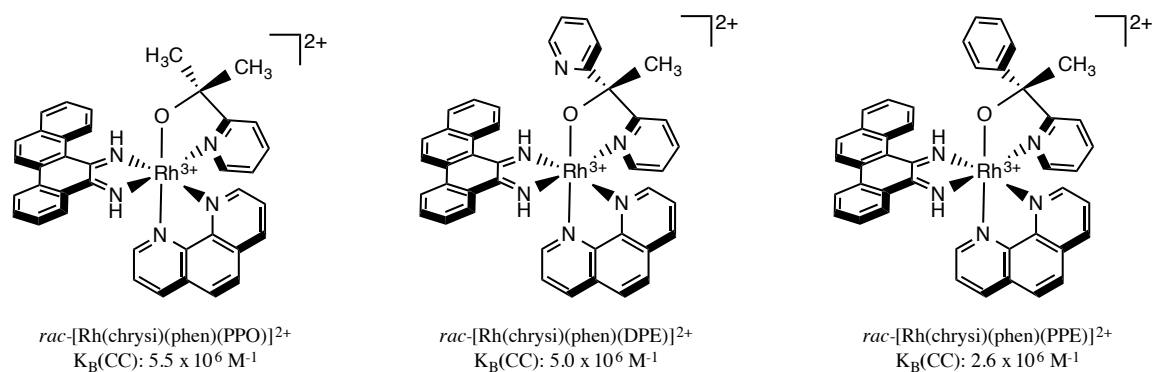


Figure 1.16 Chemical structures and binding affinities for a CC mismatch of a new family of metalloinsertor complexes bearing an unusual Rh—O ligand coordination: $[\text{Rh}(\text{chrysi})(\text{phen})(\text{PPO})]^{2+}$ (left, PPO = 1-methyl-1-(pyrid-2-yl)ethanol); $[\text{Rh}(\text{chrysi})(\text{phen})(\text{DPE})]^{2+}$ (center, DPE = 2,2'-pyridylethanol); and $[\text{Rh}(\text{chrysi})(\text{phen})(\text{PPE})]^{2+}$ (right, PPE = 1-phenyl-1-(pyrid-2-yl)ethanol). This new class of ligands forms an *N,O*-chelate, resulting in enhanced potency and selectivity, as well as a potentially new metalloinsertive binding mode that can accommodate both Δ - and Λ -enantiomers in the minor groove.

Given these recent discoveries, it may seem as though there is no longer a place for metalloinsertor conjugates in targeted therapy; metalloinsertors function magnificently on their own. And yet, the continued enhancement of metalloinsertor efficacy now more than ever enables their development not simply as chemotherapeutics in and of themselves, but also as potentially useful tools in targeted adjuvant therapy. Even common chemotherapeutics such as cisplatin are currently administered in conjunction with one or more additional drugs, each functioning separately but often synergistically within a cell.⁸⁹ The ability to functionalize metalloinsertors as cell-selective delivery agents for additional therapeutically useful cargo would be invaluable in the clinic. Additionally, as our rhodium complexes progress beyond tissue culture and into a more clinical setting, it may become necessary to modify these metalloinsertors with cell- and tissue-targeting functionalities, such as peptides or antibodies, to control biodistribution *in vivo*. It is difficult to predict how these complexes will fare in multicellular organisms and complex tumor microenvironments, just as the anticancer properties (and consequent adverse effects) of cisplatin could not have been foretold prior to their discovery. The continued modulation of both mono- and bifunctional metalloinsertors ensures a diverse repertoire of potentially powerful therapeutic tools.

1.6 Conclusions

Targeted chemotherapy holds the potential to combat the severe side effects and acquired resistance associated with classical chemotherapeutics such as cisplatin. Many years of study have focused on achieving high potency for metal complex therapeutics, but such potency has been achieved. Just as the design of organic chemotherapeutics have shifted from potent alkylators and other inhibitors of DNA synthesis to far more tai-

lored, subtle reagents, the design of novel metallotherapeutics now requires a targeted approach. There has been a paradigm shift in next generation chemotherapeutic drug design that focuses on specifically tailored therapies. The unique reactivity and coordination geometry of metal complexes make them the ideal scaffold for this new tailor-made design of targeted therapeutics. The examples discussed herein exemplify the enormous potential of this new strategy in transition metal chemotherapy and perhaps lay the groundwork for this burgeoning new field.

1.7 References

- 1 Mansour, V. H.; Rosenberg, B.; Vancamp, L.; Trosko, J. E. *Nature* **1969**, *222*, 385–386.
- 2 Wheate, N. J.; Walker, S.; Craig, G. E.; Oun, R. *Dalton Trans.* **2010**, *39*, 8113–8127
- 3 Kelland, L. R.; Sharp, S. Y.; O’Neill, C. F.; Raynaud, F. I.; Beale, P. J.; Judson, I. *R. J. Inorg. Biochem.* **1999**, *77*, 111–115.
- 4 Jamieson, E. R.; Lippard, S. J. *Chem. Rev.* **1999**, *99*, 2467-2498.
- 5 Wang, D.; Lippard, S. J. *Nat. Rev. Drug Discovery* **2005**, *4*, 307–320.
- 6 Dulhunty, A. F. *J. Physiol.* **1978**, *276*, 67-82.
- 7 Zhang, C. X.; Lippard, S. J. *Curr. Opin. Chem. Biol.* **2003**, *7*, 481-489.
- 8 Siddik, Z. H. *Oncogene* **2003**, *22*, 7265-7279.
- 9 Selvakumaran, M.; Pisarcik, D. A.; Bao, R.; Yeung, A. T.; Hamilton, T. C. *Cancer Res.* **2003**, *63*, 1311-1316.
- 10 Ferry, K. V.; Hamilton, T. C.; Johnson, S. W. *Biochem. Pharmacol.* **2000**, *60*, 1205-1313.
- 11 Johnson, S. W.; Perez, R. P.; Godwin, A. K.; Yeung, A. T.; Handel, L. M.; Ozols, R. F.; Hamilton, T. C. *Biochem. Pharmacol.* **1994**, *47*, 689-697.
- 12 Huang, J.-C.; Zamble, D. B.; Reardon, J. T.; Lippard, S. J.; Sancar, A. *Proc. Natl. Acad. Sci. U.S.A.* **1994**, *91*, 10394-10398.
- 13 McA’Nulty, M. M.; Lippard, S. J. *Mutat. Res., DNA Repair* **1996**, *362*, 75-86.

- 14 Aebi, S.; Kurdi-Haidar, B.; Gordon, R.; Cenni, B.; Zheng, H.; Fink, D.; Christen, R. D.; Boland, R.; Koi, M.; Fishel, R.; Howell, S. B. *Cancer Res.* **1996**, *56*, 3087-3090.
- 15 Fink, D.; Nebel, S.; Aebi, S.; Zheng, H.; Cenni, B.; Nehme, A.; Christen, R. D.; Howell, S. B. *Cancer Res.* **1996**, *56*, 4881-4886.
- 16 Rhyu, M. S. *J. Natl. Cancer Inst.* **1996**, *88*, 240-251.
- 17 Kehe, K.; Szinicz, L. *Toxicology* **2005**, *214*, 198-209.
- 18 Montana, A. M.; Batalla, C. *Curr. Med. Chem.* **2009**, *16*, 2235-2260.
- 19 Niedle, S.; Ismail, I. M.; Sadler, P. J. *J. Inorg. Biochem.* **1980**, *13*, 205-212.
- 20 Frey, U.; Ranford, J. D.; Sadler, P. J. *Inorg. Chem.* **1993**, *32*, 1333-1340.
- 21 Boulikas, T.; Vougiouka, M. *Oncol. Rep.* **2003**, *10*, 1663-1682.
- 22 Kasparikova, J.; Vojtiskova, M.; Natile, G.; Brabec, V. *Chem. Eur. J.* **2008**, *14*, 1330-1341.
- 23 Ibrahim, A.; Hirschfeld, S.; Cohen, M. H.; Griebel, D. J.; Williams, G. A.; Pazdur, R. *Oncologist* **2004**, *9*, 8-12.
- 24 Hall, M. D.; Mellor, H. R.; Callaghan, R.; Hambley, T. W. *J. Med. Chem.* **2007**, *50*, 3403-3410.
- 25 Johnstone, T. C.; Wilson, J. J.; Lippard, S. J. *Inorg. Chem.* **2013**, *52*, 12234-12249.
- 26 Perez, J. M.; Fuertes, M. A.; Alonso, C.; Navarro-Ranninger, C. *Crit. Rev. Oncol. Hematol.* **2000**, *35*, 109-120.
- 27 Ang, W. H.; Dyson, P. J. *Eur. J. Inorg. Chem.* **2006**, 4003-4018.

- 28 Beltran, B., Casado, P., Rodríguez-Prados, J.-C., Cutillas, P. R. *J. Proteomics* **2012**, *77*, 492–503.
- 29 Feng, L. et al. *J. Am. Chem. Soc.* **2011**, *133*, 5976–5986.
- 30 Kunick, C., Ott, I. *Angew. Chem. Int. Ed.* **2010**, *49*, 5226–5227.
- 31 Koblinski, J. E., Ahram, M., Sloane, B. F. *Clin. Chim. Acta* **2000**, *291*, 113–135.
- 32 Meggers, E. *Chem. Commun.* **2009**, 1001–1010.
- 33 Casini, A. et al. *J. Med. Chem.* **2008**, *51*, 6773–6781.
- 34 Guidi, F., et al. *J. Inorg. Biochem.* **2013**, *118*, 94–99.
- 35 Holst, F. et al. *Nat. Genet.* **2007**, *39*, 655–660.
- 36 Vessières, A., Top, S., Beck, W., Hillard, E., Jaouen, G. *Dalton Trans.* **2006**, 529–541.
- 37 Pigeon, P., Top, S., Vessières, A., Huché, M., Hillard, E., Salomon, E., Jaouen, G. *J. Med. Chem.* **2005**, *48*, 2814–2821.
- 38 Gogvadze, V., Orrenius, S., Zhivotovsky, B. *Trends Cell Biol.* **2008**, *18*, 166–173.
- 39 Wisnovsky, S. P., Wilson, J. J., Radford, R. J., Pereira, M. P., Laposa, R. R., Lippard, S. J., Kelley, S. O. *Chem. Biol.* **2013**, *20*, 1–6.
- 40 Lo, K. K.-W.; Choi, A. W.-T.; Law, W. H.-T. *Dalton Trans.* **2012**, *41*, 6021–6047.
- 41 Eriksson, M.; Leijon, M.; Hiort, C.; Norden, B.; Graslund, A. *Biochemistry* **1994**, *33*, 5031–5040.
- 42 Meijler, M. M.; Zelenko, O.; Sigman, D. S. *J. Am. Chem. Soc.* **1997**, *119*, 1135–1136.

- 43 Chen, C. H. B.; Milne, L.; Landgraf, R.; Perrin, D. M.; Sigman, D. S. *Chembiochem.* **2001**, *2*, 735–740.
- 44 Barton, J. K. *Science* **1986**, *233*, 727-734.
- 45 Erkkila, K. E.; Odom, D. T.; Barton, J. K. *Chem. Rev.* **1999**, *99*, 2777–2795.
- 46 Zeglis, B. M.; Pierre, V. C.; Barton, J. K. *Chem. Comm.* **2007**, *44*, 4565-4579.
- 47 Suh, D.; Chaires, J. B. *Bioorg. Med. Chem.* **1995**, *3*, 723-728.
- 48 Kielkopf, C. L.; Erkkila, K. E.; Hudson, B. P.; Barton, J. K.; Rees, D. C. *Nature Struct. Biol.* **2000**, *7*, 117–121.
- 49 Friedman, A. E.; Chambron, J. C.; Sauvage, J. P.; Turro, N. J.; Barton, J. K. *J. Am. Chem. Soc.* **1990**, *112*, 4960–4962.
- 50 Turro, C.; Bossmann, S. H.; Jenkins, Y.; Barton, J. K.; Turro, N. J. *J. Am. Chem. Soc.* **1995**, *117*, 9026–9032.
- 51 Olson, E. J. C.; Hu, D.; Hormann, A.; Jonkman, A. M.; Arkin, M. R.; Stemp, E. D. A.; Barton, J. K.; Barbara, P. F. *J. Am. Chem. Soc.* **1997**, *119*, 11458–11467.
- 52 Puckett, C. A.; Barton, J. K. *J. Am. Chem. Soc.* **2007**, *129*, 46–47.
- 53 McConnell, A. J.; Lim, M. H.; Olmon, E. D.; Song, H. Dervan, E. E.; Barton, J. K. *Inorg. Chem.* **2012**, *51*, 12511-12520.
- 54 Sitlani, A.; Long, E. C.; Pyle, A. M.; Barton, J. K. *J. Am. Chem. Soc.* **1992**, *114*, 2303–2312.
- 55 Hartshorn, R. M.; Barton, J. K. *J. Am. Chem. Soc.* **1992**, *114*, 5919–5925.
- 56 Boerner, L. J. K.; Zaleski, J. M. *Curr. Opin. Chem. Biol.* **2005**, *9*, 135-144
- 57 Núñez, M. E.; Barton, J. K. *Curr. Opin. Chem. Biol.* **2000**, *4*, 199-206.
- 58 Krotz, A. H.; Hudson, B. P.; Barton, J. K. *J. Am. Chem. Soc.* **1993**, *115*,

- 12577–12578.
- 59 Jackson, B. A.; Barton, J. K. *J. Am. Chem. Soc.* **1997**, *119*, 12986–12987.
- 60 Isaacs, R. J.; Rayens, W. S.; Spielmann, H. P. *J. Mol. Biol.* **2002**,
319, 191–207.
- 61 Peyret, N.; Seneviratne, P. A.; Allawi, H. T.; SantaLucia, J. *Biochemistry* **1999**,
38, 3468–3477.
- 62 Cordier, C.; Pierre, V. C.; Barton, J. K. *J. Am. Chem. Soc.* **2007**, *129*, 12287–
12295.
- 63 Zeglis, B. M.; Pierre, V. C.; Kaiser, J. T.; Barton, J. K. *Biochemistry* **2009**, *48*,
4247–4253.
- 64 Lerman, L. S. *J. Mol. Biol.* **1961**, *3*, 18–30.
- 65 Murner, H.; Jackson, B. A.; Barton, J. K. *Inorg. Chem.* **1998**, *37*,
3007–3012.
- 66 Jackson, B. A.; Alekseyev, V. Y.; Barton, J. K. *Biochemistry* **1999**, *38*, 4655–
4662.
- 67 Peyret, N.; Seneviratne, P. A.; Allawi, H. T.; SantaLucia, J. *Biochemistry* **1999**,
38, 3468–3477.
- 68 Jackson, B. A.; Barton, J. K. *Biochemistry* **2000**, *39*, 6176–6182.
- 69 Pierre, V. C.; Kaiser, J. T.; Barton, J. K. *Proc. Natl. Acad. Sci. U.S.A.* **2007**, *104*,
429–434.
- 70 Song, H. Kaiser; J. T.; Barton, J. K. *Nature Chem.* **2012**, *4*, 615–620.
- 71 Loeb, L. A. *Cancer Res.* **2001**, *61*, 3230–3239.

- 72 Bhattacharya, N. P.; Skandalis, A.; Ganesh, A.; Groden, J.; Meuth, M. *Proc. Natl. Acad. Sci. U.S.A.* **1994**, *91*, 6319–6323.
- 73 Iyer, R. R.; Pluciennik, A.; Burdett, V.; Modrich, P. L. *Chem. Rev.* **2006**, *106*, 302–323.
- 74 Carethers, J. M.; Hawn, M. T.; Chauhan, D. P.; Luce, M. C.; Marra, G.; Koi, M.; Boland, C. R. *J. Clin. Invest.* **1996**, *98*, 199–206.
- 75 Hart, J. R.; Glebov, O.; Ernst, R. J.; Kirsch, I. R.; Barton, J. K. *Proc. Natl. Acad. Sci. U.S.A.* **2006**, *103*, 15359–15363.
- 76 Ernst, R. J.; Song, H.; Barton, J. K. *J. Am. Chem. Soc.* **2009**, *131*, 2359–2366.
- 77 Ernst, R. J.; Komor, A. C.; Barton, J. K. *Biochemistry* **2011**, *50*, 10919–10928.
- 78 Komor, A. C.; Schneider, C. J.; Weidmann, A. G.; Barton, J. K. *J. Am. Chem. Soc.* **2012**, *134*, 19223–19233.
- 79 Weidmann, A. G.; Komor, A. C.; Barton, J. K. *Philos. Trans. R. Soc. A.* **2013**, *371*, 20120117.
- 80 Koi, M.; Umar, A.; Chauhan, D. P.; Cherian, S. P.; Carethers, J. M.; Kunkel, T. A.; Boland, C. R. *Cancer Res.* **1994**, *54*, 4308-4312.
- 81 Bailis, J. M.; Gordon, M. L.; Gurgel, J. L.; Komor, A. C.; Barton, J. K.; Kirsch, I. R. *PLoS One* **2013**, *8*, e78726.
- 82 Komor, A. C.; Barton, J. K. *J. Am. Chem. Soc.* **2014**, *136*, 14160-14172.
- 83 Schatzschneider, U.; Barton, J. K. *J. Am. Chem. Soc.* **2004**, *126*, 8630–8631.
- 84 Lim, M. H.; Lau, I. H.; Barton, J. K. *Inorg. Chem.* **2007**, *46*, 9528–9530.
- 85 Petitjean, A.; Barton, J. K. *J. Am. Chem. Soc.* **2004**, *126*, 14728–14729.
- 86 Ernst, R. J. *Unpublished results.*

- 87 Frankel, A. D.; Pabo, C. O. *Cell* **1988**, *55*, 1189-1193
- 88 Brunner, J.; Barton, J. K. *Biochemistry* **2006**, *45*, 12295–12302.
- 89 Homesley, H. D.; Bundy, B. N.; Hurteau, J. A.; Roth, L. M. *Gynecol. Oncol.* **1999**, *72*, 131-137.

Chapter 2: Cell-Selective Biological Activity of Rhodium Metalloinsertors Correlates with Subcellular Localization**

2.1 Introduction

The mismatch repair (MMR) machinery recognizes and repairs single base lesions and mismatches that arise from errors in DNA replication.^{1,2} Deficiencies in the MMR machinery increase the rate of mutagenesis 50-1000 fold, resulting in an enhanced susceptibility to cancer.^{3,4} Additionally, many MMR-deficient cancers exhibit resistance to chemotherapeutics such as DNA alkylators and platinating agents,⁵ as MMR proteins are responsible for recognizing the DNA adducts formed by these agents.⁶ As a strategy to target MMR-deficient cancers, we have developed a variety of bulky rhodium complexes that target DNA mismatches through metalloinsertion, a binding mode in which a sterically expansive ligand, such as chrysenequinone diimine (chrysi), inserts into the DNA base stack at the site of the mismatch and ejects the thermodynamically destabilized bases. These complexes exhibit 1000-fold selectivity over well-matched DNA and target 80% of all mismatches irrespective of sequence context.⁷⁻¹⁰

Metalloinsertion represents a general binding mode for the binding of bulky metal complexes to destabilized mismatches. With intercalative binding, well-matched,

Adapted from Weidmann, A. G., Komor A. C., Barton, J. K. "Biological Effects of Simple Changes in Functionality on Rhodium Metalloinsertors." *Philos. Trans. R. Soc. A.* **2013, 371, 20120117; and Komor, A. C.; Schneider, C. J.; Weidmann, A. G.; Barton, J. K. "Cell-Selective Biological Activity of Rhodium Metalloinsertors Correlates with Subcellular Localization." *J. Am. Chem. Soc.* **2012**, 134, 19223-19233. © 2012 American Chemical Society.

Acknowledgements: Alexis Komor synthesized $[\text{Rh}(\text{phzi})(\text{NH}_3)_4]^{3+}$, $[\text{Rh}(\text{bpy})_2\text{chrysi}]^{3+}$, $[\text{Rh}(\text{HDPA})_2\text{chrysi}]^{3+}$, and $[\text{Rh}(\text{DIP})_2\text{chrysi}]^{3+}$ complexes, and Curtis Schneider synthesized the $[\text{Rh}(\text{chrysi})(\text{phen})(\text{L})]\text{Cl}_3$ (L= HDPA, MeDPA, PrDPA) compounds. I synthesized $[\text{Rh}(\text{DPAE})_2\text{chrysi}]^{3+}$, $[\text{Rh}(\text{PrDPA})_2\text{chrysi}]^{3+}$, and the corresponding ligands, and also assisted in the ELISA, MTT, and ICP-MS (cellular uptake and nuclear and mitochondrial localization) biological experiments.

hydrogen-bonded base pairs separate, increasing the helical pitch, so that an aromatic heterocyclic ligand can stack within the DNA duplex, essentially like another base pair.¹¹ For metalloinsertion, the flat aromatic heterocyclic ligand is simply too large to insert easily into the DNA duplex and instead, to accommodate the inserting ligand, the base pairs must separate and be ejected from the helix.^{12,13} This ejection only occurs easily at destabilized mismatched sites, and thus the binding affinity for mismatches correlates with the thermodynamic instability of the mismatch, the ease of separation and ejection. Several crystal structures have shown that metalloinsertion occurs from the minor groove side with no increase in helical pitch.¹²⁻¹⁴ As a result, for the tris(chelate) metalloinsertors, binding within the small minor groove is highly enantioselective for the D-isomer.

Previously, we have demonstrated that, because of this high specificity for DNA mismatches, these rhodium metalloinsertors have unique biological properties.¹⁵⁻¹⁷ Their biological activity has been characterized in two isogenic cell lines derived from human colorectal carcinoma (HCT116), one MMR-deficient (HCT116O), the other MMR-proficient (HCT116N). The HCT116 parent cell line is a human colorectal carcinoma line deficient in the *hMLH1* gene. This gene encodes for part of the mismatch repair (MMR) machinery; consequently this cell line is MMR deficient. The HCT116N cell line has been transfected with human chromosome 3 (ch3), which restores MMR proficiency, while the HCT116O cell line has been transfected with human chromosome 2 (ch2), leaving it MMR deficient.¹⁸ Cellular proliferation assays have shown that our rhodium metalloinsertors exhibit antiproliferative activity preferentially in the MMR-deficient HCT116O line. Moreover, the extent of this cell-selectivity is dependent on binding of

the complex to a mismatched site: the higher the mismatch binding affinity, the greater the differential inhibition of cellular proliferation in MMR-deficient versus proficient cells.¹⁶ Recently, complexes prepared with more efficient cellular uptake have also shown a differential cytotoxicity in MMR-deficient versus proficient cells.¹⁷ The results therefore support the strategy of a cell-selective chemotherapeutic strategy based upon DNA mismatch targeting.

In the development of novel metalloinsertors for improved cell-selective antiproliferative activity, two complexes were discovered to have strikingly different biological activities, despite containing only minor functional group changes to their overall structure. The complexes, depicted in **Figure 2.1**, are tris(chelate) compounds that consist of two *N*-functionalized dipyriddyamine (DPA) ligands in addition to the inserting chrysi ligand. The modified DPA ligands contain either ethanol or *N*-propyl moieties, affording $[\text{Rh}(\text{DPAE})_2\text{chrysi}]^{3+}$ (**1a**) and $[\text{Rh}(\text{PrDPA})_2\text{chrysi}]^{3+}$ (**1b**), respectively. $[\text{Rh}(\text{DPAE})_2\text{chrysi}]^{3+}$ exhibits exceptional inhibition of growth selectively in MMR-deficient cells, whereas $[\text{Rh}(\text{PrDPA})_2\text{chrysi}]^{3+}$ displays little detectable cell-selectivity; instead the PrDPA complex inhibits cellular proliferation in both cell lines. Here we explore the various factors that contribute to this cell-selective biological activity for one complex with no activity for the closely related complex. We find that the selective activity in MMR-deficient cells depends not only upon a high binding affinity for single base mismatches, present for both complexes, but also upon efficient targeting of the complexes to nuclear rather than mitochondrial DNA. Specifically, genomic DNA mismatches are implicated as the target for rhodium metalloinsertors *in cellulo*, whereas the mitochondrion appears to be an undesirable target. Furthermore, this trend was

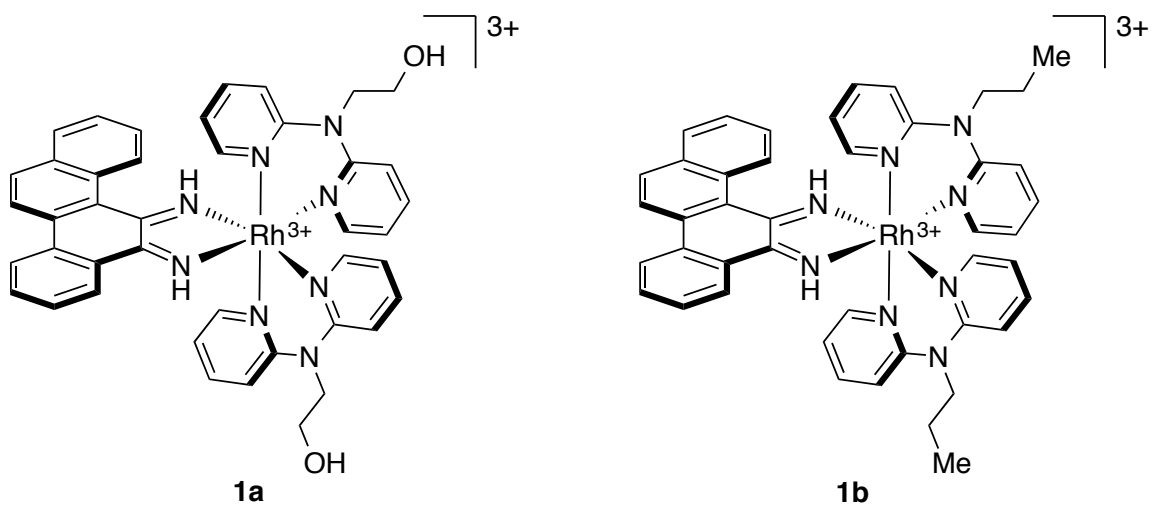


Figure 2.1 Rh(L)₂chrysi³⁺ metalloinsertors. Rh(DPAE)₂chrysi³⁺ (**1a**) contains two ethanol moieties off the central nitrogen atoms, where Rh(PrDPA)₂chrysi³⁺ (**1b**) contains instead two propyl groups. Both complexes also contain the sterically expanded 5,6-chrysenediimine (chrysi) inserting ligand, for selective binding of thermodynamically destabilized DNA mismatches.

confirmed generally in a study of a family of ten metalloinsertor complexes with similar binding affinities, but varying lipophilicities.¹⁹ These results underscore sub-cellular localization as an important factor also in therapeutic design.

2.2 Experimental Protocols

2.2.1 Materials

All organic reagents were purchased from Sigma-Aldrich unless otherwise noted. Commercially available chemicals were used as received without further purification. RhCl₃ starting material was purchased from Pressure Chemical Co. Media and supplements were purchased from Invitrogen (Carlsbad, CA). BrdU, antibodies, and buffers were purchased in kit format from Roche Molecular Biochemical (Mannheim, Germany).

Oligonucleotides were ordered from Integrated DNA Technologies and purified by HPLC using a C18 reverse-phase column (Varian, Inc). All HPLC purifications were carried out on a Hewlett-Packard 1100 HPLC. DNA purity was confirmed by MALDI-TOF mass spectrometry and quantified by UV-vis using the extinction coefficients at 260 nm estimated for single-stranded DNA. UV-vis characterizations were performed on a Beckmann DU 7400 spectrophotometer.

2.2.2 Ligand Synthesis (Scheme 2.1)

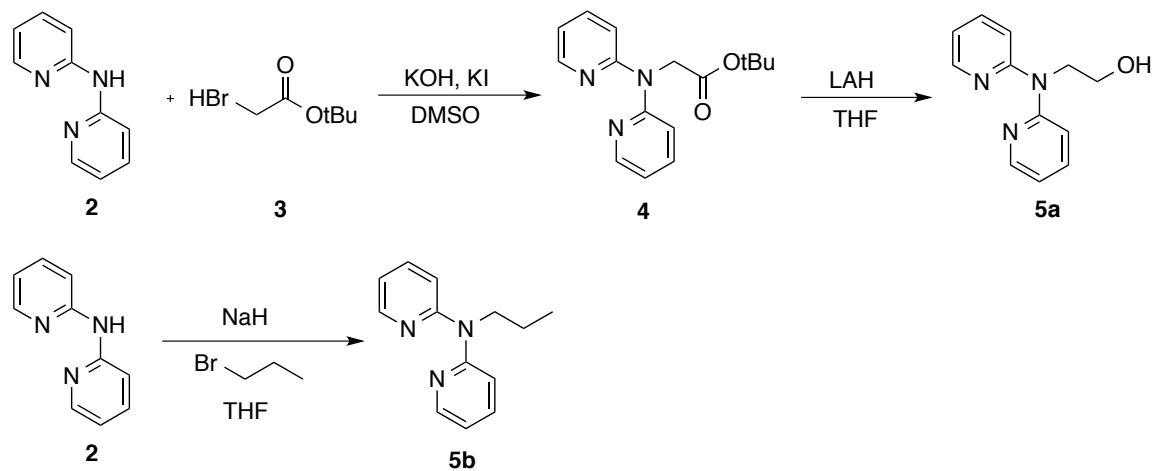
The ancillary ligands, 2-(di(pyridin-2-yl)amino)ethanol (DPAE, 5a) and *N*-propyl-*N*-(pyridin-2-yl)pyridin-2-amine (PrDPA, 5b), were synthesized from 2,2'-dipyridylamine (2) according to Scheme 1.

2.2.2.1 Tert-butyl 2-(di(pyridine-2-yl)amino)acetate (4). Tert-butyl 2-(di(pyridine-2-yl)amino)acetate (4) was prepared according to a modified literature

procedure.²⁰ Potassium hydroxide (3.0 g, 53.6 mmol, 4.6 equiv) was added to a solution of 2,2'-dipyridylamine (**2**) (2.0 g, 11.7 mmol) in 40 ml DMSO and stirred at room temperature for 16 h. Potassium iodide (200 mg, 1.2 mmol, 0.1 equiv) and tert-butyl bromoacetate (**3**) (4 ml, 2.3 equiv) were added to the mixture, and the reaction was stirred for 2 h at room temperature. The reaction mixture was extracted with diethyl ether (3 x 50 ml). The organic fractions were combined and dried over magnesium sulfate, and the solvent was removed by rotary evaporation. The crude product was isolated by flash chromatography (SiO₂, hexane/ethyl acetate = 8:2) to give a yellow oil. Yield: 2.92 g (88%). ¹H NMR (CDCl₃, 300 MHz): δ 8.33 (ddd, J = 5.0, 1.9, 0.9 Hz; 2H), 7.53 (m, 2H), 7.23 (m, 2H), 6.88 (ddd, J = 7.2, 5.0, 0.9 Hz; 2H), 4.84 (s, 2H), 1.42 (s, 9H). ESI-MS (cation): 286 m/z (M + H⁺) obsd, 286 m/z calcd.

2.2.2.2 2-(di(pyridine-2-yl)amino)ethanol (5a). To a slurry of LAH (1.17 g, 30.8 mmol, 3.0 equiv) in THF (45 ml) was added **4** (2.9 g, 10.2 mmol) at 0 °C under 1 atm Ar. The reaction was slowly warmed to room temperature over 4 h. The reaction mixture was then diluted with ethyl ether and cooled to 0 °C. The reaction was quenched via careful addition of water (4.0 ml) and then dried with magnesium sulfate. The solvent was removed in vacuo, and the crude product was purified by flash chromatography (SiO₂, hexane/ethyl acetate = 1:1) to afford DPAAE (**5a**) as a pale yellow oil. Yield: 1.2 g (55%). ¹H NMR (DMSO-d₆, 300 MHz): δ 8.27 (m, 2H), 7.62 (m, 2H), 7.16 (d, J = 8.4 Hz, 2H), 6.93 (m, 2H), 4.92 (t, J = 5.4 Hz, 1H), 4.16 (t, J = 6.5 Hz, 2H), 3.58 (q, J = 6.5 Hz, 2H). ESI-MS (cation): 216.1 m/z (M + H⁺) obsd, 215 m/z calcd.

2.2.2.3 N-propyl-N-(pyridin-2-yl)pyridin-2-amine (5b). To a slurry of sodium hydride (70 mg, 2.9 mmol) in THF (10 ml) was added **2** (500 mg, 2.9 mmol) in 5



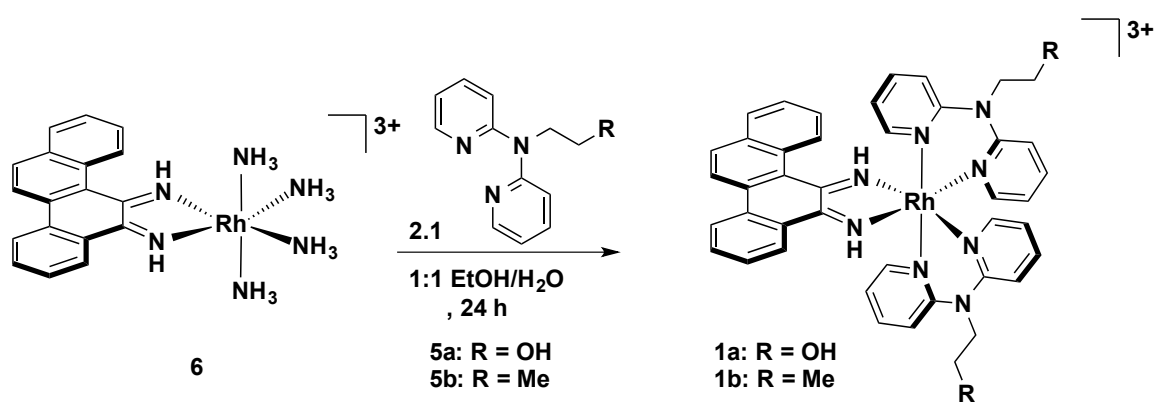
Scheme 2.1 Synthesis of ancillary ligands 2-(di(pyridine-2-yl)amino)ethanol (DPAE, **5a**) and N-propyl-N-(pyridin-2-yl)pyridin-2-amine (PrDPA, **5b**) from 2,2'-dipyridylamine (**2**).

ml THF at 0 °C under 1 atm Ar. The reaction was purged with argon for 15 min, and 1-bromopropane (468 mg, 3.8 mmol) was added dropwise and warmed to room temperature. The reaction was stirred an additional 18 h under argon at reflux temperature. The reaction mixture was extracted with dilute sodium bicarbonate, and the aqueous phase was extracted with CH₂Cl₂ (3 x 40 ml). The organic fractions were combined and dried over magnesium sulfate, and the solvent was removed *in vacuo*. **5b** was purified via flash chromatography (SiO₂, hexane/ethyl acetate = 9:1). Yield: 100 mg (25%) ¹H NMR (CDCl₃, 300 MHz): δ 8.34 (d, J = 7.7 Hz, 2H), 7.57 – 7.45 (m, 2H), 7.06 (d, J = 0.7 Hz, 2H), 6.90 – 6.79 (m, 2H), 4.19 – 4.07 (m, 2H), 1.79 – 1.65 (m, 2H), 0.99 – 0.85 (m, 3H) ppm. ESI-MS (cation): 214.1 m/z (M + H⁺) obsd, 213 m/z calcd.

2.2.3 Metal Complexes

2.2.3.1 Rh(NH₃)₄chrysi³⁺ (6**).** Rhodium precursor **6** was synthesized from Rh(NH₃)₅Cl²⁺ according to published protocols.¹⁶ The remaining complexes in this study were synthesized as described in Reference 19.** The syntheses of [Rh(DPAE)₂chrysi]³⁺ (**1a**) and [Rh(PrDPA)₂chrysi]³⁺ (**1b**) are depicted in **Scheme 2.2**.

2.2.3.2 *rac*-Rh(DPAE)₂chrysi³⁺ (1a**).** [Rh(NH₃)₄chrysi]Cl₃ (**6**) (20 mg, 0.038 mmol) and **5a** (17.8 mg, 0.082 mmol, excess) were dissolved in a 1:1 mixture of ethanol and water (100 ml) and heated under reflux for 28 h. The solvent was removed *in vacuo*, and the crude product was purified by HPLC (95:5:0.001 H₂O:MeCN:TFA), using a C18 reverse-phase column (Varian, Inc). The purified product was dried under vacuum and redissolved in a minimal volume of water. The TFA counterion was exchanged for a chloride with a Sephadex QAE-125 ion-exchange resin primed with 1M MgCl₂. Yield: 4.5 mg (13.5%). ¹H NMR (DMSO-*d*₆, 300 MHz): δ 13.47 (s, 1H), 13.03 (s, 1H), 9.27 (d,



Scheme 2.2 Synthesis of $rac\text{-}[\text{Rh}(\text{L})_2\text{chrysi}]^{3+}$, where $\text{L} = 2\text{-}(\text{di}(\text{pyridine-2-yl})\text{amino})\text{ethanol}$ (DPAE, **5a**) or $\text{N-propyl-N-(pyridin-2-yl)pyridin-2-amine}$ (PrDPA, **5b**).

$J = 8.1$ Hz, 1H), 9.02-8.75 (overlapping m, 6H), 8.52-8.27 (overlapping m, 3H), 8.21-7.60 (overlapping m, 8H) 7.41-7.01 (m, 8H), 4.23-4.04 (m, 4H), 3.82 (s, 2H), 3.71-3.54 (m, 4H) ppm; UV-vis (H_2O pH 8): 297 nm ($47,000 \text{ M}^{-1} \text{ cm}^{-1}$), 391 nm ($9,300 \text{ M}^{-1} \text{ cm}^{-1}$). ESI-MS (cation): 787.1 m/z ($\text{M} - 2\text{H}^+$), 394.2 m/z ($\text{M} - \text{H}^{2+}$) obsd, 787 m/z ($\text{M} - 2\text{H}^+$) calcd.

2.2.3.3 *rac*-Rh(PrDPA)₂chrysi³⁺ (1b). **1b** was synthesized from **6** (20 mg, 0.038 mmol) and **5b** (17 mg, 0.08 mmol) as described for **1a**. The resulting product was purified by HPLC (95:5:0.001 H_2O :MeCN:TFA) and passed through a Sephadex QAE-125 ion-exchanged resin primed with 1M MgCl_2 to give the chloride salt. Yield: 3 mg (15%). ¹H NMR ($\text{DMSO-}d_6$, 300 MHz): δ 10.08 (d, $J = 8.6$ Hz, 1H), 8.05 (dd, $J = 26.7$, 8.6 Hz, 4H), 7.58 (dd, $J = 21.1$, 8.5 Hz, 4H), 7.46-7.32 (m, 6H), 7.27-7.11 (m, 3H), 6.90-6.78 (m, 8H), 0.97-0.85 (m, 4H), 0.62 (t, $J = 7.2$ Hz, 4H), 0.02 (t, $J = 7.3$ Hz, 6H) ppm; UV-vis: (H_2O pH 8): 295 nm ($51,000 \text{ M}^{-1} \text{ cm}^{-1}$), 388 nm ($13,000 \text{ M}^{-1} \text{ cm}^{-1}$). ESI-MS (cation): 783.1 m/z ($\text{M} - 2\text{H}^+$), 392.4 m/z ($\text{M} - \text{H}^{2+}$) obsd, 783 m/z calcd.

2.2.4 Octanol/Water Partition Coefficient (log P)

Solid $[\text{Rh}(\text{DPAE})_2\text{chrysi}]^{3+}$, $[\text{Rh}(\text{PrDPA})_2\text{chrysi}]^{3+}$, and $[\text{Rh}(\text{DIP})_2\text{chrysi}]^{3+}$ were dissolved in 10 ml 1-octanol-saturated H_2O . Aliquots (2 ml) of each sample were taken in triplicate, mixed with an equal volume of H_2O -saturated 1-octanol, and vortexed for 10 s. The samples were incubated at room temperature for 4 h and centrifuged for 5 min at 3000 rpm to allow for the separation of the two phases. The concentrations of rhodium in the aqueous and organic phases were determined by UV-vis; to account for the change in the molar absorptivity of rhodium in 1-octanol, $[\text{Rh}]_{\text{oct}}$ was defined as $[\text{Rh}]_{\text{stock}} - [\text{Rh}]_{\text{aq}}$. Log P is defined as $\log([\text{Rh}]_{\text{oct}}/[\text{Rh}]_{\text{aq}})$.

2.2.5 Cell Culture

HCT116N and HCT116O cells were grown in RPMI 1640 medium containing 10% FBS, 2 mM L- glutamine, 0.1 mM nonessential amino acids, 1 mM sodium pyruvate, 100 units/mL penicillin, 100 µg/mL streptomycin, and 400 µg/mL Geneticin (G418). Cells were grown in tissue culture flasks (Corning Costar, Acton, MA) at 37 °C and 5% CO₂ humidified atmosphere.

2.2.6 Cellular Proliferation ELISA

ELISAs were performed with HCT116N and HCT116O cells as described in the literature.²¹ Cells were incubated with varying concentrations of rhodium for the durations specified, then grown in rhodium-free media for the remainder of the 72 h period. After 48 h, BrdU was added, and at 72 h, BrdU incorporation was quantified by antibody assay.²¹ Cellular proliferation was expressed as a ratio of BrdU incorporation into treated cells versus that of untreated cells, and standard errors were calculated from five replicates.

2.2.7 Cellular Proliferation MTT

MTT experiments were performed with HCT116N and HCT116O cells as described in the literature.²² HCT116N and HCT116O cells were inoculated with rhodium and plated in 96-well plates at 50,000 cells/well. Cells were incubated for 24, 48, or 72h at 37 °C under humidified atmosphere. After the incubation period, MTT was added, and the cells were incubated for an additional 4 h. The resulting formazan crystals were solubilized over a period of 24 h at 37 °C, 5% CO₂. Formazan formation was quantified *via* electronic absorption at 550-600 nm with a reference wavelength of 690

nm. Cell viability is expressed as a function of formazan formation and normalized to that of untreated cells. Standard errors were calculated from five replicates.

2.2.8 Binding Competition Titrations

A 29-mer DNA hairpin containing a CC mismatch (*5'-GGCAGGCATG-GCTTTTGGCCATCCCTGCC-3') (underline denotes the mismatch; asterisk denotes the radiolabel) was labeled with ^{32}P at the 5'-end according to established procedures.²³ A 1:1 mixture of labeled and unlabeled DNA was prepared in buffer (100 mM NaCl, 20 mM NaP_i , pH 7.1) to a final concentration of 2 μM . The hairpin was annealed by heating to 90 $^\circ\text{C}$ for 10 min and slowly cooled to room temperature. To prepare samples for gel electrophoresis, 5 μL of a 4 μM solution of $[\text{Rh}(\text{bpy})_2\text{chrysi}]\text{Cl}_3$ (which photocleaves the DNA backbone at the site of a mismatch or abasic site upon irradiation⁸⁻¹⁰) and varying concentrations of non-photocleaving competitor complex (5 μL) were added to 2 μM annealed DNA hairpin (10 μL). A light control (10 μL DNA, 10 μL H_2O), a dark control (10 μL DNA, 5 μL $\text{Rh}(\text{bpy})_2\text{chrysi}^{3+}$, 5 μL Rh, no irradiation), and a positive control (10 μL DNA, 5 μL $\text{Rh}(\text{bpy})_2\text{chrysi}^{3+}$, 5 μL H_2O) were also prepared. Samples were vortexed and, except for the dark control, irradiated on an Oriel (Darmstadt, Germany) 1000-W Hg/Xe solar simulator (340-440 nm) for 15 min. Samples were then incubated at 37 $^\circ\text{C}$ for 20 min, dried, then electrophoresed through a 20 % denaturing polyacrylamide gel. The gel was exposed on a phosphor screen, phosphorimaged (See **Figure 2.2** for a representative autoradiogram), and the amounts of DNA cleavage were quantified using ImageQuant.

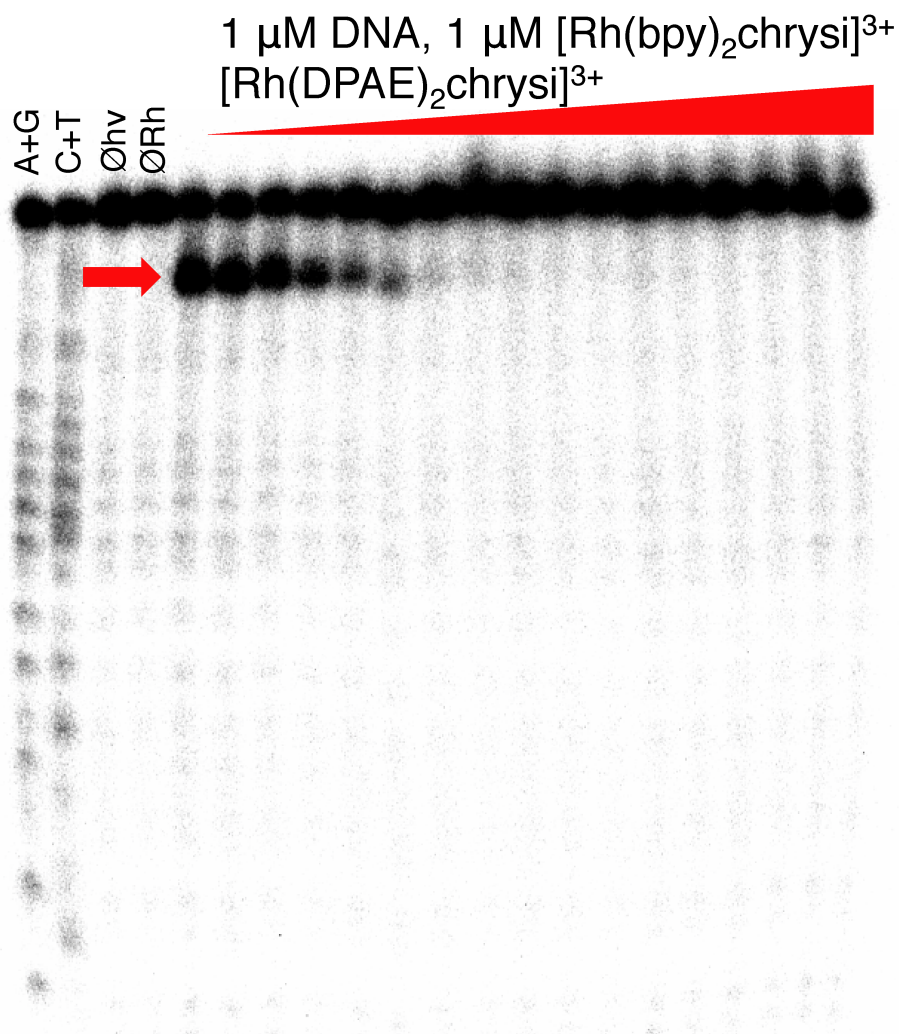


Figure 2.2 Binding affinities determined through DNA photocleavage. The DNA hairpin sequence is *5'-GGCAGGCATGGCTTTTTGCCATCCCTGCC-3' (underline denotes the mismatch, asterisk denotes the radiolabel). Samples were irradiated for 15 min and electrophoresed on a 20% denaturing PAGE gel. A light control (ØRh, without rhodium) and a dark control (Øhv, without irradiation) were included. A representative autoradiogram of a photocleavage competition titration between 1 μM *rac*- $[\text{Rh}(\text{bpy})_2\text{chrysi}]^{3+}$ and 0-50 μM $[\text{Rh}(\text{DPAE})_2\text{chrysi}]^{3+}$ is shown. Arrow indicates the position of the mismatch.

To determine the K_B values of each complex, competition gels were run in triplicate for each complex, and the percent DNA cleavage at each concentration was averaged and plotted as a function of $\log [Rh]$. The data were fitted to a sigmoidal curve using OriginPro 8.1. K_B values were determined by calculating the concentration of rhodium at the inflection points of the curve and solving simultaneous equilibria involving DNA, $Rh(bpy)_2chrysi^{3+}$, and the competitor complex in Mathematica 8.0. The dissociation constant K_D is defined as $1/K_B$.

2.2.9 Whole-Cell Rhodium Accumulation

HCT116O cells were plated in 6-well plates at 1.0×10^6 cells/well (3 ml media), and allowed 24 h to adhere. The cells were then incubated with 10 μM rhodium (except for $[Rh(DIP)_2chrysi]^{3+}$, which was administered at 2 μM) for a periods of 1, 3, 6, 12, or 24 h. Cells were lysed with 1% SDS and sonicated Qsonica Ultrasonic processor for 10 sec at 20% amplitude. Samples were aliquoted (0.8 ml) and diluted with 2% HNO_3 (0.8 ml), and cellular rhodium content was quantified on an HP-4500 ICP-MS unit. The remainder of the cell lysates were analyzed for protein content via bicinchoninic acid (BCA) assay.²⁴ Rhodium counts were normalized to cellular protein content, and standard errors were calculated from three replicates.

2.2.10 Mitochondrial Rhodium Accumulation

HCT116O cells were plated in 75 cm^2 culture flasks at 2.0×10^7 cells/plate and incubated at 37 $^{\circ}C$, 5% CO_2 for 24 h. Rhodium was added to 10 μM (except for $[Rh(DIP)_2chrysi]^{3+}$, which was administered at 2 μM) and cells were grown for an additional 24 h. The cells were then harvested by trypsinization and centrifuged for 5 min at 1,200 rpm. The supernatants were decanted, and the cell pellets were resuspended in 1

ml cold PBS (pH 7.2). The cells were centrifuged again for 5 min at 1,200 rpm. The supernatants were discarded, and the resultant pellets were resuspended in 0.5 ml mitochondrial extraction buffer (200 mM mannitol, 68 mM sucrose, 50 mM Pipes, 50 mM KCl, 5 mM EGTA, 2 mM MgCl₂; 1 mM DTT and protease inhibitors were added right before use). The samples were incubated on ice for 20 min, and the suspensions were homogenized via passage through a needle and syringe (35x). The homogenized cells were then centrifuged for 5 min at 750 rpm. The supernatants were collected and spun again at 14,000 g for 10 min. The supernatants were decanted, and the resulting mitochondrial pellet was suspended in 0.8 ml H₂O via probe sonication. All samples were diluted 1x with 2% HNO₃. Aliquots (20 uL) were used in a BCA assay to determine mitochondrial protein content, which was carried out according to standard protocol. Rh counts from ICP MS were converted to ppb and normalized to mitochondrial protein content (ng Rh/mg protein). As the mitochondria were isolated from whole cells, the rhodium content is strictly mitochondrial and therefore cannot be directly compared to total cellular rhodium accumulation. It should be noted that the Rh counts obtained are a lower-bound estimate, given the possibility of rhodium diffusion during organelle isolation. However, the experiments were performed in triplicate and were repeated by different experimenters at different times, and the results are comparable. The purity of mitochondrial fractions was ascertained by Western blot.²⁵

2.2.11 Nuclear Rhodium Accumulation

HCT1160 cells were plated in 75 cm² culture flasks at 1.5 x 10⁷ cells/plate and incubated at 37 °C , 5% CO₂, for 24 h. Rhodium was then added to 10 uM (except for [Rh(DIP)₂chrysi]³⁺, which was administered at 2 μM) and cells were grown for an

additional 24 h. The cells were trypsinized according to standard protocol, and the cell pellets were washed with 3 mL 1x PBS (pH 7.2) and spun at 1200 rpm for 5 min. The supernatant was discarded, and the pellets were resuspended in 1 mL 1x PBS and divided into 2 x 0.5 mL aliquots (nuclear and whole cell). The samples were spun at 450 g for 5 minutes at 4 °C. The supernatants were decanted and the whole cell pellets were dissolved in 1 mL Milli-Q water. The nuclear pellets were dissolved in 1 mL hypotonic buffer (20 mM Tris-HCl, pH 7.4; 10 mM NaCl, 3 mM MgCl₂) and incubated on ice for 15 min. After 15 min, 50 uL of NP-40 detergent were added and the samples were vortexed for 10 s. Samples were then spun at 3000 g for 10 min at 4 °C. The supernatants were discarded, and the nuclear pellets were dissolved in 1 mL Milli-Q water *via* sonication. All samples were diluted 1x with 2% HNO₃. 20 uL aliquots were used in a BCA assay to determine nuclear protein content, which was carried out according to standard protocol. Rh counts from ICP MS were converted to ppb and normalized to nuclear protein content (ng Rh/mg protein). Experiments were performed in biological triplicate, and standard errors were calculated from 6 replicates.

2.3 Results

2.3.1 Synthesis and Characterization of [Rh(DPAE)₂chrysi]³⁺ and [Rh(PrDPA)₂chrysi]³⁺

The complexes studied were prepared in a straightforward manner. The ancillary ligands, 2-(di(pyridin-2-yl)amino)ethanol (DPAE, **5a**) and *N*-propyl-*N*-(pyridin-2-yl)pyridin-2-amine (PrDPA, **5b**), were synthesized from 2,2'-dipyridylamine,²⁰ and the rhodium precursor, [Rh(NH₃)₄chrysi]³⁺ (**6**), is synthesized from [Rh(NH₃)₅Cl]²⁺.¹⁶ The *rac*-tris(chelate) complexes (**1a**, **1b**) are prepared by reacting **6** with either **5a** or **5b** (2.1

equiv) in a 1:1 mixture of ethanol and water at reflux temperature (Scheme 2). The octanol/water partition coefficients ($\log P$) were determined to be -1.5 and -1.0 for $[\text{Rh}(\text{DPAE})_2\text{chrysi}]^{3+}$ and $[\text{Rh}(\text{PrDPA})_2\text{chrysi}]^{3+}$, respectively, illustrating that simple functional group manipulations can appreciably alter the lipophilicity of a complex. These $\log P$ values for $[\text{Rh}(\text{DPAE})_2\text{chrysi}]^{3+}$ and $[\text{Rh}(\text{PrDPA})_2\text{chrysi}]^{3+}$ may be compared to that of $[\text{Rh}(\text{DIP})_2\text{chrysi}]^{3+}$, a highly lipophilic complex ($\log P = 1.3$) but with no cell-selective activity, given its poor binding to mismatches.

2.3.2 DNA Binding Affinity

Previously, a correlation between DNA binding affinity and inhibitory effects on MMR-deficient cells was established.¹⁶ In general, complexes that bind DNA mismatches with the highest affinity were found to have the greatest differential activity *in cellulo*, with the most effective complexes showing $K_B = 10^7 - 10^8 \text{ M}^{-1}$ for a CC mismatch. We thus sought to examine whether a difference in binding affinity might account for the differences seen in biological activities.

Since $[\text{Rh}(\text{DPAE})_2\text{chrysi}]^{3+}$ and $[\text{Rh}(\text{PrDPA})_2\text{chrysi}]^{3+}$ do not promote DNA photocleavage, DNA binding affinities were measured on a 29mer hairpin sequence – 5'-GGCAGGCATGGCTTTTTGCCATCCCTGCC-3' (underline denotes the mismatch) – containing a CC mismatch in a competition assay through photocleavage by $[\text{Rh}(\text{bpy})_2\text{chrysi}]^{3+}$.²³ For a CC mismatch, we find $K_B = 6.8 \times 10^6 \text{ M}^{-1}$ and $2.5 \times 10^6 \text{ M}^{-1}$ for $[\text{Rh}(\text{DPAE})_2\text{chrysi}]^{3+}$ and $[\text{Rh}(\text{PrDPA})_2\text{chrysi}]^{3+}$, respectively (see **Figure 2.3**). The binding affinity of $[\text{Rh}(\text{DPAE})_2\text{chrysi}]^{3+}$ for a CC-mismatch is therefore only slightly greater than that of $[\text{Rh}(\text{PrDPA})_2\text{chrysi}]^{3+}$. Both complexes show affinities well within the range where differential effects on biological activities have been seen.¹⁶ Thus,

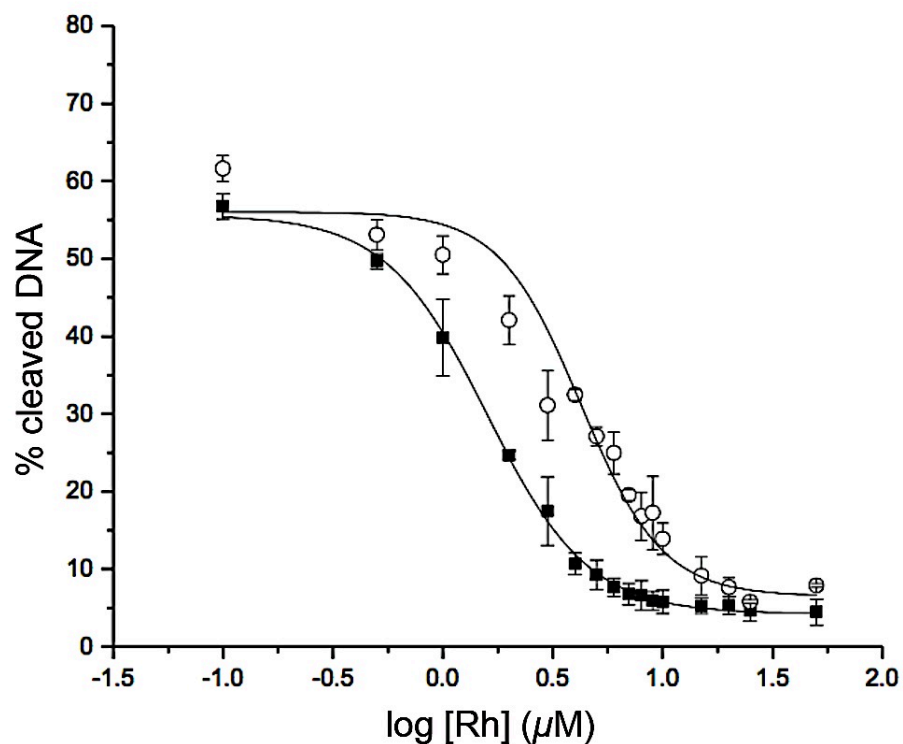


Figure 2.3 Sigmoidal curves (Boltzmann fit) for competition titrations with $\text{Rh}(\text{DPAE})_2\text{chrysi}^{3+}$ (■) and $\text{Rh}(\text{PrDPA})_2\text{chrysi}^{3+}$ (○). K_B was calculated by solving simultaneous equilibria at the inflection point of each curve. Experiments were conducted in buffer (50 mM NaCl, 10 mM NaPi, pH 7.1) using 1 μM DNA and 1 μM *rac*- $\text{Rh}(\text{bpy})_2\text{chrysi}^{3+}$, with 0-50 μM *rac*- $[\text{Rh}(\text{DPAE})_2\text{chrysi}]^{3+}$ or *rac*- $[\text{Rh}(\text{PrDPA})_2\text{chrysi}]^{3+}$ competitor complex. Error bars are calculated from three independent experiments performed for each complex.

binding affinity alone cannot account for the difference in biological activity between the two complexes.

The DNA binding affinities for all metalloinsertors in this study were determined in a similar manner. The results, along with those of all previously reported compounds,^{16,19} are shown in **Figure 2.4**. Interestingly, despite the variance in both the ancillary ligands and number of hydrogen-bond donors, all compounds (except the extremely bulky $[\text{Rh}(\text{DIP})_2(\text{chrysi})]^{3+}$) exhibit binding affinities within essentially the same order of magnitude, varying from $2.3 \times 10^6 \text{ M}^{-1}$ to $4.4 \times 10^7 \text{ M}^{-1}$.

2.3.3 Cellular Proliferation ELISA

We first tested for the selective effects on cellular proliferation of *rac*- $[\text{Rh}(\text{DPAE})_2\text{chrysi}]^{3+}$ and *rac*- $[\text{Rh}(\text{PrDPA})_2\text{chrysi}]^{3+}$ using the ELISA assay in the isogenic HCT116 cell lines testing for BrdU incorporation.²¹ HCT116N and HCT116O cells were incubated with varying concentrations of each complex, and the proliferation of each cell line was measured over time as a function of incorporation of the thymidine analog BrdU.²¹ The differential activity of rhodium treatment is defined as the difference between the normalized percentages of BrdU incorporation for the two cell lines.

As shown in **Figure 2.5**, $[\text{Rh}(\text{DPAE})_2\text{chrysi}]^{3+}$ exhibits differential inhibition of growth in the MMR-deficient cell line as early as 6 h. This activity is quite high and early compared to metalloinsertors tested in previous studies.¹⁶ By contrast, and remarkably, $[\text{Rh}(\text{PrDPA})_2\text{chrysi}]^{3+}$ displays little detectable selectivity for MMR-deficient cells; no activity is seen at 6 or 12 h. After 24 h of treatment with $[\text{Rh}(\text{PrDPA})_2\text{chrysi}]^{3+}$, inhibition of growth is observed in both cell lines, with little difference between them.

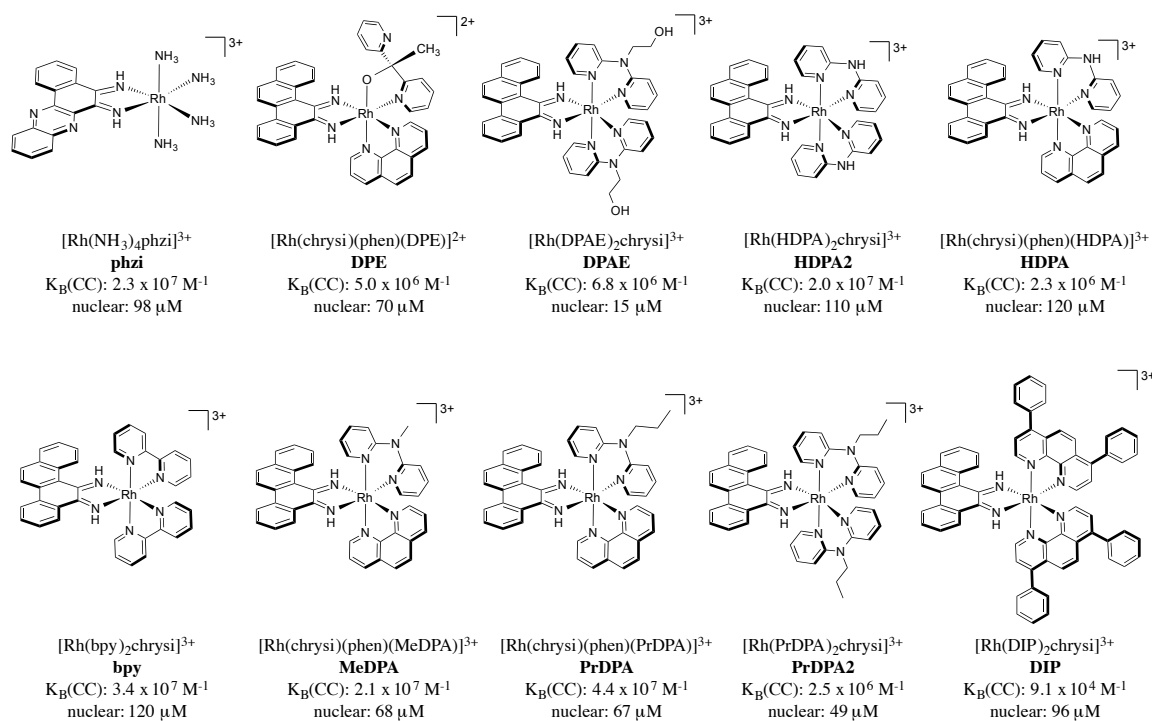


Figure 2.4 Chemical structures, binding affinities for CC mismatches, and

approximated nuclear concentration of all compounds studied. Binding affinities for $[Rh(DIP)_2(chrysi)]^{3+}$, $[Rh(HDPA)_2(chrysi)]^{3+}$, and $[Rh(bpy)_2(chrysi)]^{3+}$ are previously reported.^{10,16} All other compounds' DNA binding affinities were measured on the 29mer hairpin 5'-GGCAGGCATGGCTTTTGCCATCCCTGCC-3' (underline denotes the mismatch) in a competition assay through photocleavage by $[Rh(bpy)_2chrysi]^{3+}$. To determine nuclear rhodium concentrations, HCT116O cells were incubated in media containing 10 μM of each rhodium complex (except $[Rh(DIP)_2(chrysi)]^{3+}$, which was administered at 2 μM) for 24 h. The cells were harvested by trypsinization and the nuclei isolated. Rhodium content was quantified by ICP-MS first normalized to number of nuclei, then divided by the volume of the nucleus of a HCT116O cell, which was approximated as a sphere with radius 8 μm .³¹

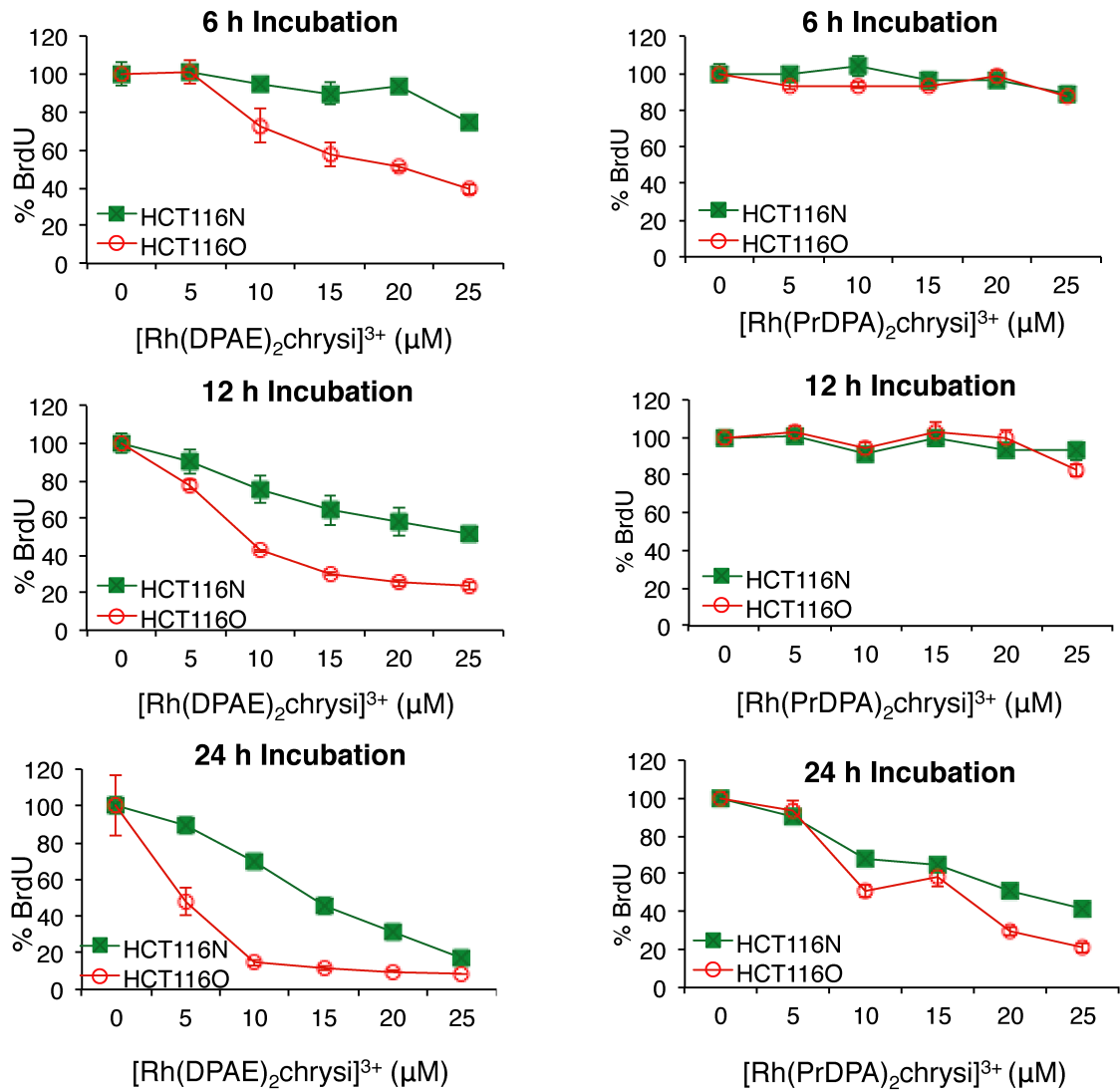


Figure 2.5 Inhibitory effects of $[\text{Rh}(\text{DPAE})_2\text{chrysi}]^{3+}$ (left) and $[\text{Rh}(\text{PrDPA})_2\text{chrysi}]^{3+}$ (right) as a function of incubation time on cellular proliferation in the MMR-proficient HCT116N (green) and MMR-deficient HCT116O (red) cell lines. Shown are plots of BrdU incorporation (a measure of DNA synthesis and therefore cellular proliferation) normalized to the BrdU incorporation of untreated cells as a function of rhodium concentration. Standard error bars for five trials are shown.

The biological effects of $[\text{Rh}(\text{DPAE})_2\text{chrysi}]^{3+}$ and $[\text{Rh}(\text{PrDPA})_2\text{chrysi}]^{3+}$ in MMR-proficient and MMR-deficient cells are representative of a larger trend observed among metalloinsertors. **Figure 2.6** summarizes the inhibitory effects, as determined by the ELISA, for all ten compounds at 10 μM rhodium concentration and 24 h of incubation (except $[\text{Rh}(\text{DIP})_2(\text{chrysi})]^{3+}$, which is shown at 2 μM), as these are the same conditions used for all ICP-MS experiments. There are four compounds with high selectivity for the MMR-deficient HCT116O cells ($[\text{Rh}(\text{NH}_3)_4(\text{phzi})]^{3+}$, $[\text{Rh}(\text{chrysi})(\text{phen})(\text{DPE})]^{3+}$, $[\text{Rh}(\text{DPAE})_2(\text{chrysi})]^{3+}$, and $[\text{Rh}(\text{HDPA})_2(\text{chrysi})]^{3+}$, all shown in different shades of blue), displaying differential inhibitions of $63 \pm 5\%$, $55 \pm 3\%$, $55 \pm 3\%$, and $52 \pm 2\%$, respectively. $[\text{Rh}(\text{chrysi})(\text{phen})(\text{HDPA})]^{3+}$ and $[\text{Rh}(\text{bpy})_2(\text{chrysi})]^{3+}$ exhibit modest selectivity with differential inhibitions of $27 \pm 2\%$ and $8 \pm 2\%$ at 24 h (shown in green in **Figure 2.6**). It should be noted that at longer incubation times the differential inhibition of $[\text{Rh}(\text{bpy})_2(\text{chrysi})]^{3+}$ increases.^{xx} $[\text{Rh}(\text{chrysi})(\text{phen})(\text{MeDPA})]^{3+}$, also shown in green, exhibits delayed biological activity. At 24 h incubation times, this complex does not display significant inhibition of DNA synthesis toward either cell line. The remaining compounds ($[\text{Rh}(\text{chrysi})(\text{phen})(\text{PrDPA})]^{3+}$, $[\text{Rh}(\text{PrDPA})_2(\text{chrysi})]^{3+}$, and $[\text{Rh}(\text{DIP})_2(\text{chrysi})]^{3+}$, shown in red) exhibit no selectivity for the MMR-deficient HCT116O cell line, and inhibit DNA synthesis similarly in both cell lines. It should be noted that none of the complexes studied show a differential inhibition favoring the HCT116N cell line, although that is the common result for many DNA damaging agents.

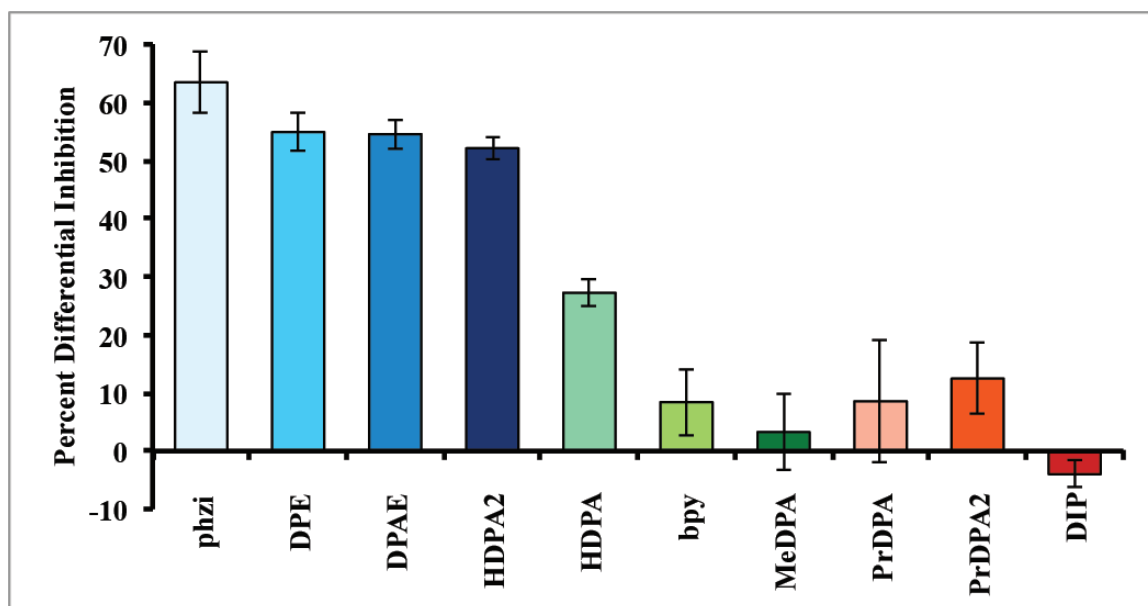


Figure 2.6 Inhibitory effects of rhodium metalloinsertors as a function of metalloinsertor identity. The percent differential inhibition is defined as the difference of the normalized percentages of cellular proliferation between the two cell lines, HCT116O versus HCT116N. ELISA analyses were performed as in **Figure 2.5**. Cells were incubated with 10 μM rhodium complex for 24 h (except $[\text{Rh}(\text{DIP})_2(\text{chrysi})]^{3+}$, which was administered at 2 μM).

2.3.4 MTT Cytotoxicity Assay

We next assayed for cytotoxicity using the MTT assay for mitochondrial function. Mitochondrial enzymes in metabolically active cells reduce 3-(4,5-dimethylthiazol-2-yl)-2,5-diphenyltetrazolium bromide (MTT), a yellow tetrazole to purple formazan, which can be quantified by its characteristic absorbance at 570 nm.²² As a result, viable cells appear deep purple, while dead cells remain yellow. The absorbance is typically an indicator of the percentage of viable cells present in the medium; however, it more directly reflects the metabolic activity of the cells, and specifically mitochondrion function.²⁶⁻²⁸ HCT116N and HCT116O cells were treated with varying concentrations of rhodium and incubated for 24, 48, or 72 h, after which the cells were exposed to MTT reagent for 4 h. The resulting formazan crystals were solubilized in acidified SDS and quantified using electronic absorption spectroscopy. The percentage of viable cells in a given sample is expressed as a function of the absorbance of formazan at 570 nm. We were interested in particular in comparing the two matched rhodium complexes – $[\text{Rh}(\text{DPAE})_2\text{chrysi}]^{3+}$ and $[\text{Rh}(\text{PrDPA})_2\text{chrysi}]^{3+}$ – directly. Neither showed significant differential effects in cytotoxicity at 24h. However, while we observe that cells treated with $[\text{Rh}(\text{DPAE})_2\text{chrysi}]^{3+}$ exhibit little cytotoxic effect at 24 h (**Figure 2.7**), cells treated with $[\text{Rh}(\text{PrDPA})_2\text{chrysi}]^{3+}$, show some loss in viability; for cells incubated with $[\text{Rh}(\text{PrDPA})_2\text{chrysi}]^{3+}$, the percentage of viable cells begins to decrease by 24 h, indicative of a change in metabolic activity. This effect for $[\text{Rh}(\text{PrDPA})_2\text{chrysi}]^{3+}$, however, is not found to be cell-selective.

With longer incubation periods, a selective cytotoxic effect is observed with $[\text{Rh}(\text{DPAE})_2\text{chrysi}]^{3+}$ in the MTT assay. After 48h incubation, $[\text{Rh}(\text{DPAE})_2\text{chrysi}]^{3+}$

exhibits a differential cytotoxicity of $41 \pm 5\%$ at its optimal concentration ($25 \mu\text{M}$), while $[\text{Rh}(\text{PrDPA})_2\text{chrysi}]^{3+}$ effects cytotoxicity in both cell lines equally (**Figure 2.8**). These

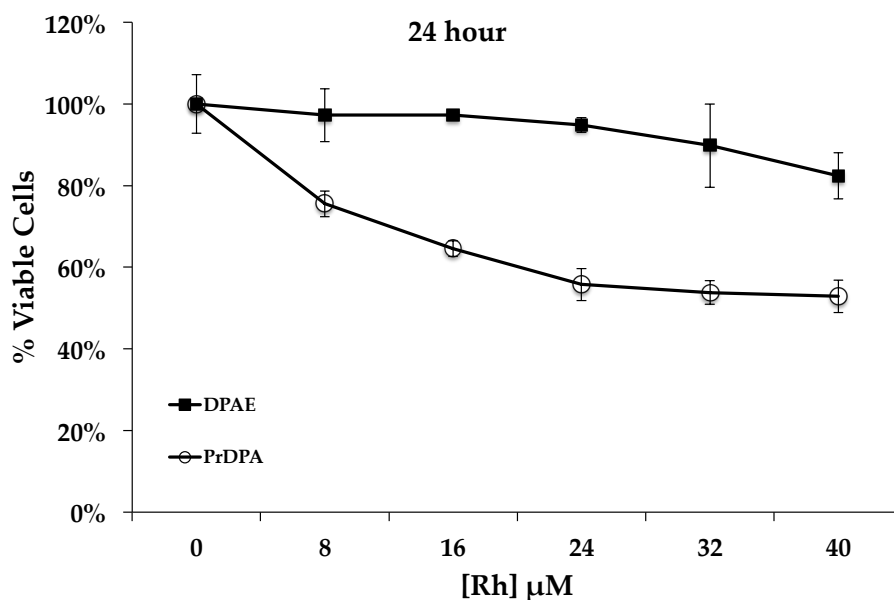


Figure 2.7 Cell viability of HCT116O cells treated with either $[\text{Rh}(\text{DPAE})_2\text{chrysi}]^{3+}$ (■) or $[\text{Rh}(\text{PrDPA})_2\text{chrysi}]^{3+}$ (○) over a 24 h period, as determined by MTT assay. Cells were plated in a 96-well format at densities of 5×10^4 cells/well and treated with the concentrations of rhodium metalinsertors indicated. After 24h, cells were labeled with MTT for 4h. The percentage of cell viability is normalized to that of untreated cells. The experiment was also performed with HCT116N cells, with similar results, as no differential cytotoxicity is observed with either complex at 24h. Standard error bars for five trials are shown.

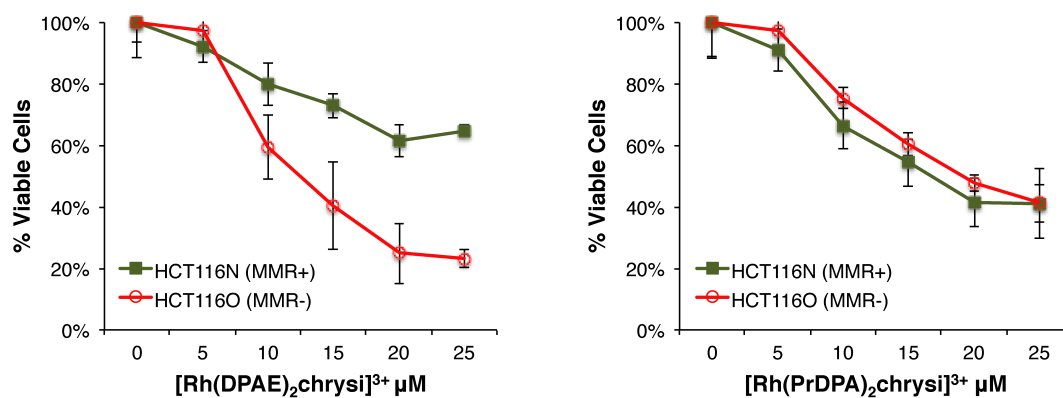


Figure 2.8 Differential cytotoxicities of rhodium metalloinsertors $[\text{Rh}(\text{DPAE})_2\text{chrysi}]^{3+}$ (left) and $[\text{Rh}(\text{PrDPA})_2\text{chrysi}]^{3+}$ (right). HCT116N (green) and HCT116O (red) cells were plated in 96-well format at densities of 5×10^4 cells/well and treated with the concentrations of rhodium metalloinsertors indicated. After 48 hours, the cells were labeled with MTT for 4 hours. The percentage of cell viability is normalized to that of untreated cells. Standard error bars for five trials are shown. The experiment was also performed with a 72h incubation period, with similar results (data not shown), and reflects the trends observed for all ten metalloinsertors with respect to the effects of lipophilicity on cell-selective biological activity.¹⁹

results are consistent with the activities of each complex in the ELISA and with the overall trends observed for all ten metalloinsertor complexes.¹⁹

2.3.5 Cellular Uptake of Metal Complexes

We explored the accumulation of rhodium in whole-cell extracts using inductively coupled plasma mass spectrometry (ICP-MS). Could the difference in biological function be explained through a difference in cellular uptake? To determine whole-cell uptake, HCT116O cells were incubated in media containing 10 μM rhodium for 24 h. Cells were rinsed with phosphate-buffered saline (PBS, pH 7.2) and lysed in a 1% SDS solution. Rhodium content was quantified using ICP-MS and normalized to cellular protein content as determined by a bicinchoninic acid (BCA) assay.²⁴

As is evident in **Figure 2.9**, it is apparent that it is $[\text{Rh}(\text{PrDPA})_2\text{chrysi}]^{3+}$ that is more efficiently taken up inside cells. $[\text{Rh}(\text{PrDPA})_2\text{chrysi}]^{3+}$ exhibits significantly more cellular rhodium accumulation than $[\text{Rh}(\text{DPAE})_2\text{chrysi}]^{3+}$ – about a four-fold increase. The whole-cell uptake of $[\text{Rh}(\text{PrDPA})_2\text{chrysi}]^{3+}$ after 24h was measured to be 705 ± 140 ng Rh/mg cellular protein, whereas accumulation of $[\text{Rh}(\text{DPAE})_2\text{chrysi}]^{3+}$ at 24h was determined to be 165 ± 65 ng Rh/mg cellular protein. HCT116N cells were treated similarly, and the same trends in uptake and localization were observed for both cell lines. The increased lipophilicity of $[\text{Rh}(\text{PrDPA})_2\text{chrysi}]^{3+}$ afforded by the alkyl moieties likely contributes to this enhanced cellular accumulation. Based upon cellular accumulation, then, $[\text{Rh}(\text{PrDPA})_2\text{chrysi}]^{3+}$ might be expected to show greater biological efficacy, contrasting what we observe.

The cellular rhodium accumulation was studied further over several incubation periods for all complexes. HCT116O cells were treated with 10 μM of each rhodium

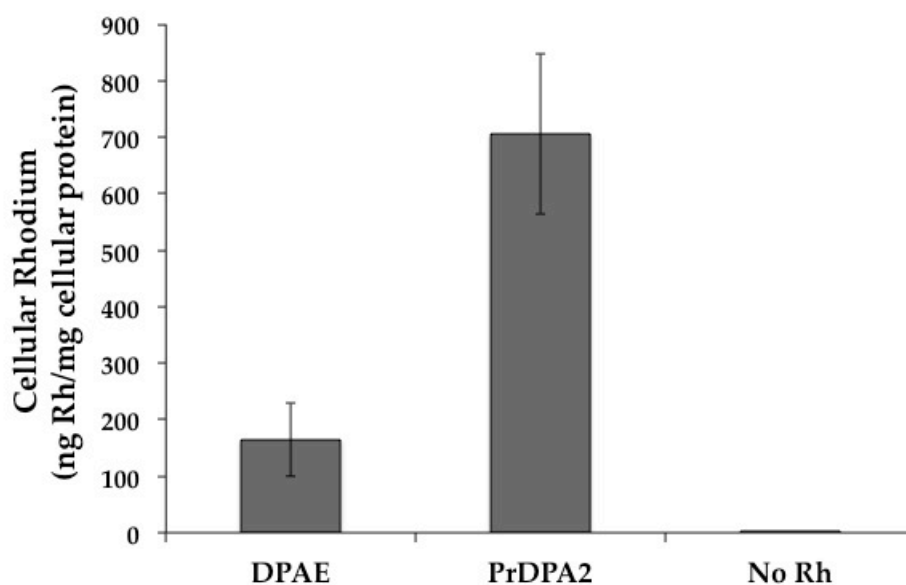


Figure 2.9 ICP-MS assay for rhodium uptake in whole cell extracts. HCT116O cells were incubated in media containing 10 μM of either $\text{Rh}(\text{DPAE})_2\text{chrysi}^{3+}$ (“DPAE”) or $\text{Rh}(\text{PrDPA})_2\text{chrysi}^{3+}$ (“PrDPA2”) for 24 h. Rhodium content was quantified by ICP-MS and normalized to cellular protein content, which was determined by BCA assay (See Section 2.2.9). $[\text{Rh}(\text{PrDPA})_2\text{chrysi}]^{3+}$ exhibits a four-fold greater uptake into the cell than $[\text{Rh}(\text{DPAE})_2\text{chrysi}]^{3+}$, a result of its increased lipophilicity.

complex (except $[\text{Rh}(\text{DIP})_2\text{chrysi}]^{3+}$, which was administered at 2 μM) for 1, 3, 6, 12, or 24 h. Whole cell lysates were analyzed for rhodium levels by ICP-MS and normalized to protein content as described above (**Figure 2.10**). The experiment was repeated with HCT116N cells to confirm that cellular uptake is not different for the HCT116O versus N cells and to verify consistency in trends among the ten complexes.

There seems to be a variety of different modes of uptake at play. The most lipophilic compounds, $[\text{Rh}(\text{chrysi})(\text{phen})(\text{PrDPA})]^{3+}$, $[\text{Rh}(\text{PrDPA})_2(\text{chrysi})]^{3+}$, and $[\text{Rh}(\text{DIP})_2(\text{chrysi})]^{3+}$, exhibit gradual uptake into the HCT116O cells, suggestive of passive diffusion. This is consistent with previous studies conducted on luminescent $[\text{Ru}(\text{L})_2\text{dppz}]^{2+}$ (dppz = dipyrido[3,2-a:2',3'-c]phenazine) analogues, demonstrating cellular accumulation through passive diffusion, facilitated by the negative potential difference across the cell membrane,^{29,30} The two compounds that exhibit delayed biological activity in the ELISA assay ($[\text{Rh}(\text{chrysi})(\text{phen})(\text{MeDPA})]^{3+}$ and $[\text{Rh}(\text{bpy})_2(\text{chrysi})]^{3+}$) exhibit no increase in cellular rhodium levels after initial uptake at 1 hour. Furthermore, the two compounds with HDPA ligands exhibit an enhanced cellular uptake despite reduced lipophilicities. They show a very high initial uptake, followed by a slight increase over the next 23 hours. The MeDPA compound does not exhibit the increase in uptake that we had expected, given its enhanced lipophilicity compared to the HDPA analog and likely pointing to a completely different mechanism of uptake. The two compounds with PrDPA ligands do exhibit enhanced uptakes compared to their respective HDPA analogs at 24 hr, but not nearly to the degree we would have expected based on lipophilicities. However, both the PrDPA compounds appear to be taken up through passive diffusion, unlike the HDPA compounds. Perhaps

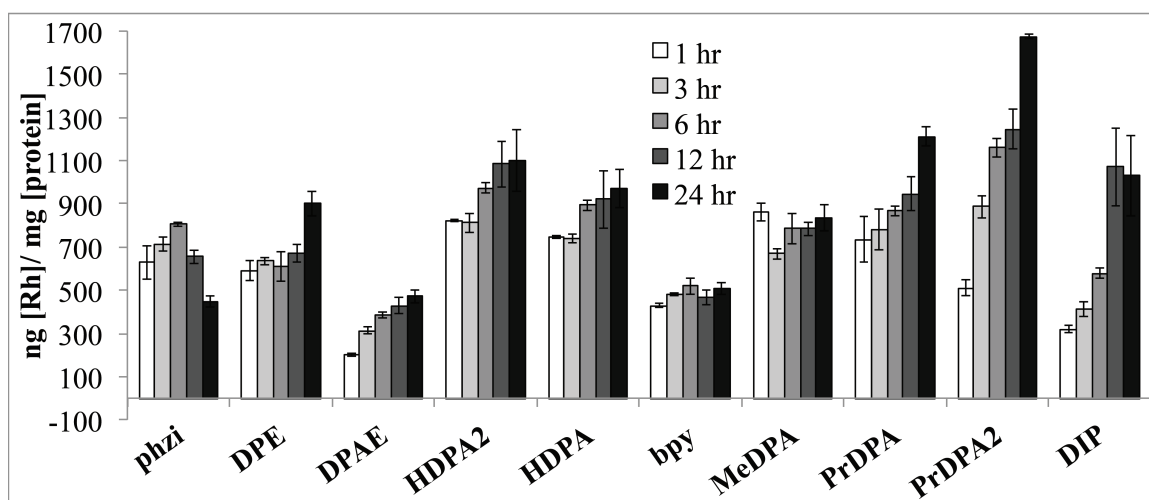


Figure 2.10 ICP-MS assay for whole-cell rhodium accumulation. HCT1160 cells were treated with 10 μM of each rhodium complex (except $[\text{Rh}(\text{DIP})_2(\text{chrysi})]^{3+}$, which was administered at 2 μM) for 1, 3, 6, 12, or 24 h. The cells were analyzed for rhodium content by ICP-MS. The rhodium counts were normalized to protein content, which was determined by a BCA assay. See Section 2.2.9.

the fact that the HDPA ligand has the potential to form hydrogen bonds *in cellulose* is important to its path into the cell. The compounds that exhibit the highest selectivities in the biological assays ($[\text{Rh}(\text{chrysi})(\text{phen})(\text{DPE})]^{3+}$, $[\text{Rh}(\text{DPAE})_2(\text{chrysi})]^{3+}$, and $[\text{Rh}(\text{NH}_3)_4(\text{phzi})]^{3+}$) by no means have the highest overall rhodium levels. In fact, all three of them have among the lowest amount of rhodium uptake into cells.

2.3.7 ICP-MS Assay for Nuclear Rhodium Levels

HCT116O cells were treated with 10 μM of each rhodium complex (except $[\text{Rh}(\text{DIP})_2(\text{chrysi})]^{3+}$, which was administered at 2 μM) for 24 h. The cells were harvested by trypsinization and the nuclei were isolated. Nuclear rhodium levels were determined by ICP-MS and normalized to protein content. The protein content was converted to number of nuclei by the conversion factors 3.28×10^{-8} mg [nuclear protein]/nuclei (found by counting cells or nuclei with a hemacytometer followed by lysing and protein quantification). The rhodium concentrations were then divided by nuclei density to obtain ng of rhodium per nucleus. The process was repeated with HCT116N cells to confirm that the two cell lines behave similarly and to verify consistency in trends among the ten compounds. These numbers can be used to estimate nuclear concentrations by approximating the nucleus of a HCT116O cell as a sphere with radius 4 μm .³¹ The approximate nuclear rhodium concentrations, so determined, are reported in **Figure 2.4**.

As can be seen in **Figure 2.11**, there is little correlation between cell-selective activity and nuclear rhodium concentration. In fact, all nuclear rhodium concentrations except for that of $[\text{Rh}(\text{DPAE})_2(\text{chrysi})]^{3+}$ are within a factor of 2 of each other and hardly vary among the 10 compounds. When we approximate the nuclear concentrations in molarity of the 10 compounds, all compounds are present in the nucleus at concentrations

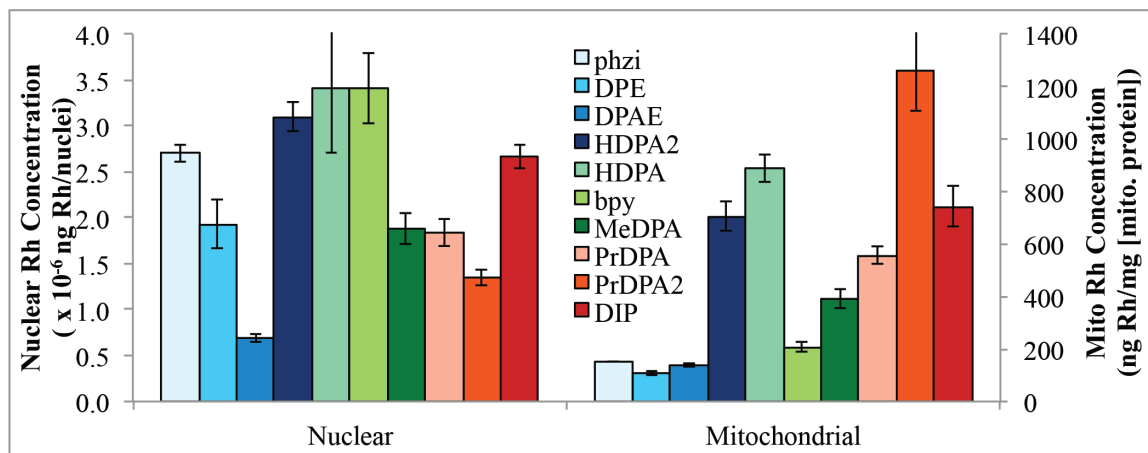


Figure 2.11 ICP-MS assay for nuclear and mitochondrial rhodium accumulation.

HCT1160 cells were treated with 10 μ M of each rhodium complex (except $[\text{Rh}(\text{DIP})_2(\text{chrysi})]^{3+}$, which was administered at 2 μ M) for 24 h. The cells were harvested by trypsinization and appropriate organelle isolation procedures performed. The mitochondrial rhodium counts were normalized to protein content, which was determined by a BCA assay. The nuclear rhodium numbers were normalized to number of nuclei.

on the order of 10^{-5} to 10^{-4} M. These concentrations are all more than 2 orders of magnitude higher than the binding affinities for *in vitro* mismatch detection (yet below non-specific DNA binding levels). Thus, even estimating the error on these numbers to be an order of magnitude, all compounds are present in the nucleus at concentrations sufficient for mismatch binding.

2.3.8 ICP-MS Assay for Mitochondrial Rhodium Levels

HCT1160 cells were treated with 10 μ M of each rhodium complex (except $[\text{Rh}(\text{DIP})_2(\text{chrysi})]^{3+}$, which was administered at 2 μ M) for 24 h. The cells were harvested by trypsinization, the mitochondria were isolated, and the rhodium levels were analyzed by ICP-MS and normalized to protein content. The results are summarized in **Figure 2.11** alongside the nuclear concentrations. The fact that the three compounds with the most cell-selective biological activity ($[\text{Rh}(\text{NH}_3)_4(\text{phzi})]^{3+}$, $[\text{Rh}(\text{chrysi})(\text{phen})(\text{DPE})]^{3+}$, and $[\text{Rh}(\text{DPAE})_2(\text{chrysi})]^{3+}$, shown in blue) have the lowest mitochondrial rhodium accumulation, 152 ± 3 ng [Rh]/ mg [mitochondrial protein], 106 ± 7 ng [Rh]/ mg [mitochondrial protein], and 141 ± 8 ng [Rh]/ mg [mitochondrial protein], respectively, is striking. This correlation indicates that the biological target of our rhodium metalloinsertors is genomic DNA rather than mitochondrial DNA.

Furthermore, the three compounds that exhibit no selectivity for the MMR-deficient HCT1160 cell line in both biological assays ($[\text{Rh}(\text{chrysi})(\text{phen})(\text{PrDPA})]^{3+}$, $[\text{Rh}(\text{PrDPA})_2(\text{chrysi})]^{3+}$, and $[\text{Rh}(\text{DIP})_2(\text{chrysi})]^{3+}$, shown in red) display the highest levels of mitochondrial rhodium accumulation, 560 ± 30 ng [Rh]/ mg [mitochondrial protein], 1260 ± 150 ng [Rh]/ mg [mitochondrial protein] and 740 ± 70 ng [Rh]/ mg [mitochondrial protein], respectively. This result points to mitochondrial targeting as

responsible for the promiscuous biological activity associated with these three compounds that detracts from the cell-selective activity. The two HDPA-containing compounds stray from the trends observed with the other eight compounds.

2.4 Discussion

2.4.1 Biological Activity of Rhodium Metalloinsertors

The compounds displayed in **Figure 2.1** and **Figure 2.4** were synthesized initially in order to investigate the biological effects of varying the lipophilicity of the metalloinsertor. Surprisingly, all compounds exhibited binding affinities within the same order of magnitude (except $[\text{Rh}(\text{DIP})_2(\text{chrysi})]^{3+}$, which was included in the study as a reference compound with extreme lipophilicity, poor binding to mismatches, and no selectivity in our biological assays). The differences among these nine compounds in the ELISA and MTT assays therefore arise from primarily biological effects rather than mismatch binding.

Two of these complexes in particular, $[\text{Rh}(\text{DPAE})_2\text{chrysi}]^{3+}$ and $[\text{Rh}(\text{PrDPA})_2\text{chrysi}]^{3+}$, most simply illustrate the sensitivity of these biological effects to the lipophilicity of the complex. These metalloinsertors are highly similar in structure and DNA binding affinity (displaying K_B values within a factor of 2 at a CC mismatch), but only the DPAE complex exhibits cell-selective targeting of MMR-deficient cells. It is remarkable that this biological effect depends so sensitively on the chemical structure of the ancillary ligands. Substitution of the terminal alcohols on the dipyriddyamine ligands for methyl groups is sufficient to extinguish the differential inhibition of cellular proliferation. It is moreover neither mismatch binding nor whole cell uptake that is

responsible for this effect; the complexes show quite similar DNA binding affinities and, indeed, there is superior whole-cell uptake of $[\text{Rh}(\text{PrDPA})_2\text{chrysi}]^{3+}$.

For all compounds, the cytotoxic effects seen in the MTT assay reflect the antiproliferative activity seen in the ELISA. Both compounds that exhibit delayed activity in the ELISA, $[\text{Rh}(\text{chrysi})(\text{phen})(\text{MeDPA})]^{3+}$ and $[\text{Rh}(\text{bpy})_2(\text{chrysi})]^{3+}$, do not show any significant cytotoxicity in the MTT assay. Furthermore, the four compounds with the largest differential inhibitions in the ELISA assay, $[\text{Rh}(\text{NH}_3)_4(\text{phzi})]^{3+}$, $[\text{Rh}(\text{chrysi})(\text{phen})(\text{DPE})]^{3+}$, $[\text{Rh}(\text{DPAE})_2(\text{chrysi})]^{3+}$, and $[\text{Rh}(\text{HDPA})_2(\text{chrysi})]^{3+}$, also show the largest differential cytotoxicities by the MTT assay. Finally, the three compounds with no differential activity in the ELISA assay, $[\text{Rh}(\text{chrysi})(\text{phen})(\text{PrDPA})]^{3+}$, $[\text{Rh}(\text{PrDPA})_2(\text{chrysi})]^{3+}$, and $[\text{Rh}(\text{DIP})_2(\text{chrysi})]^{3+}$, also show no differential cytotoxicity in the MTT assay. It is important to distinguish the absence of differential activity, where the compound shows no selectivity for one cell line over the other and affects both cell lines to the same degree, versus the absence of all activity, where the compound shows no appreciable biological effect on either cell line.

Significantly, the biological activities of these compounds vary dramatically despite their similar binding affinities. Interestingly, the effect of appending a lipophilic alkyl chain to the back of the HDPA ligand either significantly slows down all activity, as with the MeDPA derivative, or instead abolishes the selectivity of the compound for the MMR-deficient HCT116O cell line, as with the PrDPA derivatives. While the mechanism of inhibition is not yet fully understood, one possible scenario is protein recognition of the metalloinsertor-mismatch complex, generating a covalent protein-DNA lesion. Bulky tethers off the back of the metalloinsertor may inhibit the formation of such

a lesion, leading to the aforementioned observations. Yet another explanation for the results might be that the increased lipophilicity of the metalloinsertor enhances uptake into the cell but also alters the subcellular localization of the complex once it has entered the cell. This altered subcellular localization could be the reason for the lack of selectivity of the compound for one cell line over the other. Indeed, the least lipophilic compounds have the most selective biological activity, while the more lipophilic compounds exhibit no selective biological activity.

2.4.2 Biological Effects of Simple Changes in Functionality on Rhodium Metalloinsertors

The analyses of subcellular rhodium accumulation in the nucleus and mitochondria have revealed significant structure-activity trends, primarily associated with ligand lipophilicity, across a family of ten metalloinsertor complexes. This structure activity relationship is illustrated most dramatically in the matched $[\text{Rh}(\text{DPAE})_2\text{chrysi}]^{3+}$ and $[\text{Rh}(\text{PrDPA})_2\text{chrysi}]^{3+}$ complexes. As illustrated in **Figure 2.12**, mitochondrial rhodium content in cells incubated with $[\text{Rh}(\text{PrDPA})_2\text{chrysi}]^{3+}$ exceeds that of cells grown in the presence of $[\text{Rh}(\text{DPAE})_2\text{chrysi}]^{3+}$ by nearly 10 fold. As with whole-cell uptake, the mitochondrial accumulation of $[\text{Rh}(\text{PrDPA})_2\text{chrysi}]^{3+}$ can likely be attributed to the lipophilic ancillary ligands, facilitating uptake of the lipophilic cation in response to mitochondrial membrane potential. It is understandable that this greater accumulation of $[\text{Rh}(\text{PrDPA})_2\text{chrysi}]^{3+}$ in mitochondria likely accounts for the MTT results.

Interestingly, while the more lipophilic $[\text{Rh}(\text{PrDPA})_2(\text{chrysi})]^{3+}$ complex has about a four-fold greater uptake into the cell than the polar $[\text{Rh}(\text{DPAE})_2(\text{chrysi})]^{3+}$ complex, it exhibits a ten-fold greater mitochondrial accumulation than the DPAE

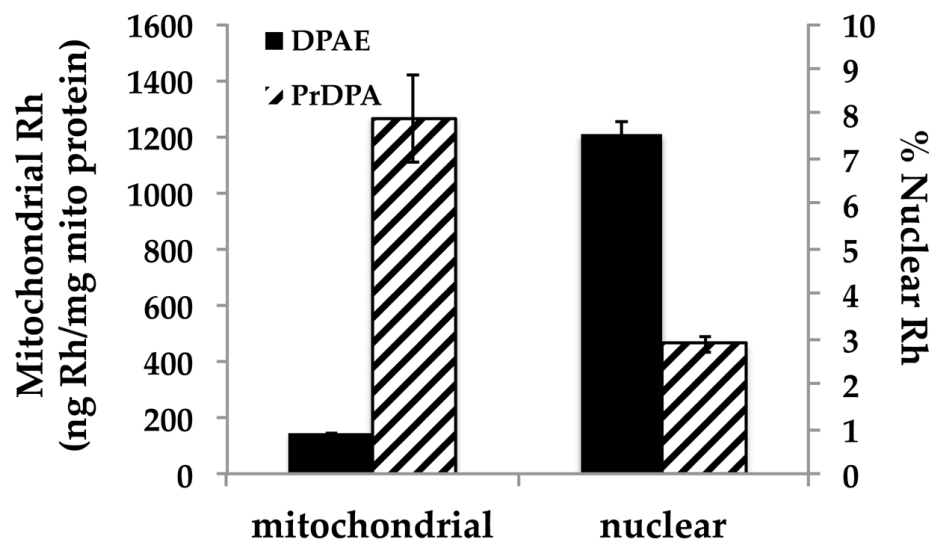


Figure 2.12 ICP-MS assay for rhodium uptake in nuclear and mitochondrial fractions. HCT1160 cells were incubated in media containing 10 μM of either $\text{Rh}(\text{DPAE})_2\text{chrysi}^{3+}$ (black) or $\text{Rh}(\text{PrDPA})_2\text{chrysi}^{3+}$ (hashed) for 24 h. The cells were harvested by trypsinization and appropriate organelle isolation procedures performed. The mitochondrial rhodium counts (left axis) were normalized to protein content, which was determined by a BCA assay. The nuclear rhodium numbers (right axis) were normalized to number of nuclei and expressed as a percentage of the total cellular rhodium.

complex, and only a two-fold greater nuclear concentration. However, the significantly increased cellular accumulation of $[\text{Rh}(\text{PrDPA})_2\text{chrysi}]^{3+}$ results in a higher proportion of rhodium in the cytosol and mitochondria, and it is here where cytotoxic effects that are not cell-selective must be triggered. By contrast, there is a comparatively smaller amount of extranuclear $[\text{Rh}(\text{DPAE})_2\text{chrysi}]^{3+}$, which by extension results in a lower mitochondrial concentration. Furthermore, as can be seen in **Figure 2.12**, a larger *percentage* of total cellular $[\text{Rh}(\text{DPAE})_2\text{chrysi}]^{3+}$ localizes in the nucleus, despite accruing in lower concentrations than the other complexes studied, including $[\text{Rh}(\text{PrDPA})_2\text{chrysi}]^{3+}$ (**Figures 2.4** and **2.11**). In the case of $[\text{Rh}(\text{PrDPA})_2\text{chrysi}]^{3+}$, in contrast, less than 3% of the total cellular rhodium resides in the nucleus. Clearly, it is nuclear trafficking, in conjunction with a lower fraction of extranuclear rhodium, that is responsible for the biological efficacy of $[\text{Rh}(\text{DPAE})_2\text{chrysi}]^{3+}$. Indeed, for $[\text{Rh}(\text{PrDPA})_2\text{chrysi}]^{3+}$, the nuclear rhodium content may largely reside in the membrane. For the DPAE complex, MMR-selective effects of the complex prevail over any nonspecific consequences of mitochondrial accumulation.

Perhaps most significantly, these data identify quite simply that metalloinsertors target mismatch lesions in genomic DNA rather than those in mitochondrial DNA. It is this nuclear mismatch targeting that is responsible for the differential biological activity in MMR-deficient cells that we observe.

2.4.3 Metalloinsertor Uptake and Nuclear Accumulation

The biological implications of ligand lipophilicity seen with $[\text{Rh}(\text{DPAE})_2\text{chrysi}]^{3+}$ and $[\text{Rh}(\text{PrDPA})_2\text{chrysi}]^{3+}$ are in fact general trends among metalloinsertor complexes. Table **2.1** displays qualitative nuclear and mitochondrial uptake properties, as well as the

Table 2.1 Qualitative nuclear^a and mitochondrial^b uptake properties, as well as the presence or absence of cell-selective biological activity^c for all ten metalloinsertors.

Compound	Nuclear Conc. ^a	Mito.Conc. ^b	Cell-Selective Activity ^c
[Rh(NH ₃) ₄ phzi] ³⁺	+	–	+
[Rh(chrysi)(phen)(DPE)] ²⁺	+	–	+
[Rh(DPAE) ₂ chrysi] ³⁺	+	–	+
[Rh(HDPA) ₂ chrysi] ³⁺	+	+	+
[Rh(chrysi)(phen)(HDPA)] ³⁺	+	+	+
[Rh(bpy) ₂ chrysi] ³⁺	+	+	–
[Rh(chrysi)(phen)(MeDPA)] ³⁺	+	+	–
[Rh(chrysi)(phen)(PrDPA)] ²⁺	+	+	–
[Rh(PrDPA) ₂ chrysi] ³⁺	+	+	–
[Rh(DIP) ₂ chrysi] ³⁺	+	+	–

^a Compound is considered to have “+” nuclear concentration if its nuclear concentration is sufficient for mismatch detection given its binding affinity. ^b Compound is considered to have “+” mitochondrial concentration if its mitochondrial rhodium concentration is ≥ 200 ng Rh/mg [mito protein]. ^c Compound is considered to have “+” cell-selective activity if its differential inhibition of DNA synthesis as measured by ELISA of the MMR-proficient line versus the MMR-deficient line is $\geq 25\%$ at 24h of incubation, 10 μ M compound concentration.

presence or absence of cell-selective biological activity for all ten metalloinsertors. Importantly, the biological effects seen in both assays can be explained by the subcellular localization of the metalloinsertors. If passive diffusion were the dominant mode of cellular uptake for these metalloinsertors,^{29,30} the more lipophilic compounds would be expected to have increased cellular uptake. And indeed, except for the HDPA compounds, the most lipophilic compounds do exhibit the greatest cellular accumulation. However, the more lipophilic compounds are in general associated with little differential biological activity; high accumulations of these metalloinsertors are toxic.

By altering L in $[\text{Rh}(\text{chrysi})(\text{phen})(\text{L})]^{3+}$ from HDPA to MeDPA to PrDPA, we do not observe an increase in uptake. In fact, the HDPA complex seems to show enhanced uptake in comparison with those that are more lipophilic. Furthermore, both compounds that possess HDPA ligands display both enhanced and accelerated uptake. This is likely due to additional uptake pathways facilitating the influx of complexes containing HDPA. Indeed, several bis(cyclometalated) iridium(III) polypyridine complexes have been shown to employ more than one mechanism of uptake,³² and this may be the case for several of our metalloinsertors. In comparing $[\text{Rh}(\text{PrDPA})_2(\text{chrysi})]^{3+}$ to $[\text{Rh}(\text{DPAE})_2(\text{chrysi})]^{3+}$, it appears that by altering the methyl group of PrDPA to an alcohol, uptake is decreased by a factor of four, yet only the DPAE compound has cell-selective activity. Lastly, the most polar compound, $[\text{Rh}(\text{NH}_3)_4(\text{phzi})]^{3+}$, displays a peak in uptake at 3 hours, after which cellular rhodium levels seem to decrease steadily. This is most likely caused by an efflux mechanism, that is, pumping the complex out of the cell. The ATP-binding cassette protein ABCG2 has been reported to be overexpressed in HCT116 cells,³³ is known to exhibit substrate promiscuity,³⁴ and may be responsible.

Contrary to what would be expected, three of the four compounds with the best activity have among the lowest cellular uptake at 24 hours, while the three compounds with no cell-selective activity have among the highest cellular uptake at 24 hours. It appears as though increased cellular uptake is actually detrimental to the unique cell-selective behavior of our metalloinsertors.

Significantly, the nuclear rhodium concentrations vary only slightly among the ten compounds. Importantly, by approximating the nucleus of an HCT116O cell as a sphere with diameter 8 μm ,³¹ all of our metalloinsertors are present in the nucleus at sufficient concentrations for mismatch binding, given their in vitro binding affinities (See **Figure 2.4**). Moreover, all metalloinsertors are below non-specific DNA binding concentrations, which precludes non-specific DNA binding as a possible cause of the non-selective toxicity seen with 3 of our metalloinsertors. The only difference between the two cell lines is the presence of a functional copy of the MLH1 gene in the HCT116N cell line, which encodes for a MMR protein found in the nucleus.³⁵ Therefore, any interactions the rhodium complexes have with the cell that are not associated with the nucleus may account for their nonspecific biological activity. Consequently, if nuclear DNA were the only cellular target for these metalloinsertors, then all compounds should exhibit similar differential activity due to their similar nuclear concentrations. However, these metalloinsertors could also interact with mitochondrial DNA, or become sequestered in lipid membranes throughout the cell (including the nuclear membrane, which would cause the nuclear rhodium concentration of such a complex to appear higher than it actually is), both of which would result in nonspecific biological activity.

2.4.4 Mitochondrial Accumulation of Rhodium Metalloinsertors

Importantly, the metalloinsertors that display highly cell-selective biological activity are generally associated with lower mitochondrial rhodium accumulation (**Figure 2.11**, complexes shown in blue), while the metalloinsertors that display non-selective toxicity show larger mitochondrial rhodium accumulation (**Figure 2.11**, complexes shown in red). These observations suggest that it is nuclear DNA targeting of our metalloinsertors that is responsible for their cell-selective biological activities rather than mitochondrial DNA targeting.

The two compounds $[\text{Rh}(\text{DPAE})_2(\text{chrysi})]^{3+}$ and $[\text{Rh}(\text{PrDPA})_2(\text{chrysi})]^{3+}$ exhibit this phenomenon quite simply. The only structural difference between the two compounds is the substitution of the methyl group of the PrDPA ligand for a primary alcohol in the DPAE ligand. While this substitution is structurally minute, the consequences of such a substitution are extreme from a biological standpoint. This substitution causes a large increase in polarity for the DPAE complex, as can be quantified by a decrease in the logP values from -1.0 to -1.5. Significantly, this increase in polarity is accompanied by an increase in cell-selective biological activity. While the more lipophilic $[\text{Rh}(\text{PrDPA})_2(\text{chrysi})]^{3+}$ complex exhibits no selectivity for the MMR-deficient cell line, the more polar $[\text{Rh}(\text{DPAE})_2(\text{chrysi})]^{3+}$ complex is highly selective for the MMR-deficient line over the MMR-proficient line. Furthermore, this small structural change results in drastic changes in uptake and localization of the compounds.

It should be noted, however, that mitochondrial accumulation is not always associated with non-selective toxicity. The presence of the HDPA ligand enhances and accelerates uptake significantly, and even leads to increased mitochondrial accumulation, yet complexes containing HDPA show high selective biological activities. In fact, it has

recently been reported that changes in polarity can affect whether mitochondria-targeted peptides simply accumulate in the mitochondrial matrix or disrupt the mitochondrial membrane activity and result in apoptosis.³⁶ Furthermore, while the antimetabolite methotrexate normally exhibits toxicity toward mammalian cells, when it is conjugated to a mitochondrial penetrating peptide, the altered subcellular localization reduces its toxicity by 3 orders of magnitude.³⁷

2.4.5 General Implications for Design

This work supports the hypothesis that nuclear DNA mismatch binding is responsible for the unique cell-selective biological activity of our rhodium metalloinsertors. Indeed, out of ten compounds studied, all ten exhibit sufficient nuclear uptake for mismatch binding. Furthermore, the fact that the three compounds that are not selective for the MMR-deficient cell line have enhanced mitochondrial accumulation implies that mitochondrial mismatch DNA targeting is not responsible for cell-selective behavior (**Figure 2.13**). As the only difference between the two cell lines is a functional copy of the MLH1 gene, a gene that encodes for a nuclear MMR protein, the cell-selective behavior of our metalloinsertors must be related to this MMR deficiency. As the mitochondria are the location of oxidative phosphorylation, where reactive oxygen species are unavoidably formed as byproducts, mitochondrial DNA has higher levels of oxidative damage than nuclear DNA.³⁸ While these DNA defects could very well be targets of our metalloinsertors, mtDNA repair pathways do exist,³⁹ and in most cases are distinct from their nuclear counterparts.⁴⁰ Specifically, the mitochondrial MMR proteins MSH2, MSH3, MSH6, and MLH1 have been shown to be absent from the

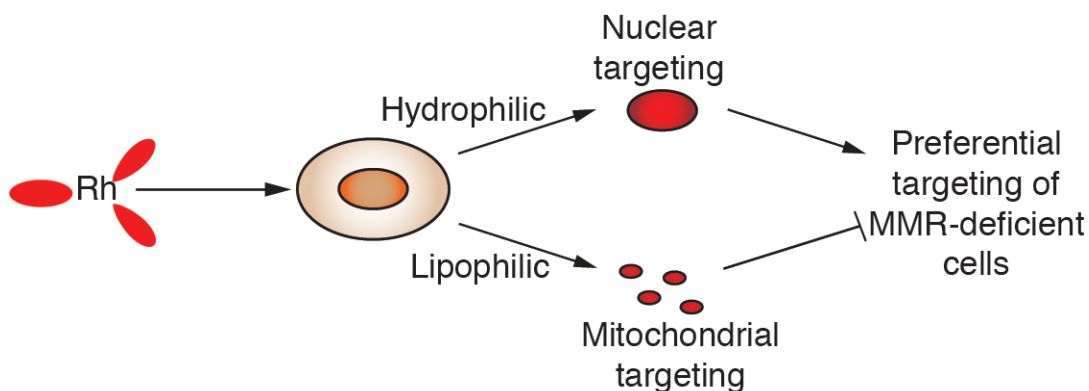


Figure 2.13 Model for the requirements for cell-selective targeting of MMR-deficient cells by rhodium metalloinsertors. All metalloinsertors localize to the nucleus in concentrations sufficient for mismatch binding. Mismatch recognition in genomic DNA is postulated as the preferred biological target of metalloinsertors for cell-selective biological activity in MMR-deficient cells. Complexes bearing lipophilic ancillary ligands also exhibit high mitochondrial uptake, which abolishes any selective effects and induces nonspecific cell death.

mitochondria.⁴¹ The targeting of defects in mitochondrial DNA therefore cannot be responsible for the unique cell-selective behavior of our metalloinsertors.

2.5 Conclusions

This work shows that in general, more extranuclear rhodium leads to nonselective biological activity. All compounds tested are present in the nucleus at sufficient concentrations for mismatch detection. However, the more lipophilic compounds, which display enhanced uptake into the cells, tend to localize more in the mitochondria, thus giving rise to nonspecific biological activity. While the more polar compounds ($[\text{Rh}(\text{NH}_3)_4(\text{phzi})]^{3+}$, $[\text{Rh}(\text{chrysi})(\text{phen})(\text{DPE})]^{2+}$, and $[\text{Rh}(\text{DPAE})_2(\text{chrysi})]^{3+}$) do not have the largest amount of cellular rhodium, there is consequently a smaller amount of rhodium in the mitochondria. This, coupled with sufficient nuclear rhodium for mismatch binding, gives rise to high MMR-deficient cell-selective biological activities for these three compounds. It seems that by increasing lipophilicity in an effort to increase uptake via passive diffusion, the subcellular localization is altered, leading to a larger amount of cellular rhodium residing in the mitochondria and less selectivity for the MMR-deficient cell line. This tradeoff in uptake for selectivity is in contrast to current strategies to improve the efficacy of cisplatin by increasing uptake of the drug.^{42,43} More generally, these results highlight that the relative accumulation of complex in different organelles needs to be considered, not simply cellular accumulation.

Most importantly, these data support the notion that the cell-specific activity we observe is caused by nuclear DNA mismatch targeting by our metalloinsertors. This exciting new result gives us key information in designing the next generation of rhodium metalloinsertors as cell-specific chemotherapeutics.

3.6 References

- 1 Wildenberg J., Meselson M. *Proc. Natl. Acad. Sci. USA*. **1975**, 72, 2202-2206.
- 2 Wagner, R. Jr., Meselson M. *Proc. Natl. Acad. Sci. USA*. **1976**, 73, 4135-4139.
- 3 Iyer, R. R., Pluciennik, A., Burdett, V. Modrich, P. L. *Chem. Rev.* **2006**, 106, 302-323.
- 4 Parsons, R., Li, G.-M., Longley, M., Modrich, P., Liu, B., Berk, T., Hamilton, S. R., Kinzler, K. W., Vogelstein, B. *Science*. **1995**, 268, 738-740.
- 5 Fink, D., Aebi, S., Howell, S. B. *Clin. Cancer Res.* **1998**, 4, 1-6.
- 6 Fram, R. J., Cusick, P. S., Wilson, J. M., Marinus, M. G. *Mol. Pharmacol.* **1985**, 28, 51-55.
- 7 Zeglis, B. M., Pierre, V. C., Barton, J. K. *Chem. Comm.* **2007**, 44, 4565-4579.
- 8 Jackson, B. A., Barton, J. K. *J. Am. Chem. Soc.* **1997**, 119, 12986-12987.
- 9 Jackson, B. A., Alekseyev, V. Y., Barton, J. K. *Biochemistry*. **1999**, 38, 4655-4662.
- 10 Jackson, B. A., Barton, J. K. *Biochemistry*. **2000**, 39, 6176-6182.
- 11 Keilkopf, C. L., Erkkila, K. E., Hudson, B. P., Barton, J. K., Rees, D. C. *Nat. Struct. Biol.* **2000**, 7, 117-121.
- 12 Pierre, V. C., Kaiser, J. T., Barton, J. K. *Proc. Natl. Acad. Sci. USA*. **2007**, 104, 429-434.
- 13 Zeglis, B. M., Pierre, V. C., Kaiser, J. T., Barton, J. K. *Biochemistry*. **2009**, 48, 4247-4253.
- 14 Song, H., Kaiser, J. T., Barton, J. K. *Nat. Chem.* **2012**, 4, 615-620.
- 15 Hart, J. R., Glebov, O., Ernst, R. J., Kirsch, I. R., Barton, J. K. *Proc. Natl. Acad. Sci. USA*. **2006**, 103, 15359-15363.

- 16 Ernst, R. J., Song, H., Barton, J. K. *J. Am. Chem. Soc.* **2009**, *131*, 2359-2366.
- 17 Ernst, R. J., Komor, A. C., Barton, J. K. *Biochemistry*, **2011**, *50*, 10919-10928.
- 18 Koi, M., Umar, A., Chauhan, D. P., Cherian, S. P., Carethers, J. M., Kunkel, T. A., Boland, C. R. *Cancer Res.* **1994**, *54*, 4308-4312.
- 19 Komor, A. C.; Schneider, C. J.; Weidmann, A. G.; Barton, J. K. *J. Am. Chem. Soc.* **2012**, *134*, 19223-19233.
- 20 Kirin, S. I., Yennawar, H. P., Williams, M. E. *Eur. J. Inorg. Chem.* **2007**, 3686-3694.
- 21 Gratzner, H. G. *Science*. **1982**, *218*, 474-475.
- 22 Mosmann, T. *J. Immunol. Methods*. **1983**, *65*, 55-63.
- 23 Zeglis, B. M., Barton, J. K. *Nature Protoc.* **2007**, *2*, 357-371.
- 24 Smith, P. K., Krohn, R.I., Hermanson, G.T., Mallia, A.K., Gartner, F.H., Provenzano, M.D., Fujimoto, E.K., Goeke, N.M., Olson, B.J., Klenk, D.C. *Anal. Biochem.* **1985**, *150*, 76-85.
- 25 Ahmad, K. A., Iskandar, J. L., Hirpara, K. B., Clement, M-V., Pervaiz, S. *Cancer Res.* **2004**, *64*, 7867-7878.
- 26 Wagner, B. K., Kitami, T., Gilbert, T. J., Peck, D., Ramanathan, A., Schreiber, S. L., Golub, T. R., Mootha, V. K. *Nat. Biotechnol.* **2008**, *26*, 343-351.
- 27 Yakes, F. M., Van Houten, B. *Proc. Natl. Acad. Sci. USA.* **1997**, *94*, 514-519.
- 28 Madesh, M., Bhaskar, L., Balasubramanian, K. A. *Mol. Cell. Biochem.* **1997**, *167*, 81-87.
- 29 Puckett, C. A.; Barton, J. K. *J. Am. Chem. Soc.* **2007**, *129*, 46-47.
- 30 Puckett, C. A.; Barton, J. K. *Biochemistry* **2008**, *47*, 11711-11716.

- 31 Fujioka, A.; Terai, K.; Itoh, R. E.; Aoki, N.; Nakamura, T.; Kuroda, S.; Nishida, E.; Matsuda, M. *J. Biol. Chem.* **2006**, *281*, 8917-8926.
- 32 Zhang, Y.; Lo, K. K-W. *Inorg. Chem.* **2009**, *48*, 6011-6025.
- 33 Candeil, L.; Gourdier, I.; Peyron, D.; Vezzio, N.; Copois, V.; Bibeau, F.; Orsetti, B.; Scheffer, G. L.; Ychou, M.; Khan, Q. A.; Pommier, Y.; Pau, B.; Martineau, P.; Del Rio, M. *Int. J. Cancer* **2004**, *109*, 848-854.
34. Eckford, P. D. W.; Sharom, F. J. *Chem. Rev.* **2009**, *109*, 2989-3011.
- 35 Fink, D.; Nebel, S.; Aebi, S.; Zheng, H.; Kim, H. K.; Christen, R. D.; Howell, S. B. *Cancer* **1997**, *76*, 890-893.
- 36 Horton, K. L.; Pereira, M. P.; Stewart, K. M.; Fonseca, S. B.; Kelley, S. O. *ChemBioChem.* **2012**, *13*, 476-485.
- 37 Pereira, M. P.; Kelley, S. O. *J. Am. Chem. Soc.* **2011**, *133*, 3260-3263.
- 38 Yakes, F. M.; Van Houten, B. *Proc. Natl. Acad. Sci. USA* **1997**, *94*, 514-519.
- 39 Tomkinson, A. E.; Bonk, R. T.; Linn, S. *J. Biol. Chem.* **1988**, *263*, 12532-12537.
- 40 Liu, P.; Demple, B. *Environ. Mol. Mutagen.* **2010**, *51*, 417-426.
- 41 de Souza-Pinto, N. C.; Mason, P. A.; Hashiguchi, K.; Weissman, L.; Tian, J.; Guay, D.; Lebel, M.; Stevensner, T. V.; Rasmussen, L. J.; Bohr, V. A. *DNA Repair* **2009**, *8*, 704-719.
- 42 Fuertes, M. A.; Alonso, C.; Perez, J. M. *Chem. Rev.* **2003**, *103*, 645-662.
- 43 Gately, D. P.; Howell, S. B. *Br. J. Cancer* **1993**, *67*, 1171-1176.

Chapter 3: Construction and Application of a Rh-Pt DNA

Metalloinsertor Conjugate*

3.1 Introduction

Platinum anti-cancer compounds are among the most successful and most widely used chemotherapeutic agents to date.¹ By forming covalent adducts with the DNA bases, platinum chemotherapeutics cause lesions that inhibit transcription and DNA repair, leading to apoptosis.² However, while cisplatin and carboplatin have been highly successful in the treatment of testicular, cervical, ovarian, and non-small cell lung cancers, their use is limited by severe side effects and resistance.^{2,3} Specifically, cancers that exhibit deficiencies in the mismatch repair (MMR) machinery are largely resistant to cisplatin treatment, as MMR proteins are among those responsible for the recognition of Pt-DNA lesions.^{4,5} MMR-deficient cancers, which comprise 15% of sporadic colorectal cancer cases and 18% of all solid tumors, can be treated in part with oxaliplatin, which employs a *trans* 1,2-diaminocyclohexane non-leaving group ligand instead of the amines.⁶⁻⁸ As a result, oxaliplatin-DNA adducts are poorly recognized by MMR proteins, rendering the drug highly effective against cisplatin-resistant cancers *in vitro*.⁸ However, the efficacy of oxaliplatin *in vivo* is severely limited, and treatment must be administered in combination with a variety of drugs, such as 5-fluorouracil and leucovorin.^{8,9} Although this combinatorial approach does increase the response rate of oxaliplatin treatment, the improvement is modest, and the overall efficacy in the later stages of colorectal cancer is still very low.

*Adapted from Weidmann, A. G.; Barton, J. K. *Inorg. Chem.* **2014**, *53*, 7812-7814.

Rhodium metalloinsertors may offer a promising strategy in the development of new therapies for such cancers. These bulky, octahedral rhodium (III) complexes bind specifically to DNA base pair mismatches,¹⁰ which are amplified in cells with defective MMR machinery.^{6,7} This selectivity is achieved through *metalloinsertion*, a general binding mode in which a sterically expansive ligand inserts into the base stack at the site of the thermodynamically destabilized mismatch, ejecting the mismatched bases from the duplex.¹¹⁻¹³ It is postulated that this large lesion created upon rhodium mismatch binding is recognized *in cellulo*, leading to a selective cellular response. Metalloinsertors exhibit cytotoxicity preferentially in MMR-deficient cells, and the extent of this selectivity correlates with mismatch binding affinity and localization to the nucleus, where they target mismatches in genomic DNA.¹⁴⁻¹⁷

The design of bifunctional drug conjugates is a burgeoning field in chemotherapy, especially as a strategy to circumvent resistance.¹⁸ Here, we present a bimetallic oxaliplatin-metalloinsertor conjugate (RhPt), that displays dual DNA binding behavior *in vitro*. Additionally, RhPt exhibits enhanced cytotoxicity and cellular uptake in MMR-deficient HCT1160 human colorectal cancer cells compared to first-line platinum therapeutics therapeutics as well as its unconjugated subunits. The cytotoxicity of RhPt appears to be triggered by an apoptotic cell death pathway, and its potency is attributed to the improved cellular uptake of the complex.

3.2 Experimental Protocols

3.2.1 Materials

A2780cis cells, cisplatin, oxaliplatin, and all organic reagents were purchased from Sigma-Aldrich unless otherwise noted. Commercially available chemicals were

used as received without further purification. RhCl_3 and K_2PtCl_4 starting material were purchased from Pressure Chemical Co (Pittsburgh, PA). Sep-pak C_{18} solid-phase extraction (SPE) cartridges were purchased from Waters Chemical Co. (Milford, MA). Media and supplements were purchased from Invitrogen (Carlsbad, CA). BrdU, antibodies, and buffers were purchased in kit format from Roche Molecular Biochemical (Mannheim, Germany). Simian virus 40 (SV40) T-large antigen, origin-containing pUC HSO plasmid DNA, HeLa cell extract, and all buffers and reagents for the SV40 DNA replication assay were purchased in kit format from CHIMERx (Milwaukee, WI).

Oligonucleotides were ordered from Integrated DNA Technologies and purified by HPLC using a C_{18} reverse-phase column (Varian, Inc; Corona, CA). All HPLC purifications were carried out on a Hewlett-Packard 1100 HPLC. DNA purity was confirmed by MALDI-TOF mass spectrometry and quantified by UV-visible spectroscopy (UV-vis) using the extinction coefficients at 260 nm estimated for single-stranded DNA. UV-vis characterizations were performed on a Beckmann DU 7400 spectrophotometer. Radiolabeled [^{32}P]-ATP was purchased from MP Biomedicals (Santa Ana, CA).

The syntheses of chrysene-5,6-dione (chrysi), $[\text{Pt}(\text{DACH})(\text{H}_2\text{O})_2]\text{SO}_4$ ($\text{DACH} = (1R,2R)\text{-}(-)\text{-}1,2\text{-diaminocyclohexane}$), and di(pyridin-2-yl)glycine (dpa-AcOH) were carried out according to published procedures.¹⁹⁻²¹ The synthesis of precursor $[\text{Rh}(\text{chrysi})(\text{HDPA})(\text{NH}_3)_2]\text{TFA}_3$ was carried out in a manner analogous to that of $[\text{Rh}(\text{chrysi})(\text{phen})(\text{NH}_3)_2]$, as described by Mürner et al.¹⁹

3.2.2 Synthesis of Rhodium Scaffold Precursor (Scheme 3.1)

3.2.2.1 $[\text{Rh}(\text{HDPA})\text{Cl}_4]\text{HDPA}$ (6)

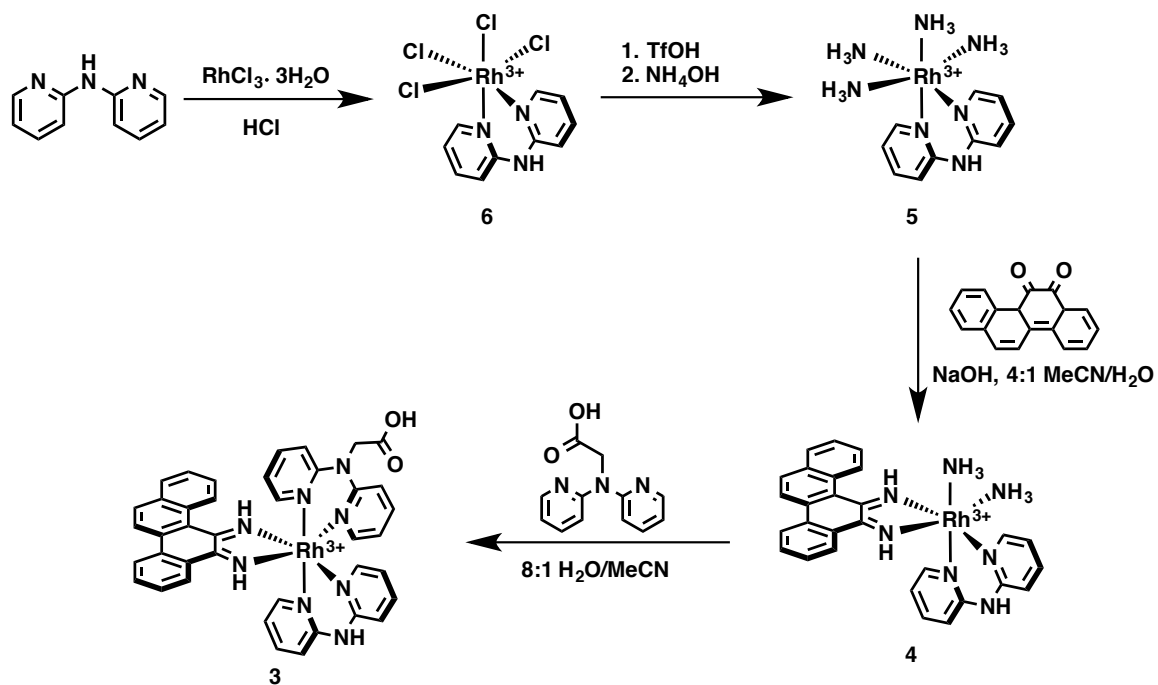
[Rh(HDPA)Cl₄]HDPA (HDPA = 2,2'-dipyridylamine) was prepared according to a modified literature protocol.¹⁹ RhCl₃•H₂O (1.9 g, 8.4 mmol) was suspended in concentrated HCl (30 ml) and refluxed for 4 h. To the dark red solution was added HDPA (1.3 g, 7.56 mmol), followed by the addition of boiling Milli-Q water (250 ml). The orange suspension was refluxed for an additional 16 h and left to stand at 4 °C. The resulting orange precipitate was filtered and washed with ethanol and diethyl ether. Yield: 2.5 g (81%). ¹H NMR (500 MHz, DMSO-d₆) δ 11.13 (s, 1H), 9.08 – 9.05 (m, 1H), 8.46 (dd, *J* = 6.2, 1.6 Hz, 1H), 7.88 (dddd, *J* = 28.2, 8.6, 7.3, 1.7 Hz, 2H), 7.19 (ddd, *J* = 7.3, 6.2, 1.4 Hz, 1H), 7.13 (dd, *J* = 8.4, 1.3 Hz, 1H), 7.06 (td, *J* = 7.6, 1.4 Hz, 2H), 6.82 (s, 2H).

3.2.2.2 [Rh(HDPA)(OTf)₄]HDPA (5)

[Rh(HDPA)Cl₄]HDPA (2.46 g, 4.19 mmol) was dissolved in neat triflic acid (10 g, 66.67 mmol) under argon at ambient temperature. The dark red solution was stirred at room temperature for 16 h, with occasional purging to release HCl gas. The solution was poured over cold diethyl ether (-78 °C), and the brown precipitate was collected by vacuum filtration. Yield: 3.58 g (82 %) ¹H NMR (500 MHz, DMSO-d₆) δ 8.59 (m, 2H), 8.02 (m, 2H), 7.25 (m, 4H).

3.2.2.3 [Rh(HDPA)(NH₃)₄](OTf)₃

[Rh(HDPA)(OTf)₄]HDPA (3.55 g, 3.39 mmol) was dissolved in concentrated aqueous ammonium hydroxide (100 ml) and refluxed for 45 min. The yellow solution was cooled to room temperature, and the solvent was removed *in vacuo*. The yellow solid was dissolved in a minimum amount of H₂O and triturated with 1:1 EtOH/Et₂O. The white precipitate was filtered to give [Rh(HDPA)(NH₃)₄]OTf₃ as an off-white powder.



Scheme 3.1 Synthesis of rhodium metalloinsertor scaffold for conjugation, $[\text{Rh}(\text{chrysi})(\text{HDPA})(\text{dpa-AcOH})]^{3+}$ (**3**).

Yield: 2.0 g (69 %). ^1H NMR (500 MHz, DMSO- d_6): δ 8.67 (d, $J = 5.5$ Hz, 1H), 8.29 (d, $J = 34.8$ Hz, 1H), 7.97 (ddd, $J = 32.5, 18.2, 8.1$ Hz, 3H), 7.50 – 7.40 (m, 2H), 7.23 (t, $J = 5.7$ Hz, 1H), 7.15 (t, $J = 6.6$ Hz, 1H), 4.69 (d, $J = 10.0$ Hz, 3H), 4.43 (s, 3H), 4.20 – 4.04 (m, 6H).

3.2.2.4 [Rh(HDPA)(chrysi)(NH₃)₂](TFA)₃ (4)

[Rh(HDPA)(NH₃)₄](OTf)₃ (2.0 g, 2.3 mmol) and chrysene-5,6-dione (chrysi, 0.66 g, 2.6 mmol) were dissolved in acetonitrile (130 ml). Aqueous sodium hydroxide (1N, 13 ml) was added, and the reaction was allowed to stir at ambient temperature for 16 h. The reaction was neutralized with 1N HCl and dried *in vacuo*. The residue was dissolved in water, desalted on a SPE cartridge (1:1:0.1 H₂O:MeCN:TFA), and dried again *in vacuo* to afford a mixture of the two *cis* diastereomers of [Rh(HDPA)(chrysi)(NH₃)₂](TFA)₃ as a bright red solid. Yield: 0.62 g (30%). ^1H NMR (500 MHz, DMSO- d_6): δ ^1H NMR (500 MHz, DMSO- d_6) δ 11.67 (s, 1H), 11.56 (d, $J = 2.9$ Hz, 1H), 9.09 (dd, $J = 6.3, 1.6$ Hz, 1H), 8.52 – 8.43 (m, 2H), 8.43 – 8.36 (m, 2H), 8.36 – 8.25 (m, 2H), 8.18 (td, $J = 8.0, 7.4, 3.0$ Hz, 3H), 8.13 (dd, $J = 8.6, 5.6$ Hz, 1H), 8.10 (dd, $J = 7.8, 1.3$ Hz, 1H), 8.08 – 8.03 (m, 2H), 7.99 (dtd, $J = 8.5, 7.2, 1.6$ Hz, 3H), 7.89 (ddd, $J = 8.5, 7.0, 1.5$ Hz, 1H), 7.74 (d, $J = 8.3$ Hz, 1H), 7.71 – 7.67 (m, 1H), 7.66 – 7.61 (m, 2H), 7.61 – 7.57 (m, 2H), 7.54 (td, $J = 7.5, 0.9$ Hz, 1H), 7.52 – 7.45 (m, 3H), 7.44 (d, $J = 1.3$ Hz, 1H), 7.44 – 7.41 (m, 2H), 7.40 (d, $J = 1.4$ Hz, 1H), 7.32 (ddddt, $J = 10.3, 6.1, 4.3, 3.0, 1.6$ Hz, 3H), 7.27 – 7.20 (m, 2H), 6.98 – 6.95 (m, 1H), 6.95 – 6.89 (m, 2H), 4.68 (d, $J = 18.2$ Hz, 6H), 4.49 (d, $J = 6.3$ Hz, 6H), 4.35 (s, 6H). ESI-MS (cation): m/z calc 562.48 (M – 2H⁺), obs. 528.0 (M – 2H – 2NH₃⁺), 580.8 (M – 2H + H₂O⁺), 587 (M + Na⁺).

3.2.2.5 [Rh(HDPA)(chrysi)(dpa-AcOH)](TFA)₃ (3)

[Rh(HDPA)(chrysi)(NH₃)₂](TFA)₃ (620 mg, 0.69 mmol) and di(pyridin-2-yl)glycine (dpa-AcOH) (240 mg, 1.05 mmol) were dissolved in 8:1 H₂O:MeCN (90 ml) and refluxed for 24 h. The solvent was removed *in vacuo*, and the crude product was purified by HPLC using a C₁₈ reverse-phase column (Varian, Inc.) on a Hewlett Packard 1100 HPLC (85:15 to 40:60 H₂O (0.1 % TFA):MeCN). Complex **3** was isolated as a dark red, hygroscopic solid. Yield: 0.55 g (73%). ¹H NMR (300 MHz, DMSO-d₆) δ 11.47 (broad s, 1H), 9.64 (s, 1H), 9.04 (d, *J* = 6.2 Hz, 1H), 8.77 (dd, *J* = 15.0, 6.8 Hz, 1H), 8.52 (d, *J* = 6.1 Hz, 1H), 8.24 (dd, *J* = 5.0, 1.8 Hz, 4H), 8.08 (dt, *J* = 16.7, 9.5 Hz, 2H), 8.01 – 7.84 (m, 4H), 7.80 – 7.74 (m, 1H), 7.71 (d, *J* = 8.1 Hz, 1H), 7.67 (s, 1H), 7.56 – 7.40 (m, 3H), 7.38 – 7.29 (m, 1H), 7.19 (t, *J* = 8.4 Hz, 4H), 6.99 – 6.86 (m, 3H), 6.86 – 6.74 (m, 1H), 4.63 (s, 2H). ESI-MS (cation): *m/z* calc 757.17 (M – 2H⁺), 379.59 (M – H²⁺), obs. 756.9, 379.1.

3.2.3 Synthesis of Rh(Amal) and RhPt (Scheme 3.2)

3.2.3.1 [Rh(HDPA)(chrysi)(diethyl-2-(2-(di(pyridin-2-yl)amino)acetamido)malonate)] (TFA)₃

[Rh(HDPA)(chrysi)(dpa-AcOH)](TFA)₃ (**3**) (100 mg, 0.09 mmol), diethyl aminomalonate hydrochloride (38 mg, 0.18 mmol), and (dimethylamino)-*N,N*-dimethyl(3*H*-[1,2,3]triazolo[4,5-*b*]pyridin-3-yloxy)methaniminium hexafluorophosphate (HATU, 83 mg, 0.22 mmol) were combined in a vial and dried under vacuum to remove all water. The solids were dissolved in anhydrous DMF (1.3 ml) under argon and stirred at room temperature for 10 min. Ethyldiisopropylamine (DIPEA, 95 μl, 0.54 mmol) was added, and the solution was allowed to stir at room temperature for 12 h. The solvent was removed *in vacuo*, and the intermediate was purified by HPLC as described above. Yield:

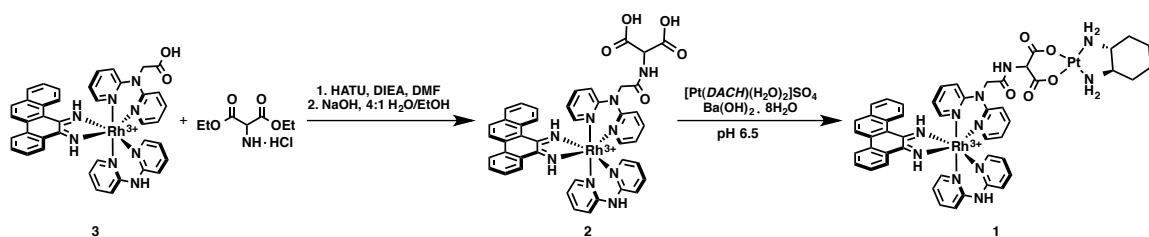
41 mg (36% by HPLC). ESI-MS (cation): m/z calc 914.24 ($M - 2H^+$), 457.12 ($M - H^{2+}$), obs. 913.9, 457.8

3.2.3.2 [Rh(HDPA)(chrysi)(2-(2-(di(pyridin-2-yl)amino)acetamido)-3-ethoxy-3-oxopropanoic acid)] (TFA)₃ (“Rh(Amal)”) (2)

To hydrolyze the ethyl esters, [Rh(HDPA)(chrysi)(diethyl-2-(2-(di(pyridin-2-yl)amino)acetamido)malonate)](TFA)₃ (41 mg, 0.033 mmol) was dissolved in a 5:1 H₂O:EtOH mixture (12 ml). 1N NaOH was added to pH 10, and the reaction was stirred at room temperature for 24 h. The solvent was removed by rotary evaporation, and complex **2** (“Rh(Amal)”) was purified by HPLC as described above. The chloride salt was obtained from a Sephadex QAE anion-exchange column equilibrated with 0.1 M MgCl₂. Yield: 12 mg (30% by HPLC). ¹H NMR (500 MHz, D₂O): δ 8.91 (dd, $J = 6.2, 1.6$ Hz, 1H), 8.23 – 8.15 (m, 1H), 8.14 – 8.11 (m, 2H), 8.08 (dd, $J = 13.5, 7.6$ Hz, 1H), 8.00 (ttd, $J = 8.3, 6.9, 1.8$ Hz, 3H), 7.94 – 7.90 (m, 1H), 7.90 – 7.85 (m, 1H), 7.83 (d, $J = 7.6$ Hz, 1H), 7.79 (d, $J = 1.7$ Hz, 1H), 7.78 – 7.76 (m, 1H), 7.59 (ddd, $J = 7.9, 6.5, 1.3$ Hz, 1H), 7.51 – 7.45 (m, 3H), 7.36 (td, $J = 6.9, 6.3, 1.4$ Hz, 2H), 7.34 – 7.30 (m, 1H), 7.29 (d, $J = 1.2$ Hz, 1H), 7.27 (ddd, $J = 4.6, 2.4, 1.0$ Hz, 1H), 7.26 (q, $J = 2.2$ Hz, 1H), 7.25 – 7.22 (m, 1H), 7.21 – 7.17 (m, 1H), 7.11 – 7.06 (m, 3H), 6.91 (ddd, $J = 7.7, 6.5, 1.4$ Hz, 1H), 4.87 (s, 2H), 3.67 (s, 1H). ESI-MS (cation): m/z calc 858.18 ($M - 2H^+$), 429.09 ($M - H^{2+}$), obs. 857.7, 429.5. UV-vis (H₂O, pH 7): 259 nm (53,500 M⁻¹ cm⁻¹), 287 nm (39,300 M⁻¹ cm⁻¹), 402 nm (6,400 M⁻¹ cm⁻¹).

3.2.3.3 “RhPt”

To a solution of Rh(Amal) (12 mg, 0.01 mmol) in H₂O (10 ml) was added aqueous Ba(OH)₂•8H₂O (54 mg, 0.17 mmol in 5 ml H₂O) to pH 11. The yellow

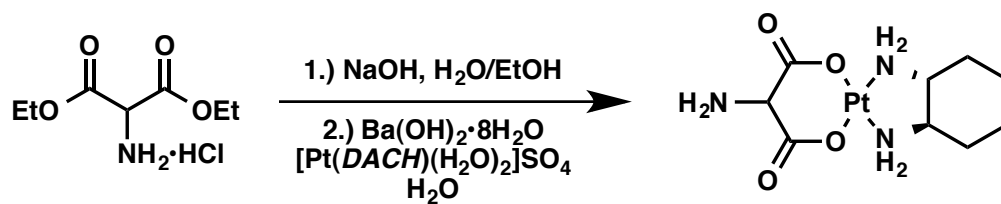


Scheme 3.2 Synthesis of conjugate “RhPt” (**1**), and its immediate precursor “Rh(Amal)” (**2**). Conjugate **1** is synthesized from **2** via chelation of the platinum subunit [Pt(*DACH*)(H₂O)₂]SO₄ (*DACH* = (1*R*,2*R*)-(-)-1,2-diaminocyclohexane) to the dicarboxylate moiety on the metalloinsertor.

suspension was sonicated and added dropwise to a stirred solution of [Pt(DACH)(H₂O)₂]₂SO₄ (76 mg, 0.17 mmol) in H₂O (10 ml) at ambient temperature. The solution turned orange upon addition of the Ba/Rh mixture, and BaSO₄ crashed out as a white precipitate. The remaining Ba(OH)₂•H₂O stock was added to the mixture until pH 7 was reached, and the reaction was allowed to stir at room temperature for 24 h. The BaSO₄ byproduct was filtered, and the filtrate was concentrated *in vacuo* and purified by HPLC. The chloride salt was obtained from a Sephadex QAE anion-exchange column equilibrated with 0.1 M MgCl₂. Yield: 7.1 mg (57% by HPLC). ¹H NMR (300 MHz, D₂O): δ 10.06 (s, 1H, chrysi NH), 8.19 (d, *J* = 6.9 Hz, 1H, chrysi CH), 8.12 (d, *J* = 13.2 Hz, 1H, chrysi CH), 8.05 (d, *J* = 9.2 Hz, 1H, chrysi CH), 8.00 – 7.92 (m, 1H, chrysi CH), 7.89 (d, *J* = 10.0 Hz, 1H, chrysi CH), 7.83 (s, 1H, chrysi CH), 7.80 (s, 1H, chrysi CH), 7.74 (s, 1H, CONH), 7.64 (d, *J* = 8.1 Hz, 2H, py), 7.55 (d, 1H, chrysi CH), 7.54 – 7.47 (m, 2H, py), 7.47 – 7.33 (m, 1H, chrysi CH), 7.23 (d, *J* = 6.1 Hz, 1H, chrysi CH), 7.13 (dt, *J* = 13.3, 6.5 Hz, 2H, py), 6.97 (dd, *J* = 14.5, 7.1 Hz, 2H, py), 6.42 – 5.93 (m, 2H, Pt-NH₂), 5.57 – 5.03 (m, 2H, Pt-NH₂), 2.43 (d, *J* = 1.3 Hz, 2H, dach CH), 1.92 (d, *J* = 10.1 Hz, 1H, dach CH), 1.43 (s, 2H, dach CH), 1.16 (s, 1H, dach CH), 0.99 (t, *J* = 10.2 Hz, 2H, dach CH). ESI-MS (cation): *m/z* calc 1165.24 (M – 2H⁺), 583.12 (M – H²⁺), obs. 1165.9, 582.9. UV-vis (H₂O, pH 7): 315 nm (27,000 M⁻¹ cm⁻¹), 389 nm (5,420 M⁻¹ cm⁻¹).

3.2.4 [Pt(DACH)(aminomalonate)] (“Pt(Amal),” Scheme 3.3)

Diethyl aminomalonate hydrochloride (110 mg, 0.52 mmol) was hydrolyzed in a solution of 4:1 H₂O:EtOH (10 ml) basified with 1N NaOH (pH 13). The reaction was stirred at room temperature overnight, neutralized with 1N HCl, and dried *in vacuo* to afford the diacid as a white solid. The resulting aminomalonic acid hydrochloride (78 mg,



Scheme 3.3 Synthesis of platinum subunit, “Pt(Amal).”

0.366 mmol) was added to a suspension of $\text{Ba}(\text{OH})_2 \cdot 8\text{H}_2\text{O}$ (58 mg, 0.183 mmol) in 10 ml H_2O . The mixture was added dropwise to a solution of $[\text{Pt}(\text{DACH})(\text{H}_2\text{O})_2]\text{SO}_4$ (81 mg, 0.183 mmol) in H_2O (20 ml) and stirred at room temperature, pH 7, for 3h. The BaSO_4 precipitate was removed by vacuum filtration, and the filtrate was left to stand at 4 °C. A yellow precipitate was filtered and dried under vacuum. The residue was dissolved in a minimum volume of water, filtered through Celite, and dried under vacuum again to give $\text{Pt}(\text{Amal})$ as a pale yellow solid. Yield: 10 mg (13%). ^1H NMR (300 MHz, D_2O): 3.96 (s, 2H), 3.74 (s, 1H), 2.26 (m, 2H), 1.98 (m, 2H), 1.40 (m, 2H), 1.31 (m, 2H), 0.99 (m, 2H). ESI-MS (cation): m/z calc 426.09, obs. 449.0 ($\text{M} + \text{Na}^+$).

3.2.5 Photocleavage Competition Titrations

A single-stranded DNA oligomer with the sequence 5'-TTAGGATCATCCCATATA-3' (underline denotes the mismatch) was labeled at the 5'-end with [^{32}P]-ATP using polynucleotide kinase (PNK) at 37 °C for 1 h. The radiolabeled DNA was purified by gel electrophoresis. A small amount of labeled DNA (less than 1% of the total amount of DNA) was annealed to either its mismatched complement (containing a CC mismatch) or a fully matched complement by heating to 90 °C in buffer (100 mM NaCl, 20 mM NaP_i , pH 7.1), followed by slow cooling to ambient temperature over 3 h, to give a final concentration of 2 μM duplex DNA. Racemic solutions of the RhPt conjugate were prepared in Milli-Q water over a range of concentrations (100 nM – 50 μM). For each sample, 4 μM *rac*- $[\text{Rh}(\text{bpy})_2\text{chrysi}]\text{Cl}_3$ (5 μl), which photocleaves DNA at mismatched sites, 2 μM annealed mismatched duplex DNA (10 μl), and the non-photocleaving RhPt at various concentrations (5 μl) were combined to give 1 μM *rac*- $[\text{Rh}(\text{bpy})_2\text{chrysi}]\text{Cl}_3$ and 1 μM duplex DNA as the final concentrations. A “light” control,

(\emptyset Rh, \emptyset Pt) consisting of 2 μ M DNA mixed with 10 μ l Milli-Q water, and a “dark” control (\emptyset *hv*), containing the DNA mixed with the highest concentration of RhPt without irradiation, were also prepared. The samples were vortexed and, except for the dark control, irradiated on an Oriel (Darmstadt, Germany) 1000-W Hg/Xe solar simulator (340-440 nm) for 15 min. The samples were then incubated at 37 °C for 10 minutes to degrade any metastable products and dried under vacuum. The irradiated samples were electrophoresed on a 20% denaturing polyacrylamide gel and exposed to a phosphor screen. The amounts of DNA in each band were analyzed by autoradiography and quantitated by phosphorimagery (ImageQuant).

3.2.6 Binding Constant Determination

As the RhPt complex does not photocleave DNA upon irradiation, the binding affinity for a CC mismatch was determined *via* a competition titration against *rac*-[Rh(bpy)₂chrysi]³⁺, which does photocleave DNA at mismatched sites. To assess the binding of the rhodium subunit of RhPt at the CC mismatch, the fraction of cleaved DNA was quantified and expressed as a percentage of the total DNA in each lane and plotted against the log of the concentration of RhPt. The data from three independent titration experiments were each fit to a sigmoidal curve using OriginPro 8.5. The concentration of rhodium at the inflection point at the curve ([Rh_{50%}]) was then used to solve simultaneous equilibria involving DNA, [Rh(bpy)₂chrysi]Cl₃, and RhPt in Mathematica 8.0 to obtain the binding constant (K_B).

DNA platination was analyzed in a similar manner, wherein the fraction of platinated DNA was quantified and expressed as a percentage of the total DNA in each

lane and plotted against the log of the concentration of RhPt. The data from three independent titrations were each plotted in OriginPro 8.5.

3.2.7 Dimethyl Sulfate Footprinting of Platinated DNA

DNA footprinting of guanine by dimethyl sulfate (DMS) was carried out according to literature procedures.²² Briefly, single stranded DNA with the sequence 5'-TTAGGATCATCCCATATA-3' (underline denotes the mismatch) was labeled at the 5'-end with [³²P]-ATP and annealed with its CC mismatched complement as described above. A solution of 1 μ M annealed DNA was platinated with either RhPt or oxaliplatin at the concentrations indicated by incubation at 37 °C for 90 min. After cooling to 25 °C, the samples were dried *in vacuo* and taken up in 5 μ l Milli-Q water. The samples were diluted with DMS buffer (50 mM sodium cacodylate, 1 mM EDTA, pH 7.5), and 2 mM calf-thymus DNA (4 μ l) was added as a carrier. Samples were cooled to 0 °C and treated with 5 μ l DMS (10% v/v in EtOH) for 5 min at 25 °C. The reaction was quenched *via* addition of the DMS stop solution (1.5 M NaOAc, 1 M β -mercaptoethanol, 250 μ g/ml yeast tRNA) at 0 °C. Following ethanol precipitation of the DNA, samples were treated with 10% aqueous piperidine and heated to 90 °C for 30 min. The piperidine was removed *in vacuo*, and samples were electrophoresed on a 20% denaturing polyacrylamide gel and exposed to a phosphor screen. The amounts of DNA in each band were analyzed by autoradiography and quantitated by phosphorimager (ImageQuant).

3.2.8 Cell Culture

3.2.8.1 HCT116N/O. HCT116N (MMR-proficient) and HCT116O (MMR-deficient) cells were grown in RPMI medium 1640 supplemented with 10% fetal bovine serum, 400 μ g/ml Geneticin (G418), 2 mM L-glutamine, 0.1 mM nonessential

amino acids, 1 mM sodium pyruvate, 100 units/ml penicillin, and 100 µg/ml streptomycin. Cells were grown in tissue culture flasks (Corning Costar, Acton, MA) at 37 °C under a humidified atmosphere (5% CO₂).

3.2.8.2 A2780cis. A2780cis cells (Sigma-Aldrich Co.) were grown in RPMI medium 1640 supplemented with 10% fetal bovine serum, 200 mM L-glutamine, 100 units/ml penicillin, and 100 µg/ml streptomycin. To retain resistance, cisplatin was added to the media every 2-3 passages to a final concentration of 1 µM. Cells were grown in tissue culture flasks (Corning Costar, Acton, MA) at 37 °C under a humidified atmosphere (5% CO₂).

3.2.9 Cellular Proliferation ELISA

The antiproliferative effects of conjugate RhPt, oxaliplatin, cisplatin, Rh(Amal) and Pt(Amal) were studied *via* enzyme-linked immunosorbent assay (ELISA).²³ HCT116N and HCT116O cells were plated in 96-well plates at 2000 cells/well and given 24 h to adhere. The cells were incubated with varying concentrations of metal complex (0 – 2 µM) and grown for an additional 24 h. In the case of Rh and Pt combination treatment, both Rh(Amal) and cisplatin were co-administered from 0 – 2 µM. The media was then replaced with fresh media free of Rh or Pt for the remainder of the 72 h experiment. Cells were labeled with BrdU 24 h before analysis, and BrdU incorporation was quantified by antibody assay. Cellular proliferation was expressed as the amount of BrdU incorporated into treated cells compared to that of the untreated controls. Errors were calculated from 5 replicates.

3.2.10 ICP-MS Assay for Whole-Cell Rh and Pt Levels

HCT116O cells (1.0×10^6) were seeded in 6-well plates containing 3 ml media and allowed 24 h to adhere. The cells were treated with 2 μ M of RhPt, Rh(Amal), Pt(Amal), cisplatin, or oxaliplatin and incubated for periods of 1, 3, 6, 12, or 24 h. After the incubation period, the media was decanted and the wells were washed with 4 x 5 ml PBS. The cells were lysed with 1 ml of a 1% sodium dodecyl sulfate (SDS) solution and sonicated using a Qsonica Ultrasonic processor for 20 s at 20% amplitude. A 750 μ l aliquot was diluted with 750 μ l of a 2% HNO₃ (v/v) solution and analyzed for rhodium and platinum content on a Thermo X Series II ICP-MS unit. ICP-MS measurements for platinum content were measured only for the three most abundant naturally occurring isotopes, ¹⁹⁴Pt (33%), ¹⁹⁵Pt (34%), and ¹⁹⁶Pt (25%). The remainder of the cell lysate was analyzed for protein content *via* a bicinchoninic assay (BCA).²⁴ Rhodium and platinum counts were normalized to protein content to obtain ng [Rh/Pt]/mg [protein], and standard errors were calculated from three replicates.

3.2.11 ICP-MS Assay for Nuclear Rh and Pt Levels

HCT116O cells were plated at 1.0×10^7 cells in 10 ml media and incubated for 24h. The cells were treated with 2 μ M of RhPt, Rh(Amal), Pt(Amal), cisplatin, or oxaliplatin and incubated for an additional 24 h. The cells were harvested by trypsinization, washed with cold PBS, and the nuclear fractions were isolated according to established procedures.¹⁶ The nuclear pellets were suspended in 800 μ l of Milli-Q water and sonicated on a Qsonica Ultrasonic processor for 20 s at 40% amplitude. A 750 μ l aliquot was diluted with 750 μ l of a 2% HNO₃ (v/v) solution and analyzed for rhodium and platinum content on a Thermo X Series II ICP-MS unit as previously described. The remainder of each sample was used for quantification of nuclear protein content by BCA

analysis. The protein content was then converted to number of nuclei by the conversion factor 3.28×10^{-8} mg [nuclear protein]/nuclei.¹⁶ Rhodium and platinum counts were then normalized to the number of nuclei, and standard errors were calculated from three replicates.

3.2.12 ICP-MS Assay for Mitochondrial Rh and Pt Levels

HCT116O cells were plated at 1.5×10^7 cells/plate and allowed 24 h to adhere. The cells were treated with 2 μ M of RhPt, Rh(Amal), Pt(Amal), cisplatin, or oxaliplatin and incubated for an additional 24 h. The cells were harvested by trypsinization, washed with cold PBS, and the mitochondrial fractions were isolated according to established procedures.¹⁶ The mitochondrial pellets were suspended in 800 μ l of Milli-Q water and sonicated on a Qsonica Ultrasonic processor for 20 s at 40% amplitude. A 750 μ l aliquot was diluted with 750 μ l of a 2% HNO₃ (v/v) solution and analyzed for rhodium and platinum content on a Thermo X Series II ICP-MS unit as previously described. The remainder of each sample was used for quantification of mitochondrial protein content by BCA analysis. Rhodium and platinum counts were normalized to protein content to obtain ng [Rh/Pt]/mg [mitochondrial protein], and standard errors were calculated from three replicates.

3.2.13 MTT Cytotoxicity Assay

The cytotoxic effects of conjugate RhPt, Rh(Amal), Pt(Amal), oxaliplatin, and cisplatin were studied *via* MTT (3-(4,5-dimethylthiazol-2-yl)-2,5-diphenyltetrazolium bromide) assay in the cisplatin-resistant A2780cis and MMR-deficient HCT116O cell lines.²⁵ Cells were plated in 96-well plates at 50,000 cells/well and incubated with varying concentrations of metal complex (100 nM – 100 μ M). For caspase-inhibition

assays, Z-VAD-FMK was added to HCT116O cells to a final concentration of 20 μM . For poly-ADP ribose polymerase (PARP) assays, the inhibitor 3,4-dihydro-5[4-(1-piperindinyl)butoxy]-1(2*H*)-isoquinoline (DPQ) was added to HCT116O cells to a final concentration of either 25 or 50 μM . Cells were incubated under humidified atmosphere for 72 h and labeled with MTT for an additional 4 h at 37 °C, 5% CO₂. The ensuing formazan crystals were dissolved with a lysis buffer (10% SDS in 10 mM HCl) according to the manufacturer's instructions. MTT reduction to formazan was quantified by electronic absorption at 570 nm (background: 690 nm), and percent viability was expressed as the amount of formazan in treated cells compared to that of the untreated controls. The data were plotted in OriginPro 8.5 and fit to a sigmoidal curve. Errors were calculated from 5 replicates.

3.2.14 Preparation of Cell Extracts for *In Vitro* DNA Replication Assay

Cell extracts were prepared according to published protocols, with slight modifications.²⁶ HCT116O cells were plated at 1.0×10^7 cells/plate and allowed 24h to adhere. Cells were treated with varying concentrations of platinum and allowed to grow for an additional 6h; a plate of untreated cells was incubated alongside platinum-treated cells as a control. Cells were harvested by trypsinization, washed with cold PBS, and resuspended in 1 ml hypotonic cell extraction buffer (20 mM HEPES (pH 7.5), 5 mM KCl, 1.5 mM MgCl₂, 1 mM DTT, protease inhibitors). Cell suspensions were incubated on ice for 10 min before lysis *via* 7 passages through a 25-gauge needle in a 1-ml syringe. Cell lysates were incubated on ice for 30 min and centrifuged at 10,000 x g at 4 °C for 10 min. The clarified lysate was collected as the supernatant, aliquoted, and stored at -80 °C. Protein concentration was determined *via* BCA assay.

3.2.15 *In Vitro* SV40 DNA Replication Assay

The cell-free simian virus 40 (SV40) DNA replication assay was carried out according to published protocols, with minor modifications.^{26,27} Briefly, 25 μ l replication reactions were prepared, each containing 30 mM HEPES (pH 7.5); 7 mM MgCl₂; 0.5 mM DTT; 4 mM ATP; 100 μ M each of dATP, dGTP, dCTP, and dTTP; 50 μ M each of CTP, GTP, and UTP; 40 mM phosphocreatine; 0.625 units creatine phosphokinase; 1 μ Ci [α -³²P]dCTP; 50 ng SV40 origin-containing pUC HSO plasmid DNA; 1 μ g SV40 large T antigen (T-Ag); and 40 μ g HeLa cell extract. Sterile water was added to bring the reaction to a final volume of 25 μ l, and the reaction was incubated at 37 °C for 4 h. The reaction was quenched *via* addition of an equal volume of stop solution (30 mM EDTA, 0.5% SDS, 200 μ g/ml proteinase K (New England BioLabs)). After incubation for 30 min at 37 °C, replication products were purified by ethanol precipitation (500 μ l EtOH, 50 μ l 7.5M NH₄OAc, 50 μ l yeast RNA co-precipitant) and electrophoresed on a 1% agarose gel. The amounts of DNA in each band were analyzed by autoradiography and quantitated by phosphorimagery (ImageQuant).

3.3 Results

3.3.1 Complexes Synthesized

We report the synthesis and characterization of a bimetallic conjugate (RhPt, **Figure 3.1**), in which an oxaliplatin derivative is tethered to a rhodium metalloinsertor through an aminomalonate leaving group ligand. The conjugate was constructed *via* a linear synthesis, in which the trisheteoleptic rhodium (III) scaffold (Synthesis shown in **Scheme 3.1**) was first functionalized with diethyl aminomalonate, followed by saponification of the diester and subsequent complexation to the platinum center

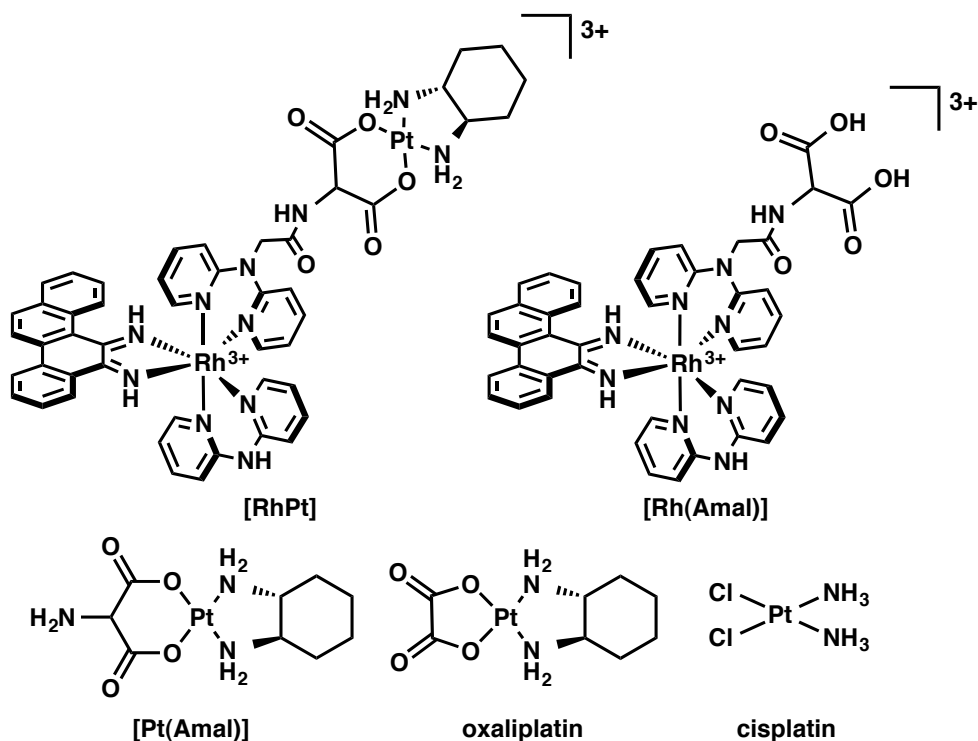


Figure 3.1 Chemical structures of complexes studied. RhPt is a bifunctional conjugate comprised of a trisheteroleptic rhodium metalloinsertor, which recognizes DNA mismatches, tethered to a *cis*-platinum (II) anticancer agent derived from oxaliplatin, which forms covalent adducts with DNA at guanine residues, through the platinum leaving group ligand. Rh(Amal) is the product resulting from the eventual hydrolysis of the platinum subunit of RhPt. Pt(Amal) is the platinum subunit of RhPt. Oxaliplatin and cisplatin are FDA-approved chemotherapeutic agents that form cytotoxic covalent crosslinks with DNA.

(**Scheme 3.2**). The platinum moiety employs the same (1*R*,2*R*)-1,2-diaminocyclohexane non-leaving group ligand as oxaliplatin, and therefore is expected to form the same DNA adducts.²⁸ The rhodium subunit contains a sterically expansive 5,6-chrysene diimine ligand (chrysi), which is responsible for the recognition of DNA mismatches.^{11,12} The aminomalonate linker is tethered to one of the non-inserting ancillary ligands, which allows the conjugate to remain intact temporarily, but ultimately enables the release of platinum, *via* hydrolysis, for DNA binding. The remaining complexes included in this work are also depicted in **Figure 3.1**. The rhodium hydrolysis product, Rh(Amal) (Compound **2** in **Scheme 3.2**), was included as a control to ensure that the biological activity of RhPt is the result of the intact conjugate and not premature hydrolysis of the subunits. The unconjugated platinum complex, Pt(Amal), was also included to account for the effects of the aminomalonate ligand on activity. The synthesis of Pt(Amal) is shown in **Scheme 3.3**. The FDA-approved chemotherapeutics oxaliplatin and cisplatin were also included for comparison.

3.3.2 DNA Binding Studies

3.3.2.1 Binding Affinity of Rhodium at a CC Mismatch

In vitro DNA binding studies were performed with RhPt and radiolabeled duplex DNA containing a CC mismatch (**Figure 3.2**) with the sequence 5*'-TTAGGATCATCCCATATA-3' (underline denotes the mismatch, asterisk denotes the radiolabel). The RhPt conjugate was bound with mismatched and well-matched duplex DNA (of the same sequence, but annealed to a fully matched complement) at varying concentrations and irradiated (340-440 nm) for 15 min. Samples were then incubated at 37 °C for 10 min to promote the formation of platinum adducts and subsequently

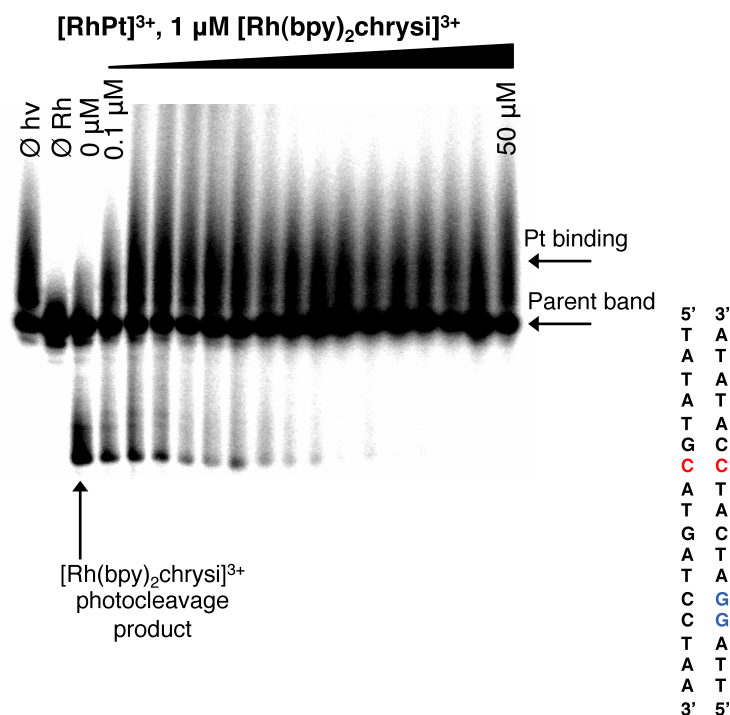


Figure 3.2 Competition titration of increasing concentrations of RhPt (0-50 µM) with 1 µM *rac*-[Rh(bpy)₂chrysi]³⁺ on 1 µM 5'-[³²P] labeled 17mer duplex DNA with a CC mismatch (denoted in red) and a d(GpG) site (denoted in blue). Samples were irradiated (340-440 nm) for 15 min and electrophoresed on a 20% denaturing polyacrylamide gel. Controls without irradiation (Øhv), and without Rh (ØRh) were included. RhPt inhibits photocleavage by [Rh(bpy)₂chrysi]³⁺ at the mismatched site. The site of photocleavage by [Rh(bpy)₂chrysi]³⁺ at the mismatch is indicated by an arrow at bands located below the unmodified parent band. Bands of reduced electrophoretic mobility, located above the unmodified parent DNA, are indicative of covalent binding by the platinum subunit.

electrophoresed on a denaturing PAGE gel. As RhPt does not cleave DNA upon irradiation, a competition titration was carried out using *rac*-[Rh(bpy)₂chrysi]³⁺, which does photocleave DNA at the site of a mismatch.¹⁰ RhPt inhibits photocleavage by *rac*-[Rh(bpy)₂chrysi]³⁺ at the mismatched site in a dose-dependent manner (**Figure 3.2**); this indicates that RhPt binds specifically to the mismatch *via* metalloinsertion. The amount of photocleaved DNA was quantified and plotted against the logarithmic concentration of RhPt (log[RhPt]), and the K_B value of RhPt was calculated by solving simultaneous equilibria at the inflection point of the titration curve (**Figure 3.3**). The binding affinity of RhPt for a CC mismatch was determined to be 1.1 x 10⁷ M⁻¹, comparable to that of monomeric metalloinsertors.^{14,16,17}

3.3.2.2 Platinum Binding to DNA

DNA binding by the conjugate also involves the formation of covalent adducts. As the platinum subunit dissociates from the conjugate *via* hydrolysis, it can covalently crosslink with DNA. Platination of the DNA is indicated by the appearance of bands with reduced electrophoretic mobility, located above the unmodified parent bands in the autoradiogram (**Figure 3.2**). The amount of platinated DNA (expressed as a fraction of the total DNA) was plotted against log[RhPt] and fit to a sigmoidal curve (**Figure 3.4**). At higher concentrations, platination diverges from the curve, but does not exceed a 1:1 ratio of Pt:DNA. No difference in platination levels was observed in DNA binding experiments with well-matched DNA.

3.3.2.3 Dimethyl Sulfate Footprinting of Pt-DNA Crosslinks

Platinum binding to DNA was further characterized by dimethyl sulfate (DMS) footprinting. DMS methylates the N7 position of guanine, resulting in cleavage at those

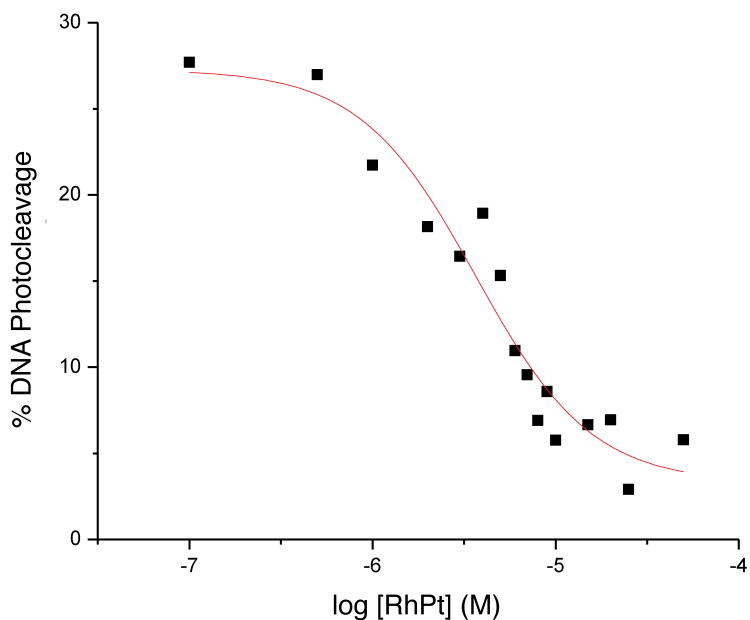


Figure 3.3 Representative sigmoidal curve (Boltzmann fit) of photocleavage competition titrations of RhPt for binding constant determination at the CC mismatch. K_B was calculated by solving simultaneous equilibria at the inflection point of the curve. Experiments were conducted in buffer (50 mM NaCl, 10 mM NaP_i, pH 7.1) using 1 μ M duplex DNA and 1 μ M rac-[Rh(bpy)₂chrysi]³⁺, with 0-50 μ M RhPt competitor complex. The binding constant was determined from three independent experiments.

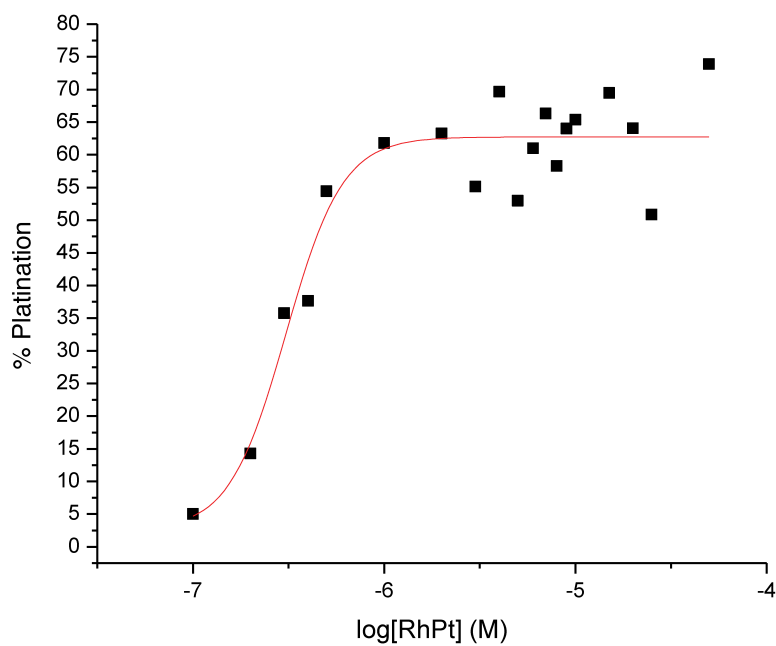


Figure 3.4 Representative sigmoidal curve fit of DNA platination by the platinum subunit of RhPt, from 0-50 μM . RhPt was incubated with duplex DNA containing a CC mismatch and a d(GpG) site at 37 $^{\circ}\text{C}$ for 10 min to promote the formation of covalent Pt-DNA adducts. Samples were electrophoresed on a 20% denaturing PAGE gel. The amount of platinated DNA is expressed as a fraction of the total DNA in each sample.

sites upon treatment with piperidine.²² Duplex DNA (1 μM) containing a single CC mismatch (see **Section 3.3.2.1** for sequence) was radiolabeled at the 5'-end with [³²P] and incubated with either oxaliplatin or RhPt for 90 min at 37 °C to promote the formation of Pt-DNA adducts. The DNA was then subjected to treatment with DMS, followed by piperidine cleavage. Free guanine residues – i.e., those not coordinated to platinum – are expected to be methylated at the N7 position by DMS and therefore susceptible to piperidine cleavage. At a 1:1 molar ratio of DNA and RhPt (**Figure 3.5**), the guanine residues on the labeled strand are protected from cleavage, signifying the formation of platinum 1,2-intrastrand adducts at the N7 positions of the d(GpG) site, as is the case for oxaliplatin.

Adenine methylation is also observed with DMS treatment (visible in the autoradiogram at high gain), but there is no evidence of platinum binding at these sites. At 50 μM RhPt (50 fold excess), only one guanine is protected, possibly due to distortions to the DNA that impede the formation of 1,2-d(GpG) adducts.

3.3.3 Quantitation of Inhibition of Cellular Proliferation Using an Enzyme-Linked Immunosorbent Assay (ELISA)

An ELISA for DNA synthesis was used to quantify the effects of RhPt and the corresponding control complexes on the proliferation of HCT116N (MMR-proficient) cells and HCT116O (MMR-deficient) cells.²⁹ Cells were treated with 0 – 2 μM of each complex (including a control where Rh and Pt complexes were added together but as separate subunits, at equal concentrations) and incubated for 24h. Thymidine analogue BrdU, which is incorporated in place of thymidine during DNA synthesis, was added to cells 24h prior to analysis. The extent of cellular proliferation was determined *via*

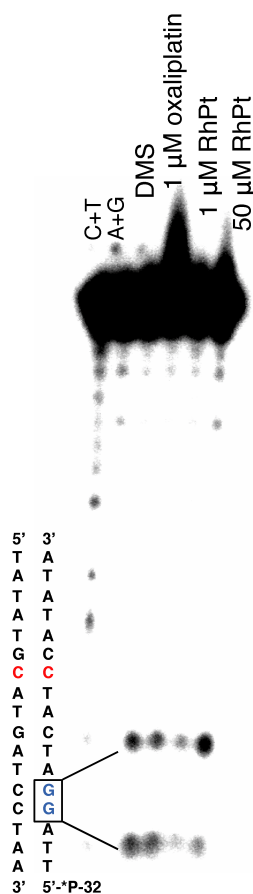


Figure 3.5 Dimethyl sulfate (DMS) footprinting of 5'-end radiolabeled duplex DNA containing a CC mismatch (denoted in red) and a d(GpG) site (denoted in blue, boxed). Samples were incubated with platinum and treated with 10% DMS, followed by piperidine cleavage. Samples were electrophoresed on a 20% denaturing PAGE gel. Lanes (left to right): Maxam Gilbert sequencing (C+T; A+G); DMS alone; oxaliplatin (1 μ M); RhPt (1 μ M); RhPt (50 μ M). Bands of high electrophoretic mobility indicate cleavage at guanine residues; covalent binding of platinum to guanine inhibits cleavage. Both oxaliplatin and RhPt form covalent 1,2-intrastrand Pt-DNA adducts at the *N7* position of guanine.

quantification of the amount of BrdU incorporated into treated cells normalized to that of untreated cells, as determined by antibody detection.²³

The results of the ELISA for RhPt compared to FDA-approved therapeutics oxaliplatin and cisplatin in the two cell lines are shown in **Figure 3.6**. No cell-selectivity was observed for RhPt; the complex inhibits growth in both HCT116N and HCT116O cell lines equally. Additionally oxaliplatin also does not display any preferential targeting of either cell line, but cisplatin exhibits a slight preference for the MMR-proficient HCT116N cell line, as has been observed in previous studies;³⁰ overall, however, cisplatin exhibits low potency at the concentration range explored in this work. RhPt exhibits antiproliferative activity similar to that of oxaliplatin and considerably outperforms cisplatin, inhibiting cell proliferation at concentrations as low as 500 nM after 24h incubation. All complexes were probed at 0-2 μ M in both cell lines as shown in **Figure 3.6**, but neither Pt(Amal) nor Rh(Amal) shows any preferential targeting of either cell line – Pt(Amal) targets both cell lines equally and Rh(Amal) displays little antiproliferative effect at the concentrations indicated (data not shown).

The inhibitory effects of all complexes on HCT116O cells at 2 μ M after 24h incubation are shown in **Figure 3.7**. At 2 μ M, RhPt inhibits cellular proliferation by $79 \pm 1\%$, compared to $75 \pm 3\%$ for oxaliplatin. Interestingly, RhPt exhibits increased activity compared to either of its monomeric subunits alone: at 2 μ M, Pt(Amal) inhibits cell proliferation by $65 \pm 2\%$, while Rh(Amal) inhibition is only $17 \pm 4\%$. At 2 μ M cisplatin treatment, to which HCT116O cells are known to exhibit resistance, DNA synthesis is stalled by only $27 \pm 3\%$, and co-treatment of cisplatin with the rhodium subunit confers little synergistic effect.

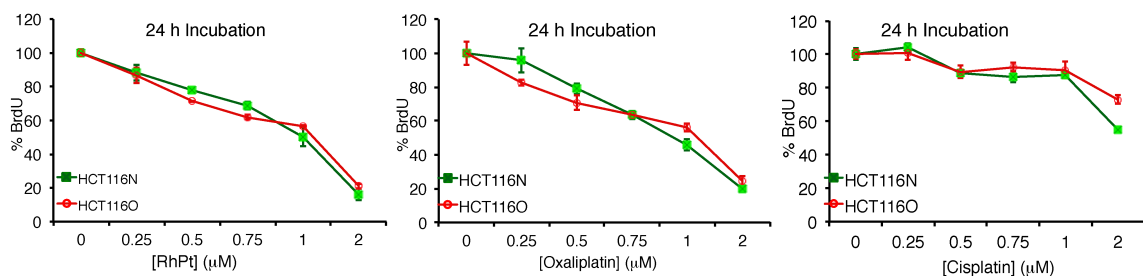


Figure 3.6 Inhibitory effects of RhPt (left), oxaliplatin (center), and cisplatin (right) on cellular proliferation. DNA synthesis is shown as a function of percent BrdU incorporation normalized to that of untreated cells. MMR-proficient HCT116N (green) and MMR-deficient HCT116O (red) cells were plated in 96-well plates and allowed 24 h to adhere. Cells were then treated with 0-2 μM of the indicated metal complex for 24 h, after which the medium was removed and replaced with fresh, drug-free medium for the remainder of the 72 h period. BrdU was added to the medium 24 h prior to ELISA analysis. Standard error bars were calculated from 5 replicates.

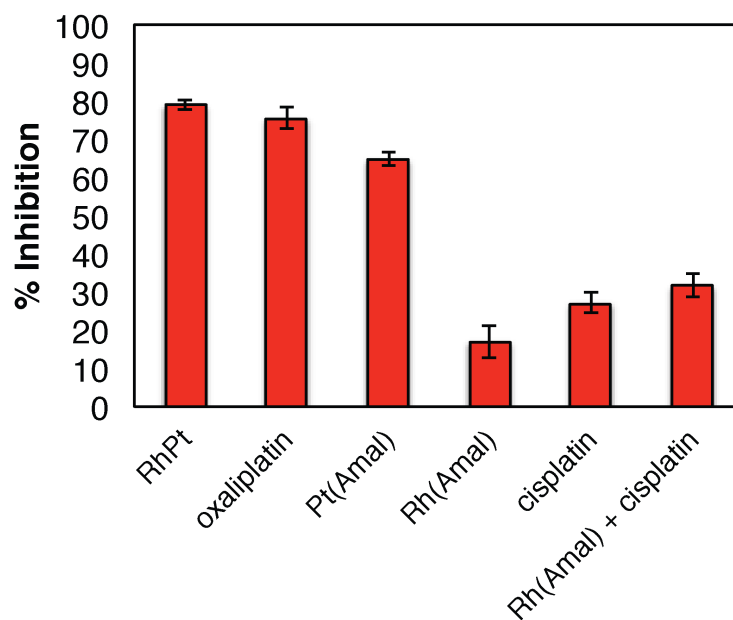


Figure 3.7 Inhibitory effects of all complexes on cellular proliferation in HCT1160 cells after 24 h treatment with 2 μ M of each complex. For combination treatment, cells were treated with 2 μ M each of cisplatin and Rh(Amal). Treatment of cells with the unconjugated Rh(Amal) in combination with the relatively non-potent cisplatin compound has no significant effect on overall inhibition of growth. Percent inhibition is expressed as the normalized percent BrdU incorporation subtracted from 100% (i.e., untreated cells, normalized). Standard errors were calculated from 5 replicates.

3.3.4 Cell-Free SV40 DNA Replication Assay

The inhibitory properties of RhPt were also explored in an *in vitro*, cell-free DNA replication assay, to corroborate the results of the ELISA. Here, the soluble extracts of eukaryotic cells could be tested for their ability to carry out replication on exogenous viral DNA in the presence of *cis*-platinum. Simian virus 40 (SV40) is a well-characterized model system for the examination of DNA replication *in vitro*.²⁶ Requiring only the SV40 large tumor antigen (T-Ag), dNTPs, and the SV40 origin of replication, DNA synthesis can be carried out using the native proteins supplied by the eukaryotic cell extract.^{26,27}

To each *in vitro* replication reaction was added 40 μg soluble HeLa (procured in kit form) or 25 μg HCT116O (isolated according to the procedure described in **Section 3.2.14**) cell extract, and either oxaliplatin to a final concentration of 0 or 2 μM , or RhPt to a final concentration of 0, 2, 10, or 20 μM . Replication of pUC HSO plasmid DNA containing the SV40 origin was carried out at 37 °C for 4h in the presence of radiolabeled [α -³²P]dCTP. A mock reaction containing HSO plasmid DNA lacking the SV40 origin was included as a negative control. Replication products were isolated, separated by non-denaturing agarose gel electrophoresis, and identified by autoradiography.

In the initial studies carried out with HCT116O cell extract, no appreciable replication could be observed, even in the absence of platinum (**Figure 3.8**). It is possible that the HCT116O cells require a different cell extraction protocol in order to obtain active cell lysate. It is also possible that HCT116O cell extract cannot support *in vitro* replication of viral DNA. As the positive control using the commercially provided HeLa

cell extract appeared to work (**Figure 3.8**, Lane 1), the remainder of the experiments were carried out using HeLa lysate.

The effects of platinum treatment on SV40 replication in HeLa extract are shown in **Figure 3.9**. As expected based on the results in the ELISA, both oxaliplatin and RhPt significantly inhibit replication of SV40 origin-containing DNA. RhPt exhibits a dose-dependent response. However, RhPt and oxaliplatin treatment have differing effects on the replication products produced. Treatment with 2 μM oxaliplatin results in a marked decrease in the formation of all replication products: circular supercoiled DNA (Form I), circular nicked DNA (Form II), and linear DNA (Form III). In contrast, treatment with 2 μM RhPt yields a slight increase in Form I product compared to the untreated control, but a significant decrease in Form II and Form III DNA is observed. It is possible that the cellular processing of oxaliplatin adducts differs somewhat from that of RhPt; nevertheless, it is clear that these results support those observed in the ELISA in that RhPt stalls replication and DNA synthesis in a cellular environment.

3.3.5 MTT Cytotoxicity

The cytotoxic effects of all complexes were probed *via* MTT assay. Metabolically active cells are capable of reducing the yellow tetrazole (3-(4,5-dimethylthiazol-2-yl)-2,5-diphenyltetrazolium bromide (MTT) to purple formazan crystals, which can be dissolved in acidified SDS to obtain a characteristic absorbance at 570 nm. Quantification of formazan by electronic absorption indicates the amount of metabolically active cells in each sample. MMR-deficient human colorectal carcinoma HCT116O cells and cisplatin-resistant A2780cis human ovarian cancer cells were treated with a broad concentration range of metal complex (100 nM – 100 μM) and incubated for 72h. The percent viability

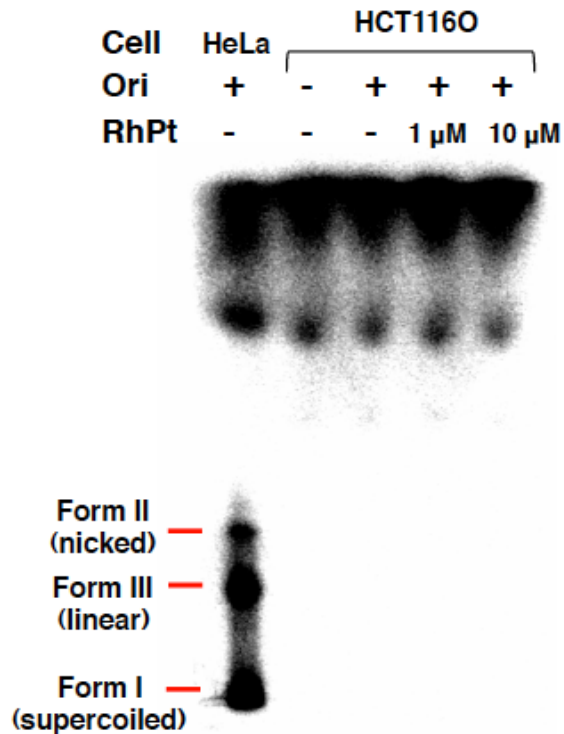


Figure 3.8 Cell-free *in vitro* SV40 replication assay. HCT116O cells were plated at 1×10^7 cells and allowed 24 h to adhere. Cells were then treated with 0, 1, or 10 μ M RhPt for 6 h, harvested, and soluble cell lysates were isolated. Cell lysates were incubated with SV40-origin containing plasmid DNA in the presence of [α - 32 P]dCTP at 37 $^{\circ}$ C for 4 h. Untreated HeLa cell extract was included as a positive control, and untreated HCT116O cell extract in the presence of plasmid DNA lacking the SV40 origin (“Ori –”) was included as a negative control. No replication is observed for any of the HCT116O cell extracts.

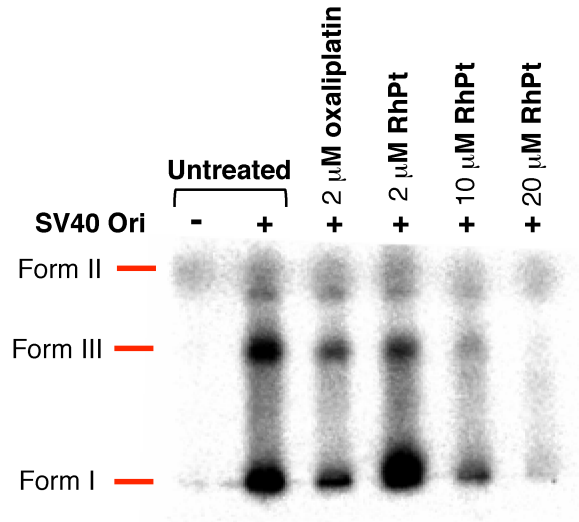


Figure 3.9 Cell-free *in vitro* SV40 replication assay. HeLa cell extract was treated with either oxaliplatin (2 μ M) or RhPt (2, 10, or 20 μ M) and allowed to replicate plasmid DNA containing the SV40 origin in the presence of [α - 32 P]dCTP at 37 $^{\circ}$ C for 4 h. A reaction was carried out on plasmid DNA lacking the SV40 origin as a negative control (“Ori -”). A positive control containing untreated HeLa extract was also included. Treatment with 2 μ M oxaliplatin decreases the levels of all replication products – Form I (supercoiled), Form II (circular nicked), and Form III (linear). Treatment with RhPt confers a dose-dependent effect on SV40 replication. Initially, the presence of RhPt results in a decrease of Form II and Form III DNA, primarily. At higher concentrations (10 μ M and above), a decrease in all replication products is observed.

is defined as the amount of formazan in cells treated with rhodium and/or platinum normalized to that of untreated cells. The dose-response curves for HCT116O and A2780cis cells are shown in **Figure 3.10** and **Figure 3.11**, respectively. For HCT116O cells, RhPt (shown in black in **Figure 3.10**) is the most potent of all complexes studied. The A2780cis cell line exhibits a similar sensitivity to RhPt (shown in black in **Figure 3.11**) as the HCT116O line; however, oxaliplatin and Pt(Amal) are significantly more active in A2780cis cells.

LC₅₀ values, defined as the concentration at which 50% of the cells are viable after 72h treatment with metal complex, were also determined for all of the complexes, which are summarized in **Table 3.1**. With an LC₅₀ value of 9.01 μ M, RhPt exhibits a 3-fold increase in cytotoxicity over both oxaliplatin and cisplatin in the HCT116O cell line, and is also significantly more potent than either of its unconjugated components. This is in contrast to its activity in the A2780cis cells: while RhPt exhibits similar potency in this cell line (LC₅₀ = 8.9 μ M), its monomeric platinum counterpart Pt(Amal) is significantly more potent.

3.3.6 ICP-MS Assay for Whole-Cell Rhodium and Platinum Levels

As RhPt displays high cytotoxicity but no preferential targeting of MMR-deficient cells, we next explored whether its cellular uptake properties explained its enhanced potency. HCT116O cells were treated with 2 μ M metal complex for periods of 1, 3, 6, 12, or 24h. The cell lysates were then analyzed for rhodium and/or platinum content by inductively coupled plasma mass spectrometry (ICP-MS) and normalized to protein content as determined by BCA assay (See **Section 3.2.10**). The cellular uptake of platinum for RhPt, oxaliplatin, cisplatin, and Pt(Amal) is depicted in **Figure 3.12a**.

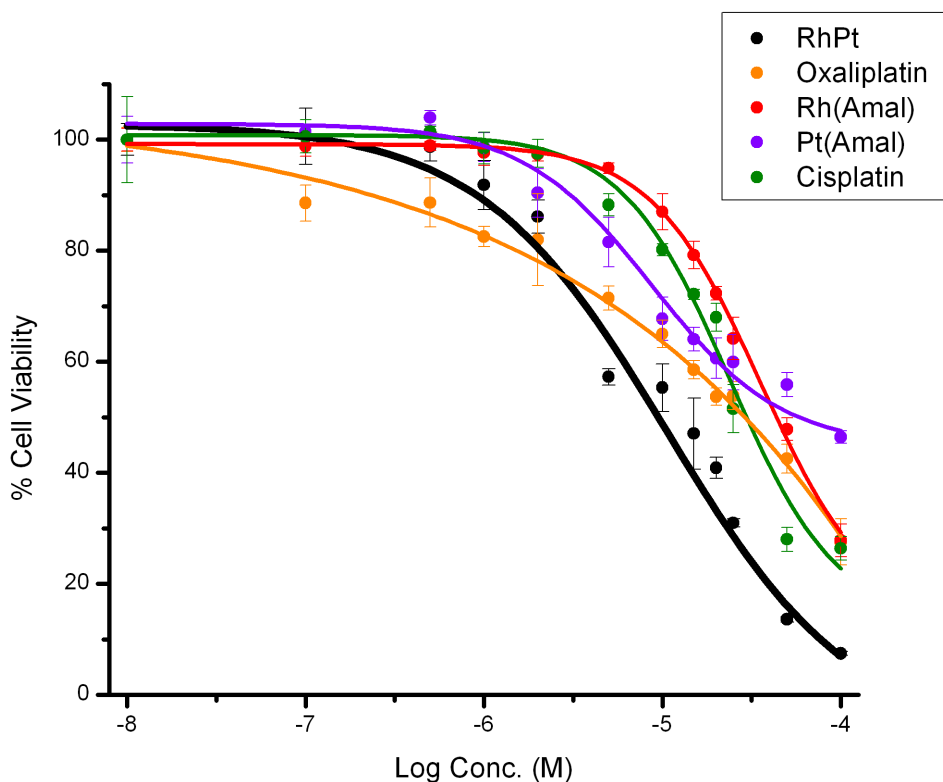


Figure 3.10 Dose-response cytotoxicity curves of HCT116O cells treated with RhPt (black), oxaliplatin (orange), Rh(Amal) (red), Pt(Amal) (purple), and cisplatin (green). Cells were treated with 0-100 μ M of each metal complex and incubated for 72 h. After the incubation period, cells were treated with the MTT reagent for 4 h, and the resulting formazan crystals were solubilized with acidified SDS. Percent cell viability is defined as the percentage of formazan normalized to that of untreated cells. Data were fit to a sigmoidal curve, and LC₅₀ values were obtained (See **Table 3.1**). Standard errors were calculated from 5 replicates.

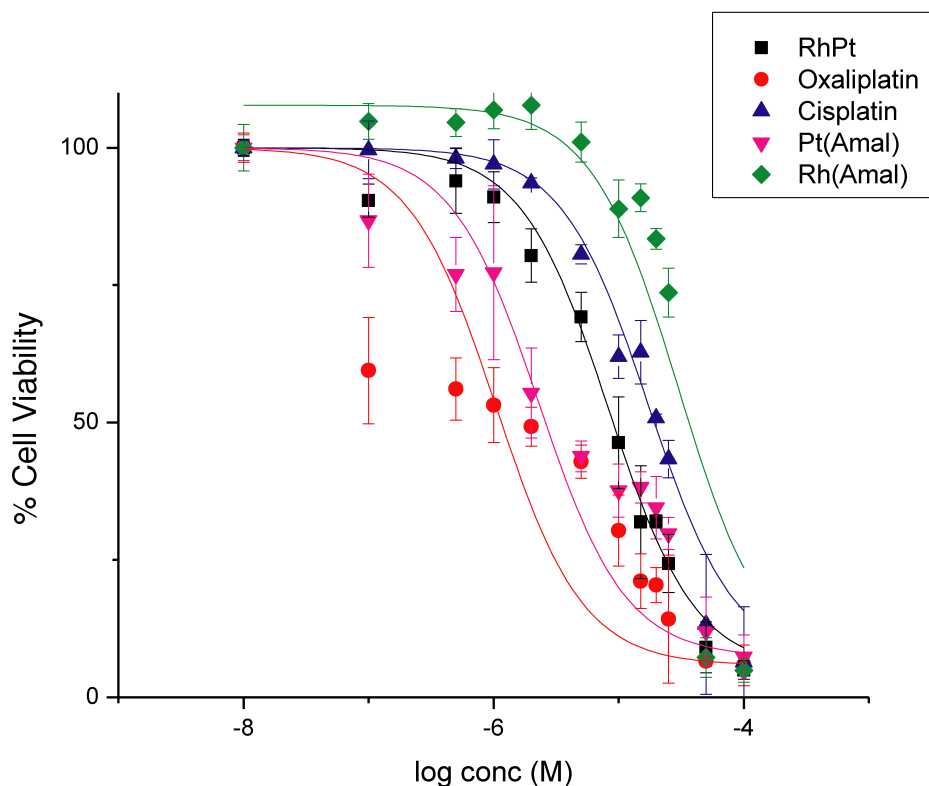


Figure 3.11 Dose-response cytotoxicity curves of cisplatin-resistant A2780cis cells treated with RhPt (black), oxaliplatin (red), Rh(Amal) (green), Pt(Amal) (fuschia), and cisplatin (blue). Cells were treated with 0-100 μM of each metal complex and incubated for 72 h. After the incubation period, cells were treated with the MTT reagent for 4 h, and the resulting formazan crystals were solubilized with acidified SDS. Percent cell viability is defined as the percentage of formazan normalized to that of untreated cells. Data were fit to a sigmoidal curve, and LC_{50} values were obtained (See **Table 3.1**). Standard errors were calculated from 5 replicates.

Table 3.1 LC₅₀ Values^a of Metal Complexes in HCT116O and A2780cis Cells

Complex	LC₅₀ HCT116O	LC₅₀ A2780cis
RhPt	9.01 μM	8.9 μM
Oxaliplatin	27.5 μM	1.15 μM
Cisplatin	29.5 μM	18.7 μM
Pt(Amal)	43.3 μM	2.66 μM
Rh(Amal)	57.2 μM	35.9 μM

^a LC₅₀ refers to the concentration at which 50% of the cells are viable after 72 h, as determined by MTT assay. Cells were plated in 96-well plates at densities of 5×10^4 cells/well and treated with varying concentrations of the indicated metal complex. After the 72 h period, cells were treated with MTT for an additional 4 h. The resulting formazan crystals were solubilized with a solution of 10% SDS and 10 mM HCl, and absorbances were recorded at 570 nm. LC₅₀ values were calculated from the titration curves of three independent experiments

Across all time points (except for 24 h), the platinum content of RhPt (blue bars) far exceeds that of the monomeric platinum complexes studied. The mechanism of platinum uptake for RhPt also seems to differ from that of the other platinum complexes. Cellular accumulation of RhPt is relatively high at earlier time points, but steadily decreases after 6h, possibly due to an efflux mechanism. By contrast, oxaliplatin (orange bars) displays a relatively high initial uptake at 1 h, followed by a decrease in platinum content at 3 h, with little change at later time points. The cellular concentration of cisplatin (green bars) is comparatively quite low, and remains largely unchanged over the 24 h period. Pt(Amal) (purple bars), the monomeric platinum counterpart of RhPt, exhibits uptake similar to that of cisplatin, with only slight increases in platinum content after 1 h.

The cellular uptake of rhodium is shown adjacently in **Figure 3.12b**. For RhPt (gray bars), the cellular rhodium content exceeds that of platinum, suggesting that the conjugate hydrolyzes at some point. However, comparison to the cellular uptake of the synthesized hydrolysis product, Rh(Amal) (red bars), shows that the rhodium uptake is significantly higher – nearly an order of magnitude at some time points – in cells treated with RhPt. Furthermore, the pattern of cellular uptake over time differs for the two complexes, with RhPt displaying high rhodium uptake at early timepoints, followed by a gradual decrease at later time points – highly similar to the uptake patterns of the platinum subunit. The cellular rhodium content of Rh(Amal), in contrast remains largely unchanged over the 24 h period. Therefore, the divergence in rhodium vs. platinum accumulation for RhPt is unlikely due to significant conjugate hydrolysis occurring prior to being taken up into the cell.

3.3.7 ICP-MS Assay for Nuclear Rhodium and Platinum Levels

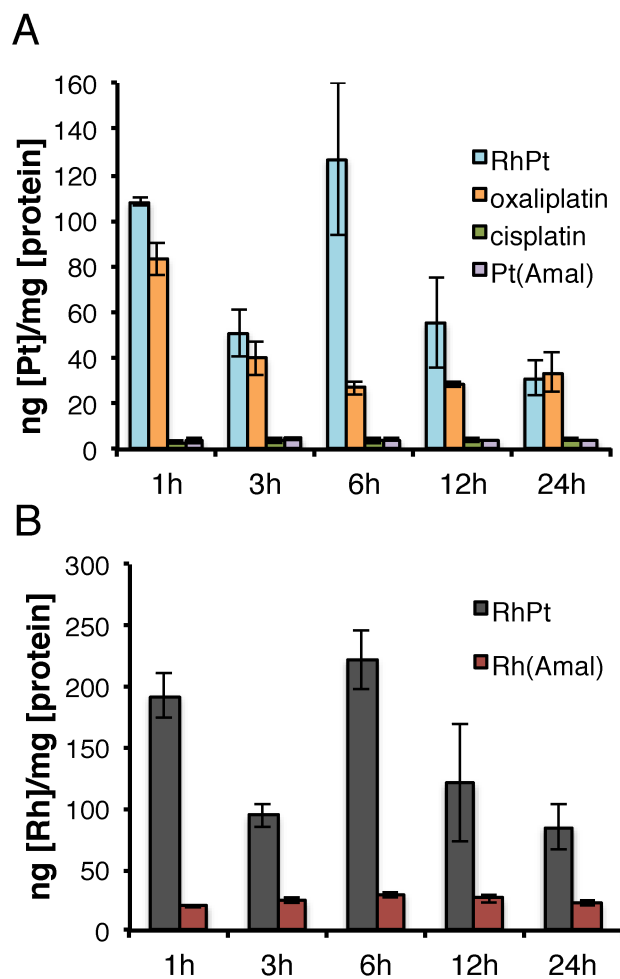


Figure 3.12 Cellular accumulation of metal complexes in HCT116O cells. Adherent cells (1×10^6) were treated with $2 \mu\text{M}$ complex for the durations indicated. Cells were analysed for rhodium and platinum content by ICP-MS, and normalized to cellular protein content as determined by BCA assay. (A) Whole-cell platinum uptake of RhPt (blue), oxaliplatin (orange), cisplatin (green), and Pt(Amal) (purple). (B) Whole-cell rhodium uptake of RhPt (gray) compared to hydrolysis product Rh(Amal) (red).

The nuclear uptake of all complexes were determined using ICP-MS. HCT116O cells were treated with 2 μ M metal complex for 24 h, and the nuclei were isolated as described above. Rhodium and platinum levels were measured via ICP-MS and normalized to the number of nuclei. The nuclear rhodium and platinum levels for RhPt are shown in **Figure 3.13a** (left axis), expressed as ng [metal]/nuclei. Rhodium uptake is depicted in gray, and platinum uptake is shown in blue. The nuclear concentrations of the two metals are similar, indicating that nuclear uptake of the intact conjugate may be occurring. The nuclear rhodium uptake was compared between RhPt and Rh(Amal) and is shown in **Figure 3.13b** (left axis). Significantly, the nuclear rhodium uptake of RhPt exceeds that of Rh(Amal) by nearly an order of magnitude, which further supports the notion that RhPt is taken up into the nucleus as an intact conjugate, rather than hydrolyzing beforehand.

Figure 3.13c (left axis) shows nuclear platinum levels of the remaining complexes compared to RhPt, expressed as ng [Pt]/nuclei. Overall, there is little variation in the nuclear uptake of platinum. As a result, it is unlikely that the enhanced potency of RhPt can be attributed to nuclear localization alone.

The levels of nuclear rhodium and platinum for all complexes were converted to molar concentrations by approximating the nucleus of an HCT116 cell as a sphere with radius 4 μ m.³¹ The values are summarized in **Table 3.2**. Notably, RhPt localizes to the nucleus in concentrations sufficient for rhodium mismatch binding (given its *in vitro* binding affinity) yet below nonspecific DNA binding levels.¹⁶

3.3.8 ICP-MS Assay for Mitochondrial Rhodium and Platinum Levels

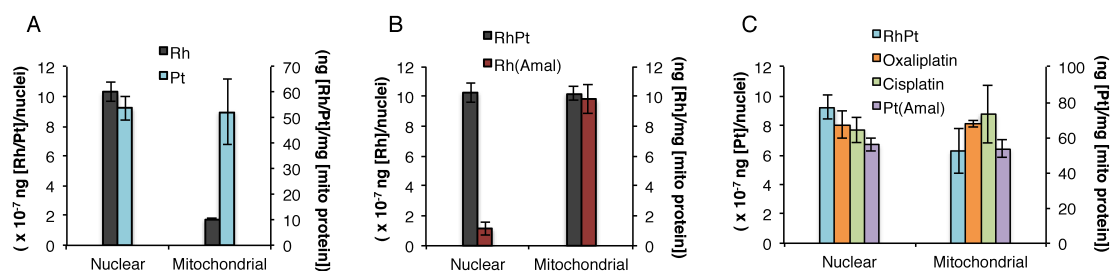


Figure 3.13 Subcellular localization of metal complexes. HCT1160 cells were incubated with 2 μ M metal complex for 24h, and the appropriate organelle isolation procedures were performed. Metal content was analyzed by ICP-MS and normalized to protein content as determined by BCA assay. Nuclear metal content is expressed as ng[Metal]/nuclei, and mitochondrial metal content is expressed as ng[M]/mg [mitochondrial protein]. (A) Nuclear (left axis) and mitochondrial (right axis) uptake of RhPt. The uptake of rhodium is shown in gray, and platinum is shown in blue. (B) Nuclear (left axis) and mitochondrial (right axis) uptake of rhodium for RhPt (gray) and hydrolysis product Rh(Amal) (red). (C) Nuclear (left axis) and mitochondrial (right axis) uptake of platinum for RhPt (blue), oxaliplatin (orange), cisplatin (green), and Pt(Amal) (purple).

Table 3.2 Subcellular Distribution of Metal Complexes in HCT116O Cells*

Complex	Nuclear^a	Mitochondrial^b
RhPt	18 ± 2 μM Pt 37 ± 2 μM Rh	52 ± 13 Pt 10 ± 0.4 Rh
Rh(Amal)	4 ± 1 μM	9.8 ± 0.9
Pt(Amal)	13 ± 1 μM	54 ± 5
Oxaliplatin	15 ± 2 μM	68 ± 2
Cisplatin	14 ± 2 μM	73 ± 17

*Nuclear versus mitochondrial metal uptake are normalized differently, mitigating their comparison. ^a Nuclear concentrations were obtained by dividing metal content by the volume of the nucleus, estimated as a sphere with radius 4 μm.³¹ Errors were calculated from three replicates. ^b Mitochondrial metal content is normalized to mitochondrial protein using by BCA analysis, and is expressed as (ng [metal]/mg [mito protein]).

The complexes were also analyzed for mitochondrial localization. HCT116O cells were treated with 2 μ M metal for 24 h, and mitochondria were isolated as described above. Rhodium and platinum counts were determined by ICP-MS and normalized to mitochondrial protein content, as determined by BCA assay. The mitochondrial localization of rhodium and platinum for all complexes are shown in **Figure 3.13** and summarized in **Table 3.2**. The mitochondrial localization of rhodium and platinum for RhPt is depicted in **Figure 3.13a** (right axis). Unlike the nuclear metal content, the mitochondrial rhodium and platinum levels differ substantially, with mitochondrial platinum uptake \sim 5 fold greater than that of rhodium. Again, comparison of RhPt with its hydrolysis counterpart, Rh(Amal), offers further insight into the biological behavior of the conjugate. **Figure 3.13b** (right axis) displays the mitochondrial rhodium content for the two complexes, and they are nearly identical, with 10 ± 0.4 ng [Rh]/mg [mitochondrial protein] for RhPt, and 9.8 ± 0.9 ng [Rh]/mg [mitochondrial protein] for Rh(Amal). The highly similar rhodium content of RhPt and Rh(Amal) further suggests that the conjugate has hydrolyzed, and that the rhodium and platinum subunits enter the mitochondria as separate entities.

Mitochondrial platinum content is shown in **Figure 3.13c** (right axis). Mitochondrial localization does not appear to correlate with cytotoxicity, cellular uptake, or nuclear localization, and in fact the mitochondrial platinum content is quite similar across all complexes. Overall, it does not appear that the subcellular localization of platinum plays a significant role in altering the biological behavior of the complexes in this work.

3.3.9 Caspase and PARP Inhibition Assays

To further understand the biological activity of RhPt, we examined the mechanism of cell death. It has been previously established that rhodium metalloinsertors trigger a necrotic mechanism of cell death involving severe depletion of cellular ATP,¹⁵ which is dependent upon DNA repair protein poly-ADP ribose polymerase (PARP).³² Consequently, co-treatment of HCT116N HCT116O cells with rhodium metalloinsertor and an inhibitor of PARP, such as 3,4-dihydro-5[4-(1-piperidinyl)butoxy]-1(2*H*)-isoquinoline (DPQ),³³ resulted in an increase in cell viability of HCT116O cells compared to treatment with rhodium alone, essentially abolishing the differential cytotoxicity between the MMR-proficient and MMR-deficient cell lines. This result indicates that metalloinsertors induce PARP-dependent (necrotic) cell death.¹⁵

Here, HCT116N and HCT116O cells were treated with RhPt (20 μ M) and DPQ (25 or 50 μ M) for 72h, and cell viability was assayed by MTT. **Figure 3.14** (left, gray) depicts the results for the HCT116O cells, but the same results are observed in the HCT116N cell line (data not shown). DPQ alone, at either concentration, effects no change in cell viability compared to untreated cells. When cells were treated with RhPt in combination with varying concentrations of DPQ, a statistically significant *decrease* in cell viability (17% in HCT116O cells with 25 μ M DPQ) is observed compared to treatment with RhPt alone, as determined by an unpaired two-tailed *t* test ($p < 0.0001$). This is in direct contrast to the previous study on rhodium metalloinsertors,¹⁵ suggesting that RhPt cytotoxicity is PARP-independent and therefore not necrotic.

The experiment was also performed in the presence of a pan-caspase inhibitor, Z-VAD-FMK. By irreversibly binding to the active site of caspases, Z-VAD-FMK inhibits apoptosis.³⁴ While the previous study on metalloinsertor cytotoxicity concluded that

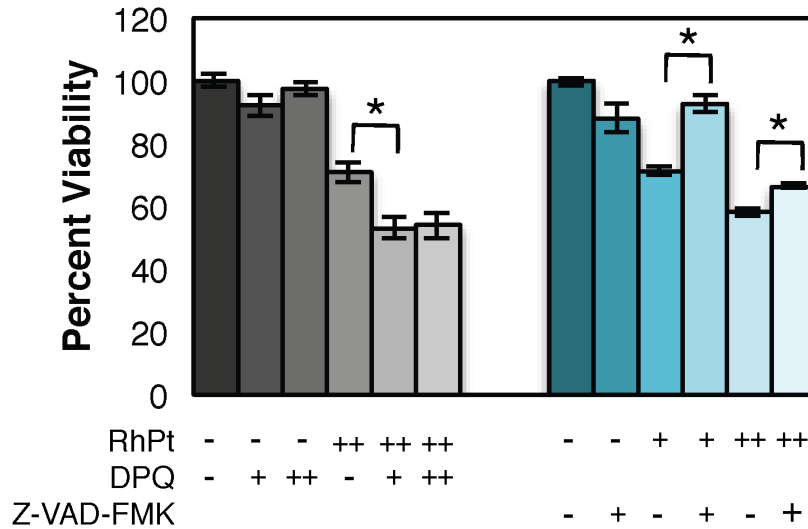


Figure 3.14 Cell viability in HCT1160 cells after 72h with PARP and caspase inhibitors. Viability is normalized to untreated controls. Left (gray): PARP inhibition assay. Cells were treated with 0 (-) or 20 μ M (++) RhPt and 0 (-), 25 (+), or 50 μ M (++) DPQ. DPQ does not increase the viability of cells treated with RhPt. Right (blue): Caspase inhibition assay. Cells were treated with 0 (-), 10 (+) or 20 μ M (++) RhPt and 0 (-) or 20 μ M (++) Z-VAD-FMK. Z-VAD-FMK increases viability in RhPt-treated cells. Addition of either inhibitor alone does not affect viability. * $p < 0.0001$ (unpaired two-tailed t-test).

caspase inhibition has no effect on rhodium metalloinsertor cytotoxicity in HCT116N and HCT116O cells,¹⁵ it is well-established that platinum complexes, namely cisplatin and oxaliplatin, typically induce apoptosis.^{35,36} As such, we sought to determine whether RhPt cytotoxicity results from an apoptotic cell death mechanism.

HCT116N and HCT116O cells were treated with 0, 10, or 20 μM RhPt and either 0 or 20 μM Z-VAD-FMK for 72h. As can be seen in **Figure 3.14** (right, blue), caspase inhibition increases the viability of HCT116O cells treated with RhPt (the same results are observed with HCT116N cells). At 10 μM RhPt and 20 μM Z-VAD-FMK, cell viability is $91 \pm 3\%$, compared to $70 \pm 1\%$ for RhPt alone, a nearly 21% increase in cell viability. At higher concentrations of RhPt (20 μM), the effects of caspase inhibition are subtler (a 7% increase in cell viability upon co-treatment with Z-VAD-FMK compared to RhPt alone), but in both cases the difference was determined to be statistically significant by unpaired two-tailed t test ($p < 0.0001$). These results indicate that RhPt triggers caspase-dependent, and therefore apoptotic cell death.

3.4 Discussion

3.4.1 DNA Binding Behavior

The RhPt conjugate was originally synthesized with the intention of conferring the selectivity of rhodium metalloinsertors for DNA mismatches and MMR-deficient cells to a highly potent platinum agent derived from the chemotherapeutic oxaliplatin. While selectivity was not achieved with this complex, it does exhibit its intended dual binding to DNA *via* metalloinsertion at mismatched sites and the formation of 1,2-intrastrand crosslinks at the $N7$ position of guanine residues. Additionally, the binding

affinity of the rhodium subunit at the mismatch is similar to those previously reported for rhodium metalloinsertor complexes.^{14,16,17}

That RhPt performs both noncovalent metalloinsertion and covalent platinum binding establishes the bifunctionality of the conjugate (**Figure 3.15**). The lack of interplay between the rhodium and platinum binding modes suggests that each subunit functions independently and without inhibition of the other; that is, platinum binding does not alter the apparent equilibrium of metalloinsertion in the minor groove, nor does rhodium binding impede DNA platination.

3.4.2 Antiproliferative and Cytotoxic Activity in MMR-Deficient Cells

The antiproliferative effects of RhPt were explored in the isogenic human colorectal carcinoma cell lines HCT116N (MMR-proficient) and HCT116O (MMR-deficient) using an antibody assay for DNA synthesis.²³ RhPt exhibits antiproliferative activity similar to that of oxaliplatin and considerably outperforms cisplatin, which preferentially targets HCT116N cells. RhPt does not preferentially target either cell line. However, it is active at submicromolar concentrations, and in fact is more potent than either of its unconjugated subunits, including co-treatment with rhodium and platinum separately. The ability of RhPt to disrupt DNA synthesis was further corroborated with the *in vitro* replication assay, wherein the conjugate effectively stalls DNA replication. Furthermore, RhPt exhibits three-fold enhanced cytotoxicity over cisplatin and oxaliplatin in MMR-deficient cells, and is also substantially more potent than the Rh(Amal) and Pt(Amal) subunits. Although RhPt does not selectively inhibit proliferation of MMR-deficient cells, there is likewise no resistance – i.e., RhPt does not preferentially inhibit proliferation of MMR-*proficient* cells, and thus does not face the

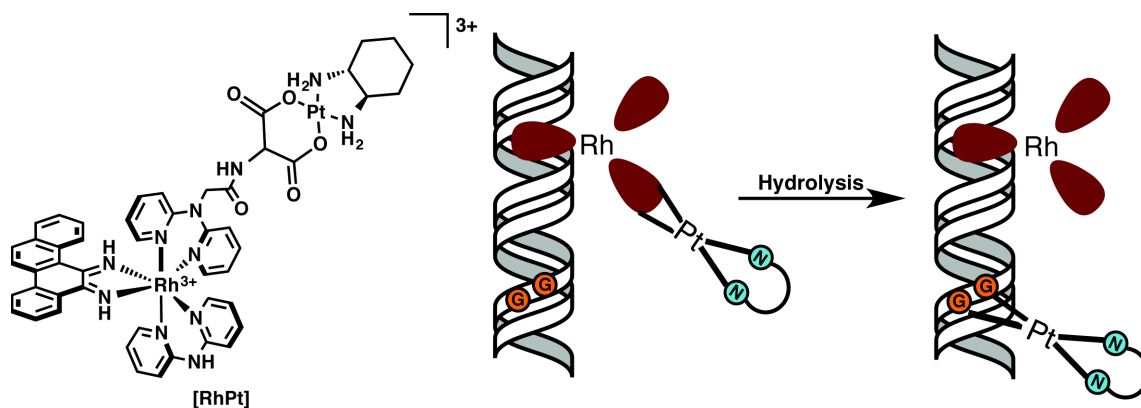


Figure 3.15 The bifunctional DNA metalloinsertor conjugate (“RhPt”). The complex interacts with DNA through metalloinsertion at a base pair mismatch followed by formation of a covalent Pt-DNA adduct. In mismatch repair-deficient cells, RhPt exhibits enhanced cellular uptake and cytotoxicity over traditional platinum therapeutics.

same clinical limitations as cisplatin or DNA alkylating agents like MNNG.³⁷ The ELISA studies demonstrated that the conjugate exhibits the same anti-proliferative behavior as oxaliplatin, the first-line therapy in the treatment of late-stage colorectal cancer. Although oxaliplatin typically shows little cross-resistance with cisplatin in cell culture studies, only a modest increase in potency is observed with the MMR-deficient HCT116O cell line. As RhPt exhibits a 3 fold increase in potency over both cisplatin and oxaliplatin in this cell line, the conjugate could potentially offer another avenue for treatment of cisplatin-resistant cancers.

3.4.3 Cellular Uptake and Subcellular Localization of Metal Complexes

Cellular uptake was examined *via* inductively coupled plasma mass spectrometry (ICP-MS) (**Figure 3.12**). The cellular uptake of both rhodium and platinum for RhPt generally exceeds that of the monomeric complexes, with RhPt displaying high initial uptake that decreases over time, possibly due to an efflux mechanism.³⁸ Furthermore, the differences in uptake between RhPt and hydrolysis product Rh(Amal) suggest that the conjugate does not hydrolyze prior to entry into the cell, and is taken up in its intact form. Overall, it would appear that RhPt possesses enhanced cellular uptake properties not inherent to either subunit alone. The localization of each complex was also examined (**Figure 3.13** and **Table 3.2**). Little differentiation is observed in the subcellular distribution of the complexes, with the notable exception of a substantial increase in the nuclear rhodium concentration of RhPt compared to Rh(Amal). Curiously, this enhanced nuclear targeting of rhodium does not result in cell-selective activity.

It is likely that the enhanced potency of RhPt can be attributed largely to its increased cellular uptake properties compared to the other complexes studied in this

work. However, other than localizing to the nucleus in concentrations sufficient for DNA binding, it would appear that the subcellular localization of RhPt has little effect on its potency and does not explain its lack of cell-selectivity. This is in contrast to previous studies of monomeric rhodium metalloinsertors, wherein non-selective cytotoxicity arises from high mitochondrial rhodium content.^{16,17} In the case of RhPt, the conjugate appears to hydrolyze prior to entry into the mitochondria, given that the mitochondrial rhodium content is identical to that of its hydrolysis product, Rh(Amal), while diverging substantially from mitochondrial platinum concentrations. Furthermore, the mitochondrial rhodium content is extremely low (~10 ng Rh/mg [mitochondrial protein]), while earlier studies of metalloinsertor localization have shown that cells can support an order of magnitude higher mitochondrial rhodium without losing cell-selectivity.^{16,17}

3.4.4 Mechanism of Cell Death

To further understand the biological activity of RhPt, we examined the mechanism of cell death. It has been previously established that rhodium metalloinsertors trigger necrosis dependent upon DNA repair protein poly-ADP ribose polymerase (PARP).¹⁵ Cytotoxicity studies revealed that the viability of cells treated with RhPt does not increase in the presence of PARP inhibitor, suggesting PARP-independent cell death. In fact, co-treatment with RhPt and PARP inhibitor is even more potent than treatment with either compound alone. This is consistent with previous studies demonstrating that inhibition of PARP can sensitize cells to *cis*-platinum through activation of the mitochondrial pathway of apoptosis, even in cell lines that are platinum-resistant.^{39,40} The assay was also performed with caspase inhibitor. The viability of RhPt-treated cells increases under conditions of caspase inhibition, signifying that the conjugate triggers

caspase-dependent – and therefore apoptotic – cell death (**Figure 3.14**). This is consistent with studies of platinum cytotoxicity generally; it is well established that cisplatin and oxaliplatin typically trigger apoptosis.^{35,36} This result may, in part, explain the lack of cell-selectivity observed for RhPt. By initiating apoptosis, rather than necrosis, it is possible that the highly selective biological response to mismatch recognition by rhodium is overridden by the effects of high concentrations of platinum in the cell.

Curiously, the PARP pathway appears to play vastly different roles in response to treatment with rhodium versus platinum: inhibition of the pathway in the presence metalloinsertor alone protects MMR-deficient cells from Rh-induced toxicity, while conferring synergistic cytotoxicity in the presence of a *cis*-platinum moiety. It is possible that conjugation of apoptosis-inducing *cis*-platinum (II) agents may be incompatible with the unique selectivity of metalloinsertors.

3.5 Conclusions

In this work, we examined the biological effects of conjugation of a DNA metalloinsertor with a platinum drug. *In vitro*, the complex successfully exhibits bifunctionality *via* dual DNA binding. In MMR-deficient cells, this strategy affords enhanced cellular uptake and potency over the individual subunits as well as versus traditional chemotherapeutics. However, RhPt is not without its limitations. The platinum subunit appears to dominate the cellular response, resulting in a loss of cell selectivity. Nevertheless, the biological analysis of RhPt provides insight into the behavior of bifunctional DNA targeting agents, as well as a foundation for the design of future conjugates that are both potent and selective in their cellular targeting.

3.6 References

- 1 Wang, D.; Lippard, S. J. *Nature Rev. Drug Discov.* **2005**, *4*, 307-320.
- 2 Jamieson, E. R., Lippard, S. J. *Chem. Rev.* **1999**, *99*, 2467-2498.
- 3 Decatris, M. P., Sundar, S., O'Byrne, K. J. *Cancer Treat. Rev.* **2004**, *30*, 53–81.
- 4 Fink, D.; Aebi, S.; Howell, S. B. *Clin. Cancer Res.* **1998**, *4*, 1-6.
- 5 Aebi, S.; Fink, D.; Gordon, R.; Kim, H. K.; Zheng, H.; Fink, J. L.; Howell, S. B. *Clin. Cancer Res.* **1997**, *3*, 1763-1767.
- 6 Arzimanoglou, I. I.; Gilbers, F.; Barber, H. R. K. *Cancer* **1998**, *82*, 1808-1820.
- 7 Lawes, D. A.; SenGupta, S.; Boulos, P. B. *Eur. J. Surg. Oncol.* **2003**, *29*, 201-212.
- 8 Ibrahim, A.; Hirschfeld, S.; Cohen, M. H.; Griebel, D. J.; Williams, G. A.; Pazdur, R. *The Oncologist* **2004**, *9*, 8-12.
- 9 Rothenberg, M. L., et al. *J. Clin. Oncol.* **2003**, *21*, 2059-2069.
- 10 Jackson, B. A.; Barton, J. K. *J. Am. Chem. Soc.* **1997**, *119*, 12986-12987.
- 11 Jackson, B. A., Barton, J. K. *Biochemistry* **2000**, *39*, 6176–6182.
- 12 Jackson, B. A., Alekseyev, V. Y., Barton, J. K. *Biochemistry* **1999**, *38*, 4655–4662.
- 13 Pierre, V. C., Kaiser, J. T., Barton, J. K. *Proc. Natl. Acad. Sci. U.S.A.* **2007**, *104*, 429–434.
- 14 Ernst, R. J.; Song, H.; Barton, J. K. *J. Am. Chem. Soc.* **2009**, *131*, 2359.
- 15 Ernst, R. J.; Komor, A. C.; Barton, J. K. *Biochemistry* **2011**, *50*, 10919-10928.
- 16 Komor, A. C.; Schneider, C. J.; Weidmann, A. G.; Barton, J. K. *J. Am. Chem. Soc.* **2012**, *134*, 19223-19233.

- 17 Weidmann, A. G.; Komor, A. C.; Barton, J. K. *Philos. Trans. R. Soc. A.* **2013**, *371*, 20120117.
- 18 Wisnovsky, S. P.; Wilson, J. J.; Radford, R. J.; Pereira, M. P.; Chan, M. R.; Laposa, R. R.; Lippard, S. J.; Kelley, S. O. *Chem. Biol.* **2013**, *20*, 1323-1328.
- 19 Muerner, H.; Jackson, B. A.; Barton, J. K. *Inorg. Chem.* **1998**, *37*, 3007-3012.
- 20 Gandolfi, O.; Apfelbaum, H. C.; Blum, J. *Inorg. Chim. Acta* **1987**, *135*, 27-31.
- 21 Kirin, S. I.; Yennawar, H. P.; Williams, M. E. *Eur. J. Inorg. Chem.* **2007**, *23*, 3686-3694.
- 22 Brabec, V.; Leng, M. *Proc. Natl. Acad. Sci. U.S.A.* **1993**, *90*, 5345-5349.
- 23 Gratzner, H. G. *Science*, **1982**, *218*, 474-475.
- 24 Smith, P. K.; Krohn, R. I.; Hermanson, G. T.; Mallia, A. K.; Gartner, F. H.; Provenzano, M. D.; Fujimoto, E. K.; Goeke, N. M.; Olson, B. J.; Klenk, D. C. *Anal. Biochem.* **1985**, *150*, 76-85.
- 25 Mosmann, T. *J. Immunol. Methods* **1983**, *65*, 55-63.
- 26 Li, J. J.; Kelly, T. J. *Proc. Natl. Acad. Sci. U.S.A.* **1984**, *81*, 6973-6977.
- 27 Liu, J.-S.; Kuo, S.-R.; McHugh, M. M.; Beerman, T. A.; Melendy, T. *J. Biol. Chem.* **2000**, *275*, 1391-1397.
- 28 Woynarowski, J. M.; Faivre, S.; Herzig, M. C.; Arnett, B.; Chapman, W. G.; Trevino, A. V.; Raymond, E.; Chaney, S. G.; Vaisman, A.; Varchenko, M.; Juniewicz, P. E. *Mol. Pharmacol.* **2000**, *58*, 920-927.
- 29 Koi, M.; Umar, A.; Chauhan, D. P.; Cherian, S. P.; Carethers, J. M.; Kunkel, T. A.; Boland, C. R. *Cancer Res.* **1994**, *54*, 4308-4312.

- 30 Hart, J. R., Glebov, O., Ernst, R. J., Kirsch, I. R., Barton, J. K. *Proc. Natl. Acad. Sci. U.S.A.* **2006**, *103*, 15359–15363.
- 31 Fujioka, A.; Terai, K.; Itoh, R. E.; Aoki, N.; Nakamura, T.; Kuroda, S.; Nishida, E.; Matsuda, M. *J. Biol. Chem.* **2006**, *281*, 8917-8926.
- 32 Ha, H.C., Snyder, S. H. *Proc. Natl. Acad. Sci. U.S.A.* **1999**, *96*, 13978-13982.
- 33 Costantino, G., Macchiarulo, A., Camaioni, E., and Pellicciari, R. *J. Med. Chem.* **2001**, *44*, 3786-3794.
- 34 Vandenabeele, P., Vanden Berghe, T., and Festjens, N. *Sci. STKE*, **2006**, *358*, pe44.
- 35 Siddik, Z. H. *Oncogene* **2003**, *22*, 7265.
- 36 Arango, D.; Wilson, A. J.; Shi, Q.; Corner, G. A.; Arañes, M. J.; Nicholas, C.; Lesser, M.; Mariadason, J. M.; Augenlicht, L. H. *Br. J. Cancer* **2004**, *91*, 1931.
- 37 Carethers, J. M.; Hawn, M. T.; Chauhan, D. P.; Luce, M. C.; Marra, G.; Koi, M.; Boland, C. R. *J. Clin. Invest.* **1996**, *98*, 199-206.
- 38 Eckford, P. D. W.; Sharom, F. *J. Chem. Rev.* **2009**, *109*, 2989.
- 39 Michels, J.; Vitale, I.; Senovilla, L.; et al. *Cell Cycle* **2013**, *12*, 877-883.
- 40 Sakogawa, K.; Aoki, Y.; Misumi, K.; et al. *Cancer Sci.* **2013**, *104*, 1593-1599.

Chapter 4: Targeting Platinum to DNA Mismatches via Conjugation to a Metalloinsertor Containing a Rh—O Bond

4.1 Introduction:

Platinum anticancer agents comprise an essential component in the current repertoire of chemotherapeutics. *Cis*-platinum (II) complexes such as cisplatin (**Figure 4.1**) and its derivatives have been extremely successful in the treatment of a variety of cancers, but are also associated with a litany of severe side effects and resistance.¹⁻⁵ These side effects arise primarily as a result of the mechanism by which *cis*-platinum complexes function biologically: slow displacement of labile leaving group ligands, such as chlorides or carboxylate groups, activates the platinum center for the formation of cytotoxic, covalent adducts with DNA.^{1,6} Although these complexes preferentially bind the nucleophilic *N7* position of consecutive guanine residues to form what are known as 1,2-intrastrand crosslinks, the nature of *cis*-platinum binding is inherently nonspecific and can target the DNA of non-cancerous cells as well as malignant ones.² Additionally, although DNA is widely considered to be the primary therapeutic target of cisplatin, platinum (II) complexes possess the ability to react with a number of biological ligands once inside the cell, including proteins. A major source of cisplatin resistance, for example, is the chelation and subsequent inactivation by sulfur-containing molecules, such as glutathione.⁷ Indeed, it is reported that only 1% of intracellular cisplatin reaches the genome.⁸ The ability to tune platinum therapeutics to target specific biomarkers of cancer would be invaluable in the development of next-generation platinum drugs.

Our laboratory has focused largely on the development of octahedral rhodium (III) complexes for the targeted therapy of cisplatin-resistant cancers. These complexes

selectively bind thermodynamically destabilized sites, such as base pair mismatches, in DNA.⁹ Mismatches, which arise naturally as a consequence of DNA replication, lead to cancerous mutations if left uncorrected by the complex of proteins known as the mismatch repair (MMR) machinery.^{10,11} As a result, deficiencies in the MMR pathway result in a buildup of these single base lesions in the genome, leading to several types of cancer. These malignancies are largely resistant to cisplatin and other classical chemotherapeutics, as MMR is also one of the DNA repair pathways that recognizes and processes cisplatin-DNA lesions.¹²

Our rhodium complexes recognize DNA mismatches not through the formation of covalent adducts, as with *cis*-platinum therapeutics, but rather through a non-covalent binding mode that involves the insertion of a sterically expansive aromatic ligand, such as 5,6-chrysenequinone diimine (chrysi) (**Figure 4.1**) into the base stack of the duplex. This binding occurs from the minor groove at the site of the mismatch, extruding the destabilized, mismatched nucleobases from the helix out into the major groove.¹³⁻¹⁸ This binding mode, termed metalloinsertion, targets 80% of all mismatches with over 1000-fold specificity, in all sequence contexts.¹³ More recently, we have demonstrated that these metalloinsertor complexes also target mismatched DNA in genomic DNA: metalloinsertors exhibit cytotoxicity preferentially in MMR-deficient colorectal cancer cells compared to isogenically matched MMR-proficient cells, and this selectivity is contingent on the localization of these complexes to the nucleus.¹⁹⁻²³

Rhodium metalloinsertors are a robust class of complexes that offer a promising alternative for targeting MMR-deficient cancers and circumventing resistance. New generations of metalloinsertors have exhibited increased potency surpassing that of

cisplatin, while still maintaining selective targeting to MMR-deficiency.^{22,24} While these compounds are currently being explored as chemotherapeutic agents, they also hold promise as potential adjuvants that could confer their unique selectivity onto other therapeutic cargo. Recent efforts have focused on the development of bimetallic Rh-Pt complexes that bifunctionally target DNA through both metalloinsertion at mismatched sites as well as through the formation of covalent platinum crosslinks. Previous iterations of metalloinsertor-platinum complexes have included the conjugation of a platinum center to the rhodium complex through its inert amine ligand²⁵ as well as the temporary attachment of the two metal centers via the labile platinum leaving group ligand.²⁶

In the case of the first generation conjugate, in which a cisplatin analogue was tethered to a rhodium metalloinsertor via an alkane-modified non-leaving group (ammine) ligand, metalloinsertion at a mismatch successfully directed platinum binding preferentially toward mismatched DNA over a well-matched duplex. However, this preferential binding was highly dependent on the presence and location of a d(GpG) site (the preferred binding site of cisplatin); if there was no d(GpG) site, or if it was inaccessible to the platinum center due to limitations in the length and flexibility of the alkyl tether, then platination levels were reduced and the complex exhibited no selectivity. Preferential platination of mismatched DNA was only achieved when the d(GpG) site was located where the tether most favored interactions between the platinum center and the DNA.²⁵ Unsurprisingly, this limitation reduces the applications of the conjugate in a biological system; indeed, when characterized in the isogenic HCT116N (MMR-proficient) and HCT116O (MMR-deficient) human colorectal cancer cell lines,

the conjugate displayed no selective antiproliferative activity in the MMR-deficient line and in fact exhibited a slight preference for the MMR-proficient cell line.²⁷

To overcome the structural limitations of the first-generation Rh-Pt conjugate, a second-generation metalloinsertor-platinum conjugate was developed wherein the platinum (II) moiety was tethered to the rhodium metalloinsertor via its leaving group ligand. Here, platination of DNA (or other biological ligands) would not occur until the platinum subunit had dissociated from the rhodium center, thereby circumventing the limitations incurred by the alkyl linker. As a result, a d(GpG) site could become platinated irrespective of its distance from a base pair mismatch. Ideally, the conjugate would remain intact while rhodium ferried the platinum subunit towards mismatches, followed by hydrolysis and platination of mismatched DNA. Again, this complex displayed no cell-selective targeting of MMR-deficiency, although it also did not display a preference for the MMR-proficient line. Additionally, this conjugate exhibited similar levels of platination in both mismatched and well-matched DNA *in vitro*.²⁶

In our latest efforts to develop selective bifunctional conjugates, we turn to a new family of metalloinsertor complexes, developed and characterized only in the last two years. Each complex in this new generation of metalloinsertors contains an unusual ligand coordination involving a Rh—O bond. In all cases, a tris-heteroleptic Rh(III) center employs the inserting chrysi ligand, a 1,10-phenanthroline (phen) non-inserting ancillary ligand, and a 2-pyridylethanol ligand that forms an *N,O*-chelate. In this family of metalloinsertors, the hydroxyl group coordinates the Rh(III) center as an X-type ligand, reducing the overall charge of the complex from [3+] to [2+]. As a result, the pK_a of the chrysi immines, normally singly deprotonated when bound to DNA, is increased

above biological pH, leading to a puckering of the ligand. An alternate mode of metalloinsertion has previously been proposed to accommodate these distortions in structure. These complexes also exhibit unprecedented potency ($IC_{50} = 300$ nM, where IC_{50} represents the concentration at which 50% of the cells are viable) in MMR-deficient cells, while maintaining excellent cell-selectivity, making them promising new scaffolds for conjugate design.²⁴

The original complex in this family, $[Rh(\text{chrysi})(\text{phen})(\text{DPE})]^{2+}$, (**Figure 4.1**) contains a 1,1-di(pyridin-2-yl)ethanol (DPE) ligand that was originally intended to chelate via both pyridine rings to afford the all-nitrogen coordination environment observed for earlier generations of metalloinsertors.²² The hydroxyl group was included as a moiety that could potentially be functionalized for conjugation. It was only after structural characterization of the complex through X-ray crystallography that the true binding mode was revealed. It was later found that a number of functional groups could be introduced into this ligand structure in place of the extraneous pyridine without sacrificing DNA binding ability, cell-selectivity, or potency.²⁴ Here, we sought to develop the first generation conjugate derived from this new family, through coordination of the “dangling” pyridine to a second metal center. This pyridine still represents a viable chelating environment that could be exploited to confer selectivity onto other inorganic therapeutic cargo, such as *cis*-platinum anticancer agents. We have synthesized a new bifunctional metalloinsertor complex, wherein a cisplatin group is attached to $[Rh(\text{chrysi})(\text{phen})(\text{DPE})]^{2+}$ via coordination to the extraneous pyridine. This conjugate,

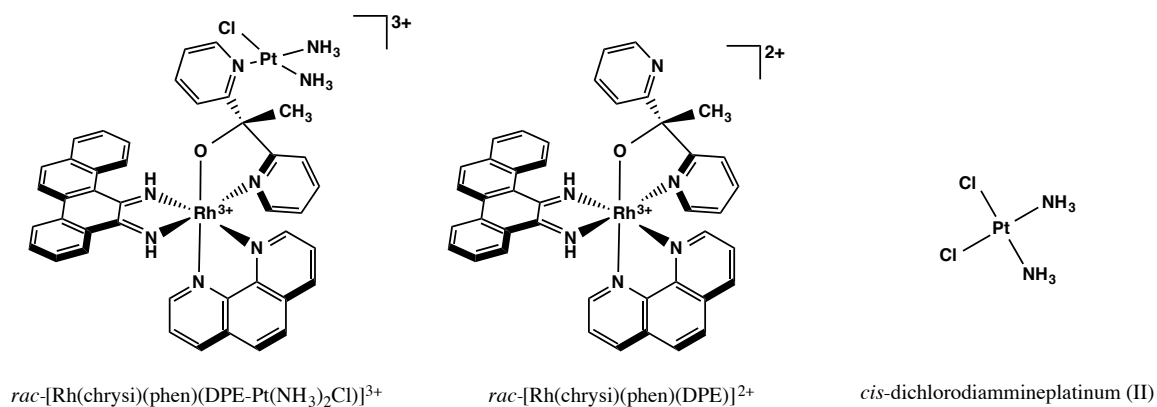


Figure 4.1 Chemical structures of complexes studied. [Rh(chrysi)(phen)(DPE-Pt(NH₃)₂Cl)]³⁺ (left) is a bifunctional comprised of a trisheteroleptic rhodium metalloinsertor, which recognizes DNA mismatches, tethered to a *cis*-platinum (II) anticancer agent, which forms covalent adducts with DNA. [Rh(chrysi)(phen)(DPE)]²⁺ (center) is the rhodium metalloinsertor parent complex, which contains an unusual Rh—O axial coordination that contributes to its enhanced efficacy. *Cis*-dichlorodiammineplatinum (II) (right) is the FDA-approved chemotherapeutic known as cisplatin.

$[\text{Rh}(\text{chrysi})(\text{phen})(\text{DPE-Pt}(\text{NH}_3)_2\text{Cl})]^{3+}$ (**Figure 4.1**), preferentially targets platinum to mismatched DNA *in vitro* and forms unusual, nonclassical covalent adducts.

4.2 Experimental

4.2.1 Materials

A2780cis cells, cisplatin, and all organic reagents were purchased from Sigma-Aldrich unless otherwise noted. Commercially available chemicals were used as received without further purification. RhCl_3 starting material was purchased from Pressure Chemical Co (Pittsburgh, PA). Sep-pak C_{18} solid-phase extraction (SPE) cartridges were purchased from Waters Chemical Co. (Milford, MA). Media and supplements were purchased from Invitrogen (Carlsbad, CA). BrdU, antibodies, and buffers were purchased in kit format from Roche Molecular Biochemical (Mannheim, Germany).

Oligonucleotides were ordered from Integrated DNA Technologies and purified by HPLC using a C_{18} reverse-phase column (Varian, Inc; Corona, CA). All HPLC purifications were carried out on a Hewlett-Packard 1100 HPLC. DNA purity was confirmed by MALDI-TOF mass spectrometry and quantified by UV-visible spectroscopy (UV-vis) using the extinction coefficients at 260 nm estimated for single-stranded DNA. UV-vis characterizations were performed on a Beckmann DU 7400 spectrophotometer. Radiolabeled $[\text{}^{32}\text{P}]\text{-ATP}$ was purchased from MP Biomedicals (Santa Ana, CA).

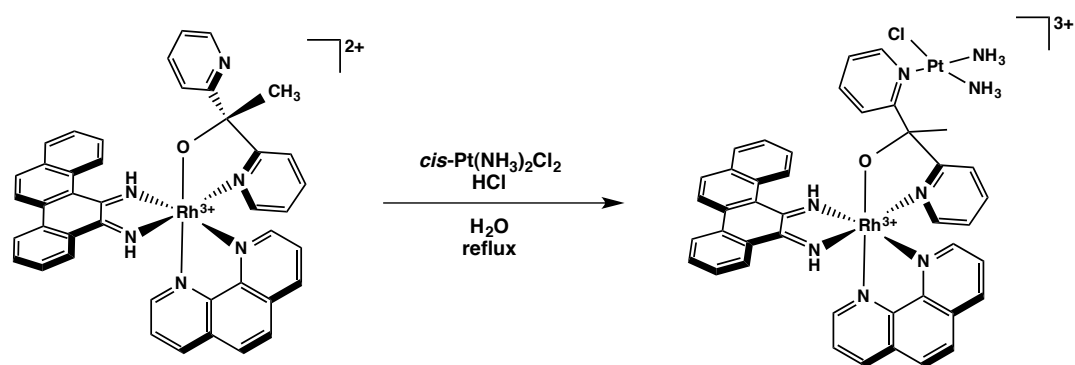
The syntheses of chrysene-5,6-dione (chrysi), 1,1-di(pyridin-2-yl)ethanol (DPE), and $[\text{Rh}(\text{chrysi})(\text{phen})(\text{DPE})]^{2+}$ were carried out according to published procedures.^{22,28,29}

4.2.2 Synthesis of $[\text{Rh}(\text{chrysi})(\text{phen})(\text{DPE-Pt}(\text{NH}_3)_2\text{Cl})]^{3+}$ (Scheme 4.1)

A 250 ml round bottomed flask was charged with [Rh(chrysi)(phen)(DPE)]TFA₂ (272 mg, 0.28 mmol) (prepared according to literature procedures) and cisplatin (305 mg, 1 mmol, 3.57 equiv) in 100 ml H₂O. One drop of concentrated HCl was added, and the solution was stirred at reflux for an additional 48 h. The reaction was hot-filtered through a medium glass frit and purified by reverse-phase HPLC (85:15:0.1 to 40:60:0.1 H₂O/MeCN/TFA gradient). Fractions were pooled and dried *in vacuo* to afford the bimetallic product as a red-brown solid. To obtain the complex as the chloride salt, [Rh(DPE)Pt]TFA₃ was redissolved in 50 mM HCl_(aq) and freeze-dried under high vacuum. This process was repeated three times until the TFA counterion was eliminated. Yield: 60 mg (16% by HPLC). ¹H NMR (500 MHz, D₂O): δ 9.39 (d, *J* = 5.3 Hz, 1H), 8.95 (d, *J* = 8.0 Hz, 1H), 8.90 (d, *J* = 6.7 Hz, 2H), 8.87 – 8.68 (m, 1H), 8.49 – 8.35 (m, 1H), 8.34 – 8.27 (m, 1H), 8.24 – 8.18 (m, 1H), 8.14 – 8.11 (m, 1H), 8.07 (d, *J* = 10.3 Hz, 1H), 8.03 (s, 1H), 8.00 (d, *J* = 6.7 Hz, 2H), 7.96 (d, *J* = 8.0 Hz, 2H), 7.90 (d, *J* = 7.9 Hz, 1H), 7.81 (s, 1H), 7.72 (d, *J* = 7.5 Hz, 1H) 7.68 – 7.60 (m, 1H), 7.57 (s, 1H), 7.52 (t, *J* = 7.5 Hz, 1H), 7.41 (s, 2H), 7.32 (d, *J* = 6.8 Hz, 2H), 7.27 – 7.17 (m, 1H), 7.00 (d, *J* = 7.8 Hz, 1H), 3.66 – 3.59 (m, 3H), 3.54 (dd, *J* = 5.6, 3.5 Hz, 3H), 2.95 (s, 3H). ESI-MS (cation, **Figure 4.2**): *m/z* calc 1003.251, obs. 1001.8 (M – 2H⁺). UV-vis (H₂O, pH 7.0): 270 nm (134,700 M⁻¹ cm⁻¹), 303 nm (72,400 M⁻¹ cm⁻¹), 442 nm (19,200 M⁻¹ cm⁻¹), 581 nm (10,600 M⁻¹ cm⁻¹).

4.2.3 Photocleavage Competition Titrations

A single-stranded DNA oligomer with the sequence 5*'-TTAGGATCATCCCATATA-3' (underline denotes the mismatch, asterisk denotes the radiolabel) was labeled at the 5'-end with [³²P]-ATP as described in **Section 4.2.3** and



Scheme 4.1 Synthesis of $[\text{Rh}(\text{chrysi})(\text{phen})(\text{DPE-Pt}(\text{NH}_3)_2\text{Cl})]^{3+}$

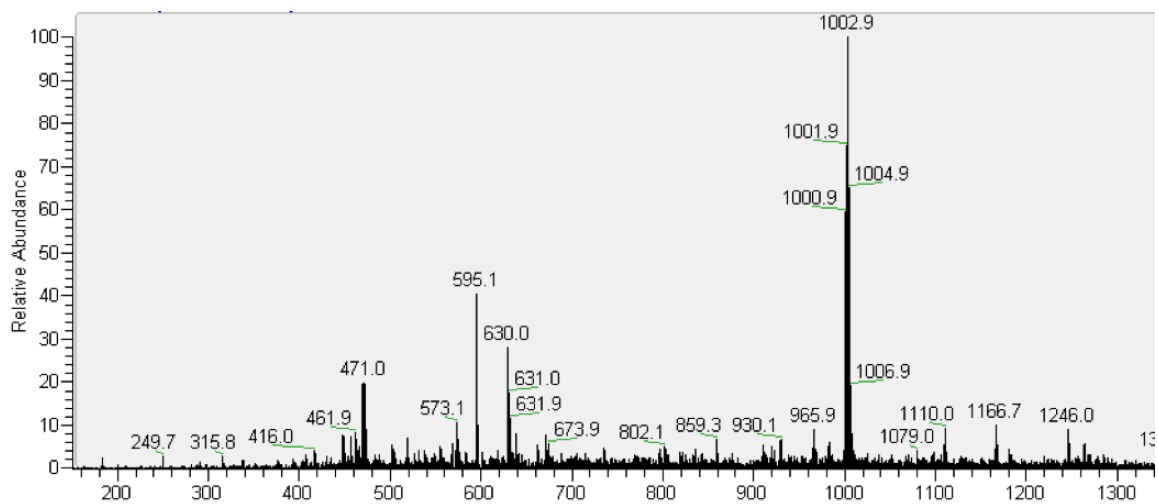


Figure 4.2 ESI-MS spectrum of $[\text{Rh}(\text{chrysi})(\text{phen})(\text{DPE-Pt}(\text{NH}_3)_2\text{Cl})]^{3+}$; $m/z = 1000.9$ – 1006.9 (indicative of the Rh and Pt isotope patterns), calc 1003.251.

annealed with a complement containing a CC mismatch at the position indicated. Racemic solutions of $[\text{Rh}(\text{chrysi})(\text{phen})(\text{DPE-Pt}(\text{NH}_3)_2\text{Cl})]^{3+}$ were prepared in Milli-Q water over a range of concentrations (100 nM – 50 μM). For each sample, 4 μM *rac*- $[\text{Rh}(\text{bpy})_2\text{chrysi}]\text{Cl}_3$ (5 μl), which photocleaves DNA at mismatched sites, 2 μM annealed mismatched duplex DNA (10 μl), and the non-photocleaving competitor complex at various concentrations (5 μl) were combined to give 1 μM *rac*- $[\text{Rh}(\text{bpy})_2\text{chrysi}]\text{Cl}_3$, 1 μM duplex DNA, and 75 mM $\text{NaCl}_{(\text{aq})}$ as the final concentrations. Samples were irradiated on an Oriel (Darmstadt, Germany) 1000-W Hg/Xe solar simulator (340-440 nm) for 15 min, incubated at 37 °C for 10 min, and dried *in vacuo*. The irradiated samples were electrophoresed on a 20% denaturing polyacrylamide gel and exposed to a phosphor screen. The amounts of DNA in each band were analyzed by autoradiography and quantitated by phosphorimagery (ImageQuant).

4.2.4 Binding Constant Determination

As the $[\text{Rh}(\text{chrysi})(\text{phen})(\text{DPE-Pt}(\text{NH}_3)_2\text{Cl})]^{3+}$ complex does not photocleave DNA upon irradiation, the binding affinity for a CC mismatch was determined *via* a competition titration against *rac*- $[\text{Rh}(\text{bpy})_2\text{chrysi}]^{3+}$, which does photocleave DNA at mismatched sites. To assess the binding of the rhodium subunit of $[\text{Rh}(\text{chrysi})(\text{phen})(\text{DPE-Pt}(\text{NH}_3)_2\text{Cl})]^{3+}$ at the CC mismatch, the fraction of cleaved DNA was quantified and expressed as a percentage of the total DNA in each lane and plotted against the log of the concentration of $[\text{Rh}(\text{chrysi})(\text{phen})(\text{DPE-Pt}(\text{NH}_3)_2\text{Cl})]^{3+}$. The data from three independent titration experiments were each fit to a sigmoidal curve using OriginPro 8.5. The concentration of rhodium at the inflection point at the curve ($[\text{Rh}_{50\%}]$) was then used to solve simultaneous equilibria involving DNA, $[\text{Rh}(\text{bpy})_2\text{chrysi}]\text{Cl}_3$, and

$[\text{Rh}(\text{chrysi})(\text{phen})(\text{DPE-Pt}(\text{NH}_3)_2\text{Cl})]^{3+}$ in Mathematica 8.0 to obtain the binding constant (K_B).

DNA platination was analyzed in a similar manner, wherein the fraction of platinated DNA was quantified and expressed as a percentage of the total DNA in each lane

4.2.5 Platinum Binding to Mismatched and Well-Matched Duplex DNA

A single-stranded DNA oligomer with the sequence 5*'-TTAGGATCATCCATATA-3' (underline denotes the mismatch, asterisk denotes the radiolabel) was labeled at the 5'-end with [^{32}P]-ATP and polynucleotide kinase (PNK) at 37 °C for 2 h. The radiolabeled DNA was purified by gel electrophoresis and annealed to either its mismatched complement (containing a CC mismatch) or a fully matched complement strand by heating to 90 °C in buffer (100 mM NaCl, 20 mM NaP_i, pH 7.1), followed by slow cooling to ambient temperature over 2 h, to give a final concentration of 2 μM duplex DNA. Racemic solutions of $[\text{Rh}(\text{chrysi})(\text{phen})(\text{DPE-Pt}(\text{NH}_3)_2\text{Cl})]^{3+}$ were prepared in 50 mM NaCl_(aq) over a range of concentrations (100 nM – 5 μM). For each sample, 2 μM annealed mismatched duplex DNA (10 μl) was mixed with $[\text{Rh}(\text{chrysi})(\text{phen})(\text{DPE-Pt}(\text{NH}_3)_2\text{Cl})]^{3+}$ at various concentrations (10 μl) to give 1 μM duplex DNA and 75 mM NaCl_(aq) as the final concentrations. A “light” control, (ØRh, ØPt) consisting of 2 μM DNA mixed with 10 μl Milli-Q water, and a “dark” control (Ø *hv*), containing the DNA mixed with the highest concentration of competitor complex without irradiation, were also prepared. The samples were incubated at 37 °C for periods of 1, 3, or 18h to promote the formation of the platinated DNA adducts. After the incubation period, samples were quenched with 50 μl of 0.1 M NaCl_(aq) and cooled to 4

°C for 30 min. Except for the dark controls, samples were irradiated on an Oriol (Darmstadt, Germany) 1000-W Hg/Xe solar simulator (340-440 nm) for 15 min and dried *in vacuo*. The irradiated samples were electrophoresed on a 20% denaturing polyacrylamide gel and exposed to a phosphor screen. The amounts of DNA in each band were analyzed by autoradiography and quantitated by phosphorimager (ImageQuant).

4.2.6 Dimethyl Sulfate Footprinting of Platinated DNA

DNA footprinting of guanine by dimethyl sulfate (DMS) was carried out according to literature procedures.³⁰ Briefly, single stranded DNA with the sequence 5'-TTAGGATCATCCCATATA-3' (underline denotes the mismatch) was labeled at the 5'-end with [³²P]-ATP and annealed with its CC mismatched complement as described above. A solution of 1 μM annealed DNA was platinated with either [Rh(chrysi)(phen)(DPE-Pt(NH₃)₂Cl)]³⁺ (1 or 5 μM) or cisplatin (1 μM) by incubation at 37 °C for 90 min. The platination reaction was quenched via addition of 0.1 M NaCl_(aq) followed by cooling to 4 °C for 30 min. Samples were purified by ethanol precipitation and dried *in vacuo*. The samples were taken up in 5 μl Milli-Q water, diluted with DMS buffer (50 mM sodium cacodylate, 1 mM EDTA, pH 7.5), and 2 mM calf-thymus DNA (4 μl) was added as a carrier DNA. Samples were cooled to 0 °C and treated with 5 μl DMS (10% v/v in EtOH, prepared immediately before use) for 5 min at 25 °C. The reaction was quenched *via* addition of the DMS stop solution (1.5 M NaOAc, 1 M β-mercaptoethanol, 250 μg/ml yeast tRNA) at 0 °C. Following ethanol precipitation of the DNA, samples were treated with 10% aqueous piperidine and heated to 90 °C for 30 min. The piperidine was removed *in vacuo*, and samples were electrophoresed on a 20% denaturing polyacrylamide gel and exposed to a phosphor screen. The amounts of DNA

in each band were analyzed by autoradiography and quantitated by phosphorimager (ImageQuant).

4.2.7 Cell Culture

4.2.7.1 HCT116N/O. HCT116N (MMR-proficient) and HCT116O (MMR-deficient) cells were grown in RPMI medium 1640 supplemented with 10% fetal bovine serum, 400 µg/ml Geneticin (G418), 2 mM L-glutamine, 0.1 mM nonessential amino acids, 1 mM sodium pyruvate, 100 units/ml penicillin, and 100 µg/ml streptomycin. Cells were grown in tissue culture flasks (Corning Costar, Acton, MA) at 37 °C under a humidified atmosphere (5% CO₂).

4.2.7.2 A2780cis. A2780cis cells (Sigma-Aldrich Co.) were grown in RPMI medium 1640 supplemented with 10% fetal bovine serum, 200 mM L-glutamine, 100 units/ml penicillin, and 100 µg/ml streptomycin. To retain resistance, cisplatin was added to the media every 2-3 passages to a final concentration of 1 µM. Cells were grown in tissue culture flasks (Corning Costar, Acton, MA) at 37 °C under a humidified atmosphere (5% CO₂).

4.2.8 MTT Cytotoxicity Assay

The cytotoxic effects of conjugate $[\text{Rh}(\text{chrysi})(\text{phen})(\text{DPE-Pt}(\text{NH}_3)_2\text{Cl})]^{3+}$, $[\text{Rh}(\text{chrysi})(\text{phen})(\text{DPE})]^{2+}$, and cisplatin were studied *via* MTT (3-(4,5-dimethylthiazol-2-yl)-2,5-diphenyltetrazolium bromide) assay in the cisplatin-resistant A2780cis, MMR-proficient HCT116N, and MMR-deficient HCT116O cell lines.³¹ For biological experiments, $[\text{Rh}(\text{chrysi})(\text{phen})(\text{DPE-Pt}(\text{NH}_3)_2\text{Cl})]^{3+}$ and cisplatin were prepared in saline solution (20 mM NaCl), and $[\text{Rh}(\text{chrysi})(\text{phen})(\text{DPE})]^{2+}$ was dissolved in deionized water. Cells were plated in 96-well plates at 50,000 cells/well and incubated with varying

concentrations of metal complex for 72h under humidified atmosphere. After the incubation period, MTT was added, and the cells were incubated for an additional 4 h. The resulting formazan crystals were solubilized over a period of 24 h at 37 °C, 5% CO₂. Formazan formation was quantified *via* electronic absorption at 550-600 nm with a reference wavelength of 690 nm. Cell viability is expressed as a function of formazan formation and normalized to that of untreated cells. Standard errors were calculated from 5 replicates.

4.2.9 MTT Caspase and PARP Inhibition Assays

The cytotoxic effects of conjugate $[\text{Rh}(\text{chrysi})(\text{phen})(\text{DPE-Pt}(\text{NH}_3)_2\text{Cl})]^{3+}$ and cisplatin were studied *via* MTT (3-(4,5-dimethylthiazol-2-yl)-2,5-diphenyltetrazolium bromide) assay in the HCT116O and HCT116N cell lines. Cells were plated in 96-well plates at 50,000 cells/well and incubated with 0 or 5 μM of metal complex. For caspase-inhibition assays, Z-VAD-FMK was added to a final concentration of 35 μM . For poly-ADP ribose polymerase (PARP) assays, the inhibitor 3,4-dihydro-5[4-(1-piperidinyloxy)butoxy]-1(2*H*)-isoquinoline (DPQ) was added to a final concentration of 50 μM . Controls wherein cells were treated with inhibitor alone in the absence of metal complex were included. Cells were incubated under humidified atmosphere for 72 h and labeled with MTT for an additional 4 h at 37 °C, 5% CO₂. The ensuing formazan crystals were dissolved with a lysis buffer (10% SDS in 10 mM HCl) according to the manufacturer's instructions. MTT reduction to formazan was quantified by electronic absorption at 570 nm (background: 690 nm), and percent viability was expressed as the amount of formazan in treated cells compared to that of the untreated controls.

4.3 Results

4.3.1 DNA Binding Studies

The rhodium mismatch recognition and covalent platinum binding of DNA were analyzed with mismatched and well-matched DNA oligomers with the sequence on 20% denaturing PAGE gels. Although mismatch recognition and platinum adduct formation can be visualized simultaneously under the same conditions (**Figure 4.3**), platinum binding is optimally observed under saline conditions (75-100 mM NaCl_(aq)). While this affords thermodynamic control over the DNA platination reaction, thereby enhancing selective platination of mismatched DNA, high salt concentrations make quantification of photocleavage at the mismatched site challenging. As a result, metalloinsertion at the mismatch was analyzed separately from platination of mismatched and well-matched DNA, under aqueous conditions.

4.3.1.1 Binding Affinity of Rhodium at a CC Mismatch

In vitro DNA binding studies were performed with racemic aqueous solutions of [Rh(chrysi)(phen)(DPE-Pt(NH₃)₂Cl)]³⁺ and radiolabeled hairpin DNA containing a CC mismatch with the sequence 5*'-GGCAGGCATGGCTTTTGGCCATCCCCTGCC-3' (underline denotes the mismatch; asterisk denotes the radiolabel) Single-stranded DNA was labeled at the 5'-end with [³²P]-ATP and polynucleotide kinase (PNK) at 37 °C for 2h as described above. The conjugate was bound with mismatched hairpin DNA at varying concentrations and irradiated (340-440 nm) for 15 min. Samples were then incubated at 37 °C for 10 min and electrophoresed on a 20% denaturing PAGE gel. As [Rh(chrysi)(phen)(DPE-Pt(NH₃)₂Cl)]³⁺ does not cleave DNA upon irradiation, a competition titration was carried out using [Rh(bpy)₂chrysi]³⁺, which does photocleave DNA at the site of a mismatch.¹⁰ The conjugate inhibits photocleavage by *rac*-

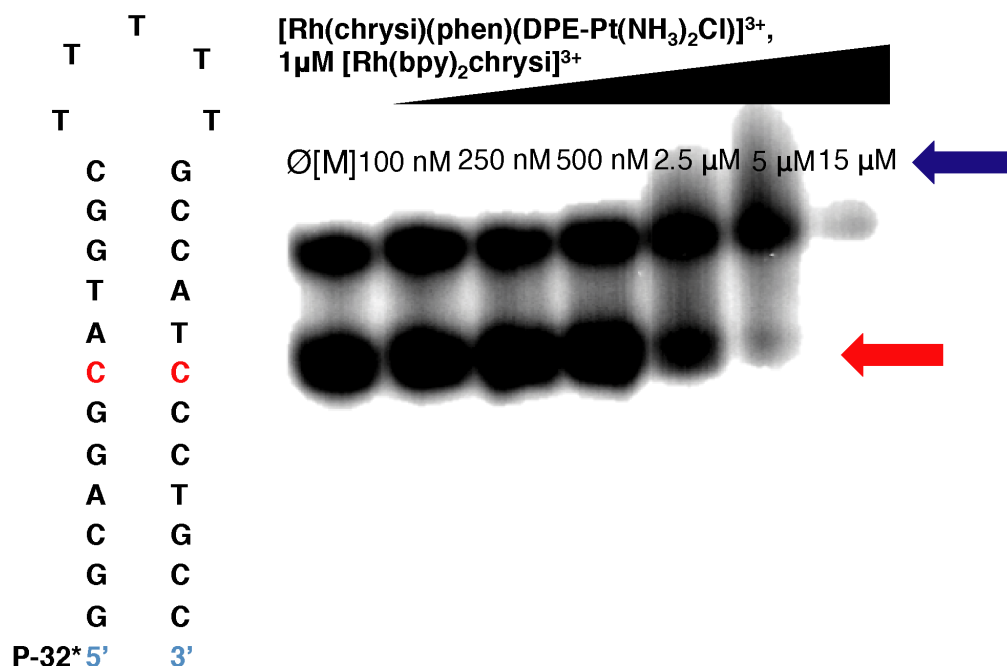


Figure 4.3 Competition titration of increasing concentrations of $[\text{Rh}(\text{chrysi})(\text{phen})(\text{DPE-Pt}(\text{NH}_3)_2\text{Cl})]^{3+}$ (0-15 μM) with 1 μM *rac*- $[\text{Rh}(\text{bpy})_2\text{chrysi}]^{3+}$ on 1 μM 5'- ^{32}P labeled 29mer hairpin DNA of the sequence indicated containing a CC mismatch (denoted in red). Samples were irradiated (340-440 nm) for 15 min and electrophoresed on a 20% denaturing polyacrylamide gel. Controls without Rh were included (\emptyset [M]). $[\text{Rh}(\text{chrysi})(\text{phen})(\text{DPE-Pt}(\text{NH}_3)_2\text{Cl})]^{3+}$ inhibits photocleavage by $[\text{Rh}(\text{bpy})_2\text{chrysi}]^{3+}$ at the mismatched site. The site of photocleavage by $[\text{Rh}(\text{bpy})_2\text{chrysi}]^{3+}$ at the mismatch is indicated by a red arrow at bands located below the unmodified parent band. Bands of reduced electrophoretic mobility, located above the unmodified parent DNA and indicated by a blue arrow, are indicative of covalent binding by the platinum subunit.

[Rh(bpy)₂chrysi]³⁺ at the mismatched site in a dose-dependent manner (**Figure 4.3**); this indicates that the complex binds specifically to the mismatch *via* metalloinsertion. Experimental conditions were carried out to minimize platinum adduct formation, thus limiting interference of covalent platinum binding on the equilibrium binding constant of the rhodium subunit at the mismatch. Nevertheless, some platinum binding is observed to occur simultaneously with mismatch binding, as indicated by the presence of slowly migrating bands located above the unmodified parent band. This result suggests that the complex is capable of binding mismatched DNA bifunctionally, through simultaneous metalloinsertion at the mismatched site as well as the formation of covalent platinum crosslinks. The amount of photocleaved DNA was quantified and plotted against the logarithmic concentration of the complex (log[RhPt]), and the K_B value of RhPt was calculated by solving simultaneous equilibria at the inflection point of the titration curve (**Figure 4.4**). The binding affinity of RhPt for a CC mismatch was determined to be $4.8 \times 10^6 \text{ M}^{-1}$, comparable to that of monomeric metalloinsertors.^{20,22,23}

4.3.1.2 Platination of Mismatched and Well-Matched DNA

The formation of platinum-DNA crosslinks was analyzed *in vitro* via gel electrophoresis. Dissociation of the labile chloride ligand from the platinum center in solution enables the formation of covalent platinum adducts with DNA. The reaction between the conjugate and mismatched (CC) and well-matched duplex DNA oligomers was analyzed as a function of incubation time at 37 °C as well as complex concentration.

A time-course experiment was used to explore the formation of Pt-DNA adducts with radiolabeled duplex DNA of the sequence 5*'-TTAGGATCATCCATATA-3' (underline denotes the site of a CC mismatch, asterisk denotes the radiolabel) annealed

with either its mismatched or fully matched complement strands. Racemic mixtures of $[\text{Rh}(\text{chrysi})(\text{phen})(\text{DPE-Pt}(\text{NH}_3)_2\text{Cl})]^{3+}$ (1 μM) and mismatched or well-matched DNA (1 μM) were incubated in buffer (75 mM NaCl, 10 mM NaP_i, pH 7.1) at 37 °C for periods of either 1, 3, or 18 h. After the incubation period, samples were quenched with 0.1 M NaCl_(aq), cooled to 4 °C, and electrophoresed on a 20% denaturing PAGE gel. Platination of the DNA is indicated by the appearance of bands with reduced electrophoretic mobility, located above the unmodified parent bands in the autoradiogram.

The resulting autoradiogram is shown in **Figure 4.5**. The $[\text{Rh}(\text{chrysi})(\text{phen})(\text{DPE-Pt}(\text{NH}_3)_2\text{Cl})]^{3+}$ conjugate exhibits a clear preference for mismatched DNA over fully matched oligomers after 1 and 3 hr incubation periods. The 18h incubations resulted in complete degradation of the DNA, and the bands could not be observed above background.

The amount of platinated DNA was quantified as a fraction of the total DNA in each sample (**Figure 4.6**). At incubation periods of 1 and 3 hours, platination of mismatched DNA over well-matched is enhanced by 20% and 17%, respectively. At 1h, 61% of mismatched DNA contains covalent platinum adducts, compared to 41% of fully matched DNA. Longer incubation (3h) results in a slight decrease in the differential platination of mismatched over well-matched DNA (56% versus 39%, respectively). Samples incubated for 18 h were not quantified.

DNA platination was also analyzed in a dose-dependent manner, as can be seen in **Figure 4.7**. Racemic mixtures of $[\text{Rh}(\text{chrysi})(\text{phen})(\text{DPE-Pt}(\text{NH}_3)_2\text{Cl})]^{3+}$ (0.1 – 5 μM) and mismatched or well-matched DNA (1 μM) were incubated at 37 °C for 2h and

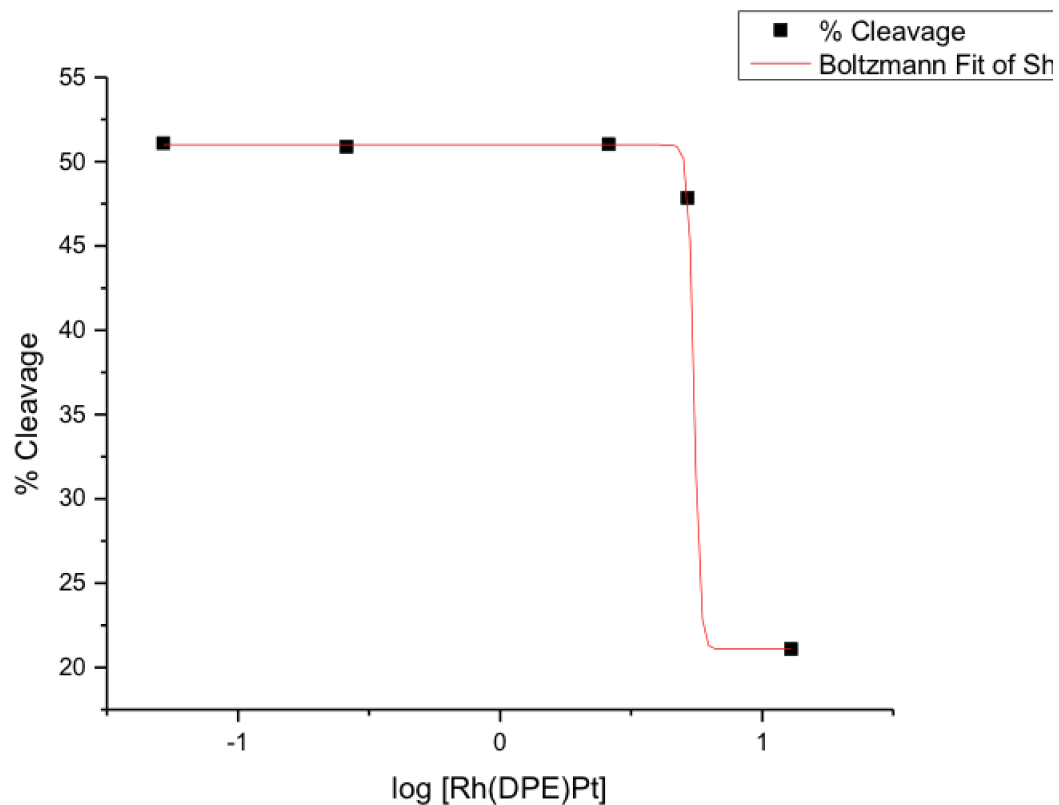


Figure 4.4 Representative sigmoidal curve (Boltzmann fit) of photocleavage competition titrations of $[\text{Rh}(\text{chrysi})(\text{phen})(\text{DPE-Pt}(\text{NH}_3)_2\text{Cl})]^{3+}$ for binding constant determination at the CC mismatch. K_B was calculated by solving simultaneous equilibria at the inflection point of the curve. Experiments were conducted in buffer (50 mM NaCl, 10 mM NaP_i, pH 7.1) using 1 μM hairpin DNA and 1 μM $\text{rac-}[\text{Rh}(\text{bpy})_2\text{chrysi}]^{3+}$, with 0-15 μM $[\text{Rh}(\text{chrysi})(\text{phen})(\text{DPE-Pt}(\text{NH}_3)_2\text{Cl})]^{3+}$ competitor complex.

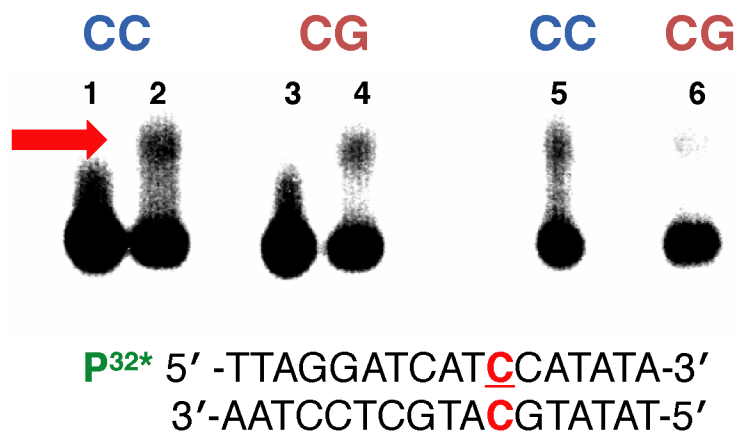


Figure 4.5 Autoradiogram depicting the formation of covalent platinum adducts with mismatched and well-matched DNA duplexes ($1 \mu\text{M}$) as a function of time. $[\text{Rh}(\text{chrysi})(\text{phen})(\text{DPE-Pt}(\text{NH}_3)_2\text{Cl})]^{3+}$ ($1 \mu\text{M}$) was incubated with 5' end radiolabeled duplex DNA of the sequence indicated (bottom; the site of the CC mismatch is denoted in red) as well as the corresponding well-matched duplex in buffer (75 mM NaCl , 10 mM NaP_i , $\text{pH } 7.1$) at $37 \text{ }^\circ\text{C}$ for 1, 3, or 18h. Samples were irradiated for 15 min and electrophoresed on a 20% denaturing PAGE gel. Platinum crosslinking of DNA is indicated by the appearance of slow-moving bands located above the unmodified parent DNA; platinated DNA is denoted by a red arrow. Lanes: (1) untreated duplex DNA containing a CC mismatch; (2) mismatched DNA incubated with metal complex for 1h; (3) untreated well-matched DNA; (4) well-matched DNA incubated with metal complex for 1h; (5) mismatched DNA treated with metal complex for 3h; (6) well-matched DNA treated with metal complex for 3h. Samples treated with metal complex for 18h were degraded on the gel and are not visible in the autoradiogram.

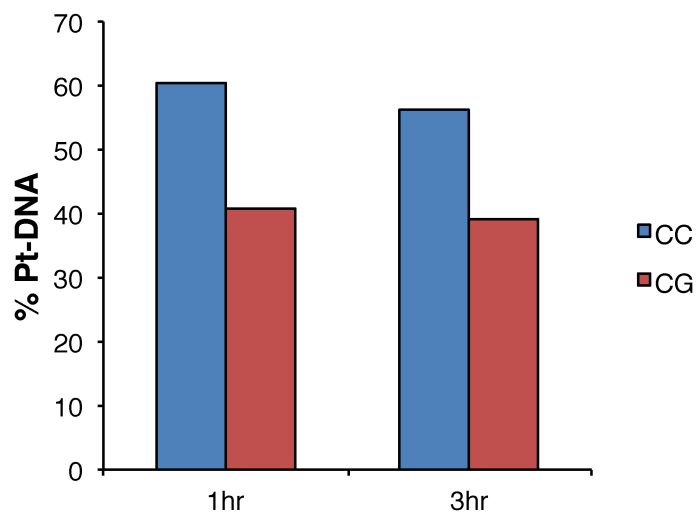


Figure 4.6 Quantification of platinumation of mismatched (CC, blue) and well-matched (CG, red) duplex DNA ($1 \mu\text{M}$) by $[\text{Rh}(\text{chrysi})(\text{phen})(\text{DPE-Pt}(\text{NH}_3)_2\text{Cl})]^{3+}$ ($1 \mu\text{M}$). Samples were incubated at 37°C for 1, 3, or 18h and electrophoresed on a 20% denaturing PAGE gel. The amount of platinumated DNA (% Pt-DNA) is expressed as a fraction of the total DNA in each sample. Samples heated for 18h were degraded and not quantified.

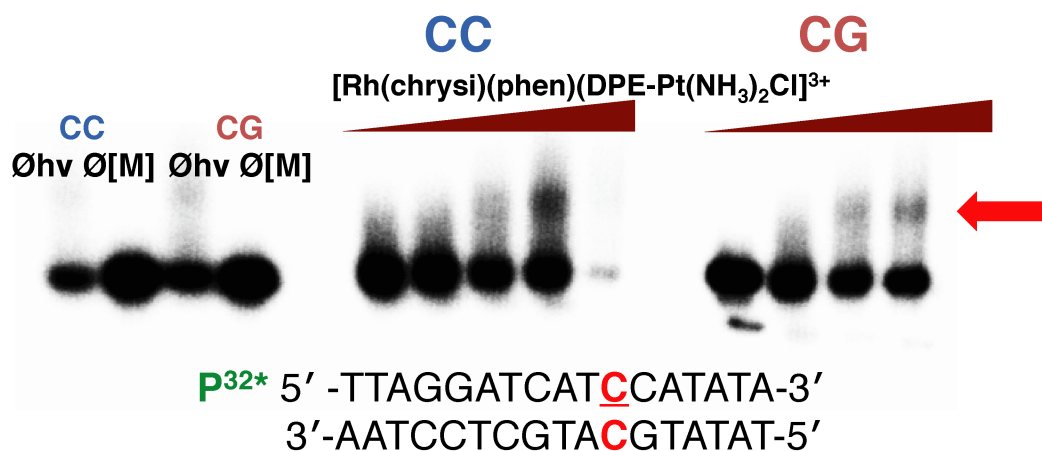


Figure 4.7 Autoradiogram depicting the formation of covalent platinum adducts with mismatched and well-matched DNA duplexes (1 μM) as a function of metalloinsertor concentration. $[\text{Rh}(\text{chrysi})(\text{phen})(\text{DPE-Pt}(\text{NH}_3)_2\text{Cl})]^{3+}$ (100 nM – 5 μM) was incubated with 5' end radiolabeled duplex DNA of the sequence indicated (bottom; the site of the CC mismatch is denoted in red) as well as the corresponding well-matched duplex in buffer (75 mM NaCl, 10 mM NaP_i, pH 7.1) at 37 °C for 2h. Samples were irradiated for 15 min and electrophoresed on a 20% denaturing PAGE gel. Controls without irradiation ($\emptyset hv$) and without metal complex ($\emptyset [M]$) were included for each type of DNA (mismatched DNA is denoted by “CC” in blue; well-matched DNA is denoted by “CG” in red) and are depicted on the left. Platinum crosslinking of DNA is indicated by the appearance of slow-moving bands located above the unmodified parent DNA; platinated DNA is denoted by a red arrow. Platination of mismatched DNA is shown in the center (denoted by “CC” in blue, and platination of well-matched DNA is shown on the right (denoted by “CG” in red).

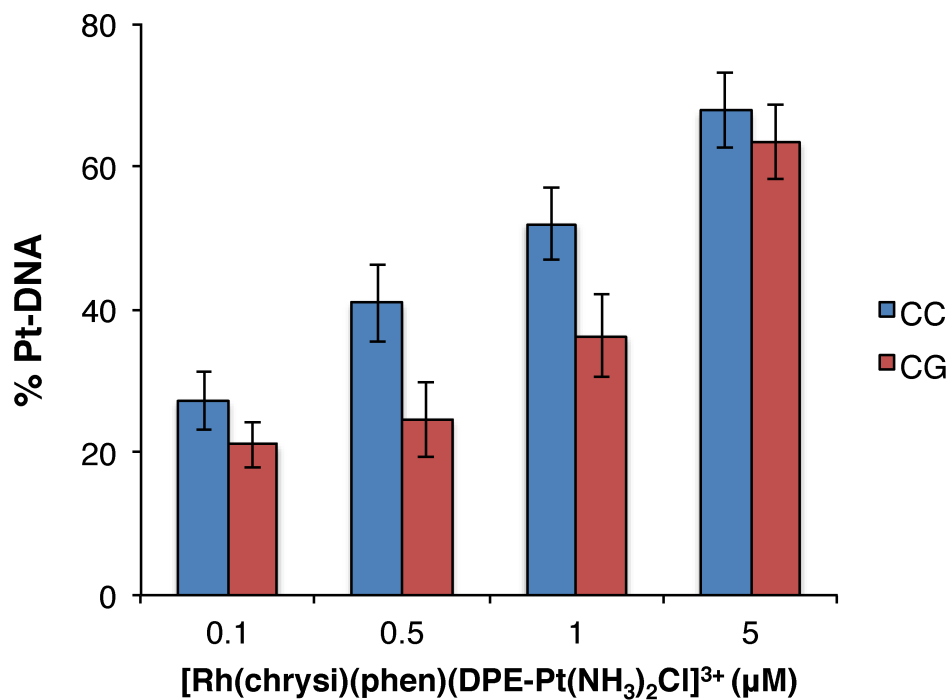


Figure 4.8 Quantification of platinumation of mismatched (CC, blue) and well-matched (CG, red) duplex DNA (1 μM) by [Rh(chrysi)(phen)(DPE-Pt(NH₃)₂Cl)]³⁺ (0.1 – 5 μM). Samples were incubated at 37 °C for 2h and electrophoresed on a 20% denaturing PAGE gel. The amount of platinumated DNA (% Pt-DNA) is expressed as a fraction of the total DNA in each sample.

electrophoresed on a 20% denaturing polyacrylamide gel. The platinum-DNA bands were quantified by autoradiography, shown in **Figure 4.8**, revealing a preference for mismatched DNA at low concentrations (0.1 – 1 μM) of conjugate. At 500 nM $[\text{Rh}(\text{chrysi})(\text{phen})(\text{DPE-Pt}(\text{NH}_3)_2\text{Cl})]^{3+}$, $41 \pm 5.4\%$ of mismatched duplex contains platinum adducts versus $25 \pm 5.3\%$ of well-matched DNA. Optimal selectivity is achieved at stoichiometric Pt:DNA (1 μM), with $52 \pm 5.1\%$ platinated mismatched DNA versus $36 \pm 5.7\%$ ($p < 0.05$ by unpaired two-tailed t test). Unsurprisingly, this differential platinum binding diminishes at high concentrations of the complex, and mismatched and well-matched DNA is platinated equally; 72% and 70% platination of mismatched and well-matched DNA is observed, respectively. It would appear as though the formation of platinum crosslinks is guided at least in part by mismatch recognition by the rhodium subunit.

4.3.1.3 Dimethyl Sulfate Footprinting of Pt-DNA Crosslinks

To probe the potential site of platinum adduct formation, dimethyl sulfate (DMS) footprinting was carried out for platinated mismatched and well-matched DNA duplexes. Typically, the preferential binding site of platinum is the $N7$ position of guanine; DMS methylation at guanine $N7$ induces cleavage of the DNA at these residues.³⁰ The degree of DMS-induced guanine cleavage indicates whether platinum is coordinated. Uncoordinated guanines will incur relatively high levels of cleavage upon DMS treatment, while platinated sites will be protected. Duplex DNA (1 μM) containing a single CC mismatch, as well as a similarly well-matched sequence (see **Section 4.3.1.2** for sequence) was radiolabeled at the 5'-end with $[^{32}\text{P}]$ and incubated with either cisplatin (1 μM) or $[\text{Rh}(\text{chrysi})(\text{phen})(\text{DPE-Pt}(\text{NH}_3)_2\text{Cl})]^{3+}$ (1 or 5 μM) for 90 min at 37 °C to

promote the formation of Pt-DNA adducts; untreated controls of mismatched and well-matched DNA were also included. The DNA was then purified and subjected to treatment with 10% DMS, followed by cleavage by piperidine (1 M) and denaturing gel electrophoresis (20% polyacrylamide).

The resulting autoradiogram is shown in **Figure 4.9**. The cleavage products of the two guanine residues in the radiolabeled strand are indicated by bands of high electrophoretic mobility located below the unmodified parent bands. For both mismatched and well-matched DNA, treatment with $[\text{Rh}(\text{chrysi})(\text{phen})(\text{DPE-Pt}(\text{NH}_3)_2\text{Cl})]^{3+}$ conjugate does not confer protection of the guanine residues from DMS methylation and cleavage. In fact, a marked *increase* in guanine cleavage product is observed with conjugate-bound DNA at both 1 and 5 μM treatment, compared to untreated and cisplatin-treated DNA. Furthermore, this increase is observed for both guanine residues, which occur consecutively in the sequence. However, the conjugate clearly forms covalent adducts, as is indicated by the presence of slow-migrating bands located above the unmodified parent bands. The $[\text{Rh}(\text{chrysi})(\text{phen})(\text{DPE-Pt}(\text{NH}_3)_2\text{Cl})]^{3+}$ complex does not coordinate at the expected guanine sites; rather, the alternative platinum binding site likely results in a conformational change to the DNA that enhances the accessibility of both guanine residues to methylation by DMS.

4.3.2 MTT Cytotoxicity Assay

The cytotoxic effects of $[\text{Rh}(\text{chrysi})(\text{phen})(\text{DPE-Pt}(\text{NH}_3)_2\text{Cl})]^{3+}$ were probed via MTT cytotoxicity assay (MTT = (3-(4,5-dimethylthiazol-2-yl)-2,5-diphenyltetrazolium

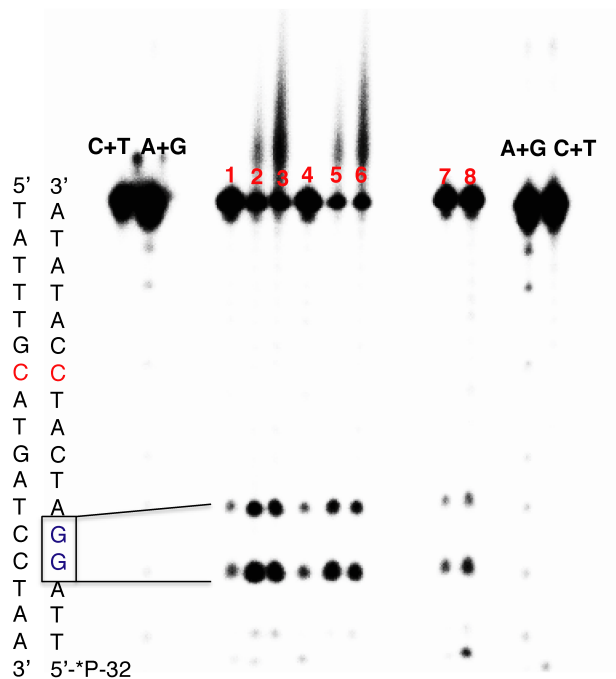


Figure 4.9 Dimethyl sulfate (DMS) footprinting of 5'-end radiolabeled duplex DNA containing a CC mismatch (denoted in red) and a d(GpG) site (denoted in blue, boxed). Samples were incubated with platinum and treated with 10% DMS, followed by piperidine cleavage. Samples were electrophoresed on a 20% denaturing PAGE gel. Lanes: (1) CC-mismatched DNA in the absence of platinum; (2) mismatched DNA with 1 μ M conjugate; (3) mismatched DNA with 5 μ M conjugate; (4) well-matched DNA in the absence of platinum; (5) well-matched DNA with 1 μ M conjugate; (6) well-matched DNA with 5 μ M conjugate; (7) mismatched DNA with 1 μ M cisplatin; (8) well-matched DNA with 1 μ M cisplatin; Maxam-Gilbert sequencing lanes (C+T; A+G) are located on the far left and far right of the gel. Bands of high electrophoretic mobility below the unmodified parent bands represent sites of guanine cleavage.

bromide). Metabolically active cells reduce MTT to formazan, which has a characteristic absorbance at 570 nm. Quantification of formazan by electronic absorption indicates the amount of viable cells in each sample.³¹ The isogenically matched human colorectal carcinoma cell lines HCT116N (MMR-proficient) and HCT116O (MMR-deficient) as well as cisplatin-resistant A2780cis human ovarian cancer cells were plated in 96-well plates at 5.0×10^5 cells/well and treated with varying concentrations of $[\text{Rh}(\text{chrysi})(\text{phen})(\text{DPE-Pt}(\text{NH}_3)_2\text{Cl})]^{3+}$. Cells were also treated with each parent subunit, $[\text{Rh}(\text{chrysi})(\text{phen})(\text{DPE})]^{2+}$ and cisplatin, for 72h under humidified atmosphere. Percent viability is defined as the ratio of the amount of formazan in treated cells to that of untreated cells. The cytotoxic effects of the complexes in the HCT116N and HCT116O cell lines are shown in **Figure 4.10**.

As expected, the $[\text{Rh}(\text{chrysi})(\text{phen})(\text{DPE})]^{2+}$ parent complex displays cell-selective cytotoxicity in the MMR-deficient HCT116O line, with an IC_{50} value of approximately 3.5 μM . Cisplatin exhibits no effect in either cell line, possibly due to being administered from saline solution, to provide an adequate control for the $[\text{Rh}(\text{chrysi})(\text{phen})(\text{DPE-Pt}(\text{NH}_3)_2\text{Cl})]^{3+}$ complex, which is also prepared in aqueous NaCl (20 mM). The conjugate displays intermediary cytotoxic effects compared to its monomeric rhodium and platinum subunits: the cell-selectivity of the rhodium subunit is abolished, as both MMR-proficient and MMR-deficient cell lines are targeted equally. However, the conjugate exhibits enhanced potency compared to its platinum subunit ($\text{IC}_{50} \approx 10 \mu\text{M}$), signifying that conjugation to rhodium does play some role in enhancing the efficacy of the cisplatin parent complex, either through increased cellular uptake or DNA targeting. The potency of $[\text{Rh}(\text{chrysi})(\text{phen})(\text{DPE-Pt}(\text{NH}_3)_2\text{Cl})]^{3+}$ is also

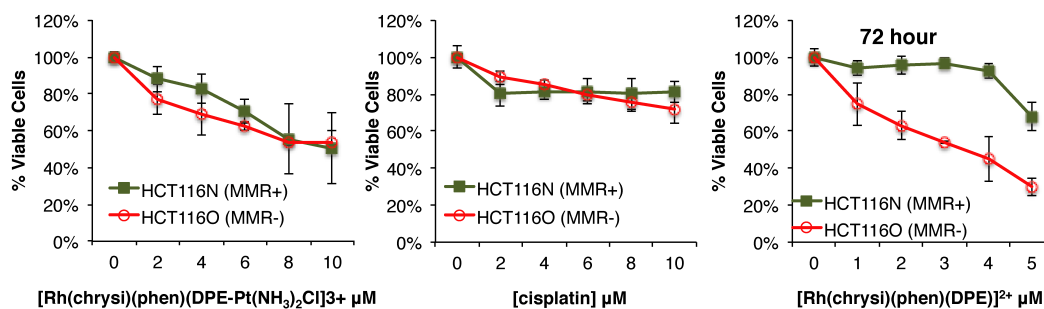


Figure 4.10 MTT cytotoxicity assay of HCT116N (MMR-proficient) and HCT116O (MMR-deficient) cells treated with $[\text{Rh}(\text{chrysi})(\text{phen})(\text{DPE-Pt}(\text{NH}_3)_2\text{Cl})]^{3+}$ (left), cisplatin (center), and $[\text{Rh}(\text{chrysi})(\text{phen})(\text{DPE})]^{2+}$. Cells were incubated with each complex at the concentrations indicated for 72h. After the incubation period, cells were treated with the MTT reagent for 4 h, and the resulting formazan crystals were solubilized with acidified SDS. Percent cell viability is defined as the percentage of formazan normalized to that of untreated cells. Standard errors were calculated from 5 replicates.

comparable to the previous-generation metalloinsertor-oxaliplatin conjugate, which has an IC₅₀ value of 9 μM in the HCT116O cell line.²⁶

The complexes were also examined in the cisplatin-resistant ovarian carcinoma A2780cis cell line (**Figure 4.11**). At 5 μM treatment, [Rh(chrysi)(phen)(DPE-Pt(NH₃)₂Cl)]³⁺ imparts a 19% decrease in cell viability compared to cisplatin (and a 30% decrease in viability compared to untreated cells); however, the conjugate is less potent, albeit by a small margin, than [Rh(chrysi)(phen)(DPE)]²⁺ or both rhodium and platinum subunits added separately.

4.3.3 Caspase and PARP Inhibition Assays

Characterization of a previous metalloinsertor-platinum conjugate revealed that the cytotoxic effects arose not from the necrotic cell death mechanism induced by monomeric metalloinsertors,²¹ but rather through an apoptotic pathway more characteristic of *cis*-platinum complexes.^{26,32,33} Here, we examined whether [Rh(chrysi)(phen)(DPE-Pt(NH₃)₂Cl)]³⁺ also triggers apoptosis, which may account for its lack of cell-selectivity. HCT116N and HCT116O cells were treated with conjugate (5 μM) and poly-ADP ribose polymerase (PARP) inhibitor 3,4-dihydro-5[4-(1-piperindinyl)butoxy]-1(2*H*)-isoquinoline (“DPQ,” 50 μM)³⁴ for 72h, and cell viability was assayed by MTT. Cells were treated similarly with DPQ (50 μM) and cisplatin (5 μM) as a control. The addition of PARP inhibitor DPQ protects cells from necrotic death, as PARP mediates this pathway through severe depletion of cellular ATP.³⁵ As can be seen in **Figure 4.12**, treatment of both cell lines with DPQ alone effects no change in viability. Similarly, DPQ has no effect on the viability of cells treated with [Rh(chrysi)(phen)(DPE-Pt(NH₃)₂Cl)]³⁺. HCT116N cells exhibit 66 ± 2.0% cell viability

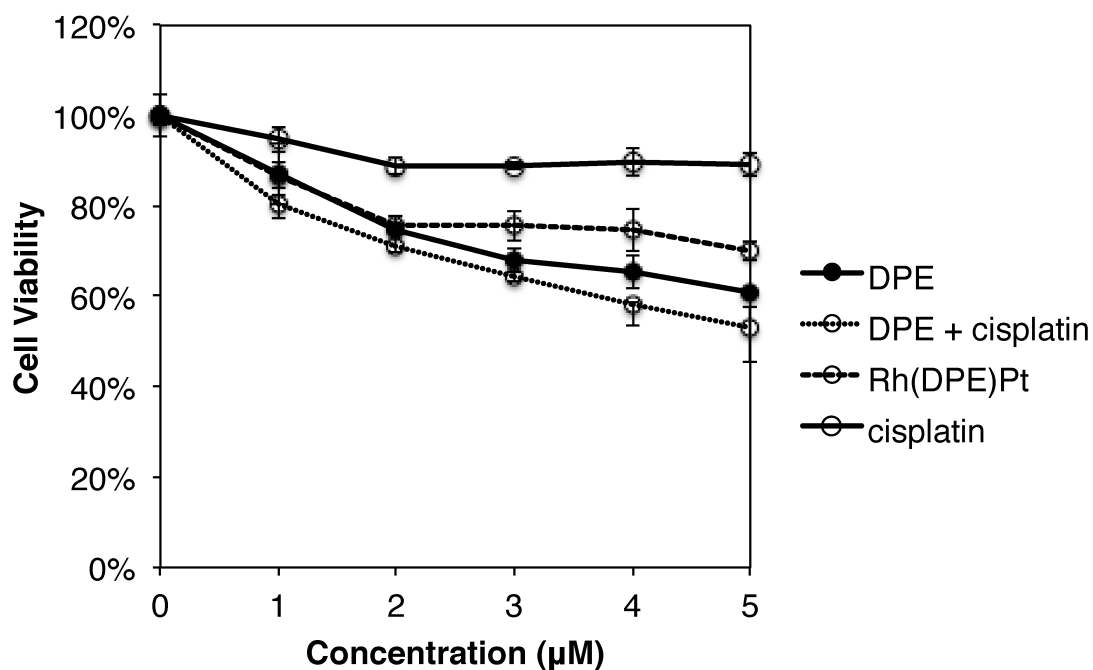


Figure 4.11 MTT cytotoxicity assay of cisplatin-resistant A2780cis cells treated with $[\text{Rh}(\text{chrysi})(\text{phen})(\text{DPE})]^{2+}$ (“DPE,” solid line, closed circles), cisplatin (solid line, open circles), a combination of $[\text{Rh}(\text{chrysi})(\text{phen})(\text{DPE})]^{2+}$ and cisplatin (“DPE + cisplatin,” dotted line, open circles), and $[\text{Rh}(\text{chrysi})(\text{phen})(\text{DPE-Pt}(\text{NH}_3)_2\text{Cl})]^{3+}$ (“Rh(DPE)Pt,” dashed line, open circles). Cells were incubated with each complex at the concentrations indicated for 72h. After the incubation period, cells were treated with the MTT reagent for 4 h, and the resulting formazan crystals were solubilized with acidified SDS. Percent cell viability is defined as the percentage of formazan normalized to that of untreated cells. Standard errors were calculated from 5 replicates.

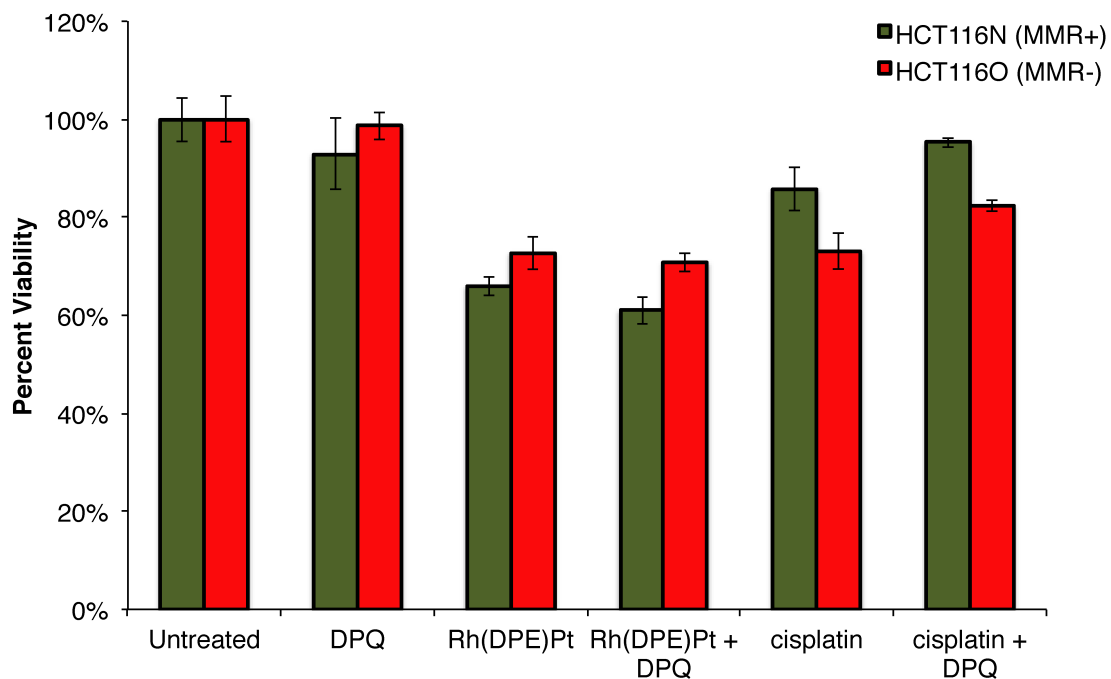


Figure 4.12 Cell viability in HCT116N (green, MMR-proficient) and HCT116O (red, MMR-deficient) cells after 72h treatment with PARP inhibitor DPQ. Viability is normalized to untreated controls. Treatment with DPQ (50 μ M) alone has no effect on cell viability. Likewise, DPQ does not increase the viability of cells treated with [Rh(chrysi)(phen)(DPE-Pt(NH₃)₂Cl)]³⁺ (“Rh(DPE)Pt,” 5 μ M). A modest increase in viability is observed when cells are exposed to DPQ in combination with cisplatin (5 μ M).

in the presence of conjugate alone, and $61 \pm 2.8\%$ viability with metal complex administered in combination with PARP inhibitor. For HCT116O cells, viability is $73 \pm 3.4\%$ and $71 \pm 2.0\%$ in the presence of the conjugate alone and the combination treatment, respectively. These results indicate that the cytotoxic effects of $[\text{Rh}(\text{chrysi})(\text{phen})(\text{DPE-Pt}(\text{NH}_3)_2\text{Cl})]^{3+}$ in HCT116 cells are independent of the PARP pathway and therefore do not proceed via necrosis.

Curiously, co-treatment of cells with cisplatin ($5 \mu\text{M}$) and DPQ ($50 \mu\text{M}$) results in a statistically significant increase ($p < 0.0001$ by unpaired two-tailed t test) in cell viability compared to treatment with cisplatin alone: the percentage of viable HCT116N cells increases from $86 \pm 4.3\%$ to $95 \pm 1.0\%$ upon the addition of PARP inhibitor, and the fraction of viable HCT116O cells increases from $73 \pm 3.6\%$ to $82 \pm 1.1\%$. While these are modest changes overall, these results suggest that cisplatin induces necrosis in these cell lines to some degree.

The experiment was also performed in the presence of a pan-caspase inhibitor, Z-VAD-FMK. By irreversibly binding to the active site of caspases, Z-VAD-FMK inhibits apoptosis.³⁶ Previously, it has been shown that appendage of a platinum moiety to a metalloinsertor triggers caspase-dependent cell death, signifying apoptosis rather than necrosis.²⁶ Here, treatment of HCT116N and HCT116O cells with $[\text{Rh}(\text{chrysi})(\text{phen})(\text{DPE-Pt}(\text{NH}_3)_2\text{Cl})]^{3+}$ in combination with caspase inhibitor results in a similar outcome. Cells were treated with $[\text{Rh}(\text{chrysi})(\text{phen})(\text{DPE-Pt}(\text{NH}_3)_2\text{Cl})]^{3+}$ ($5 \mu\text{M}$) or cisplatin ($5 \mu\text{M}$) in combination with Z-VAD-FMK ($35 \mu\text{M}$) for 72h, and cell viability was determined by MTT cytotoxicity assay (**Figure 4.13**).

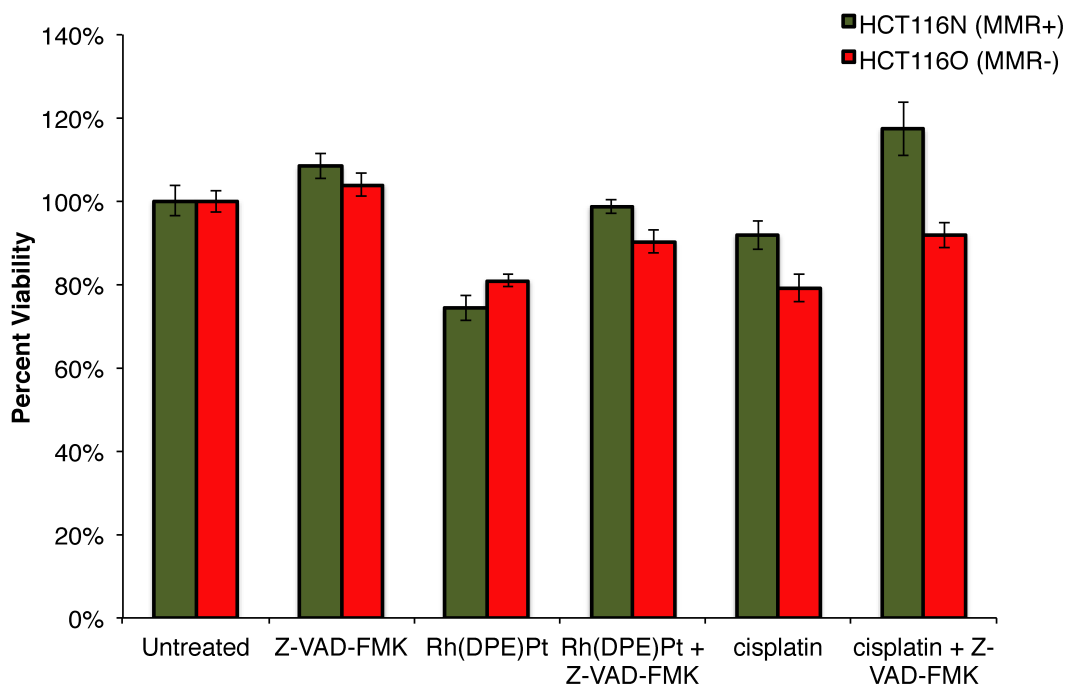


Figure 4.13 Cell viability in HCT116N (green, MMR-proficient) and HCT116O (red, MMR-deficient) cells after 72h treatment with caspase inhibitor Z-VAD-FMK. Viability is normalized to untreated controls. Treatment with Z-VAD-FMK (35 μM) alone has no effect on cell viability. When administered in combination with [Rh(chrysi)(phen)(DPE-Pt(NH₃)₂Cl)]³⁺ (“Rh(DPE)Pt,” 5 μM), a statistically significant increase in viability is observed in both cell lines. A similar result is observed when caspase inhibitor is added in combination with cisplatin (5 μM). These results signify caspase-dependent apoptosis ($p < 0.0001$ by unpaired two-tailed t-test).

A clear increase in cell viability upon addition of the caspase inhibitor is observed for both cell lines treated with conjugate. In fact, caspase inhibition almost completely abolishes the cytotoxic effects of the conjugate: the percentage of viable HCT116N cells increases from $74 \pm 3.0\%$ with $[\text{Rh}(\text{chrysi})(\text{phen})(\text{DPE-Pt}(\text{NH}_3)_2\text{Cl})]^{3+}$ alone to $99 \pm 1.6\%$ upon addition of Z-VAD-FMK, and the percentage of viable HCT116O cells is similarly enhanced from $81 \pm 1.5\%$ to $90 \pm 2.7\%$. For both cell lines, these differences were determined to be statistically significant by unpaired two-tailed *t*-test ($p < 0.0001$). These results, in combination with the results of the MTT assay in combination with PARP inhibitor, signify that the cytotoxicity of $[\text{Rh}(\text{chrysi})(\text{phen})(\text{DPE-Pt}(\text{NH}_3)_2\text{Cl})]^{3+}$ is caspase-dependent and PARP-independent. $[\text{Rh}(\text{chrysi})(\text{phen})(\text{DPE-Pt}(\text{NH}_3)_2\text{Cl})]^{3+}$ induces an apoptotic mode of cell death in both HCT116N and HCT116O cell lines.

The cisplatin-treated cells display similar results upon addition of Z-VAD-FMK: cell viability increases $25 \pm 2.9\%$ and $13 \pm 0.3\%$ for HCT116N and HCT116O cells, respectively, compared to treatment with cisplatin alone ($p < 0.0001$ by unpaired two-tailed *t* test). Exposure of cisplatin-treated cells to caspase inhibitor results in a markedly more dramatic increase in cell viability compared to treatment with PARP inhibitor, suggesting that while some cells may be undergoing necrotic cell death, the apoptotic pathway is likely the major mechanism of cisplatin cytotoxicity.

4.4 Discussion

4.4.1 Synthesis of $[\text{Rh}(\text{chrysi})(\text{phen})(\text{DPE-Pt}(\text{NH}_3)_2\text{Cl})]^{3+}$

We have synthesized a new bimetallic Rh-Pt metalloinsertor derived from a recently characterized family of complexes bearing axial Rh—O bonds.²⁴ Metalloinsertors containing these ligands, which coordinate through a five-membered

pyridylethanol ring, have been shown to exhibit enhanced potency and cell-selectivity in MMR-deficient cells.^{22,24} Furthermore, these complexes can accommodate a wide variety of functional groups incorporated into the *N,O*-coordinating ligand without sacrificing DNA binding ability or biological activity, making this class of complexes an attractive scaffold for the development of next-generation bifunctional metalloinsertor conjugates.

The metalloinsertor parent complex, $[\text{Rh}(\text{chrysi})(\text{phen})(\text{DPE})]^{2+}$ (**Figure 4.1**), contains a non-coordinating pyridine functionality within the pyridyl-ethanol ligand scaffold. This extraneous pyridine serves as the site of coordination for cisplatin. Simple reflux of commercially available cisplatin with the rhodium parent complex under acidic conditions displaces one of the labile chloride ligands on the platinum center, affording $[\text{Rh}(\text{chrysi})(\text{phen})(\text{DPE-Pt}(\text{NH}_3)_2\text{Cl})]^{3+}$ (**Figure 4.1**) in a single step in reasonable yield (**Scheme 4.1**). This conjugate, then, contains a platinum center with only a single labilization site at the remaining chloride, and is therefore expected to form “monofunctional” platinum adducts – that is, the platinum will only coordinate a single nucleobase on the DNA, rather than binding two nearby residues and forming the classical 1,2- or 1,3-intrastrand crosslinks characteristic of the cisplatin parent complex.

Monofunctional platinum anticancer complexes, particularly those with the general structure $\text{cis-}[\text{Pt}(\text{NH}_3)_2(\text{L})\text{Cl}]^+$ (where L is an N-heterocycle), have been heavily investigated by Lippard and others.³⁷⁻⁴⁰ Long considered to be clinically irrelevant due to the inactivity of the first studied monofunctional compounds, $[\text{Pt}(\text{dien})\text{Cl}]^+$ (dien = diethylenetriamine) and $[\text{Pt}(\text{NH}_3)_3\text{Cl}]^+$,⁴¹⁻⁴³ interest in this class of complexes has been renewed in recent years with the development of more active analogues, such as pyriplatin ($\text{cis-}[\text{Pt}(\text{NH}_3)_2(\text{pyridine})\text{Cl}]^{2+}$)⁴⁴ and the highly potent phenanthriplatin (cis-

[Pt(NH₃)₂(phenanthridine)Cl](NO₃)), which is being investigated as a new chemotherapeutic agent.^{45,46} These complexes have been shown to form monofunctional adducts with single bases on DNA, usually at the N7 position of guanine.^{37,44} These crosslinks distort the DNA in a manner that is structurally distinct from that of cisplatin and other bifunctional *cis*-platinum (II) complexes, resulting in considerably less bending and unwinding of the DNA.⁴⁷⁻⁵⁰ These complexes thus exert their anticancer activity via different biological mechanisms, providing orthogonality in the treatment of cisplatin-resistant cancers.⁴⁷ In addition to the distinctive DNA binding exhibited by *cis*-[Pt(NH₃)₂(L)Cl]⁺ complexes, the presence of the bulky N-heterocycle protects the metal center from deactivating protein thiols as well as recognition by nucleotide excision repair proteins, which repair Pt-DNA adducts and lead to resistance.^{37,44,51} As a result, monofunctional, cationic platinum (II) complexes are a growing class of platinum-based drugs that can be effective against cisplatin-resistant cancers.

The synthesis and characterization of [Rh(chrysi)(phen)(DPE-Pt(NH₃)₂Cl)]³⁺ represents the first example of a monofunctional platinum complex conjugated to a rhodium metalloinsertor, as well as the first example of a bifunctional conjugate developed from the Rh—O metalloinsertor family. The DNA binding behavior of the complex has been characterized *in vitro*, and the cytotoxic activity was explored in three human cancer cell lines.

4.4.2 DNA Binding Behavior

The [Rh(chrysi)(phen)(DPE-Pt(NH₃)₂Cl)]³⁺ was designed as previous iterations of Rh-Pt metalloinsertor conjugates, comprising a rhodium (III) subunit coordinated to a 5,6-chrysenequinone diimine ligand for base pair mismatch recognition and a thermally

activated platinum subunit for covalent DNA binding. The complex was analyzed for both mismatch binding and platinum crosslinking on hairpin and duplex radiolabeled DNA containing a CC mismatch. The conjugate is capable of simultaneous metalloinsertion at a mismatch and platinum adduct formation with hairpin DNA (**Figure 4.3**). Additionally, platinum binding was explored with mismatched and well-matched duplex DNA, and it was revealed that the complex preferentially binds mismatched DNA over well-matched sequences.

The preferential platination of mismatched DNA over well-matched *in vitro* likely results from the ability of the complex to target mismatched sites in DNA by metalloinsertion. This behavior has been shown previously in our laboratory with a metalloinsertor-cisplatin conjugate.²⁵ Here, the rhodium and platinum subunits were separated by a six-carbon alkyl linker region, and metalloinsertion at a mismatch successfully directed platinum binding preferentially toward mismatched DNA over a well-matched duplex. However, this preferential binding was highly dependent on the presence and location of a d(GpG) site (the preferred binding site of cisplatin); if there was no d(GpG) site, or if it was inaccessible to the platinum center due to limitations in the length and flexibility of the alkyl tether (i.e., situated too closely to the site of the mismatch), then minimal platination occurred. Likewise, there was no preference for mismatched DNA in these scenarios. Selective DNA platination, then, is highly sequence-dependent for this complex.

The structural limitations of the first-generation metalloinsertor-platinum conjugate do not appear to be present for $[\text{Rh}(\text{chrysi})(\text{phen})(\text{DPE-Pt}(\text{NH}_3)_2\text{Cl})]^{3+}$, despite the fact that the platinum subunit is considerably more constricted in its coordination to

the DPE ligand. The complex has been shown to platinate mismatched (and, to a lesser extent, well-matched) DNA in both hairpin and duplex sequences (See **Section 4.3.1.1** and **4.3.1.2** for sequences), including variation in the sequence context surrounding the site of the CC mismatch. Furthermore, in the case of the duplex DNA sequence, the d(GpG) site is located six and seven base pairs away from the mismatch – an unreachable distance for simultaneous metalloinsertion and platination by a complex with virtually no separation between the subunits.

We considered the possibility that the simultaneous mismatch binding and crosslinking could be the result of two or more equivalents of the complex binding to different sites on the DNA – one equivalent at the mismatch, which in turn stabilizes the duplex for coordination of a second equivalent at the distal d(GpG) site. However, DNA sequencing of the guanine residues by DMS footprinting revealed that $[\text{Rh}(\text{chrysi})(\text{phen})(\text{DPE-Pt}(\text{NH}_3)_2\text{Cl})]^{3+}$ does not form covalent adducts with either guanine on the radiolabeled strand. In fact, the binding of the conjugate results in an increase in the efficiency of guanine methylation by DMS (rather than the decrease that would be expected for platinum bound at that site), implying that the site of platination potentially distorts and/or unwinds the DNA helix in a manner that leaves the guanines more accessible to methylation.

It is currently unclear what the preferred site of coordination is for the conjugate. Preliminary DNA sequencing studies reveal no evidence of adenine binding (data not shown). The *N3* position of cytosine is nucleophilic enough to coordinate platinum – early models of monofunctional platinum complexes contained *N3*-cytosine as the N-heterocyclic ligand⁴⁸ – however, it is surprising that the considerably more nucleophilic

guanine and adenine *N7* positions are not favored binding sites, even in the case of well-matched DNA. Coordination at cytosine *N3* has been observed in a DNA oligomer, but is uncommon and typically occurs as part of a bifunctional coordination with an adjacent guanine.⁴⁹ This unusual DNA binding behavior of $[\text{Rh}(\text{chrysi})(\text{phen})(\text{DPE-Pt}(\text{NH}_3)_2\text{Cl})]^{3+}$ possibly contributes to the mismatch-selectivity of the complex *in vitro*: because coordination with the most nucleophilic sites on DNA is disfavored, coordination of the platinum center is thermodynamically directed by metalloinsertion at mismatched sites from the minor groove.

In previous generations of metalloinsertor-platinum conjugates, the rhodium and platinum subunits functioned essentially as separate entities, even in instances where platination was directed towards mismatched DNA by the rhodium subunit. This was due to the construction of the conjugates either as metastable, hydrolysable subunits or two permanently linked functionalities separated by a long, flexible alkyl chain.^{25,26} In the case of $[\text{Rh}(\text{chrysi})(\text{phen})(\text{DPE-Pt}(\text{NH}_3)_2\text{Cl})]^{3+}$, however, both metal centers directly coordinate the relatively small DPE ligand, placing them in close proximity to one another and offering little flexibility for the subunits to function independently of one another. Therefore, it is possible that the nature of the observed platinum coordination is informed by the unusual DNA binding behavior already exhibited by the $[\text{Rh}(\text{chrysi})(\text{phen})(\text{DPE})]^{2+}$ parent complex. To explain the accommodation of the bulky, “dangling” pyridine in the minor groove, as well as the mismatch binding ability of the Λ -enantiomer to B-form DNA, an alternate mode of metalloinsertion has been proposed, involving a side-on insertion of the buckled chrysi ligand such that only two benzene rings are incorporated into the nucleobase stack.²⁴ This binding mode may situate the

platinum center in a position favorable for crosslinking; however, it does not explain how the complex binds to well-matched DNA. Additional studies are necessary to further understand the nature of the DNA binding behavior of this bimetallic conjugate.

4.4.3 Characterization in Cell Tissue Culture

Encouraged by the mismatch specificity exhibited by $[\text{Rh}(\text{chrysi})(\text{phen})(\text{DPE-Pt}(\text{NH}_3)_2\text{Cl})]^{3+}$ *in vitro*, we sought to examine whether this translated to cell-selective cytotoxicity in cancer cells deficient in mismatch repair. The cytotoxic effects of the conjugate were explored in the isogenic human colorectal carcinoma cell lines HCT116N (MMR-proficient) and HCT116O (MMR-deficient) as well as the cisplatin-resistant human ovarian cancer line A2780cis. While the conjugate does not display the potency or cell-selective targeting of HCT116O cells exhibited by its $[\text{Rh}(\text{chrysi})(\text{phen})(\text{DPE})]^{2+}$ parent complex, it outperforms its other parent complex, the FDA-approved chemotherapeutic cisplatin, in all three cell lines. The lack of selective targeting of MMR-deficient cells is attributed to the complex triggering an apoptotic, rather than necrotic, mode of cell death as determined by cytotoxicity assays performed with caspase and PARP inhibitors. As has been seen previously, the appendage of a platinum (II) functionality circumvents the biological response to genomic mismatch recognition by metalloinsertors, resulting in a toxic but nonspecific apoptotic response.²⁶

Although the cell-specific biological activity of the $[\text{Rh}(\text{chrysi})(\text{phen})(\text{DPE})]^{2+}$ metalloinsertor could not be transferred to a cytotoxic platinum subunit, $[\text{Rh}(\text{chrysi})(\text{phen})(\text{DPE-Pt}(\text{NH}_3)_2\text{Cl})]^{3+}$ is quite efficacious for a monofunctional *cis*-platinum (II) compound. Early examples of monofunctional platinum complexes, such as $[\text{Pt}(\text{dien})\text{Cl}]^+$ and $[\text{Pt}(\text{NH}_3)_3\text{Cl}]^+$, display no cytotoxicity *in cellulo*.⁴¹⁻⁴³ Pyriplatin, the

exploratory lead compound for monofunctional platinum complexes and a close structural analogue of the platinum subunit of $[\text{Rh}(\text{chrysi})(\text{phen})(\text{DPE-Pt}(\text{NH}_3)_2\text{Cl})]^{3+}$, also exhibits limited potency, with reported IC_{50} values surpassing 200 μM for HCT116 cells as well as a spectrum of various cancer cell lines.⁵² Indeed, aside from phenanthriplatin, there are few examples of monofunctional platinum (II) complexes that surpass cisplatin in potency, despite the evaluation of many derivations of these complexes in a variety of cancer cell lines.⁴⁵ It is presently unclear precisely how the rhodium subunit enhances the efficacy of the monofunctional platinum center in this conjugate; it is possible that properties such as increased lipophilicity and charge afforded by attachment of the metalloinsertor enhances cellular uptake, as was seen for the previously reported metalloinsertor-oxaliplatin complex.²⁶ Perhaps the bulky rhodium center shields the platinum moiety from deactivating proteins or creates a bulky lesion that blocks DNA synthesis, as is observed with phenanthriplatin.⁵¹ Future studies may further probe the underlying biological mechanisms of this unusual complex.

4.5 Conclusions

Here we report the synthesis, *in vitro* characterization, and biological evaluation of a bimetallic Rh(III)-Pt(II) metalloinsertor conjugate that incorporates both the unusual ligand coordination of a recently characterized family of metalloinsertors as well as a monofunctional *cis*- $[\text{Pt}(\text{NH}_3)_2(\text{N-heterocycle})\text{Cl}]^+$ subunit. While not cell-selective, the conjugate displays increased potency compared to FDA-approved cisplatin in all cell lines studied. Moreover, the complex exhibits enhanced platination of mismatched over well-matched DNA *in vitro*, which may arise from uncharacteristic crosslinking of an alternative base preferentially over guanine by platinum in addition to mismatch

recognition by the rhodium subunit. The results herein confirm that rhodium metalloinsertors containing axial Rh—O bonds can be developed as scaffolds for conjugation, resulting in selective targeting of their cargo towards mismatched DNA. The ease with which these complexes can be functionalized enables the development of future conjugates incorporating alternative functionalities, such as cell-penetrating peptides or antibodies. This work also provides the foundation for exploration into non-classical platinum complexes that deviate from traditional structure-activity rules as potential mismatch-targeting agents.

3.6 References

- 1 Wang, D.; Lippard, S. J. *Nature Rev. Drug Discov.* **2005**, *4*, 307-320.
- 2 Jamieson, E. R., Lippard, S. J. *Chem. Rev.* **1999**, *99*, 2467-2498.
- 3 Decatris, M. P., Sundar, S., O'Byrne, K. J. *Cancer Treat. Rev.* **2004**, *30*, 53–81.
- 4 Fink, D.; Aebi, S.; Howell, S. B. *Clin. Cancer Res.* **1998**, *4*, 1-6.
- 5 Aebi, S.; Fink, D.; Gordon, R.; Kim, H. K.; Zheng, H.; Fink, J. L.; Howell, S. B. *Clin. Cancer Res.* **1997**, *3*, 1763-1767.
- 6 Dulhunty, A. F. *J. Physiol.* **1978**, *276*, 67-82.
- 7 Kehe, K.; Szinicz, L. *Toxicology* **2005**, *214*, 198-209.
- 8 Reedijk, J. *Chem. Rev.* **1999**, *99*, 2499-2510.
- 9 Jackson, B. A.; Barton, J. K. *J. Am. Chem. Soc.* **1997**, *119*, 12986–12987.
- 10 Loeb, L. A. *Cancer Res.* **2001**, *61*, 3230-3239.
- 11 Bhattacharya, N. P.; Skandalis, A.; Ganesh, A.; Groden, J.; Meuth, M. *Proc. Natl. Acad. Sci. U.S.A.* **1994**, *91*, 6319-6323.
- 12 Carethers, J. M.; Hawn, M. T.; Chauhan, D. P.; Luce, M. C.; Marra, G.; Koi, M.; Boland, C. R. *J. Clin. Invest.* **1996**, *98*, 199-206.
- 13 Jackson, B. A.; Barton, J. K. *Biochemistry* **2000**, *39*, 6176–6182.
- 14 Jackson, B. A.; Alekseyev, V. Y.; Barton, J. K. *Biochemistry* **1999**, *38*, 4655–4662.
- 15 Pierre, V. C.; Kaiser, J. T.; Barton, J. K. *Proc. Natl. Acad. Sci. U.S.A.* **2007**, *104*, 429.
- 16 Cordier, C.; Pierre, V. C.; Barton, J. K. *J. Am. Chem. Soc.* **2007**, *129*, 12287–12295.

- 17 Zeglis, B. M.; Pierre, V. C.; Kaiser, J. T.; Barton, J. K. *Biochemistry* **2009**, *48*, 4247.
- 18 Song, H.; Kaiser, J. T.; Barton, J. K. *Nature Chem.* **2012**, *4*, 615–620.
- 19 Hart, J. R.; Glebov, O.; Ernst, R. J.; Kirsch, I. R.; Barton, J. K. *Proc. Natl. Acad. Sci. U.S.A.* **2006**, *103*, 15359–15363.
- 20 Ernst, R. J.; Song, H.; Barton, J. K. *J. Am. Chem. Soc.* **2009**, *131*, 2359–2366.
- 21 Ernst, R. J.; Komor, A. C.; Barton, J. K. *Biochemistry* **2011**, *50*, 10919–10928.
- 22 Komor, A. C.; Schneider, C. J.; Weidmann, A. G.; Barton, J. K. *J. Am. Chem. Soc.* **2012**, *134*, 19223–19233.
- 23 Weidmann, A. G.; Komor, A. C.; Barton, J. K. *Philos. Trans. R. Soc. A.* **2013**, *371*, 20120117.
- 24 Komor, A. C.; Barton, J. K. *J. Am. Chem. Soc.* **2014**, *136*, 14160–14172.
- 25 Petitjean, A.; Barton, J. K. *J. Am. Chem. Soc.* **2004**, *126*, 14728–14729.
- 26 Weidmann, A. G.; Barton, J. K. *Inorg. Chem.* **2014**, *53*, 7812–7814.
- 27 Ernst, R. J. *Unpublished results*
- 28 Basu, A.; Bhaduri, S.; Sapre, N. Y.; Jones, P. G. *J. Chem. Soc., Chem. Commun.* **1987**, *22*, 1724–1725.
- 29 Muerner, H.; Jackson, B. A.; Barton, J. K. *Inorg. Chem.* **1998**, *37*, 3007–3012.
- 30 Brabec, V.; Leng, M. *Proc. Natl. Acad. Sci. U.S.A.* **1993**, *90*, 5345–5349.
- 31 Mosmann, T. *J. Immunol. Methods* **1983**, *65*, 55–63.
- 32 Siddik, Z. H. *Oncogene* **2003**, *22*, 7265.
- 33 Arango, D.; Wilson, A. J.; Shi, Q.; Corner, G. A.; Arañes, M. J.; Nicholas, C.; Lesser, M.; Mariadason, J. M.; Augenlicht, L. H. *Br. J. Cancer* **2004**, *91*, 1931.

- 34 Costantino, G., Macchiarulo, A., Camaioni, E., and Pellicciari, R. *J. Med. Chem.* **2001**, *44*, 3786-3794.
- 35 Ha, H.C., Snyder, S. H. *Proc. Natl. Acad. Sci. U.S.A.* **1999**, *96*, 13978-13982.
- 36 Vandenabeele, P., Vanden Berghe, T., and Festjens, N. *Sci. STKE*, **2006**, *358*, pe44.
- 37 Johnstone, T. C.; Wilson, J. J.; Lippard, S. J. *Inorg. Chem.* **2013**, *52*, 12234-12249.
- 38 Hollis, L. S.; Amundsen, A. R.; Stern, E. W. *J. Med. Chem.* **1989**, *32*, 128-136.
- 39 Baird, C. L.; Griffiths, A. E.; Baffic, S.; Bryant, P.; Wolf, B.; Lutton, J.; Berardini, M.; Arvanitis, G. M. *Inorg. Chim. Acta* **1997**, *256*, 253-262.
- 40 Sundquist, W. I.; Bancroft, D. P.; Lippard, S. J. *J. Am. Chem. Soc.* **1990**, *112*, 1590-1596.
- 41 Macquet, J. P.; Butour, J. L. *J. Natl. Cancer Inst.* **1983**, *70*, 899-905.
- 42 Brabec, V.; Reedijk, J.; Leng, M. *Biochemistry* **1992**, *31*, 12397-12402.
- 43 Bursova, V.; Kasparov, J.; Hofr, C.; Brabec, V. *Biophys. J.* **2005**, *88*, 1207-1214.
- 44 Lovejoy, K. S.; Todd, R. C.; Zhang, S.; McCormick, M. S.; D'Aquino, J. A.; Reardon, J. T.; Sancar, A.; Giacomini, K. M.; Lippard, S. J.
- 45 Park, G. Y.; Wilson, J. J.; Song, Y.; Lippard, S. J. *Proc. Natl. Acad. Sci. U.S.A.* **2012**, *109*, 11987-11992.
- 46 Johnstone, T. J.; Park, G. Y.; Lippard, S. J. *Anticancer Res.* **2014**, *34*, 471-476.
- 47 Lempers, E. L. M.; Bloemink, M. J.; Brouwer, J.; Kidani, Y.; Reedijk, J. *J. Inorg. Biochem.* **1990**, *40*, 23-25.
- 48 Bellon, S. F.; Lippard, S. J. *Biophys. Chem.* **1990**, *35*, 179-188.

- 49 Chottard, J. C.; Ledner, J. A.; Bauer, W. A.; Ushay, H. M.; Caravana, C.; Lippard, S. J. *J. Am. Chem. Soc.* **1980**, *102*, 2487-2488.
- 50 Keck, M. V.; Lippard, S. J. *J. Am. Chem. Soc.* **1992**, *114*, 3386-3390.
- 51 Wang, D.; Zhu, G.; Huang, X.; Lippard, S. J. *Proc. Natl. Acad. Sci. U.S.A.* **2010**, *107*, 9584-9589.
- 52 Lovejoy, K. S.; Serova, M.; Bieche, I.; Emami, S.; D'Incalci, M.; Brogini, M.; Erba, E.; Gespach, C.; Cvitkovic, E.; Faivre, S.; Raymond, E.; Lippard, S. J. *Mol. Cancer Ther.* **2011**, *10*, 1709-1719.

Chapter 5: Synthesis and Characterization of Bimetallic Rh(III)-Pt(II) DNA Mismatch Binding Complexes with Bridging Intercalator Ligands

5.1 Introduction

The development of rhodium metalloinsertors, which target thermodynamically destabilized base pair mismatches in DNA with high specificity and affinity, into bifunctional conjugates has long been a focus of the Barton laboratory. The appendage of functionalities with various biological activities to these mismatch recognition complexes affords unique compounds with dual functionalities, often enabling the targeting of otherwise nonselective compounds towards mismatched DNA.¹⁻⁴ A primary focus in the design of bifunctional metalloinsertor conjugates is the incorporation of cytotoxic, DNA crosslinking platinum (II) moieties.^{3,5} Platinum chemotherapeutics are employed in the treatment of over 50% of all cancers and have been widely successful in the treatment of several malignancies.⁶⁻¹⁰ However, single-agent therapy is increasingly uncommon, and even common chemotherapeutics like cisplatin are typically administered in conjunction with one or more drugs, each functioning separately but synergistically within the cell.¹¹ We have expanded the notion of combination therapy further, in the employment of cell-specific rhodium metalloinsertors that may function not simply as separate synergistic adjuvants, but rather as conjugated targeting agents for platinum. The ability to direct these agents towards lesions in DNA associated with carcinogenesis would be a significant enhancement in the development of targeted therapies.¹²

Several examples of metalloinsertor-platinum conjugates have already been characterized.^{3,5,13} Each generation of Rh-Pt complex is unique in its construction and biological activity. The first-generation conjugate, developed over ten years ago, involves

a trisheteroleptic $\text{Rh}(\text{chrysi})(\text{phen})(\text{bpy}')^{3+}$ metalloinsertor scaffold, where bpy' is a 2,2'-bipyridine ligand modified with an amino-alkane linker, chrysi (5,6-chrysenequinone diimine) is the sterically expansive inserting ligand for mismatch recognition, and phen (1,10-phenanthroline) serves as an additional ancillary ligand. The rhodium complex was functionalized with a cisplatin derivative via the non-leaving group ligand and was found to enhance the formation of covalent platinum adducts preferentially at mismatched DNA, provided that the preferred d(GpG) binding site was adequately accessible within the constructs of the alkyl tether.³

The structural limitations of the first-generation Rh-Pt conjugate bore biological consequences. Despite the targeted platination of mismatched DNA *in vitro*, the complex was unable to successfully inhibit proliferation in mismatch repair (MMR)-deficient cancer cells, instead targeting the isogenically matched MMR-proficient cell line, much like its cisplatin parent complex.^{14,15} This preferential targeting of MMR-proficient cells can be a potentially devastating side effect of chemotherapy, as the deleterious effects of the MMR-deficiency phenotype are allowed to further proliferate. Selection for MMR-defects resulting from chemotherapy-induced DNA damage is a major cause of secondary leukemias and other malignancies.¹⁶

The second-generation Rh-Pt complex addressed these issues: here, the platinum subunit was attached to the rhodium complex not through its inert ammine ligand, but rather through the labile leaving group.⁵ This afforded a temporary linkage between the rhodium and platinum subunits, with the intention of the conjugate remaining intact long enough for the metalloinsertor to taxi its cargo to mismatched DNA. This design strategy enabled the platinum subunit to bind DNA regardless of the location of the d(GpG) site.

In this second-generation conjugate, we employed an oxaliplatin derivative, which is active in MMR-deficient cancers, rather than the cisplatin analogue of the previous conjugate. We also replaced the lipophilic phen and bpy' ligands with ligands derived from HDPA (2,2'-dipyridylamine), a flexible, hydrophilic ligand that has been shown to display accelerated cellular uptake and selective biological activity.¹⁷⁻¹⁹ Based on previous studies establishing that highly lipophilic ligands are unfavorable for cell-selective targeting of MMR-deficiency due to uptake into mitochondria,^{19,20} elimination of the greasy alkyl chain was anticipated to enhance biological efficacy in addition to eliminating the sequence dependence of the previous complex.

This new strategy proved successful in some aspects of its design: the hydrophilic complex was able to remain intact during cellular uptake and localization to the nucleus, while displaying minimal mitochondrial sequestration. This resulted in a 3-fold enhancement in potency in MMR-deficient cells over cisplatin as well as oxaliplatin, the FDA-approved first line therapy for colorectal cancers. However, this potency was not selective for MMR-deficient cells, although the conjugate did target both cell lines equally rather than mimicking the reverse-selectivity displayed by the previous complex. Additionally, the hydrolysable construct abolished preferential targeting of mismatched DNA by platinum, resulting in the formation of Pt-DNA adducts with both mismatched and well-matched DNA.⁵

In addition to these published examples, several other iterations of bimetallic conjugates have been explored for mismatch-directed targeting of platinum.^{13,21} However, in all of these cases, the metalloinsertor was functionalized via attachment of the platinum subunit (or other cargo) to one of the non-inserting ancillary ligands. This

approach has the advantage of ligand modulation with relative synthetic ease, in addition to leaving the chrysi ligand unmodified for insertion into the nucleobase π -stack; however, the appendage of potentially bulky cargo extending from the back of the metalloinsertor has the potential to interfere with DNA binding affinity,³ or possibly *in vivo* recognition and processing of the metalloinsertor-bound DNA lesion. As a result, conjugation of cargo from the ancillary ligands of metalloinsertors can lead to unforeseen biological consequences.

Here, we present an approach to bimetallic Rh(III)/Pt(II) mismatch recognition complexes previously unexplored in our laboratory. Instead of connecting the two metal centers via the metalloinsertor ancillary ligands, we have synthesized a new inserting ligand capable of chelating both metal centers directly. Thus, there is no modular linker region between the two metal centers; rather, the ligand is modified with additional coordination sites for the direct chelation of platinum. In this way, metalloinsertion and platination are intrinsically linked, as insertion into a mismatched site would place the platinum center directly into the DNA lesion (**Figure 5.1**). Within this model, both of the ancillary ligands can potentially be varied to enhance DNA binding affinity and biological efficacy. Two complexes have been synthesized (**Figure 5.2**), $[(\text{bpy})_2\text{Rh}(\mu\text{-phendione})\text{PtX}_2]^{3+}$ and $[(\text{bpy})_2\text{Rh}(\mu\text{-bzp})\text{PtX}_2]^{3+}$ (bpy = 2,2'-bipyridine; phendione = 1,10-phenanthroline-5,6-dione; bzp = benzo[*b*][1,10]phenanthroline-5,6-dione; X = labile leaving group ligand (Cl, H₂O)), with the phendione and bzp ligands coordinating to both rhodium (*via* the imines) and platinum (*via* the distal nitrogens). In the case of $[(\text{bpy})_2\text{Rh}(\mu\text{-phendione})\text{PtX}_2]^{3+}$, the phendione ligand is capable of metalloinsertion at the site of a mismatch, but is also narrow enough to intercalate into well-matched DNA. The

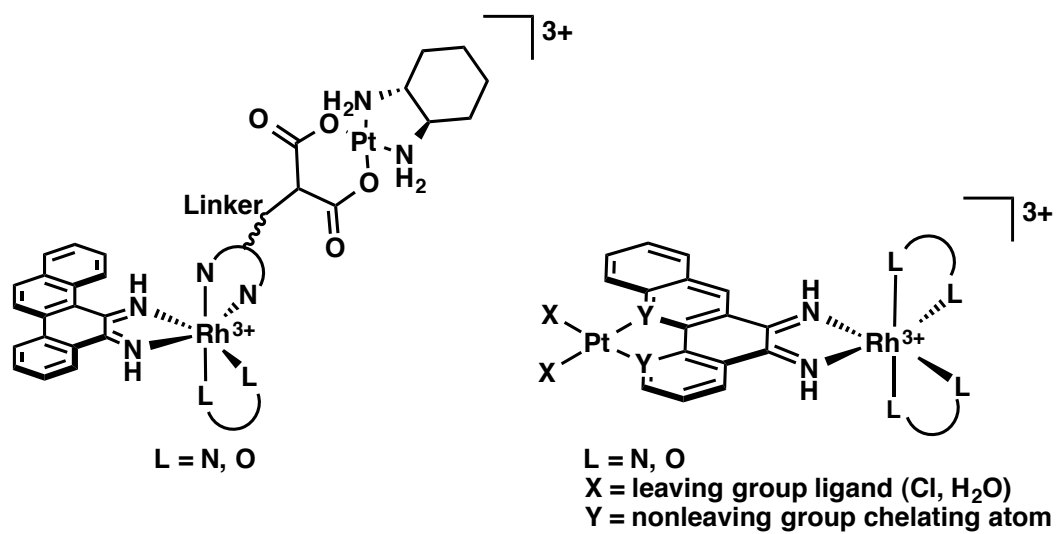


Figure 5.1 General structures of two distinct families of Rh-Pt metalloinsertor conjugates. Left: the non-inserting ancillary ligands are modified with therapeutic cargo; Right: the second metal directly chelates to the inserting ligand via a distal coordination site opposite the Rh(III) center.

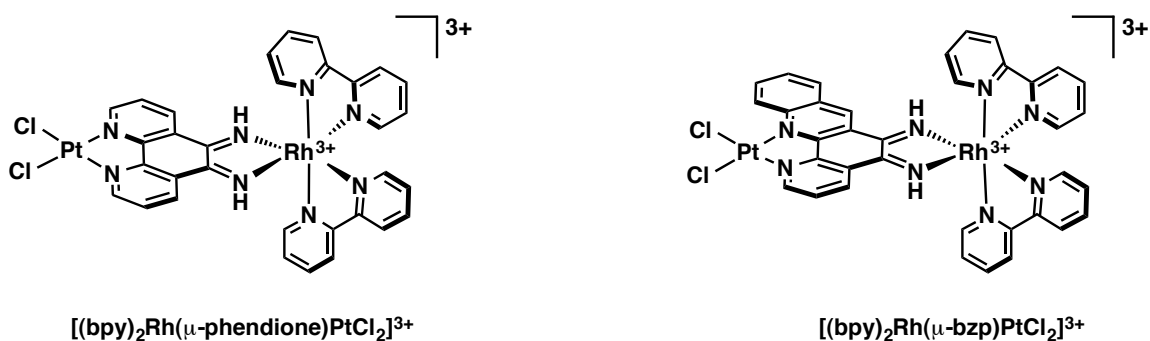


Figure 5.2 Chemical structures of two mixed-metal Rh(III)/Pt(II) metalloinsertor complexes, wherein both metal centers are coordinated to the bridging aromatic ligand that interacts with the DNA base stack. Left: $[(bpy)_2Rh(\mu\text{-phenidione})PtCl_2]^{3+}$, where phenidione (1,10-phenanthroline-5,6-dione) is an intercalating ligand that can bind at mismatched or well-matched sites; Right: $[(bpy)_2Rh(\mu\text{-bzip})PtCl_2]^{3+}$, where bzip (benzo[*b*][1,10]phenanthroline-5,6-dione) is a sterically expansive analogue of phenidione designed to selectively target destabilized mismatches. The platinum centers also contain two *cis*-labile chloride ligands that are hydrolyzed under aqueous conditions to form covalent DNA crosslinks.

complex also forms platinum crosslinks with mismatched and well-matched DNA. The $[(bpy)_2Rh(\mu\text{-bzp})PtX_2]^{3+}$ complex was synthesized with the intention of being a mismatch-specific analogue to $[(bpy)_2Rh(\mu\text{-phenidione})PtX_2]^3$. The bzp ligand appears to be theoretically too wide to intercalate into well-matched DNA, but inserts at mismatched sites. This complex displays two distinct binding modes that depend on whether the complex is interacting with DNA containing a thermodynamically destabilized site.

5.2 Experimental Protocols

5.2.1 Materials

All organic reagents were purchased from Sigma-Aldrich unless otherwise noted. Commercially available chemicals were used as received without further purification. $RhCl_3$ and K_2PtCl_4 starting material were purchased from Pressure Chemical Co (Pittsburgh, PA). Sep-pak C_{18} solid-phase extraction (SPE) cartridges were purchased from Waters Chemical Co. (Milford, MA).

Oligonucleotides were ordered from Integrated DNA Technologies and purified by HPLC using a C_{18} reverse-phase column (Varian, Inc; Corona, CA). All HPLC purifications were carried out on a Hewlett-Packard 1100 HPLC. DNA purity was confirmed by MALDI-TOF mass spectrometry and quantified by UV-visible spectroscopy (UV-vis) using the extinction coefficients at 260 nm estimated for single-stranded DNA. UV-vis characterizations were performed on a Beckmann DU 7400 spectrophotometer. Radiolabeled $[^{32}P]$ -ATP was purchased from MP Biomedicals (Santa Ana, CA).

The synthesis of $[Rh(bpy)_2(NH_3)_2]^{2+}$ was carried out according to literature procedures.¹⁷

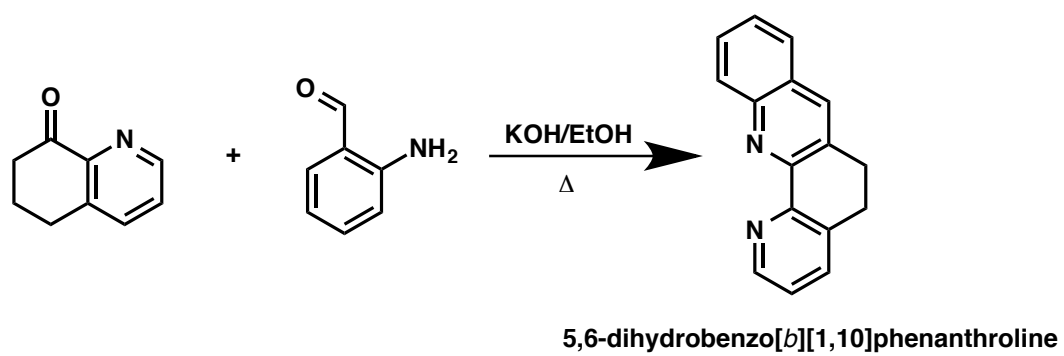
5.2.2 Ligand Synthesis

5.2.2.1 Synthesis of 5,6-dihydrobenzo[*b*][1,10]phenanthroline (Scheme 5.1)

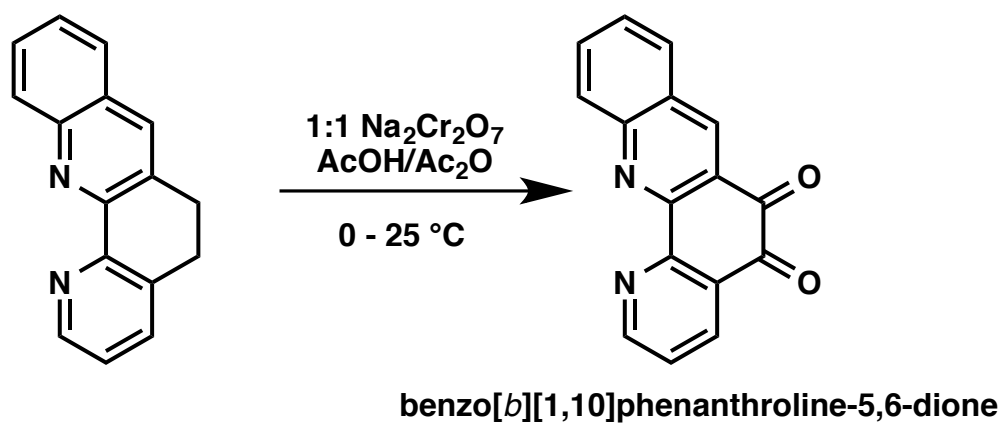
A 250 ml roundbottom flask was charged with 6,7-dihydroquinoline-8(5*H*)-one (147 mg, 1 mmol) and 2-aminobenzaldehyde (121 mg, 1 mmol) in 30 ml EtOH. A solution of KOH (151 mg, 2.7 mmol) in 5 ml EtOH was added, and the solution was heated at reflux for 24 h. After cooling to room temperature, the solvent was removed *in vacuo*, and the residue was partitioned between dichloromethane and water. The organic phase was extracted with water (3 x 50 ml), washed with brine, and dried over MgSO₄. The crude product in CH₂Cl₂ was filtered through a plug of Al₂O₃, washing with CH₂Cl₂ to afford the pure product in quantitative yield (233 mg). ESI-MS (cation): *m/z* calc. 233 (M+H⁺), obs. 233.1. ¹H NMR (500 MHz, CDCl₃) δ 8.84 – 8.81 (m, 1H), 8.41 – 8.37 (m, 1H), 8.00 (s, 1H), 7.80 – 7.74 (m, 1H), 7.68 (ddd, *J* = 8.5, 6.8, 1.5 Hz, 1H), 7.62 (dq, *J* = 7.6, 0.9 Hz, 1H), 7.52 (ddd, *J* = 8.2, 6.9, 1.2 Hz, 1H), 7.29 (dd, *J* = 7.6, 4.7 Hz, 1H), 3.18 (dd, *J* = 8.4, 5.7 Hz, 2H), 3.06 (dd, *J* = 8.4, 5.6 Hz, 2H).

5.2.2.2 Synthesis of benzo[*b*][1,10]phenanthroline-5,6-dione ("bzp") (Scheme 5.2)

To a solution of 5,6-dihydrobenzo[*b*][1,10]phenanthroline (233 mg, 1 mmol) in 1:1 glacial acetic acid:acetic anhydride (10 ml) was added sodium dichromate (524 mg, 1.76 mmol) in 1:1 AcOH:Ac₂O (10 ml) dropwise at 0 °C. The reaction was allowed to stir for 8 days, followed by dilution with water (50 ml) and neutralization with saturated aqueous sodium bicarbonate. The mixture was extracted in 75 ml portions with dichloromethane (4 x 50 ml), and the organic fractions were pooled and dried over



Scheme 5.1 Synthesis of 5,6-dihydrobenzo[*b*][1,10]phenanthroline.



Scheme 5.2 Synthesis of benzo[*b*][1,10]phenanthroline-5,6-dione (“bzp”), which contains two bidentate chelating systems: the di-quinone will condense with $[\text{Rh}(\text{bpy})_2(\text{NH}_3)_2]^{3+}$, while the phenanthroline nitrogens serve as the platinum ligand.

MgSO₄. The solvent was removed *in vacuo*, and the ligand, benzo[*b*][1,10]phenanthroline-5,6-dione (“bzp”) was used without further purification. ESI-MS (cation): *m/z* calc 261 (M + H⁺), obs. 261.

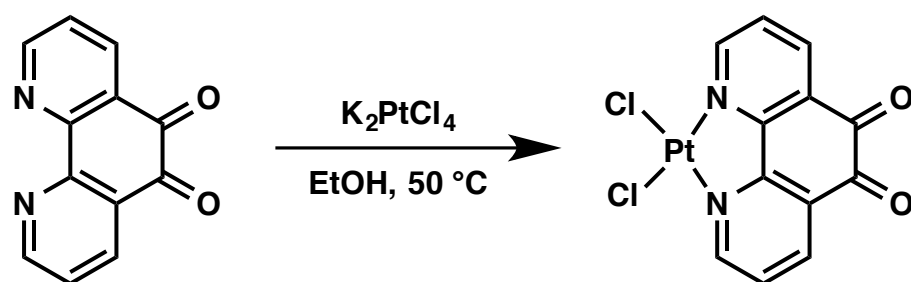
5.2.3 Synthesis of Metal Complexes

5.2.3.1 [PtCl₂(phendione)] (Scheme 5.3)

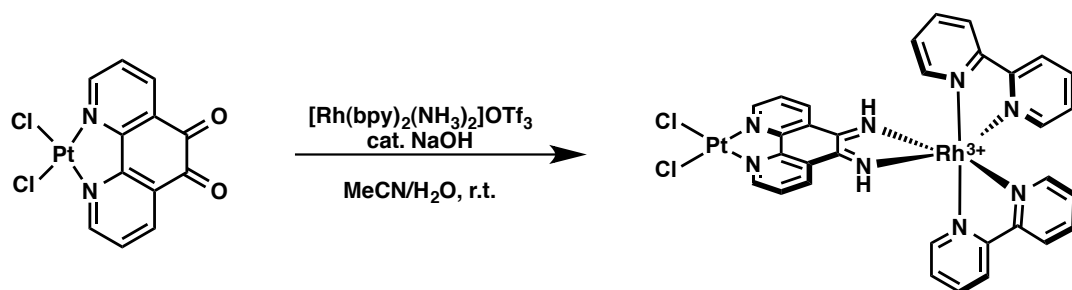
The synthesis of [PtCl₂(phendione)] was carried out as described in the literature, with minor modifications.²² 1,10-phenanthroline-5,6-dione (“phendione,” 50.6 mg, 0.24 mmol) in 20 ml EtOH was added dropwise to a solution of potassium tetrachloroplatinate (100 mg, 0.24 mmol) in 20 ml water in the dark. The mixture was heated to 50 °C for 24 h and filtered. The precipitate was washed with cold ethanol (3 x 5ml), and diethyl ether (3 x 5 ml), and the resulting green-brown solid was dried under vacuum. Yield: 91 mg (80%) ¹H NMR (500 MHz, DMSO-d₆) δ 9.53 (m, 2H), 8.91 – 8.56 (m, 2H), 8.18 – 7.86 (m, 2H). ESI-MS (anion): *m/z* calc 476 (M – H⁻), *m/z* obs. 475.1, 477.1

5.2.3.2 [(bpy)₂Rh(μ-phendione)PtCl₂]³⁺ (Scheme 5.4)

[Rh(bpy)₂(NH₃)₂][OTf₃] (83.5 mg) was dissolved in 30 ml 5:1 MeCN/H₂O. PtCl₂(phendione) (55.7 mg, 1.26 eq) was added, and the mixture was sonicated until the platinum was dissolved. NaOH (2 ml, 1 N) was then added, and an immediate color change to red-orange occurred. The reaction was stirred at room temperature in the dark for 24 h and subsequently dried *in vacuo*. The crude product was redissolved in a minimal volume of H₂O and purified by reverse-phase HPLC (85:15:0.1 to 40:60:0.1 H₂O/MeCN/TFA gradient). ¹H NMR (500 MHz, D₂O): δ 9.69 (ddd, *J* = 5.7, 1.5, 0.7 Hz, 1H), 9.11-9.06 (m, 1H), 8.64-8.59 (m, 2H), 8.51-8.49 (m, 1H), 8.47 (tdd, *J* = 8.0, 2.5, 1.5



Scheme 5.3 Synthesis of $[PtCl_2(phendione)]$, where phendione = 1,10-phenanthroline-5,6-dione.



Scheme 5.4 Synthesis of $[(\text{bpy})_2\text{Rh}(\mu\text{-phendione})\text{PtCl}_2]^{3+}$.

Hz, 2H), 8.44-8.41 (m, 1H), 8.16 (td, $J = 7.9, 1.4$ Hz, 1H), 8.10 (td, $J = 7.9, 1.3$ Hz, 1H), 8.01 (dddd, $J = 10.1, 7.5, 5.7, 1.4$ Hz, 2H), 7.62 (ddt, $J = 5.9, 1.4, 0.7$ Hz, 1H), 7.59 (ddt, $J = 5.9, 1.5, 0.7$ Hz, 1H), 7.41 (ddd, $J = 7.4, 5.8, 1.4$ Hz, 1H), 7.43 (ddd, $J = 7.5, 5.9, 1.4$ Hz, 1H). UV-vis (H₂O, pH 7.0 (**Figure 5.3**)) 337 nm (10330 M⁻¹ cm⁻¹), 380 nm (2210 M⁻¹ cm⁻¹). ESI-MS (cation) m/z calc 444 (M - H²⁺), obs. 467 (M - 2H + Na²⁺).

5.2.3.3 [Rh(bpy)₂bzp]³⁺ (Scheme 5.5)

To a 100 ml roundbottom flask was added bzp (15 mg, 0.057 mmol) and [Rh(bpy)₂(NH₃)₂]OTf₃ (51 mg, 0.057 mmol) in 40 ml 1:1 H₂O/MeCN. The mixture was basified to pH 13 with 1N NaOH, which imparted a color change from yellow to orange. The reaction was allowed to stir at room temperature. After 24h, the reaction was neutralized with 1N HCl and dried *in vacuo*. The complex was purified via passage through a Sep-pak C18 cartridge (Waters) eluting with 1:1 H₂O/MeCN containing 0.1% TFA. ¹H NMR (500 MHz, Deuterium Oxide) δ 10.04 (s, 1H), 9.53 (s, 1H), 9.12 – 8.97 (m, 1H), 8.96 – 8.89 (m, 1H), 8.74 – 8.67 (m, 2H), 8.65 (dd, $J = 8.3, 6.6$ Hz, 1H), 8.61 – 8.55 (m, 1H), 8.54 – 8.50 (m, 1H), 8.42 (t, $J = 8.0$ Hz, 1H), 8.32 (qd, $J = 7.8, 1.4$ Hz, 1H), 8.18 (td, $J = 7.9, 1.4$ Hz, 1H), 8.05 (ddd, $J = 7.5, 5.7, 1.4$ Hz, 1H), 7.98 (s, 1H), 7.81 (m, 2H), 7.73 (m, 1H), 7.69 – 7.65 (m, 1H), 7.63 – 7.57 (m, 1H), 7.55 – 7.51 (m, 1H), 7.43 (ddd, $J = 7.4, 5.8, 1.3$ Hz, 1H), 7.15 (m, 1H), 7.04 (dd, $J = 3.6, 1.9$ Hz, 1H), 6.96 – 6.89 (m, 1H). UV-vis (H₂O, pH 7.0, **Figure 5.4**): 246 nm (113,000 M⁻¹ cm⁻¹), 313 nm (59,900 M⁻¹ cm⁻¹), 350 nm (38,500 M⁻¹ cm⁻¹). ESI-MS (cation): m/z calc 671 (M - 2H⁺), 336 (M - H²⁺), 670.9 obs.

5.2.3.4 [(bpy)₂Rh(μ -bzp)PtCl₂]³⁺ (Scheme 5.6)

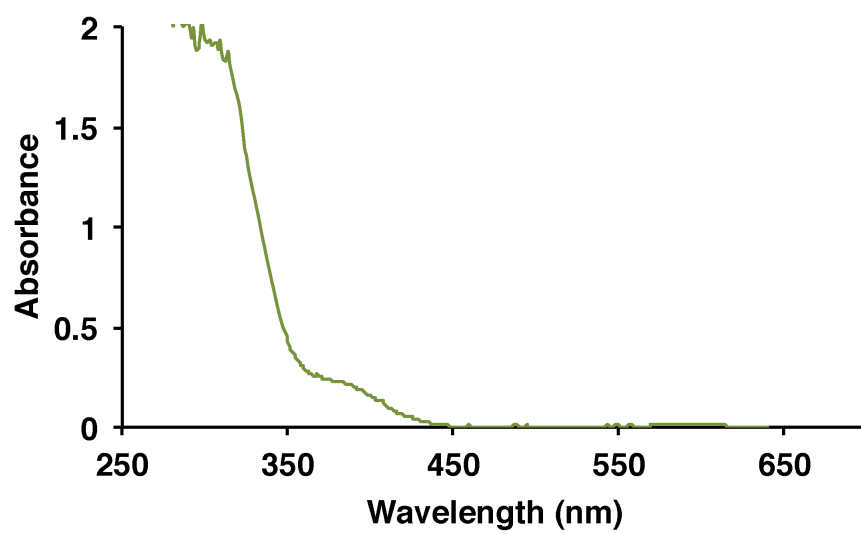
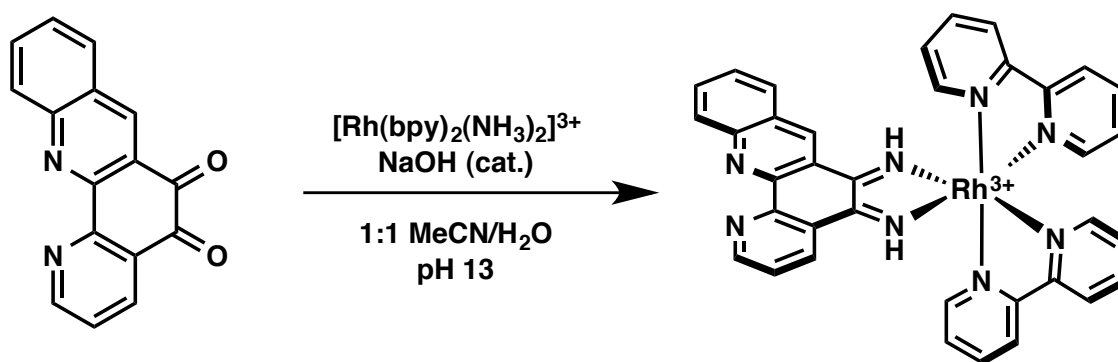


Figure 5.3 UV-visible spectrum of $[(bpy)_2Rh(\mu\text{-phenidione})PtCl_2]^{3+}$ in H_2O at pH 7.



Scheme 5.5 Synthesis of $[\text{Rh}(\text{bpy})_2\text{bzp}]^{3+}$.

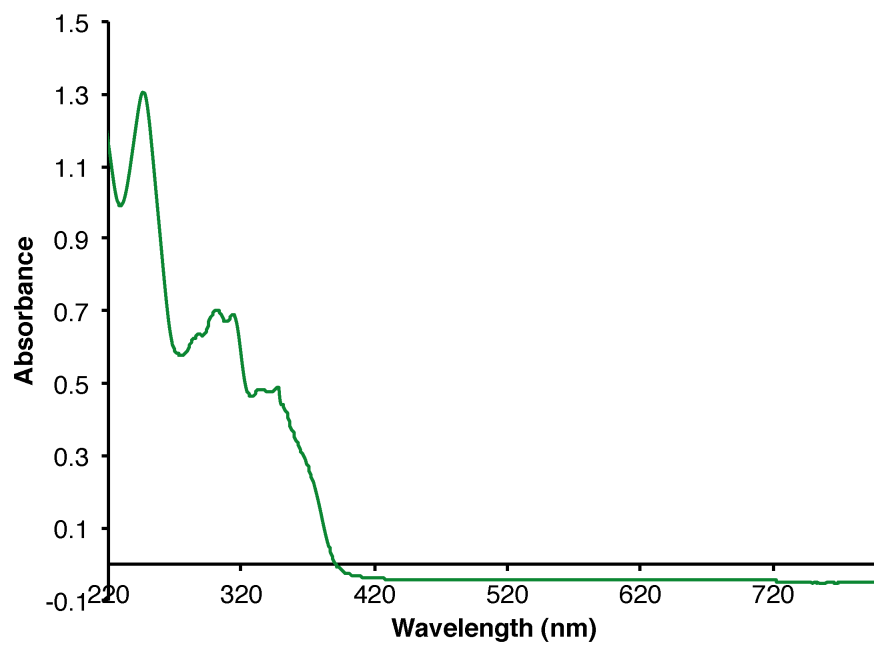


Figure 5.4 UV-visible spectrum of $[\text{Rh}(\text{bpy})_2\text{bzp}]^{3+}$ in H_2O at pH 7.

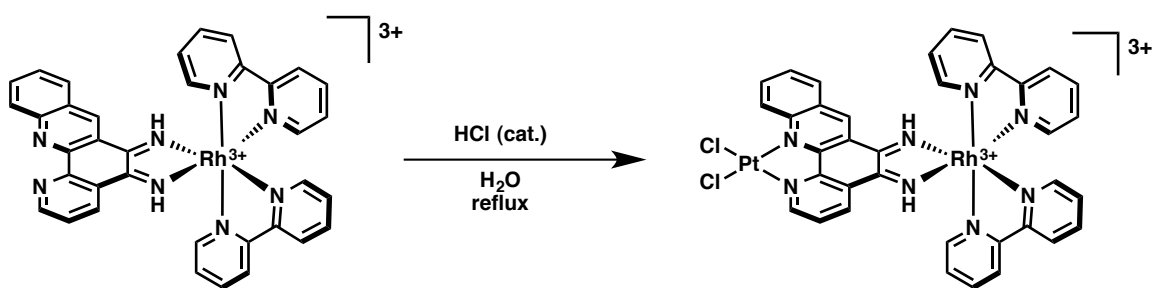
To a 250 ml round-bottomed flask was added $[\text{Rh}(\text{bpy})_2\text{bzp}]\text{TFA}_3$ (60 mg, 0.06 mmol) and K_2PtCl_4 (24.5 mg, 0.06 mmol). The solids were suspended in 50 ml Milli-Q water containing 0.1 ml 1N $\text{HCl}_{(\text{aq})}$. The mixture was heated to reflux for 24 h, during which a color change from red to brown was observed. The reaction was filtered, and the filtrate was collected and dried *in vacuo*. The crude residue was dissolved in a minimal volume of ethanol and purified by reverse-phase HPLC. The fractions containing product were identified by ESI-MS, redissolved in water, and subjected to an additional round of HPLC purification. The purified product was dried *in vacuo*, redissolved in water, and loaded onto a QAE Sephadex anion exchange column. $[(\text{bpy})_2\text{Rh}(\mu\text{-bzp})\text{PtCl}_2]^{3+}$ was eluted as the chloride salt with 1 M MgCl_2 . To remove excess MgCl_2 , the complex was desalted on a SPE column, washed with water, and eluted with methanol. The product was dried immediately to prevent ligand exchange at the platinum center. ^1H NMR (D_2O , 500 MHz) δ 9.56 (d, $J = 10.7$ Hz, 1H), 9.11 (s, 1H), 8.89 – 8.79 (m, 1H), 8.63 (d, $J = 8.1$ Hz, 1H), 8.60 – 8.50 (m, 4H), 8.48 – 8.42 (m, 1H), 8.38 (dd, $J = 14.7, 8.1$ Hz, 2H), 8.27 (d, $J = 31.9$ Hz, 6H), 8.16 – 7.99 (m, 1H), 7.99 – 7.85 (m, 2H), 7.78 (s, 1H), 7.62 (dd, $J = 24.4, 5.2$ Hz, 1H), 7.54 (s, 1H), 7.49 (s, 1H), 7.44 – 7.24 (m, 1H). ESI-MS (cation): m/z 467 ($\text{M} - \text{H}^{2+}$), 935 ($\text{M} - 2\text{H}^+$).

5.2.4 DNA Binding Behavior

5.2.4.1 Photocleavage Competition Titration of

$[\text{Rh}(\text{bpy})_2\text{chrysi}]^{3+}$ with $[(\text{bpy})_2\text{Rh}(\text{phendione})\text{PtCl}_2]^{3+}$

A 17-mer DNA strand (5*'-TTAGGATCATCCATATA-3') (underline denotes the mismatch, asterisk denotes the radiolabel) was labeled with ^{32}P at the 5'-end with $[\text{P}^{32}]\text{-ATP}$ using polynucleotide kinase (PNK) at 37 °C for 2 h. The radiolabeled DNA



Scheme 5.6 Synthesis of $[(\text{bpy})_2\text{Rh}(\mu\text{-bzp})\text{PtCl}_2]^{3+}$.

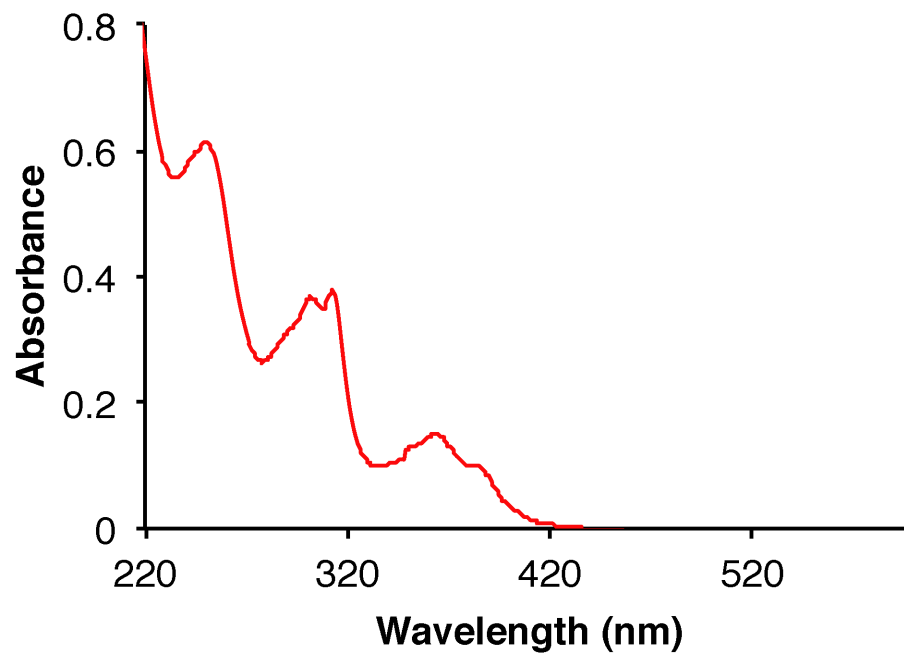


Figure 5.5 UV-visible spectrum of $[(bpy)_2Rh(\mu-bzp)PtCl_2]^{3+}$ in H_2O at pH 7.

was purified by gel electrophoresis and annealed with its fully matched complement or a complement strand containing a single CC mismatch at the designated site. To prepare samples for gel electrophoresis, 4 μM $[\text{Rh}(\text{bpy})_2\text{chrysi}]^{3+}$ (5 μL) and varying concentrations (0.5 – 50 μM) of $[(\text{bpy})_2\text{Rh}(\text{phendione})\text{PtCl}_2]^{3+}$ (5 μL) were added to 2 μM mismatched DNA duplex (10 μL). A light control (10 μL DNA, 10 μL H_2O) and a dark control (10 μL DNA, 5 μL $[\text{Rh}(\text{bpy})_2\text{chrysi}]^{3+}$, 5 μL $[(\text{bpy})_2\text{Rh}(\text{phendione})\text{PtCl}_2]^{3+}$, no irradiation) were also prepared. Samples were vortexed and, except for the dark control, irradiated on an Oriel (Darmstadt, Germany) 1000-W Hg/Xe solar simulator (340-440 nm) for 15 min. Samples were then incubated at 37 $^\circ\text{C}$ for either 30 min or 2h, dried, then electrophoresed through a 20 % denaturing polyacrylamide gel. The gel was exposed on a phosphor screen and phosphorimaged. The amounts of cleaved and platinated DNA were quantified (ImageQuant), and the fractions of DNA cleaved or platinated were normalized and plotted against the log of the concentration. The data were fit in OriginPro 8.1.

5.2.4.2 Photocleavage Titration of $[(\text{bpy})_2\text{Rh}(\mu\text{-bzip})\text{PtCl}_2]^{3+}$

A 29mer DNA hairpin with the sequence 5'-GGCAGGCATGGCTTTTTGCCATGCCTGCC-3' was labeled at the 5'-end with [^{32}P]-ATP using polynucleotide kinase (PNK) at 37 $^\circ\text{C}$ for 2 h. Mismatched hairpins of the same sequence, but containing either a CC or a GA mismatch at the sites indicated (underline denotes the site where mismatches were inserted) were similarly labeled. The radiolabeled DNA was purified by gel electrophoresis and annealed to by heating to 90 $^\circ\text{C}$ in buffer (100 mM NaCl, 20 mM NaP_i, pH 7.1), followed by slow cooling to ambient temperature over 3 h, to give a final concentration of 2 μM hairpin DNA. Racemic

solutions of $[(bpy)_2Rh(\mu-bzp)PtCl_2]^{3+}$ were prepared in Milli-Q water over a range of concentrations (estimated 1 – 50 μ M). For each sample, 2 μ M annealed hairpin DNA (10 μ l) and $[(bpy)_2Rh(\mu-bzp)PtCl_2]^{3+}$ at various concentrations (10 μ l) were combined to give 1 μ M duplex DNA as the final concentration. A “light” control, (\emptyset Rh, \emptyset Pt) consisting of 2 μ M DNA mixed with 10 μ l Milli-Q water, and a “dark” control (\emptyset *hv*), containing the DNA mixed with the highest concentration of $[(bpy)_2Rh(\mu-bzp)PtCl_2]^{3+}$ without irradiation, and a positive control, containing 1 μ M hairpin DNA containing a CC mismatch and 1 μ M *rac*- $[Rh(bpy)_2chrysi]^{3+}$ were also prepared. The samples were vortexed and, except for the dark control, irradiated on an Oriel (Darmstadt, Germany) 1000-W Hg/Xe solar simulator (340-440 nm) for 15 min. The samples were then incubated at 37 °C for 30-60 minutes to promote the formation of covalent platinum adducts and dried under vacuum. The irradiated samples were electrophoresed on a 20% denaturing polyacrylamide gel and exposed to a phosphor screen. The amounts of DNA in each band were analyzed by autoradiography and quantitated by phosphorimager (ImageQuant).

5.2.4.3 Analysis of DNA Binding

To assess the binding of photocleavage by $[(bpy)_2Rh(\mu-bzp)PtCl_2]^{3+}$ at the CC mismatch, the fraction of cleaved DNA was quantified and expressed as a percentage of the total DNA in each lane and plotted against the log of the (estimated) concentration of $[(bpy)_2Rh(\mu-bzp)PtCl_2]^{3+}$ in Origin Pro. DNA platination was analyzed in a similar manner, wherein the fraction of platinated DNA was quantified and expressed as a percentage of the total DNA in each lane and plotted against the log of the concentration of $[(bpy)_2Rh(\mu-bzp)PtCl_2]^{3+}$.

5.3 Results

5.3.1 Complexes Synthesized

Two bimetallic Rh(III)/Pt(II) DNA binding complexes have been synthesized in which both metal centers are coordinated to a bridging aromatic ligand designed to enter the DNA base stack. One complex employs a 1,10-phenanthroline-5,6-dione (“phendione”) intercalating ligand, and the other contains a benzo-fused expanded version of the phendione ligand, benzo[*b*][1,10]phenanthroline-5,6-dione (“bzp”), designed to target thermodynamically destabilized sites in DNA via the metalloinsertive binding mode. The bzp ligand is estimated to be approximately the same width as previously characterized inserting ligands 5,6-chrysenquinone (“chrysi”) and benzo[*a*]phenazine-5,6-dione (“phzi”), and thus was anticipated to target destabilized mismatched sites with equal precision.²³⁻²⁵

In both complexes, the ligands possess two bidentate coordination sites for each metal center. The di-quinone moiety coordinates to the rhodium center via base-catalyzed imine condensation with a *cis*-diammine rhodium precursor ($[\text{Rh}(\text{bpy})_2(\text{NH}_3)_2]^{3+}$).²⁶ Under condensation conditions, no evidence of N-heterocyclic chelation of the rhodium center was observed. Likewise, no chelation of the di-quinone to the platinum center was observed; in the synthesis of both complexes, platinum coordinates exclusively via the phenanthroline nitrogens. This differential coordination strategy affords a facile construction of the bimetallic system in good yields with few side products.

5.3.2 DNA Binding of $[(\text{bpy})_2\text{Rh}(\text{phendione})\text{PtCl}_2]^{3+}$

5.3.2.1 Binding of $[(bpy)_2Rh(\mu\text{-phendione})PtCl_2]^{3+}$ to a CC Mismatch

The DNA binding behavior of $[(bpy)_2Rh(\mu\text{-phendione})PtCl_2]^{3+}$ was characterized using 5'- ^{32}P -radiolabeled DNA with the sequence 5'-TTAGGATCATCCATATA-3' and its unlabeled well-matched complement as well as a complement containing a single CC mismatch (underline denotes the mismatch). As it was initially unclear whether or not $[(bpy)_2Rh(\mu\text{-phendione})PtCl_2]^{3+}$ would photocleave the DNA backbone upon binding, titrations were carried out in the absence of $[Rh(bpy)_2chrysi]^{3+}$. Increasing concentrations of the bimetallic complex were incubated with fixed concentrations of DNA and $[Rh(bpy)_2chrysi]^{3+}$, irradiated, and electrophoresed on a 20% denaturing polyacrylamide gel. A representative autoradiogram is shown in **Figure 5.6**. No photocleavage bands are observed for mismatched or well-matched DNA, but evidence of the formation of Pt-DNA crosslinks is visible. The complex exhibits a slight preference for platination of well-matched DNA versus mismatched. **Figure 5.6** also depicts the same gel but with the gain increased, and as such, a small amount of photocleavage can be observed at high concentrations of $[(bpy)_2Rh(\mu\text{-phendione})PtCl_2]^{3+}$ at the site of the mismatch, suggesting that the complex is capable of metalloinsertion. No other photocleavage was evident, so it is unclear from this experiment whether the complex can also intercalate between Watson-Crick base pairs.

The results of the initial photocleavage titration were promising, and so the mismatch recognition capabilities of $[(bpy)_2Rh(\mu\text{-phendione})PtCl_2]^{3+}$ were further characterized by means of a competition titration with $[Rh(bpy)_2chrysi]^{3+}$. A representative autoradiogram is shown in **Figure 5.7**. The fraction of DNA photocleaved

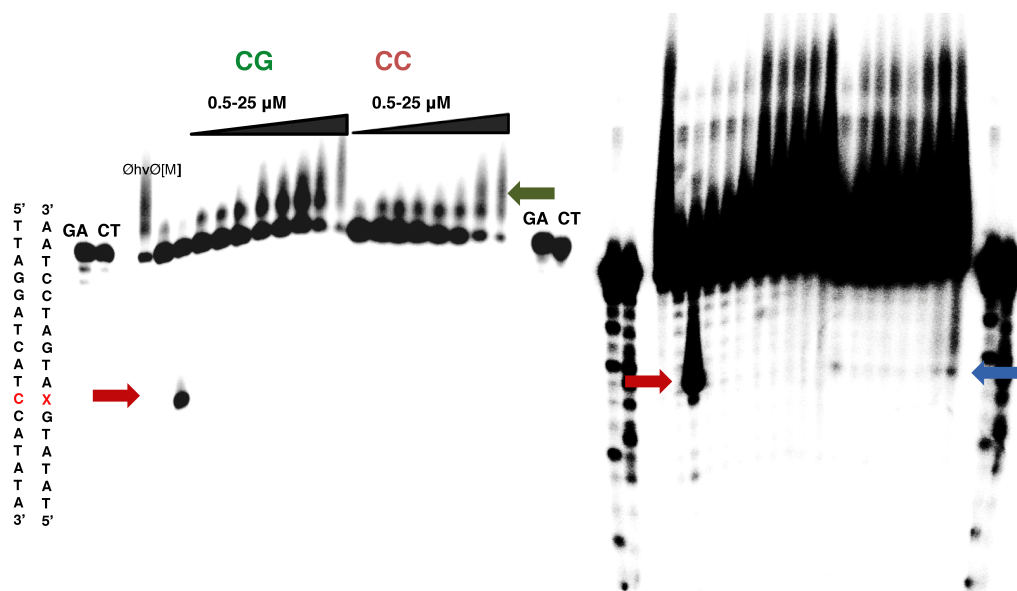


Figure 5.6 Photocleavage titration of $[(bpy)_2Rh(\mu\text{-phenidione})PtCl_2]^{3+}$ (0 – 25 μM) on 1 μM 5'- ^{32}P] labeled 17mer duplex DNA with a CC mismatch (denoted by “CC” in red) and a similarly well-matched sequence (denoted by “CG” in green). Samples were irradiated (340-440 nm) for 15 min and electrophoresed on a 20% denaturing polyacrylamide gel. Controls without irradiation ($\emptyset hv$), and without metal complex ($\emptyset [M]$) were included. A control sample of CC-mismatched duplex (1 μM) and $[Rh(bpy)_2\text{chrysi}]^{3+}$ (1 μM), which photocleaves DNA at mismatched sites, was also included; the resulting photocleavage product is indicated by the red arrow. The left autoradiogram is the photocleavage titration for both sequences at normal gain; no photocleavage by $[(bpy)_2Rh(\mu\text{-phenidione})PtCl_2]^{3+}$ is observed, although the presence of Pt-DNA adducts appear as bands of reduced electrophoretic mobility above the unmodified parent DNA (denoted by the green arrow). The right autoradiogram is the same gel at high gain, and faint photocleavage by $[(bpy)_2Rh(\mu\text{-phenidione})PtCl_2]^{3+}$ can be seen at the mismatch (denoted by the blue arrow), but not at well-matched sites.

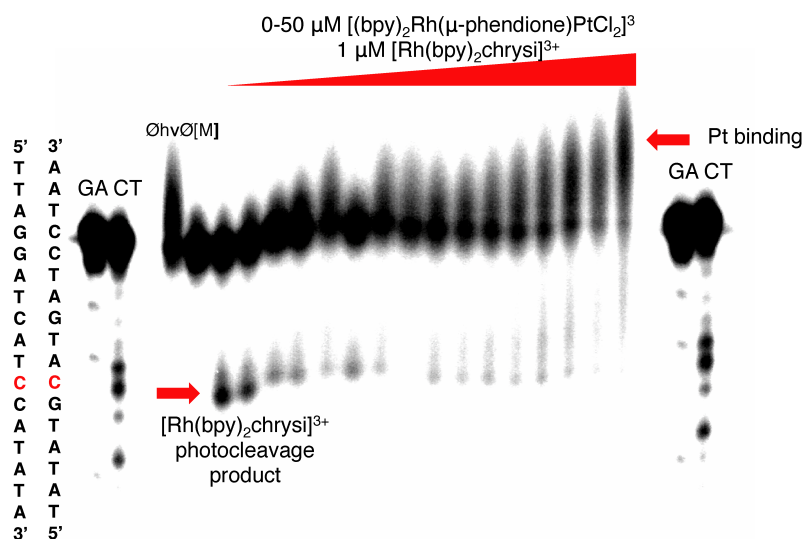


Figure 5.7 Competition titration of increasing concentrations of $[(bpy)_2Rh(\mu\text{-phendione})PtCl_2]^{3+}$ (0-50 μM) with 1 μM *rac*- $[Rh(bpy)_2chrysi]^{3+}$ on 1 μM 5'- $[^{32}\text{P}]$ labeled 17mer duplex DNA with a CC mismatch (denoted in red). Samples were irradiated (340-440 nm) for 15 min and electrophoresed on a 20% denaturing polyacrylamide gel. Controls without irradiation ($\emptyset hv$), and without metal complex ($\emptyset [M]$) were included. $[(bpy)_2Rh(\mu\text{-phendione})PtCl_2]^{3+}$ inhibits photocleavage by $[Rh(bpy)_2chrysi]^{3+}$ at the mismatched site. The site of photocleavage by $[Rh(bpy)_2chrysi]^{3+}$ at the mismatch is indicated by an arrow at bands located below the unmodified parent band. Bands of reduced electrophoretic mobility, located above the unmodified parent DNA, are indicative of covalent binding by the platinum subunit.

by $[\text{Rh}(\text{bpy})_2\text{chrysi}]^{3+}$ at the mismatch decreases with increasing concentrations of the conjugate. It is apparent that the bimetallic complex is fully capable of metalloinsertion at a CC mismatch, although the $[\text{Rh}(\text{bpy})_2\text{chrysi}]^{3+}$ is never fully outcompeted, even at high concentrations of competitor. Additionally, when the fraction of photocleaved DNA is plotted against the log of the concentration of $[(\text{bpy})_2\text{Rh}(\mu\text{-phendione})\text{PtCl}_2]^{3+}$ ($\log[\text{RhPt}]$), the data do not fit to a sigmoidal curve as is typically observed for photocleavage competition titrations with $[\text{Rh}(\text{bpy})_2\text{chrysi}]^{3+}$ (**Figure 5.8**).¹⁷ In fact, the data do not fit to any curve from which a binding affinity can be calculated. Likely, this disruption to the equilibrium binding of $[(\text{bpy})_2\text{Rh}(\mu\text{-phendione})\text{PtCl}_2]^{3+}$ to the mismatch is due to both the complex also performing intercalation at well-matched sites, as well as non-dissociation of the complex from DNA as it becomes covalently bound through the platinum center. Furthermore, distortions to the duplex caused by platinum crosslinking may also interfere with the equilibrium binding constant at the mismatch. Due to the presence of at least two – likely three – simultaneous binding interactions between $[(\text{bpy})_2\text{Rh}(\mu\text{-phendione})\text{PtCl}_2]^{3+}$ and mismatched DNA (metalloinsertion, platinum crosslinking, and metallointercalation), it is not possible to determine the binding affinity (K_B) of the complex at the mismatch.

5.3.2.2 Covalent Platinum Binding of

$[(\text{bpy})_2\text{Rh}(\text{phendione})\text{PtCl}_2]^{3+}$ to Mismatched and Well-Matched DNA

The formation of platinum-DNA crosslinks was analyzed *in vitro* via gel electrophoresis. Dissociation of the labile chloride ligands from the platinum center in solution enables the formation of covalent platinum adducts with DNA. As can be seen in the autoradiograms in **Figure 5.6** and **Figure 5.7**, platinum binding manifests as bands of

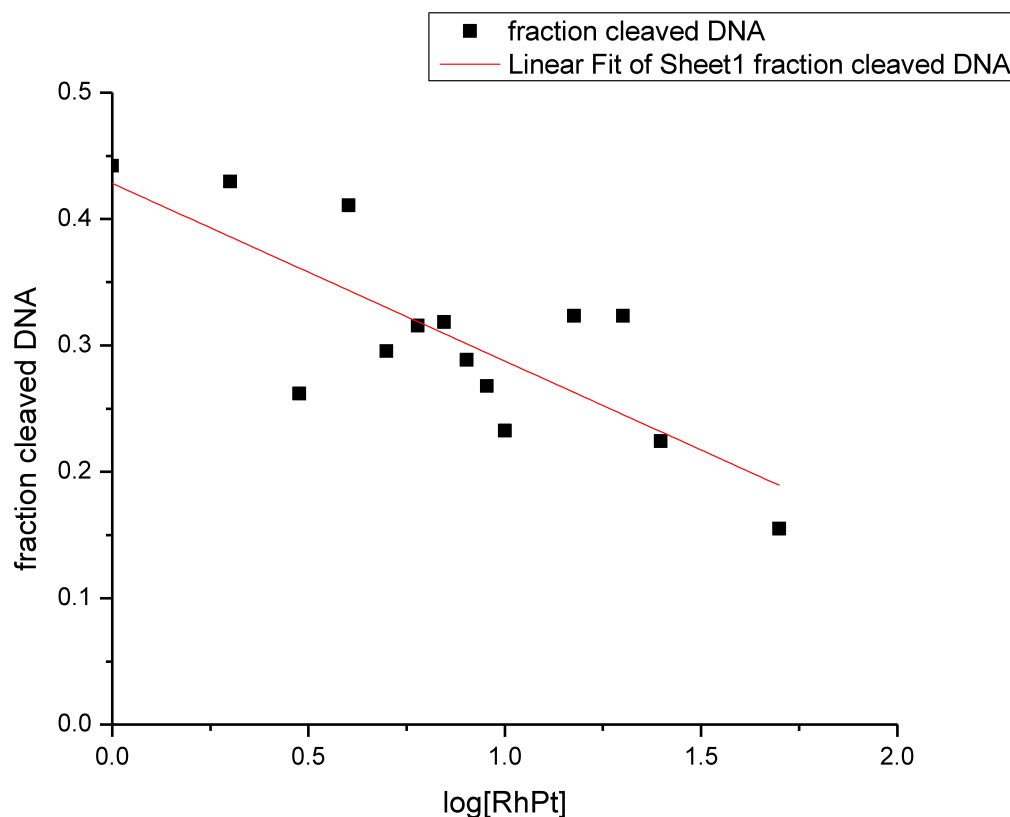


Figure 5.8 Representative plot of photocleavage competition titrations of $[(bpy)_2Rh(\mu\text{-phenidione})PtCl_2]^{3+}$ ($\log [RhPt]$) for binding constant determination at the CC mismatch. Experiments were conducted in buffer (50 mM NaCl, 10 mM NaP_i, pH 7.1) using 1 μ M duplex DNA and 1 μ M $rac\text{-}[Rh(bpy)_2chrysi]^{3+}$, with 0-50 μ M $[(bpy)_2Rh(\mu\text{-phenidione})PtCl_2]^{3+}$ competitor complex. Although the complex outcompetes $[Rh(bpy)_2chrysi]^{3+}$ at the mismatch, it does not follow the regular sigmoidal dose response curve characteristic of competition titrations, indicating that the equilibrium binding is disrupted. As such, an accurate binding affinity (K_B) for the CC mismatch could not be determined by this method. Data are representative of three independent gels.

reduced electrophoretic mobility, located above the unmodified parent DNA in the denaturing PAGE gel. In the comparison of platinum binding to mismatched versus well-matched duplex, a preference for covalent modification of well-matched DNA is apparent.

The fraction of platinated DNA by $[(bpy)_2Rh(phendione)PtCl_2]^{3+}$ was also explored as a function of both concentration and incubation time. Mismatched DNA was irradiated with varying concentrations of complex (0 – 50 μ M) for 15 min and incubated at 37 °C for either 30 min or 2 h. Samples were electrophoresed on a denaturing 20% polyacrylamide gel. The fraction of platinated DNA was quantified and plotted against the log of the concentration of metal complex. After 30 min. incubation, the fraction of Pt-DNA are plotted as a sigmoidal curve, and the percentage of platinated DNA never exceeded 100% (**Figure 5.9**), implying stoichiometric Pt:DNA binding. This behavior resembles the platinum binding characteristics of previous Rh-Pt metalloinsertor conjugates. However, platination interferes with determination of equilibrium binding.

At longer incubations, platinum crosslinking deviates significantly from previously observed behavior. As can be seen in the plot of the percentage of platinated DNA as a function of $[(bpy)_2Rh(phendione)PtCl_2]^{3+}$ concentration, the fraction of bound DNA increases exponentially with concentration (**Figure 5.10**). At the highest concentration (50 μ M metal complex) covalent binding exceeds 6:1 Pt:DNA ratio with no evidence of saturation. This curious platination behavior may be due in part to potential intercalation of the complex at several sites within the helix.

5.3.3 DNA Binding of $[(bpy)_2Rh(\mu\text{-bzip})PtCl_2]^{3+}$

5.3.3.1 Binding of $[(bpy)_2Rh(\mu\text{-bzip})PtCl_2]^{3+}$ to a CC Mismatch

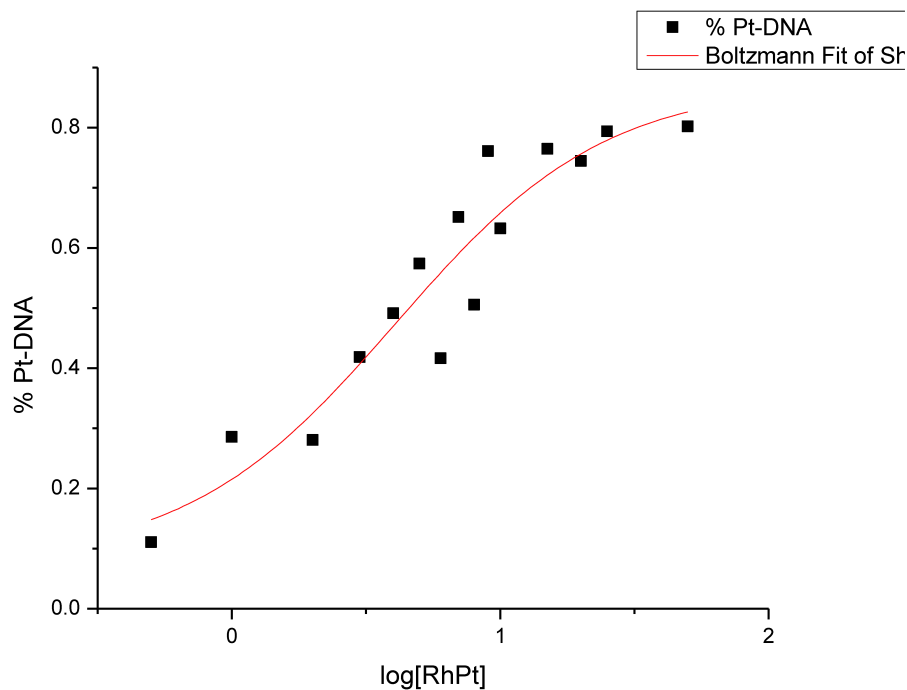


Figure 5.9 Representative sigmoidal curve fit of DNA platination by the platinum subunit of $[(bpy)_2Rh(phen)dione)PtCl_2]^{3+}$, from 0-50 μM ($\log [RhPt]$). $[(bpy)_2Rh(phen)dione)PtCl_2]^{3+}$ was incubated with duplex DNA containing a CC mismatch and a d(GpG) site at 37 °C for 30 min to promote the formation of covalent Pt-DNA adducts. Samples were electrophoresed on a 20% denaturing PAGE gel. The amount of platinated DNA is expressed as a fraction of the total DNA in each sample (%Pt-DNA). Data are representative of three independent gels.

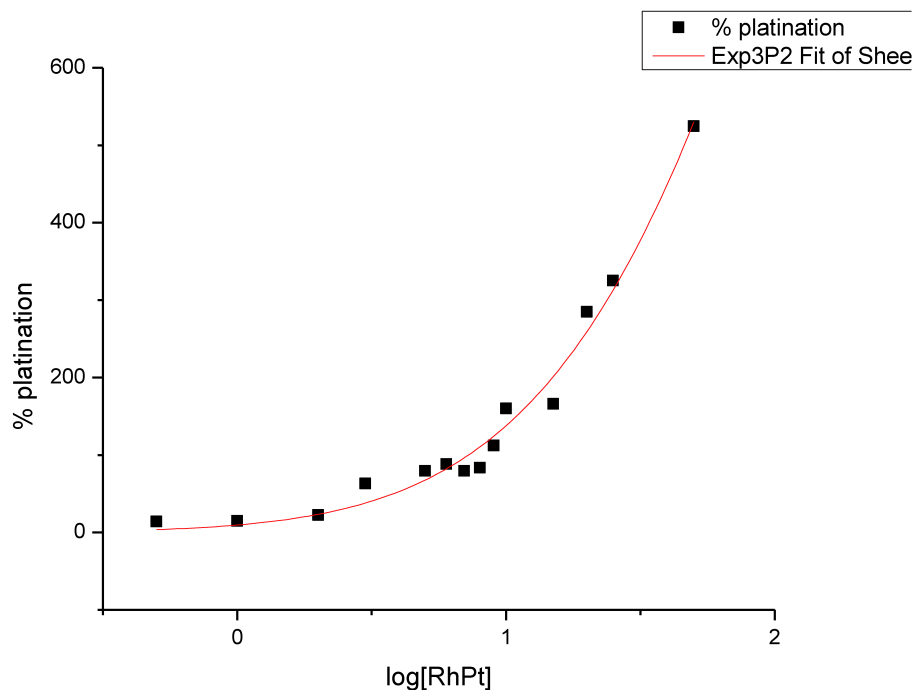


Figure 5.10 Representative exponential curve fit of DNA platinated by the platinum subunit of $[(bpy)_2Rh(phendione)PtCl_2]^{3+}$, from 0-50 μM ($\log [RhPt]$). $[(bpy)_2Rh(phendione)PtCl_2]^{3+}$ was incubated with duplex DNA containing a CC mismatch and a d(GpG) site at 37 °C for 2h to promote the formation of covalent Pt-DNA adducts. Samples were electrophoresed on a 20% denaturing PAGE gel. The amount of platinated DNA is expressed as a fraction of the total DNA in each sample (%Pt-DNA). After a 2h incubation period, a 6-fold excess of platinated DNA was observed compared to the 30 minute incubation period. Data are representative of three independent gels.

The DNA binding of $[(bpy)_2Rh(\mu-bzp)PtCl_2]^{3+}$ was analyzed with a 5'-end radiolabeled 29mer DNA hairpin containing a single CC mismatch of the sequence 5'-GGCAGGCATGGCTTTTTGCCATGCCTGCC-3' (underline denotes the mismatch) (**Figure 5.11**). A band of increased electrophoretic mobility appears at the mismatched site for samples that were irradiated in the presence of the complex, indicating photocleavage at the CC mismatch. This is confirmed by comparison to the positive control, wherein the DNA hairpin is irradiated in the presence of first-generation metalloinsertor $[Rh(bpy)_2chrysi]^{3+}$, which photocleaves DNA on the sugar-phosphate backbone at the site of the mismatch.²³ These results are in contrast with the weak photocleavage observed for the $[(bpy)_2Rh(phenidione)PtCl_2]^{3+}$ intercalator analogue. Surprisingly, whereas $[Rh(bpy)_2chrysi]^{3+}$ has previously been shown to exhibit increased photocleavage product with increasing concentrations against a fixed level of DNA – suggestive of enhanced photocleavage efficiency as a result of DNA binding²³⁻²⁵ – the photocleavage band *decreases* with increasing concentration of $[(bpy)_2Rh(\mu-bzp)PtCl_2]^{3+}$. Furthermore, the appearance of platinum-DNA crosslinks, represented as bands of reduced electrophoretic mobility located above the unmodified parent bands in the autoradiogram, *increases* as a function of $[(bpy)_2Rh(\mu-bzp)PtCl_2]^{3+}$ concentration, as expected. Quantification of the bands representing rhodium and platinum binding as a function of metalloinsertor concentration is depicted in **Figure 5.12**. Here, it appears that platinum DNA crosslinking and metalloinsertive photocleavage at a mismatch are inhibitory, rather than complementary. Furthermore, the fraction of photocleaved DNA (as well as the fraction of platinated DNA) do not follow a sigmoidal curve pattern when plotted against concentration, similar to the behavior that was observed for the

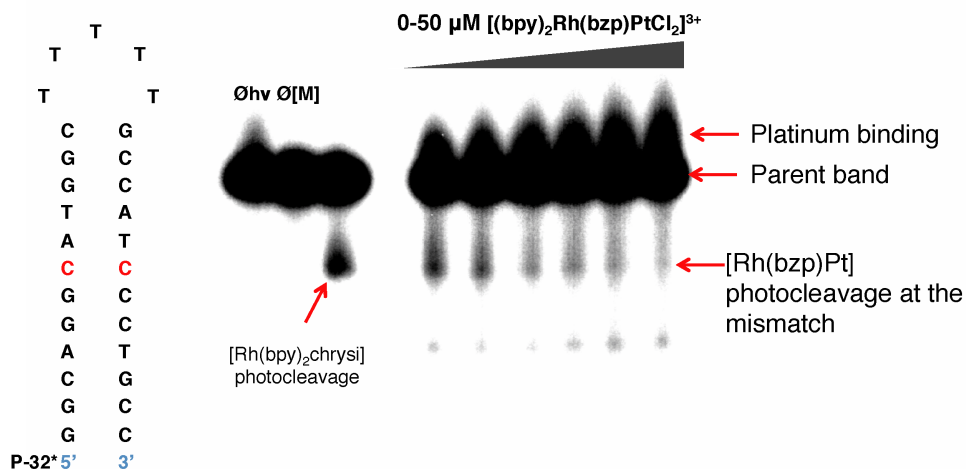


Figure 5.11 Photocleavage titration of $[(\text{bpy})_2\text{Rh}(\mu\text{-bzp})\text{PtCl}_2]^{3+}$ (0 – 50 μM) on 1 μM 5'- ^{32}P] labeled 29mer hairpin DNA with a CC mismatch (denoted by “CC” in red). Samples were irradiated (340-440 nm) for 15 min and electrophoresed on a 20% denaturing polyacrylamide gel. Controls without irradiation ($\emptyset\text{hv}$), and without metal complex ($\emptyset[\text{M}]$) were included. A control sample of CC-mismatched duplex (1 μM) and $[\text{Rh}(\text{bpy})_2\text{chrysi}]^{3+}$ (1 μM), which photocleaves DNA at mismatched sites, was also included; the resulting photocleavage product is indicated by the red arrow. Photocleavage at the CC mismatch by $[(\text{bpy})_2\text{Rh}(\mu\text{-bzp})\text{PtCl}_2]^{3+}$ can also be observed (indicated by the “Rh(bzp)Pt” arrow); however, this photocleavage unexpectedly *decreases* with increasing concentration of complex. The formation of Pt-DNA adducts is also observed, indicated by bands of reduced electrophoretic mobility above the unmodified parent DNA. Platinum binding increases with increasing concentration of $[(\text{bpy})_2\text{Rh}(\mu\text{-bzp})\text{PtCl}_2]^{3+}$.

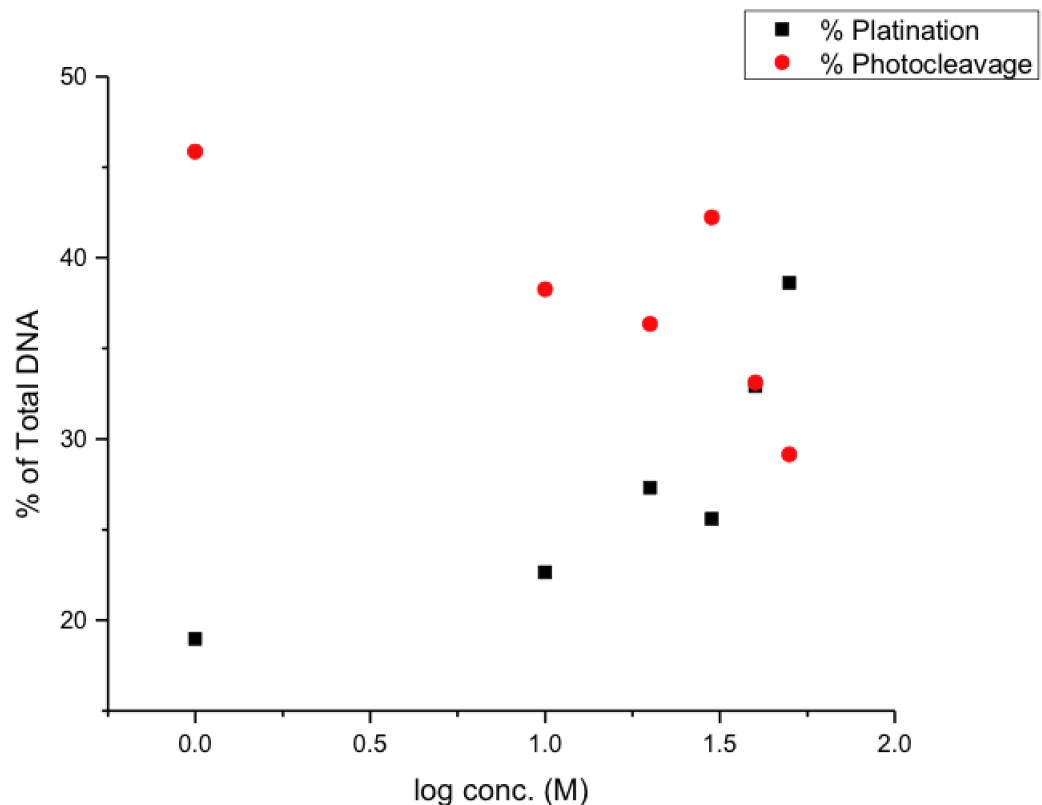


Figure 5.12 Quantification of the percentage of DNA containing a CC mismatch (1 μM) that is photocleaved (red circles) by $[(\text{bpy})_2\text{Rh}(\mu\text{-bzp})\text{PtCl}_2]^{3+}$ as a function of complex concentration (0 – 50 μM) after irradiation (340-440 nm) for 15 min followed by electrophoresis on a 20% denaturing polyacrylamide gel. The black squares represent the percentage of platinated DNA under the same conditions. Each point is expressed as the percentage of either photocleavage or platination product relative to the total DNA in each lane. The fraction of photocleaved DNA decreases, while the fraction of platinated DNA increases, implying that the two processes impede one another.

bimetallic intercalator complex. Consequently, reliable a K_B binding constant cannot be calculated for this mismatched site. Finally, it should be noted that, in addition to photocleavage at the mismatched site, additional photocleavage products also appear in the autoradiogram, albeit to a lesser degree than the mismatch photocleavage product, suggestive of non-specific binding interactions.

5.3.3.2 Binding of $[(bpy)_2Rh(\mu-bzp)PtCl_2]^{3+}$ to a GA Mismatch

Although the inhibitory relationship between mismatch recognition and platinum crosslinking for $[(bpy)_2Rh(\mu-bzp)PtCl_2]^{3+}$ was unexpected, the complex still displays moderately selective photocleavage at the site of a CC mismatch. We examined the behavior of the complex in the presence of a less thermodynamically destabilized mismatch, such as a GA site. The binding titration was carried out as described above, and the resulting autoradiogram is shown in **Figure 5.13**. Here, photocleavage does not occur at the mismatched site; however, photocleavage products can be seen at other sites throughout the sequence, primarily at purine residues (although, notably, photocleavage does *not* occur at the purine-purine mismatch). Unlike photocleavage at a CC mismatch, this nonspecific strand scission does appear to increase as a function of metalloinsertor concentration, as does the formation of Pt-DNA crosslinks, suggesting that photocleavage and platination occur concomitantly. It is curious that these alternative binding modes are observed, since the purported width of the bzp inserting ligand should preclude nonspecific intercalation. It is possible that partial intercalation, involving side-on binding of the complex to DNA, occurs in the absence of a sufficiently destabilized site and is facilitated by platinum binding. Furthermore, these nonspecific photocleavage bands are not inhibited by the increased platination; rather, photocleavage and covalent

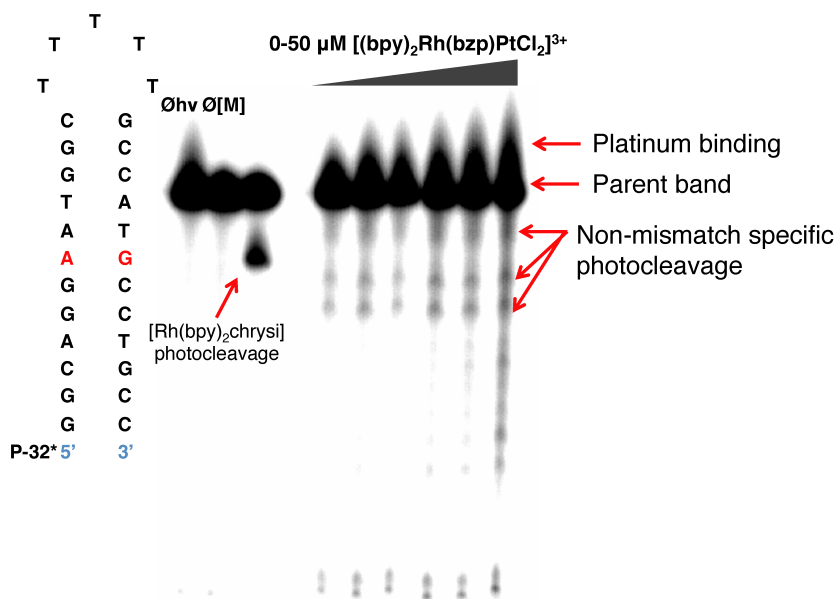


Figure 5.13 Photocleavage titration of $[(bpy)_2Rh(\mu-bzp)PtCl_2]^{3+}$ (0 – 50 μM) on 1 μM 5'- $[^{32}P]$ labeled 29mer hairpin DNA with a GA mismatch (denoted by “GA” in red). Samples were irradiated (340-440 nm) for 15 min and electrophoresed on a 20% denaturing polyacrylamide gel. Controls without irradiation ($\emptyset hv$), and without metal complex ($\emptyset [M]$) were included. A control sample of CC-mismatched duplex (1 μM) and $[Rh(bpy)_2chrysi]^{3+}$ (1 μM), which photocleaves DNA at mismatched sites, was also included; the resulting photocleavage product is indicated by the red arrow. Nonspecific photocleavage at purines by $[(bpy)_2Rh(\mu-bzp)PtCl_2]^{3+}$ can be observed; however, this photocleavage increases with increasing concentration of complex. The formation of Pt-DNA adducts is also observed, indicated by bands of reduced electrophoretic mobility above the unmodified parent DNA. Platinum binding also increases with increasing concentration of $[(bpy)_2Rh(\mu-bzp)PtCl_2]^{3+}$.

platinum binding concurrently increase with increasing concentration of the complex. The oppositional nature of photocleavage and platination, it would seem, is reserved exclusively for the recognition of thermodynamically destabilized mismatches by metalloinsertion.

5.3.3.3 Binding of $[(bpy)_2Rh(\mu-bzp)PtCl_2]^{3+}$ to Mismatched and Well-Matched DNA Hairpins

Finally, to assess whether the complex exhibits any selective DNA binding, the complex was irradiated in the presence of DNA hairpins that were either fully matched or containing a single CC mismatch. As can be seen in **Figure 5.14**, the binding of $[(bpy)_2Rh(\mu-bzp)PtCl_2]^{3+}$ to the well-matched hairpin strongly resembles that of the hairpin containing a GA mismatch (**Figure 5.13**) – that is, the complex photocleaves at the same residues (which appear to be the guanine residues) in both sequences in the absence of a thermodynamically destabilized site. Furthermore, this photocleavage pattern is concentration-dependent and concomitant with platinum binding. In the presence of a CC-mismatched hairpin, however, photocleavage at the destabilized mismatched site is largely independent of complex concentration and the extent of platinum-DNA crosslinks. Furthermore, the photocleavage products observed in the presence of well matched or GA-mismatched DNA are largely absent in the CC-mismatched sequence. It is possible that metalloinsertion at a mismatch precludes the formation of nonspecific photodamage products; some minor photodamage can be observed at well-matched sites, although these products appear to a much lesser degree than cleavage at the mismatch. As a result, the bimetallic $[(bpy)_2Rh(\mu-bzp)PtCl_2]^{3+}$

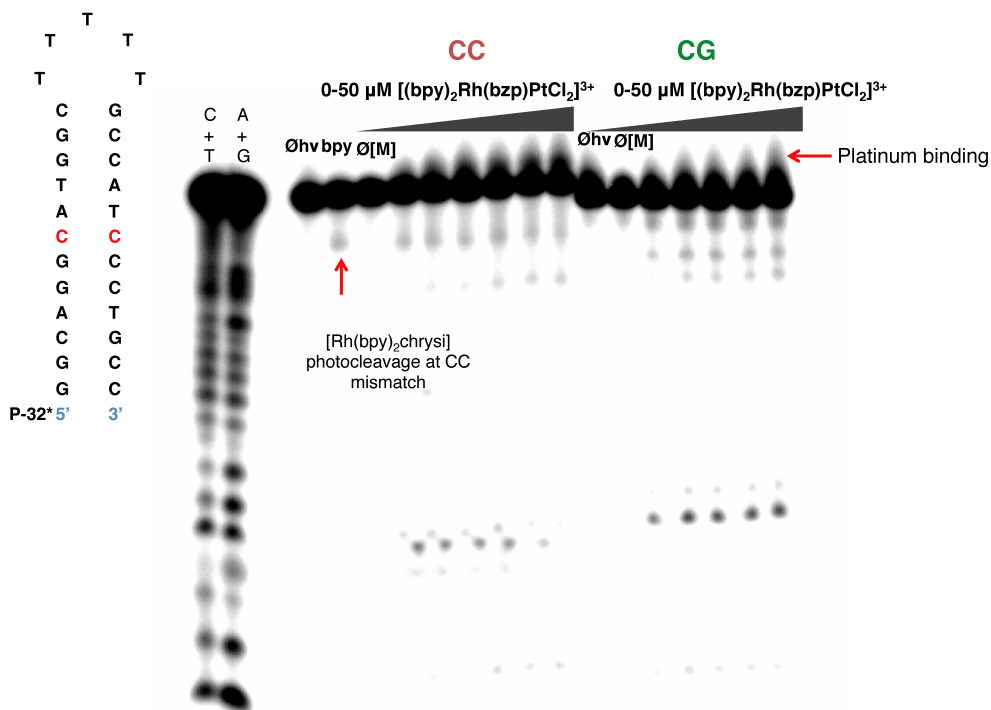


Figure 5.14 Photocleavage titration of $[(bpy)_2Rh(\mu-bzp)PtCl_2]^{3+}$ (0 – 50 μM) on 1 μM 5'- $[^{32}P]$ labeled 29mer hairpin DNA with a CC mismatch (denoted by “CC” in red) and a similarly well-matched sequence (denoted by “CG” in green). Samples were irradiated (340-440 nm) for 15 min and electrophoresed on a 20% denaturing polyacrylamide gel. Maxam-Gilbert sequencing lanes (C+T and A+G) are shown on the left. Controls without irradiation ($\emptyset hv$), and without metal complex ($\emptyset [M]$) were included. A control sample of CC-mismatched duplex (1 μM) and $[Rh(bpy)_2chrysi]^{3+}$ (1 μM), which photocleaves DNA at mismatched sites, was also included; the resulting photocleavage product is indicated by the red arrow. As shown previously in **Figure 5.11**, the complex photocleaves at the CC mismatch. In the presence of well-matched DNA, the complex behaves as in **Figure 5.13**, performing nonspecific photocleavage. For both CC-mismatched and well-matched sequences, platination (indicated by the arrow) increases with concentration.

complex displays distinctive binding modes that appear to depend on the thermodynamic stability of the nucleic acid duplex.

The percentages of platinated DNA for mismatched and well matched sequences were quantified and the results are shown in **Figure 5.15**. The complex displays little preferential binding for either type of DNA – if anything, a slight preference for well-matched DNA is observed. However, the effects of irradiation with long-wave UV light (340-440 nm) appear to have profound effects on platination levels for mismatched DNA, but not for well-matched (**Figure 5.16**). In the absence of irradiation, platination of well-matched DNA remains unchanged. For the CC-mismatched hairpin, however, platination is significantly attenuated in the dark, but is enhanced to levels similar to that of well-matched DNA upon irradiation. Although the photosensitivity of platinum complexes is known,²⁷ the light-dependence of platinum binding for mismatched DNA, but not well-matched (and, presumably, GA-mismatched DNA), serves to further confirm that at least two distinct binding modes exist for $[(bpy)_2Rh(\mu-bzp)PtCl_2]^{3+}$, depending on the thermodynamic stability of the DNA to which it binds.

5.4 Discussion

The complexes described herein are comprised of two metal centers coordinated to a planar aromatic ligand that interacts with the nucleobase π -stack of DNA. Two structural analogues were synthesized, one containing an intercalating phendione ligand, while the other incorporated a sterically expanded analogue of phendione that was anticipated to target DNA mismatches through metalloinsertion. In both cases, injection of the bridging ligand into the helix is intended to situate the square planar platinum (II) center directly in the helix at the point of intercalation/insertion, while the distally

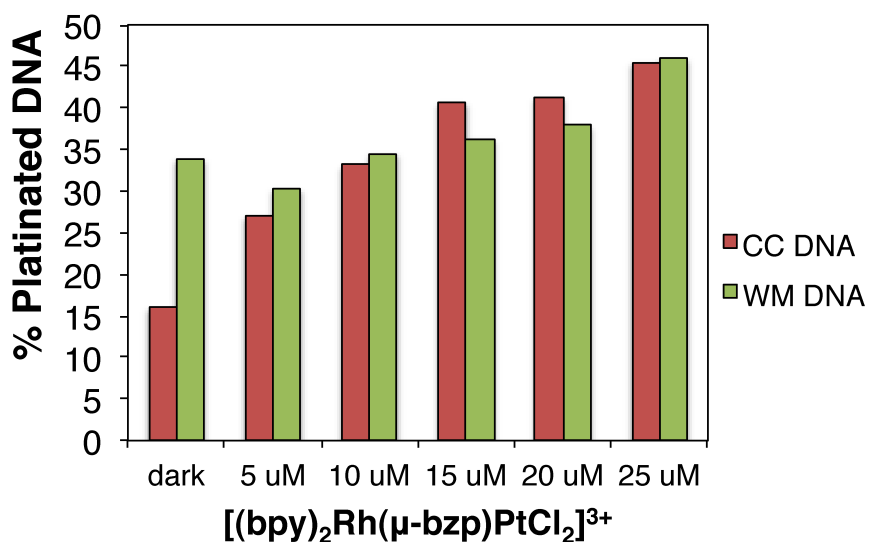


Figure 5.15 Quantification of the percentage of hairpin DNA containing a CC mismatch (red) or is fully matched (green) (1 μM) that is platinated by $[(bpy)_2Rh(\mu-bzp)PtCl_2]^{3+}$ as a function of complex concentration (0 – 50 μM) after irradiation (340–440 nm) for 15 min (except for the dark control, “dark”) followed by electrophoresis on a 20% denaturing polyacrylamide gel. Each point is expressed as the percentage of either photocleavage or platination product relative to the total DNA in each lane. Little difference in platinum crosslinking is observed for mismatched versus well-matched DNA, except in the absence of irradiation, where platinum binding of mismatched DNA is significantly attenuated. Data are representative of three independent gels.

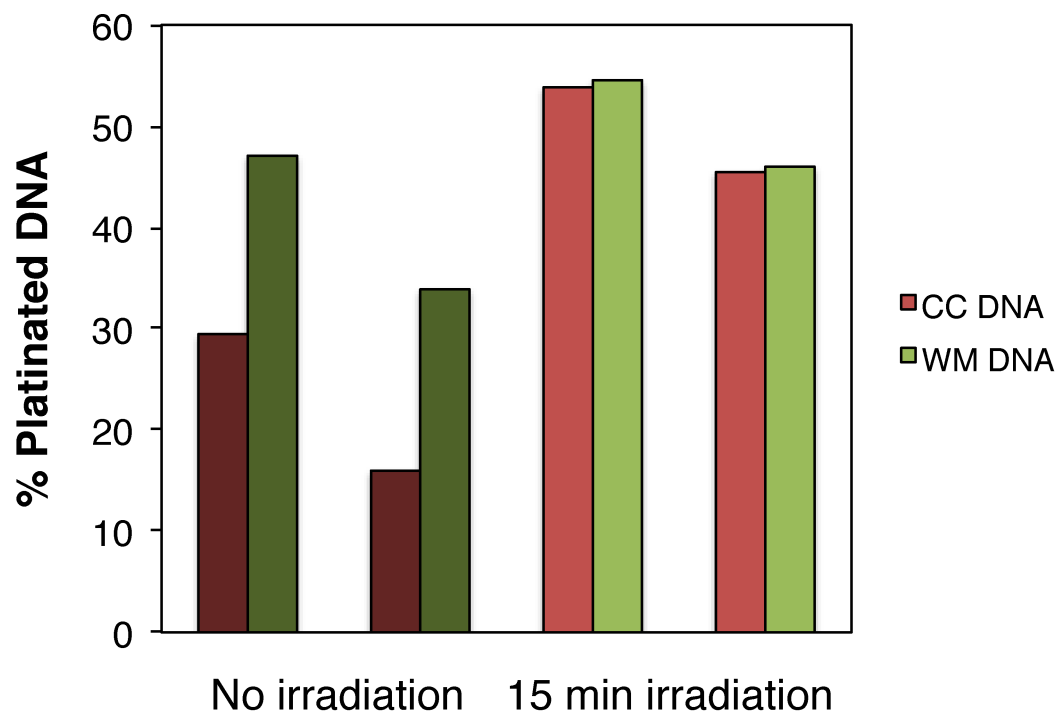


Figure 5.16 Quantification of the percentage of platinated CC-mismatched (“CC DNA,” red) and well-matched (“WM DNA,” green) hairpin DNA by $[(bpy)_2Rh(\mu-bzp)PtCl_2]^{3+}$ (50 μ M) either in the absence of irradiation (dark red and dark green for CC and WM DNA, respectively) or after 15 min irradiation (340-440 nm) (light red and light green for CC and WM DNA, respectively). Platination of mismatched DNA is attenuated in the absence of light, but irradiation has little effect on the binding of well-matched DNA.

coordinated octahedral rhodium center resides in the groove. This design contrasts with well-studied examples of dinuclear DNA binding complexes, which typically involve two inert centers (usually ruthenium (II)) that both contain sterically bulky ancillary ligands.^{28,29} Complexes of this nature are bridged by lengthy intercalating ligands and purportedly bind DNA through a kinetically slow “threading” mechanism that involves passing the bulky ancillary substituents through the base stack through severe DNA distortions.³⁰ The square planar *cis*-dichloroplatinum (II) moiety is quite flat by comparison, even with the relatively large platinum and chlorine atoms, and we considered it more likely to fit into the base stack.

DNA binding experiments have demonstrated that, in the presence of the mismatch, both the bridging intercalating and inserting ligands can successfully insert into the helix, as evidenced by the competitive displacement of the $[\text{Rh}(\text{bpy})_2\text{chrysi}]^{3+}$ at a CC mismatch. This also implies that both complexes bind the mismatched sites from the minor groove of DNA. The defining characteristic of the metalloinsertion binding mode, the ejection of the mismatched bases from the duplex to make room for the expansive incoming ligand,³¹⁻³⁴ likely also facilitates accommodation of the platinum substituent in the helix. However, the presence of the platinum center severely disrupts the apparent equilibrium of metalloinsertion for both complexes, as is evidenced by the irregular competition titration curves. It is unclear whether this is due to the formation of covalent platinum adducts, or due to the mere presence of the relatively sizeable platinum center in the base stack. It is potentially a combination of these two factors; threading intercalator complexes, for instance, display substantially reduced association and dissociation rates compared to their monomeric analogues.³⁰ Previously characterized

conjugates where the platinum is appended to a rhodium ancillary ligand have not demonstrated such interference with the binding affinity for a mismatch through the covalent coordination of DNA.^{3,5}

It was less apparent from these experiments whether the phendione complex is also able to intercalate into the duplex at Watson-Crick base pairs. The unusual platinum binding behavior at long incubation period, however, has never been observed for previous metalloinsertor-platinum conjugates – a six fold excess of platinum binding to DNA does not occur for these complexes even in 50-100 fold excess concentrations, due to duplex distortions incurred by crosslinked platinum that preclude the coordination of additional equivalents.⁵ Indeed, even the $[(bpy)_2Rh(\mu-bzp)PtCl_2]^{3+}$ analogue does not display this platination efficiency. It is possible that the intercalation of multiple equivalents of $[(bpy)_2Rh(phendione)PtCl_2]^{3+}$ stabilizes and rigidifies the duplex, enabling the coordination of extremely high platinum stoichiometries. Additionally, the positioning of the complex upon binding to DNA could affect the rates of crosslinking: metallointercalation from the major groove could potentially favor excessive platinum binding more so than metalloinsertion from the minor groove.

The behavior of the metalloinsertor analogue, $[(bpy)_2Rh(\mu-bzp)PtCl_2]^{3+}$, is even more unusual. Unlike $[(bpy)_2Rh(phendione)PtCl_2]^{3+}$, the complex displays robust photocleavage of DNA upon long-wave UV irradiation. However, $[(bpy)_2Rh(\mu-bzp)PtCl_2]^{3+}$ appears to exhibit very different binding modes depending on the thermodynamic stability of the DNA oligonucleotide to which it is bound. In the presence of fully matched DNA or DNA containing a more stabilized mismatch, such as GA, the complex performs photocleavage at several purine residues throughout the sequence.

This photocleavage is dose-dependent and increases concomitantly with increasing platination levels. It is unclear why this photocleavage occurs; it is possible that platination of the DNA at purine residues situates the bzp ligand such that a side-on intercalation of the ligand occurs. In contrast, in the presence of DNA containing a CC mismatch, $[(bpy)_2Rh(\mu-bzp)PtCl_2]^{3+}$ does photocleave at the destabilized site, but this photocleavage is not concentration-dependent, while platinum binding is. In fact, photocleavage at a mismatch and platinum crosslinking appear to be at odds with one another in the presence of mismatched DNA. It should be noted, however, that the apparent inhibition of photocleavage by platinum binding does not necessarily indicate the inhibition of metalloinsertion at the mismatch; many monomeric rhodium metalloinsertor complexes are known to bind destabilized sites with high affinity even if they do not possess photocleavage ability.^{17,19} It is possible that merely the DNA strand scission is attenuated, while the complex is still allowed to bind.

Additional evidence supporting the notion of differential binding of $[(bpy)_2Rh(\mu-bzp)PtCl_2]^{3+}$ to mismatched versus well-matched DNA is the apparent effect of UV irradiation on platinum crosslinking. In the absence of irradiation, adduct formation at DNA containing a CC mismatch is significantly attenuated, while there is no difference in the platination of well-matched DNA in the presence and absence of UV light. One potential explanation is that irradiation of mismatch-bound complex facilitates photolysis of the platinum center; perhaps the platinum center reacts with the C1' radical that forms at the deoxyribose sugar adjacent to the mismatched site upon metalloinsertor photocleavage.²³⁻²⁵ This would also explain the apparent light-independence observed with the complex in the presence of well-matched or GA-mismatched sequences, where

metalloinsertion does not occur. If the complex thus encounters a DNA oligomer sequence that precludes metalloinsertion, then the platinum is simply free to crosslink the DNA once it has been thermally or photochemically activated through the displacement of the chloride ligands. **Figure 5.17** depicts a schematic of the proposed differential binding modes for $[(bpy)_2Rh(\mu-bzp)PtCl_2]^{3+}$ at mismatched and well-matched DNA.

5.5 Conclusions

We have constructed two mixed-metal Rh-Pt complexes, $[(bpy)_2Rh(phen)dione)PtCl_2]^{3+}$ and $[(bpy)_2Rh(\mu-bzp)PtCl_2]^{3+}$, wherein the metal centers are bridged by a planar ligand possessing either intercalative or insertive DNA binding capabilities, respectively. These complexes display bifunctional DNA binding properties through both metalloinsertion at thermodynamically destabilized sites in addition to the formation of covalent platinum adducts. In the case of the $[(bpy)_2Rh(phen)dione)PtCl_2]^{3+}$, a third, intercalative binding mode is also possible. The direct insertion of the platinum metal center into the base stack at the mismatched site imparts major disruptions to the apparent equilibrium binding constant of the rhodium-chrysi moiety at the mismatch. In the case of the $[(bpy)_2Rh(\mu-bzp)PtCl_2]^{3+}$, the complex exhibits differential binding modes in the presence of mismatched versus well-matched DNA. The presence of a destabilized site alters both the intercalative/insertive properties of the bzp ligand as well as the efficiency of platinum binding. While the intended outcome of this design was the intrinsic linkage of platination to mismatch recognition, the two binding modes are in fact at odds with one another – one binding function inhibits the other at the mismatched site. In addition, these distinctive DNA binding behaviors do not lead to an enhancement of platination of mismatched DNA over well-matched; in fact, both complexes appear to

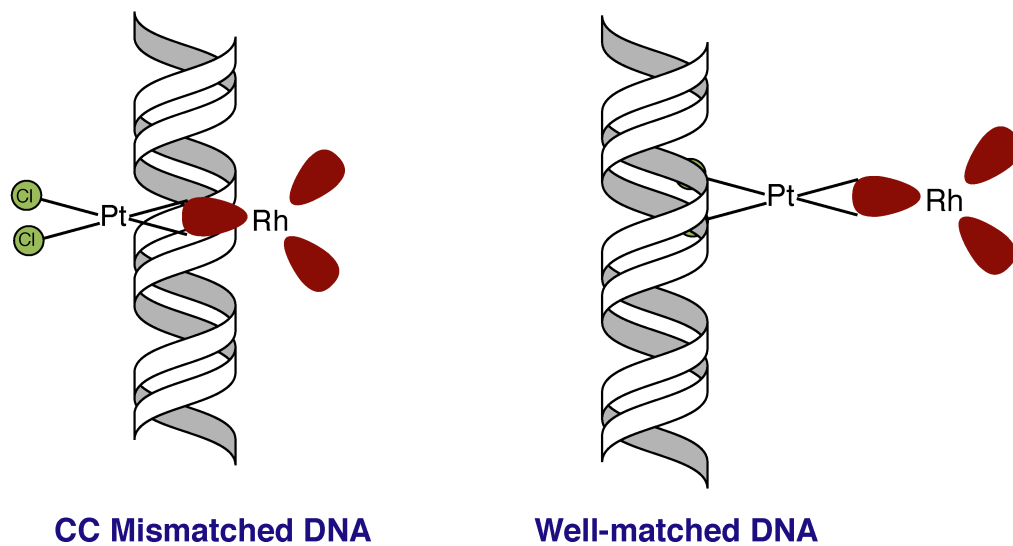


Figure 5.17 Schematic of hypothesized binding interactions of $[(bpy)_2Rh(\mu\text{-}bzp)PtCl_2]^{3+}$ in the presence of mismatched DNA (left) versus well-matched DNA (right). When the complex encounters a destabilized site, the expansive bzp ligand inserts into the duplex, placing the platinum center in the intervening space. It is possible that, upon irradiation, reaction between the resulting deoxyribose radical and the platinum center reduces photocleavage efficiency and releases the platinum, enabling crosslinking. In the absence of a destabilized site, platination of DNA is driven solely by thermal activation of the complex via hydrolysis of the labile chloride ligands.

preferentially bind well-matched DNA. While this likely limits the potential therapeutic applications of these complexes in targeted chemotherapy, the unusual DNA binding properties of these complexes merit further investigation into their biological activity.

5.6 References

- 1 Schatzschneider, U.; Barton, J. K. *J. Am. Chem. Soc.* **2004**, *126*, 8630–8631.
- 2 Lim, M. H.; Lau, I. H.; Barton, J. K. *Inorg. Chem.* **2007**, *46*, 9528–9530.
- 3 Petitjean, A.; Barton, J. K. *J. Am. Chem. Soc.* **2004**, *126*, 14728–14729.
- 4 Brunner, J.; Barton, J. K. *Biochemistry* **2006**, *45*, 12295–12302.
- 5 Weidmann, A. G.; Barton, J. K. *Inorg. Chem.* **2014**, *53*, 7812-7814.
- 6 Mansour, V. H.; Rosenberg, B.; Vancamp, L.; Trosko, J. E. *Nature* **1969**, *222*, 385–386.
- 7 Wheate, N. J.; Walker, S.; Craig, G. E.; Oun, R. *Dalton Trans.* **2010**, *39*, 8113–8127
- 8 Kelland, L. R.; Sharp, S. Y.; O'Neill, C. F.; Raynaud, F. I.; Beale, P. J.; Judson, I. *R. J. Inorg. Biochem.* **1999**, *77*, 111–115.
- 9 Jamieson, E. R.; Lippard, S. J. *Chem. Rev.* **1999**, *99*, 2467-2498.
- 10 Wang, D.; Lippard, S. J. *Nat. Rev. Drug Discovery* **2005**, *4*, 307–320.
- 11 Homesley, H. D.; Bundy, B. N.; Hurteau, J. A.; Roth, L. M. *Gynecol. Oncol.* **1999**, *72*, 131-137.
- 12 Weidmann, A. G.; Komor, A. C.; Barton, J. K. *Comments in Inorg. Chem.* **2014**, *34*, 114-123.
- 13 Weidmann, A. G.; Barton, J. K. *Manuscript in preparation* (See Thesis Chapter 4).
- 14 Ernst, R. J. *Unpublished results.*
- 15 Hart, J. R.; Glebov, O.; Ernst, R. J.; Kirsch, I. R.; Barton, J. K. *Proc. Natl. Acad. Sci. U.S.A.* **2006**, *103*, 15359–15363.

- 16 Karran, P.; Offman, J.; Bignami, M. *Biochimie* **2003**, *85*, 1149-1160.
- 17 Ernst, R. J.; Song, H.; Barton, J. K. *J. Am. Chem. Soc.* **2009**, *131*, 2359–2366.
- 18 Ernst, R. J.; Komor, A. C.; Barton, J. K. *Biochemistry* **2011**, *50*, 10919–10928.
- 19 Komor, A. C.; Schneider, C. J.; Weidmann, A. G.; Barton, J. K. *J. Am. Chem. Soc.* **2012**, *134*, 19223–19233.
- 20 Weidmann, A. G.; Komor, A. C.; Barton, J. K. *Philos. Trans. R. Soc. A.* **2013**, *371*, 20120117.
- 21 Weidmann, A. G. *Unpublished results*
- 22 Roy, S.; Hagen, K. D.; Maheswari, P. U.; Lutz, M.; Spek, A. L.; Reedijk, J.; van Wezel, G. P. *Chem. Med. Chem.* **2008**, *3*, 1427-1434.
- 23 Jackson, B. A.; Barton, J. K. *J. Am. Chem. Soc.* **1997**, *119*, 12986–12987.
- 24 Jackson, B. A.; Alekseyev, V. Y.; Barton, J. K. *Biochemistry* **1999**, *38*, 4655–4662.
- 25 Jackson, B. A.; Barton, J. K. *Biochemistry* **2000**, *39*, 6176–6182.
- 26 Murner, H.; Jackson, B. A.; Barton, J. K. *Inorg. Chem.* **1998**, *37*, 3007–3012.
- 27 Bednarski, P. J.; Mackay, F. S.; Sadler, P. J. *Anticancer Agents Med. Chem.* **2007**, *7*, 75-93.
- 28 Liu, H.-K.; Sadler, P. J. *Acc. Chem. Res.* **2011**, *44*, 349-359.
- 29 Andersson, J.; Lincoln, P. J. *Phys. Chem. B*, **2011**, *115*, 14768-14775.
- 30 Nordell, P.; Lincoln, P. J. *J. Am. Chem. Soc.* **2005**, *127*, 9670-9671.
- 31 Cordier, C.; Pierre, V. C.; Barton, J. K. *J. Am. Chem. Soc.* **2007**, *129*, 12287–12295.

- 32 Zeglis, B. M.; Pierre, V. C.; Kaiser, J. T.; Barton, J. K. *Biochemistry* **2009**, *48*, 4247–4253.
- 33 Pierre, V. C.; Kaiser, J. T.; Barton, J. K. *Proc. Natl. Acad. Sci. U.S.A.* **2007**, *104*, 429–434.
- 34 Song, H. Kaiser; J. T.; Barton, J. K. *Nature Chem.* **2012**, *4*, 615–620.

Chapter 6: Cellular Processing of Rhodium Metalloinsertors: Investigations into the Underlying Biological Mechanisms Involved in Response to Mismatch Recognition*

6.1 Introduction

DNA replication is essential for cell growth and reproduction, and ensuring the fidelity of the genome is vital for the survival of all organisms. DNA defects occur naturally during replication and as a result of chemical damage. Unchecked DNA damage can cause further mutations that lead to cellular dysfunction and disease. Specifically, single-strand defects such as mismatches, abasic sites, and oxidized bases are associated with elevated mutation rates and carcinogenesis.¹ To correct these errors and increase the fidelity of replication, cells have evolved a complex repair pathway involving nucleotide excision repair (NER), base excision repair (BER), and mismatch repair (MMR).²

The MMR machinery recognizes and repairs single base lesions that arise from errors in DNA replication.^{3,4} Deficiencies in the MMR machinery increase the rates of mutagenesis 50-1000 fold,^{5,6} a hallmark of MMR-deficiency is microsatellite instability, which refers to the gain or loss of mono-, di-, or tri-nucleotide repeat sequences within the genome.⁷ Microsatellite instability arises from uncorrected frame-shift mutations that occur during replication and is associated with human diseases such as xeroderma pigmentosum and colorectal cancer.^{8,9} In fact, mismatch repair deficiencies have been

**Acknowledgments:* Julie Bailis (Amgen) prepared the tumor samples from the *in vivo* mouse studies. Professor Jeremy Stark, Diana Yanez (City of Hope), and Kelsey Boyle (Caltech) assisted with the immunofluorescence assay and collected images by fluorescence microscopy. Kelsey Boyle also assisted with quantitative analysis of the fluorescence data. I synthesized the metalloinsertors, performed lysis and analysis of tumor samples for rhodium content by ICP-MS, carried out all HCT116 cell culture and fixation, and performed the transcription assay in the HCT116N and HCT116O cell lines.

found in approximately 80% of hereditary nonpolyposis colon cancer cases and in 16% of all solid tumors.^{9,10} Additionally, MMR-deficient cancers exhibit resistance to common chemotherapeutics such as DNA alkylators and platinating agents, as MMR proteins are responsible for recognizing the DNA adducts formed by these agents.^{11,12} The deleterious effects of MMR deficiency have demonstrated a need to develop therapeutic agents that target MMR-deficient cancers.

The development of transition metal-based chemotherapeutic agents burgeoned with the discovery of the anti-cancer properties of *cis*-dichlorodiammineplatinum (II) (cisplatin). While later generations of inorganic therapeutics have been developed with enhanced potency, the field has increasingly turned towards the development of more targeted therapies. The design of compounds that can selectively target biomarkers of cancer aims to achieve potency specifically in malignant cells over healthy cells, thus mitigating side effects arising from off-target toxicity. In recent years, inorganic compounds have been exploited for their complex geometries, stereoselectivity, and rich photochemistry in the selective targeting of DNA, proteins, and organelles that have been implicated in carcinogenesis.¹³

Our laboratory has focused on the design of octahedral rhodium (III) complexes bearing sterically expansive ligands for the selective targeting of DNA mismatches. Benzo-fused expansion of traditional intercalating ligands precludes the intercalative binding mode, resulting in exclusive targeting of thermodynamically destabilized sites.¹⁴ These complexes – dubbed “metalloinsertors” due to the complete extrusion of the mismatched base pairs from the helix and consequent insertion of the planar ligand in the

intervening space – target destabilized sites in DNA with over 1000-fold precision *in vitro*.¹⁵⁻¹⁸

The potential of rhodium metalloinsertors to recognize mismatches *in vivo* has been extensively explored. The nature of the metalloinsertion binding mode, wherein the metal complex approaches from the minor groove and ejects the mismatched bases out into the major groove, is hypothesized to create a large lesion that could be recognized by proteins in the cell.^{15,16,19} The biological activity of metalloinsertors has been characterized primarily in two isogenic cell lines derived from the HCT116 human colorectal carcinoma line. Wild-type HCT116 cells are deficient in the MLH1 protein, an essential component of the MMR protein complex. The HCT116N daughter cell line is transfected with a copy of human chromosome 3 (ch3), which encodes the *hMLH1* gene; these cells express MLH1 and restore functional mismatch repair. The HCT116O line is transfected with a copy of chromosome 2 (ch2), resulting in an isogenically matched daughter line that remains MMR-deficient.²⁰ Metalloinsertors have been shown to inhibit cell proliferation^{21,22} and induce cytotoxicity selectively in the MMR-deficient HCT116O cell line, and these cytotoxic effects proceed via a necrotic pathway.²³ Moreover, it has been shown that this cell-selectivity arises from localization of complexes to the nucleus, whereas cell death occurs indiscriminately in both cell lines upon localization to the mitochondria.^{24,25} These results support the notion that nuclear DNA is the preferred biological target of our rhodium complexes, rather than the mitochondrial genome.

The isogenically matched HCT116N and HCT116O cell lines have proven extremely useful in elucidating the mismatch sensitivity of metalloinsertors in cells. Given the dependence of cell-selective toxicity on nuclear targeting in addition to the

absence of the critical MMR protein MLH1, which repairs genomic but not mitochondrial DNA, it is feasible to conclude that the biological activity of metalloinsertors is the result of mismatch recognition within the genome. This was further validated in a recent study involving NCI-H23 lung adenocarcinoma cells that contain a doxycycline-inducible short hairpin RNA (shRNA) that suppresses expression of the MLH1 gene. This not only enabled mismatch repair to be turned on and off within the same cell line, but also removed the potential for interference arising from chromosomal instability, which can occur in the HCT116 daughter lines that have been transfected with an entire additional chromosome. The selectivity of metalloinsertors for MMR-deficiency in the inducible cell line refutes the notion that the biological activity of metalloinsertors is the result of off-target effects within the cell.²⁶

As new generations of metalloinsertors are developed with increasing potency and selectivity, we consider their potential as clinically viable alternatives to the current repertoire of treatments of MMR-related cancers. However, we still understand relatively little about the underlying mechanisms surrounding rhodium mismatch recognition in the genome. The cellular processing and downstream effects that occur in the period between the initial DNA binding event and the first stages of necrosis remain largely unclear. We have employed various fluorescence methods to probe the potential cellular pathways that may be activated in response to metalloinsertor treatment in the HCT116N and HCT116O cell lines. It has been discovered that metalloinsertors display evidence of inducing DNA strand breaks in the genome, eliciting the phosphorylation of histone H2AX (γ H2AX), which recruits DNA damage response and repair proteins.²⁷ Notably, we have observed cell-selective inhibition of transcription in MMR-deficient cells in

response to rhodium treatment, but not cisplatin. Finally, preliminary *in vivo* experiments in nude mice implanted with HCT116 tumor xenografts have revealed moderate toleration of rhodium as well as tumor uptake of metalloinsertors. Overall, it was determined that these complexes provoke a variety of rapid cellular responses at low doses and exhibit enormous potential for activity in complex biological systems.

6.2 Experimental Protocols

6.2.1 Materials

Cisplatin and all organic reagents were purchased from Sigma Aldrich unless otherwise noted. Commercially available chemicals were used as received without further purification. RhCl_3 starting material was purchased from Pressure Chemical Co (Pittsburgh, PA). Media and supplements were purchased from Invitrogen (Carlsbad, CA). Ethynyl uridine, Alexa Fluor 488®, copper sulfate, and associated buffers were purchased in kit form from Life Technologies (Carlsbad, CA). Vista Green DNA Dye, comet slides, and associated buffers and solutions were purchased in kit form from Cell Biolabs Inc. (San Diego, CA). An extraction kit for tumor cell lysis was purchased from Thermo Fisher Scientific (Waltham, MA). Antibodies for immunofluorescence assays were purchased from Abcam (Cambridge, UK).

The synthesis of 5,6-chryseno quinone (chrysi), 1-methyl-1-(pyridin-2-yl) ethanol (PPO), $[\text{Rh}(\text{HDPA})_2\text{chrysi}]\text{Cl}_3$, and $[\text{Rh}(\text{chrysi})(\text{phen})(\text{PPO})]\text{Cl}_2$ were carried out according to published protocols.^{22,28,29}

6.2.2 Cell Culture

HCT116N and HCT116O cells were grown in RPMI 1640 medium containing 10% FBS, 2 mM L- glutamine, 0.1 mM nonessential amino acids, 1 mM sodium

pyruvate, 100 units/mL penicillin, 100 µg/mL streptomycin, and 400 µg/mL Geneticin (G418). Cells were grown in tissue culture flasks (Corning Costar, Acton, MA) at 37 °C and 5% CO₂ humidified atmosphere.

6.2.3 Immunofluorescence Staining of Fixed Cells

6.2.3.1 Cell Treatment and Fixation

Immunofluorescence studies were carried out in 4-well chamber slides with removable walls. Slides were coated with 0.3 ml poly-L-lysine (Sigma) per chamber and incubated at 37 °C, 5% CO₂ for 90 minutes. The coating was aspirated, and HCT116N and HCT116O cells were seeded at 4×10^4 cells (0.5 ml media) per chamber. The slides were incubated at 37 °C under humidified atmosphere and given 24 h to adhere. Slides were treated with varying concentrations of [Rh(chrysi)(phen)(PPO)]²⁺ (0.1, 0.3, or 1 µM) or camptothecin (1 µM) for 2h at 37 °C. For time course experiments, drug-containing medium was aspirated after 2h, replaced with fresh medium, and allowed to grow at 37 °C for the appropriate durations. After the incubation period, the media was aspirated and cells were washed 2x with phosphate buffered saline (PBS, pH 7.2, 0.5 ml/chamber). Cells were fixed with 4% (w/v) paraformaldehyde in PBS (0.5 ml/chamber) for 15 min at room temperature. The fixative was aspirated and cells were washed 2x with PBS (0.5 ml each). Paraformaldehyde was quenched with 0.1 M glycine (0.5 ml/chamber) in PBS for 5 min at room temperature. The solution was removed by aspiration, and cells were washed with PBS (2 x 0.5 ml). For storage, 0.5 ml PBS was added to each chamber, and slides were stored at 4 °C until staining.

6.2.3.2 Immunofluorescence Staining

Cells were permeabilized with 0.5% Triton X-100 in PBS for 15 min, followed by aspiration and washing with 2 x 0.5 ml PBS. Cells were then blocked with 3 M bovine serum albumin (BSA) in PBS for 30 min. Primary antibodies were added (0.07 ml/chamber) as indicated in **Table 6.1** and incubated at 37 °C under humidified atmosphere for 2 h. Antibody solutions were removed and cells were washed with 2 x 0.5 ml PBS. Secondary antibodies were added (0.07 ml/chamber) as indicated in **Table 6.1** and incubated at 37 °C under humidified atmosphere for 1 h. Antibody was removed and cells were washed with 3 x 0.1 ml PBS for 5 min each (on rocker). Slides were then mounted with VECTASHIELD (1 drop/chamber) with DAPI. Slides were then dried at 4 °C overnight and imaged using fluorescence microscopy. Fluorescent images were captured using a Princeton Instruments cooled CCD digital camera from a Zeiss upright LSM 510 2-Photon confocal microscope.

6.2.3.3 Quantification and Analysis of Fluorescence Images

Fluorescent images were obtained as gray-scale data and false colorized with the corresponding dye colors using Photoshop. Quantitative analysis of protein focal accumulation (“foci”) was carried out using gray-scale images in a randomized double-blind study. Only cells with nuclei that were contained entirely within the image were counted – nuclei that were cut off at the edges were excluded from all quantitation. The numbers of foci per cell were denoted as negative (zero foci), low-staining (1-5 foci/cell), moderate-staining (6-10 foci/cell), or high-staining (>10 foci/cell). Cells displaying each type of foci were calculated as a percentage of the total cells in the collection of images for each sample. Between 3-5 images were collected for each chamber, ranging from ~30-150 cells total.

Table 6.1 Antibodies for Immunofluorescence Staining

Primary Antibody	Dilution	Secondary Antibody^a	Dilution
Mouse γ H2AX	1:500	Goat anti-mouse IgG	1:250
Rabbit FANCD2	1:250	Goat anti-rabbit IgG	1:250
Rabbit 53BP1	1:500	Goat anti-rabbit IgG	1:250
Mouse RPA	1:100	Goat anti-mouse IgG	1:250

^a Goat anti-mouse IgG secondary antibody contains an Alexa Fluor® 488 label ($\lambda_{\text{ex}} = 488$ nm). Goat anti-rabbit IgG secondary antibody contains an Alexa Fluor® 647 label ($\lambda_{\text{ex}} = 647$ nm).

6.2.4 MTT Cytotoxicity Assay

MTT experiments were performed with HCT116N and HCT116O cells as described in the literature.³⁰ HCT116N and HCT116O cells were inoculated with rhodium or camptothecin at varying concentrations and plated in 96-well plates at 50,000 cells/well. Cells were incubated for 72h at 37 °C under humidified atmosphere. After the incubation period, MTT was added, and the cells were incubated for an additional 4 h. The resulting formazan crystals were solubilized over a period of 24 h at 37 °C, 5% CO₂. Formazan formation was quantified *via* electronic absorption at 550-600 nm with a reference wavelength of 690 nm. Cell viability is expressed as a function of formazan formation and normalized to that of untreated cells. Standard errors were calculated from five replicates.

6.2.5 Comet Assay for Damage of Cellular DNA

Determination of rhodium-induced damage of genomic DNA was performed using the OxiSelect Comet Assay Kit (CellBioLabs). HCT116N and HCT116O cells were harvested by trypsinization and seeded in 6-well plates at 200,000 cells/well in 3 ml media. Cells were allowed 24 h to adhere at 37 °C under humidified atmosphere, followed by treatment with 500 nM of either camptothecin or [Rh(chrysi)(phen)(PPO)]²⁺. Untreated HCT116N and O cells were included as a control. Cells were grown for an additional 24 h and harvested by trypsinization. Cell pellets were washed with 3 ml cold PBS (pH 7.2) and resuspended in a minimal volume of PBS (~200 µl, ~4 x 10⁵ cells/ml). Cell suspensions were then combined with liquefied OxiSelect Comet Agarose (heated to 90 °C for 20 min and maintained at 37 °C prior to the experiment) at a 1:10 ratio (v:v), triturated via pipetting, and maintained at 37 °C until ready for plating. Immediately upon

removal from the 37 °C bath, the cell-agarose mixtures were triturated again and each pipetted onto a 3-well Comet Slide (75 µl/well). Slides were incubated at 4 °C in the dark for 15 min. Slides were then transferred to a basin containing pre-chilled Lysis buffer (2.5 M NaCl, 10 mM EDTA, 10 ml 10x Lysis solution from kit, 10 ml DMSO, Milli Q H₂O to 100 ml, pH 10) (25 ml/slide), and immersed at 4 °C in the dark for 30-60 min. The Lysis buffer was aspirated and replaced with pre-chilled Alkaline solution (300 mM NaOH, 1 mM EDTA, pH >13) at ~25 ml/slide for 30 min at 4 °C in the dark. The slides were then transferred to a horizontal electrophoresis chamber filled with 1 L of pre-chilled Alkaline Electrophoresis Buffer (300 mM NaOH, 1 mM EDTA, pH >13) and electrophoresed at ~20 V (450 mA) for 35 min. After electrophoresis, slides were washed with pre-chilled MilliQ water (2 x 25 ml for 2 min) followed by 70% EtOH (1 x 25 ml for 5 min). Slides were stored to dry at 4 °C in the dark until completely dry (~24 h).

For staining, a 10,000x solution of VistaGreen DNA dye was diluted to 1x in TE Buffer (10 mM Tris, pH 7.5, 1 mM EDTA) and added to each well (0.1 ml/well). Cells were protected with a coverslip and allowed to incubate at ambient temperature overnight while protected from light. Images were acquired by epi-fluorescence microscopy (excitation at 488 nm) using an Olympus IX81 with a 100× sapo objective with laser illumination at 532 nm. Fluorescent images were obtained as gray-scale data and false colorized green using Photoshop.

6.2.6 Assay for *In Cellulo* RNA Synthesis in HCT116N and O Cells

HCT116N and O cells were seeded in 96-well plates at 4×10^3 cells/well and allowed 24 h to adhere. After 24 h, cells were treated with 10 µl of 10x stock solutions of [Rh(chrysi)(phen)(PPO)]Cl₂ (0 – 1 µM final concentration) or cisplatin (0 – 10 µM final

concentration) at 37 °C under humidified atmosphere for 24 h. After the incubation period, an equal volume (100 µl) of 2 mM ethynyl uridine (EU) in pre-warmed media was added to each well, to a final concentration of 1 mM EU per well. EU pulse labeling was carried out at 37 °C under humidified atmosphere for 1 h. After the labeling period, the media was removed, and cells were fixed with 3.7% formaldehyde in phosphate buffered saline (PBS, pH 7.2) at 50 µl/well for 30 min at room temperature. The fixative was removed, and wells were washed 1x with 200 µl PBS (pH 7.2). Cells were then permeabilized with 0.5% Triton X-100 in PBS (pH 7.2) (50 µl/well for 15 minutes) and washed with PBS. A working solution of the Click-iT reaction cocktail was prepared immediately before treatment while protected from light, according to the manufacturer's instructions. The click reaction was carried out at ambient temperature for 30 minutes in the absence of light. The wells were aspirated and washed with the rinse buffer (50 µl/well). The plates were protected from light, and fluorescence readout of the wells was carried out on a Flexstation 3 Multi-Mode microplate reader (495 nm excitation, 519 nm emission, 515 nm automatic cutoff; top-read).

6.2.7 Animals

All breeding, housing, and treatment of mice were carried out at Amgen, Inc (Thousand Oaks, CA) in strict accordance with the recommendations in the Guide for the Care and Use of Laboratory Animals of the National Institutes of Health. Nude mice were implanted subcutaneously with HCT116 tumor cells. Once the tumors had grown to 50-250 mm³, mice were injected either intravenously (IV) or intraperitoneally (IP) with a single dose of rhodium (10, 20, or 100 mg/kg). Mice were sacrificed after 24h and tumors were harvested for rhodium analysis by ICP-MS.

6.2.8 Analysis of Tumor Samples for Rhodium Content by ICP-MS

Tumor samples were obtained from nude mice implanted with human HCT116 xenografts and homogenized manually at 4 °C. A nuclear protein extraction kit (Pierce from Thermo Scientific) was used for cell lysis. Nuclear and cytosolic lysates were separated from the insoluble fraction according to the manufacturer's instructions. The soluble fractions were combined and sonicated on a Qsonica Ultrasonic processor for 20 s at 40% amplitude. A 750 µl aliquot was diluted with 750 µl of a 2% HNO₃ (v/v) solution and analyzed for rhodium content by inductively coupled plasma mass spectrometry (ICP-MS) on an Agilent 8800 QqQ unit. The remainder of the cell lysate was analyzed for protein content *via* a bicinchoninic assay (BCA).³¹ Rhodium counts were normalized to protein content to obtain ng [Rh]/mg [protein].

6.3 Results

6.3.1 Immunofluorescence Staining of HCT116 Cells

Previous studies have established nuclear DNA as the preferred target of rhodium metalloinsertors for selective toxicity in MMR-deficient cells, but little is known about how the DNA-bound metalloinsertor is recognized and processed in the cell. Immunofluorescence staining was carried out on MMR-proficient HCT116N cells and MMR-deficient HCT116O cells to screen for the accumulation of proteins that localize to sites of DNA damage. Cells were plated in 4-well chamber slides and treated with either [Rh(chrysi)(phen)(PPO)]²⁺ or camptothecin (**Figure 6.1**), which induces double strand breaks in DNA,³² for 2h and either fixed or replaced with fresh media and allowed to

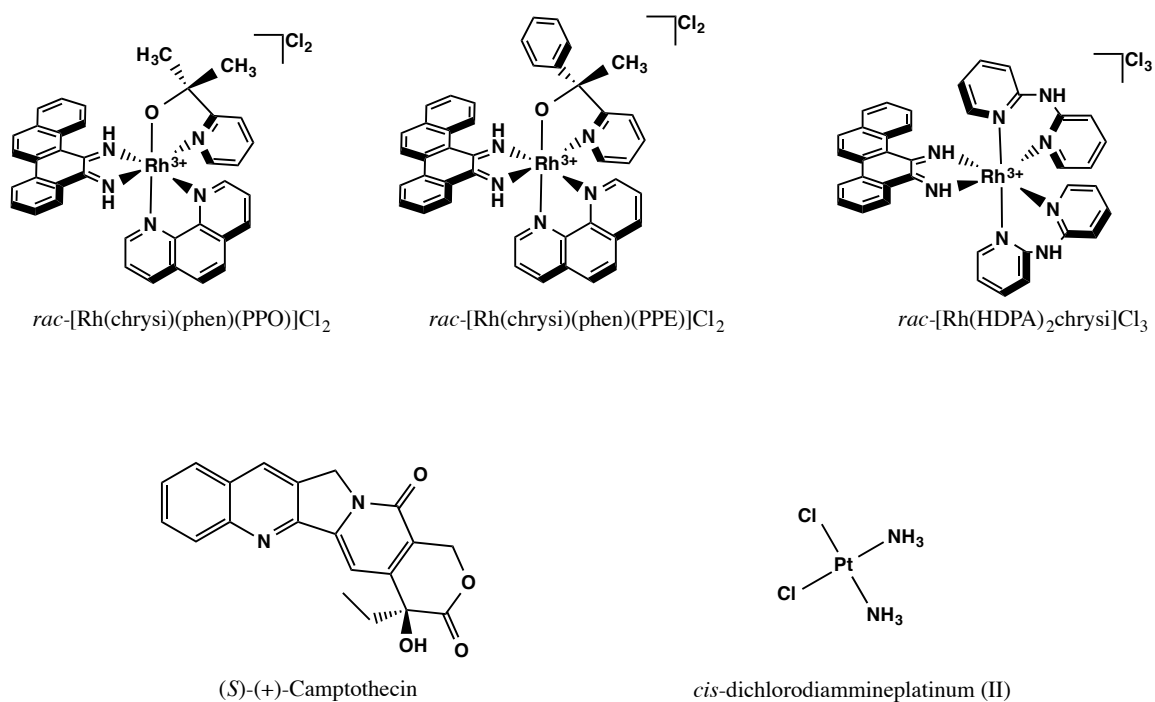


Figure 6.1 Chemical structures of complexes included in this study. Top (left to right): $[\text{Rh}(\text{chrysi})(\text{phen})(\text{PPO})]^{2+}$, $[\text{Rh}(\text{chrysi})(\text{phen})(\text{PPE})]^{2+}$ (included in *in vivo* studies), $[\text{Rh}(\text{HDPA})_2\text{chrysi}]^{3+}$ (included in *in vivo* studies). Bottom (left to right): $(S)\text{-}(+)\text{-Camptothecin}$, which was employed as a control in immunofluorescence staining; $cis\text{-dichlorodiammineplatinum (II)}$, which was used as a control in the transcription assay.

recover for periods of 6, 12, or 24h prior to fixation. Cells were then stained with antibodies for γ H2AX and p53-binding protein 1 (53BP1).

6.3.1.1 Induction of γ H2AX in HCT116 Cells

The focal accumulation of γ H2AX was examined in HCT116N and HCT116O cells in response to treatment with $[\text{Rh}(\text{chrysi})(\text{phen})(\text{PPO})]^{2+}$ for 2h followed by a cell fixation and immunofluorescence staining. Camptothecin-treated (1 μM) and untreated cells were included as controls. **Figure 6.2** shows the confocal immunofluorescence microscopy of HCT116O cells treated with rhodium (1 μM) and camptothecin and stained for γ H2AX. The focal accumulation of γ H2AX – known as “foci” – signifies the presence of double strand breaks (DSBs) in DNA.²⁷ These foci appear as punctate stains within the nucleus, indicating points of DNA damage. Nuclear co-staining with DAPI is shown in blue.

As can be seen in **Figure 6.2**, camptothecin displays characteristically high punctate staining of γ H2AX. $[\text{Rh}(\text{chrysi})(\text{phen})(\text{PPO})]^{2+}$ also induces γ H2AX foci comparable to that of camptothecin at the same concentration, and above the background fluorescence of untreated cells. The incidence of γ H2AX foci in rhodium-treated cells suggests that metalloinsertors may induce DSBs in the genome.

Immunofluorescence staining for γ H2AX was also carried out for HCT116N cells. At 1 μM rhodium, foci were detected in both cell lines. We postulated that differential fluorescence staining may be observed with lower concentrations of rhodium. Staining was carried out on HCT116N and HCT116O cells treated with 100 and 300 nM $[\text{Rh}(\text{chrysi})(\text{phen})(\text{PPO})]^{2+}$ for 2h. As can be seen in **Figure 6.3**, little difference could be observed between the two cell lines. Additionally, untreated cells display unusually high

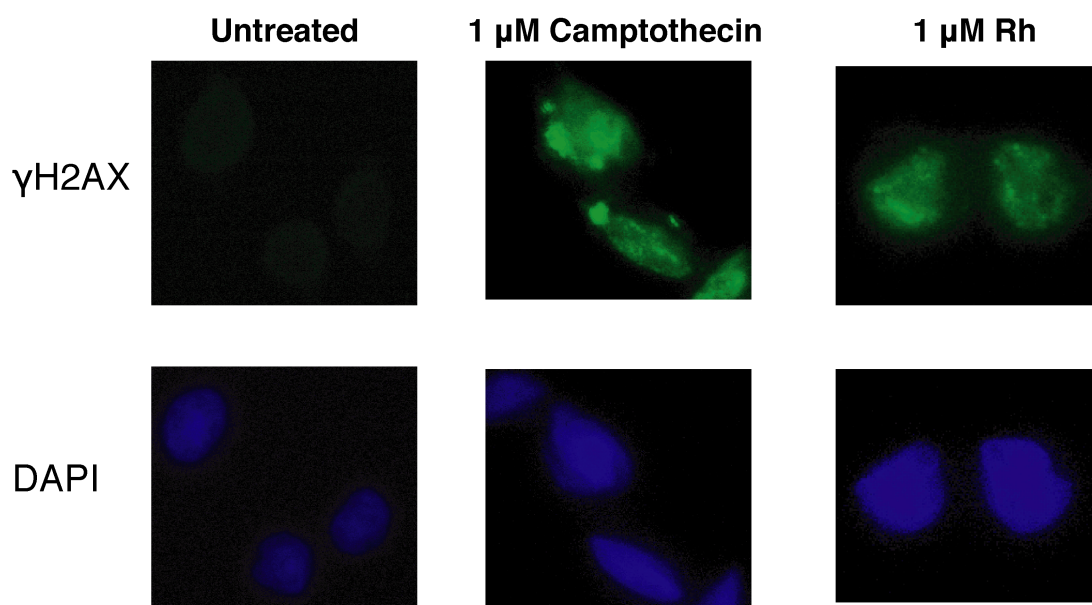


Figure 6.2 Confocal microscopy of immunofluorescence for γ H2AX (green) and nuclear staining with DAPI (blue) in fixed MMR-deficient HCT1160 cells after 2h exposure to 1 μ M camptothecin or $[\text{Rh}(\text{chrysi})(\text{phen})(\text{PPO})]^{2+}$.

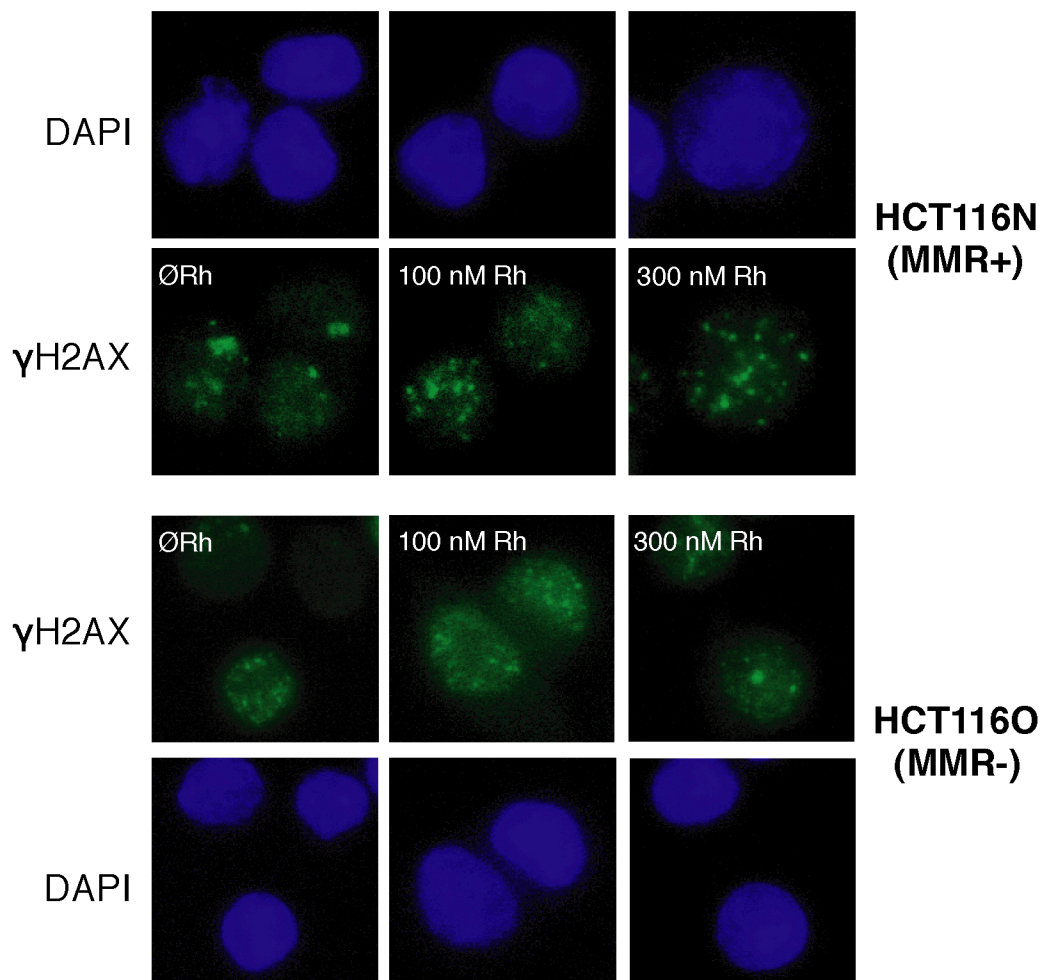


Figure 6.3 Confocal microscopy of immunofluorescence for γ H2AX (green) and nuclear staining with DAPI (blue) in fixed MMR-proficient HCT116N (top) and MMR-deficient HCT116O (bottom) cells after 2h exposure to 0, 100, or 300 nM $[\text{Rh}(\text{chrysi})(\text{phen})(\text{PPO})]^{2+}$.

nuclear pan-staining as well as γ H2AX foci in both cell types. It is possible that the incidence of γ H2AX foci in untreated cells is the result of inherent DNA damage arising from chromosomal instability or mutagenesis in these cancerous cells. Cells treated with 100 nM rhodium display similar fluorescence staining to that of untreated cells. The addition of 300 nM resulted in more observable γ H2AX foci, marginally above background pan-staining.

The appearance of γ H2AX foci occurs rapidly, after only two hours exposure to rhodium. This implies that metalloinsertor complexes trigger a cellular response almost immediately upon entry into the nucleus. It is surprising, however, that evidence of DNA damage arises in both MMR-proficient and MMR-deficient cells in response to rhodium treatment, when antiproliferative and cytotoxic effects are only observed in the MMR-deficient cell line. We considered the possibility that γ H2AX accumulates as an early response to the foreign rhodium complexes surrounding the genome, but postulated that the amount of γ H2AX may vary between the cell lines if allowed to recover in medium absent of rhodium. HCT116N and HCT116O cells were treated with 300 nM metalloinsertor for 2h and allowed to grow in fresh media for 6, 12, or 24h. Cells were then stained for γ H2AX and imaged by confocal immunofluorescence microscopy. **Figure 6.4** shows the induction of γ H2AX in HCT116N and HCT116O cells over time. Quantitation of foci in both cell lines was carried out, and cells were designated either as γ H2AX-negative (having zero foci), low- γ H2AX (1-5 foci per cell), moderate- γ H2AX (6-10 foci per cell), or high- γ H2AX (>10 foci per cell). As can be seen in **Figure 6.5**, the number of γ H2AX foci does vary in both cell lines over time, with either zero or low-foci counts in cells fixed immediately after treatment (“0 hr”), followed by an increase in the

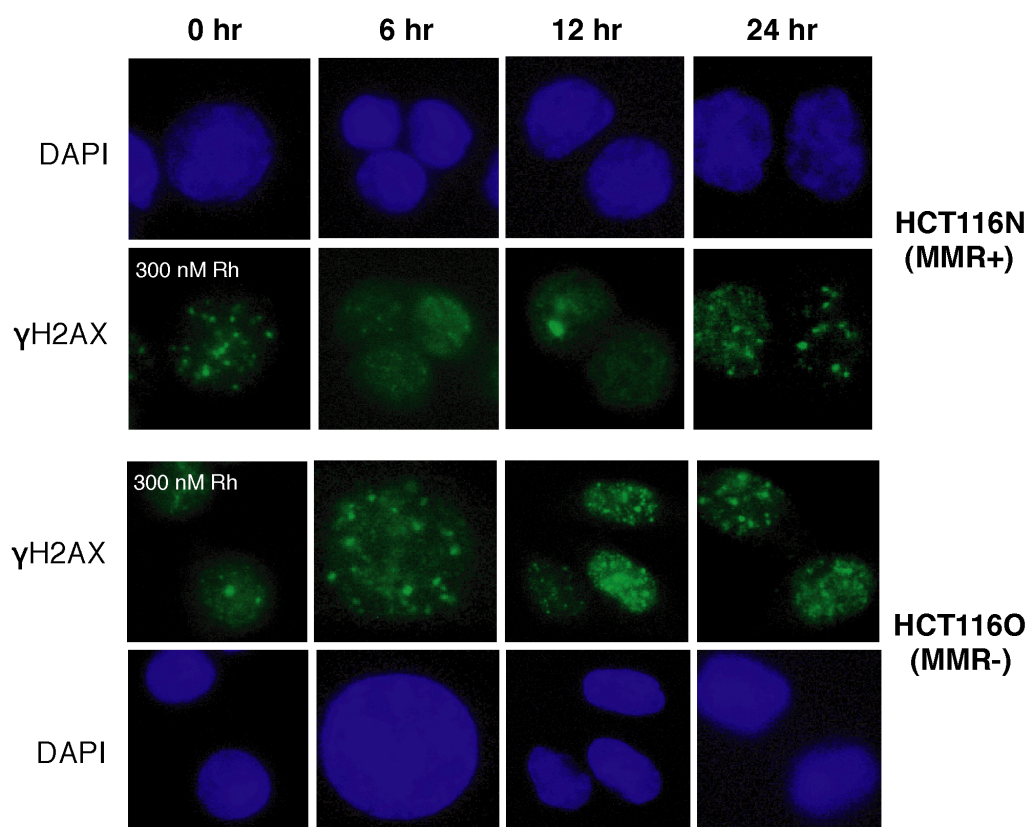


Figure 6.4 Confocal microscopy of immunofluorescence for γ H2AX (green) and nuclear staining with DAPI (blue) in fixed MMR-proficient HCT116N (top) and MMR-deficient HCT116O (bottom) cells after 2h exposure to 300 nM $[\text{Rh}(\text{chrysi})(\text{phen})(\text{PPO})]^{2+}$, followed by growth in non-rhodium containing medium for 6, 12, or 24h prior to fixation and staining. The “0 hr” time point refers to cells that were fixed immediately after rhodium treatment.

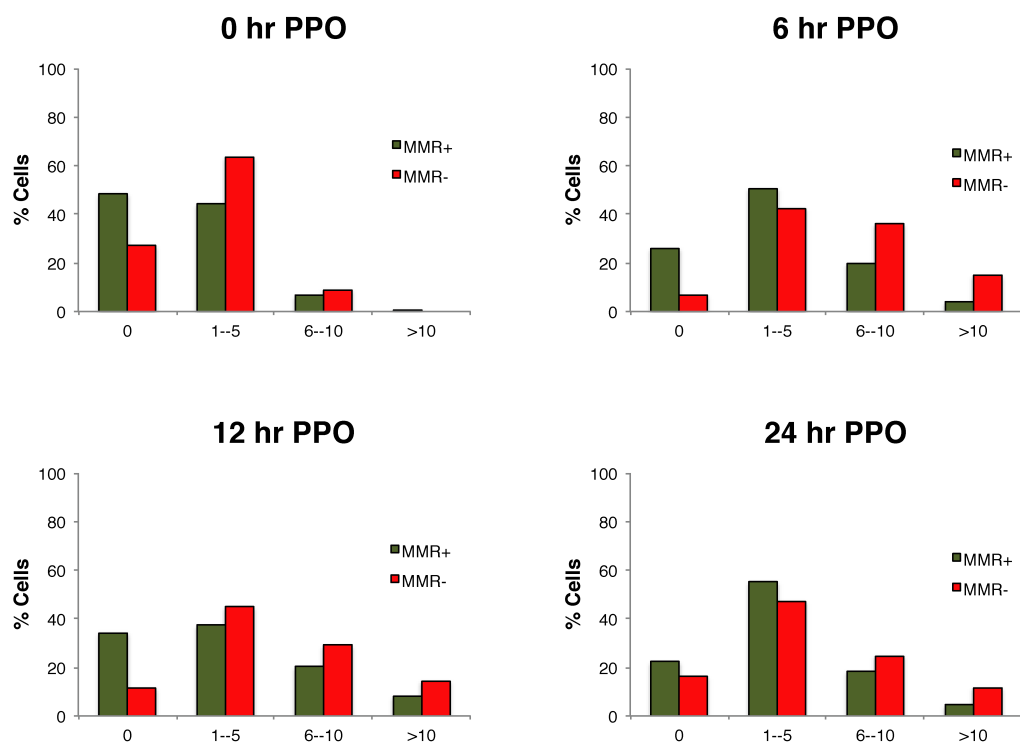


Figure 6.5 Quantitation of γ H2AX foci in HCT116N (MMR+, green) and HCT116O (MMR-, red) cells over time. Cells were exposed to $[\text{Rh}(\text{chrysi})(\text{phen})(\text{PPO})]^{2+}$ (300 nM) for 2h. After the treatment period, rhodium-containing medium was removed, replaced with fresh medium, and allowed to incubate for an additional 6, 12, or 24h. In the case of the 0 hr time point, cells were fixed immediately after rhodium treatment. Foci were quantified in each cell and designated as γ H2AX-negative (0 foci), low- γ H2AX (1-5 foci/cell), moderate- γ H2AX (6-10 foci/cell), or high- γ H2AX (>10 foci/cell). The percentage of each cell type was calculated as a fraction of the total cells in the images collected for each sample. For each sample, 3-5 images ($n = 30-150$ cells) were collected.

percentage of moderate- to high-foci counts after 6 and 12h recovery. The percentage of highly γ H2AX-positive cells decreases slightly in both cell lines between 12 and 24h.

To examine whether there was any difference in the γ H2AX response in HCT116N versus HCT116O cell lines, we calculated the percentage of combined moderate- and high- γ H2AX foci in each cell line (as a fraction of the total cells in each sample) over time – that is, cells containing ≥ 6 foci each were considered to be above background (γ H2AX-positive) based upon the quantification of γ H2AX in untreated cells (*vide infra*). As can be seen in **Figure 6.6**, there is a slight increase in the percentage of γ H2AX-positive cells in HCT116O cells (“MMR-”) versus HCT116N cells (“MMR+”) treated with rhodium, with 7 – 28% γ H2AX-positive HCT116N cells, and 9 – 52% γ H2AX-positive HCT116O cells. The trends in γ H2AX induction over time are also illustrated more clearly: an increase in double-strand breaks occurs 0 – 6h after rhodium exposure and remains steady from 6 – 12h. Between 12 and 24h, a slight decrease in γ H2AX is observed, possibly as a result of cell death.

Figure 6.6 also shows the time course data for camptothecin (“CT”) and untreated cells. Cells displaying moderate- to high- γ H2AX foci (≥ 6 foci/cell) were calculated as a percentage of total cells in the collection of images for each sample. As expected, a high percentage of cells treated with camptothecin are γ H2AX-positive across all time points. In HCT116N cells, the percentage of γ H2AX-positive cells remains constant between 0 – 12h, with a large increase ($>96\%$) at 24h. In contrast, the HCT116O cells treated with camptothecin follow a pattern similar to those treated with metalloinsertor: an increase from 0 – 6h (90 – 92%) followed by a decrease at 24h (66%). The full quantification of camptothecin-treated and untreated cells over time are depicted

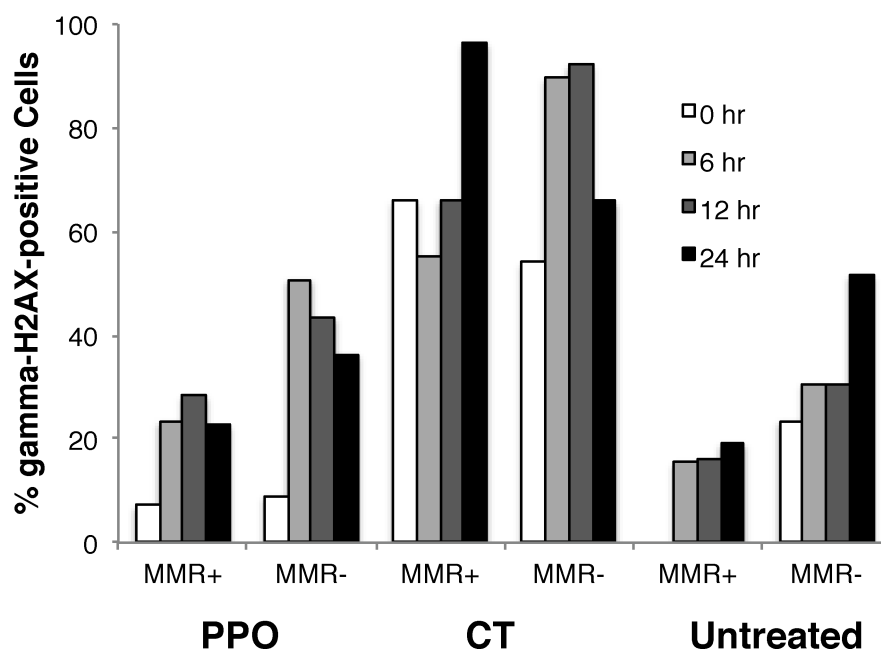


Figure 6.6 Quantitation of γ H2AX-positive cells in HCT116N (MMR+) and HCT116O (MMR-) cells treated with $[\text{Rh}(\text{chrysi})(\text{phen})(\text{PPO})]^{2+}$ (PPO, 300 nM) or camptothecin (CT, 1 μM) for 2h followed by growth in media absent of drug for a period of 6, 12, or 24h. For each time point, an untreated control was included, as well as a 0 hr time point in which treated cells were fixed immediately after drug exposure. Cells containing ≥ 6 foci/cell were designated as γ H2AX-positive, and the percentage of γ H2AX-positive cells was calculated as a fraction of the total cells in the images collected for each sample. For each sample, 3-5 images ($n = 30-150$ cells) were collected.

in **Figure 6.7**. The untreated cells exhibit lower percentages of γ H2AX-positivity compared to treated cells, although γ H2AX staining is higher in the HCT116O cell line (24 – 52%) than in the HCT116N line (15 – 19%). This is possibly due to the incidence of DSBs arising spontaneously from microsatellite instability and a lack of mismatch repair. Additionally, DSBs may also occur as a result of chromosomal instability, as both cell types are transfected with an extra chromosome. Due to the relatively high occurrence of γ H2AX and DSBs in untreated cells, it is difficult to determine whether rhodium metalloinsertors in fact play a meaningful role in triggering γ H2AX induction in treated cells. Further studies are required to ascertain the statistical significance of these results.

6.3.1.2 Induction of 53BP1 in HCT116 Cells

To further elucidate the mechanisms that respond to metalloinsertor treatment, we stained for additional proteins that signal DNA damage. Staining for replication protein A (RPA), which binds to single stranded DNA and is involved in homologous recombination,³³ and Fanconi anemia group D2 protein (FANCD2), which colocalizes with the BRCA1 complex involved in DNA DSB repair,³⁴ produced no discernable foci in rhodium-treated cells (data not shown). Staining for 53BP1, which promotes non-homologous end-joining-mediated repair of DSBs,³⁵ was successfully visualized for cells treated with $[\text{Rh}(\text{chrysi})(\text{phen})(\text{PPO})]^{2+}$ and camptothecin. **Figure 6.8** depicts the induction of 53BP1 in HCT116N and HCT116O cells treated with rhodium or camptothecin (as well as untreated cells) for 2h followed by fixation and costaining with DAPI and γ H2AX. Foci corresponding to 53BP1 localization are observed for both

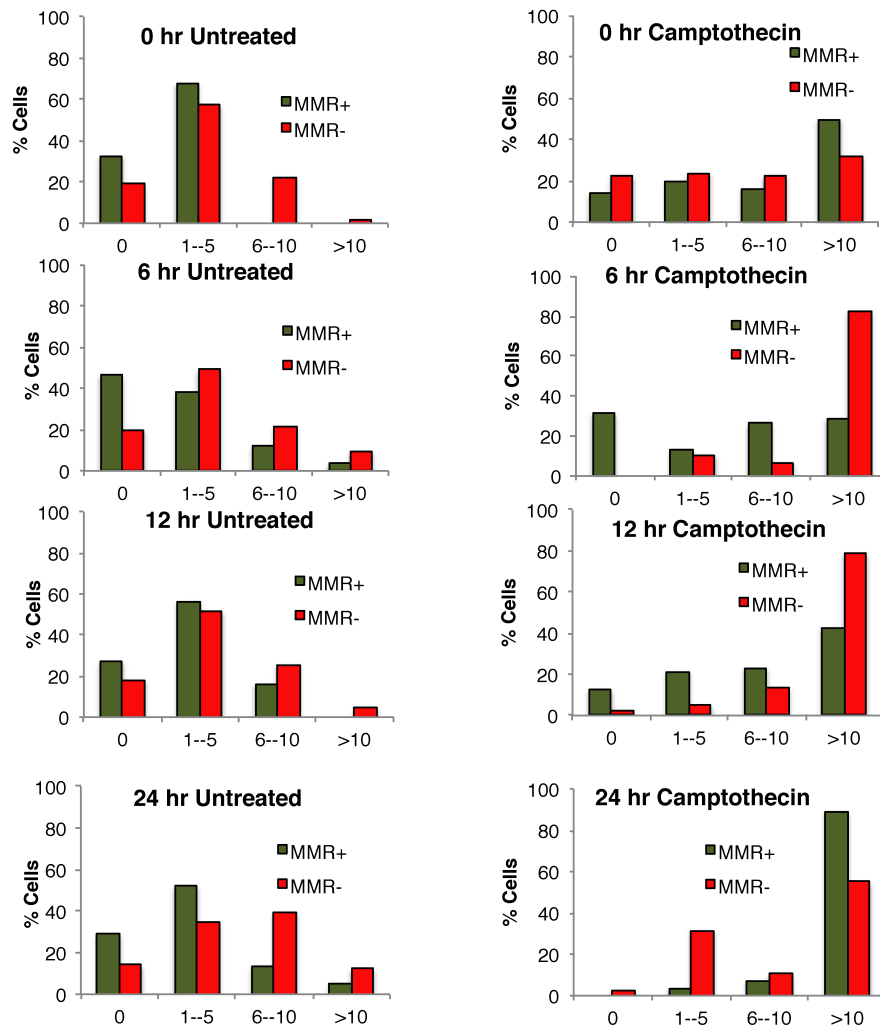


Figure 6.7 Quantitation of γ H2AX foci in HCT116N (MMR+, green) and HCT116O (MMR-, red) cells over time. Cells were untreated or exposed to camptothecin⁺ (1 μ M) for 2h, followed by growth in fresh media for an additional 6, 12, or 24h. In the case of the 0 hr time point, cells were fixed immediately after treatment. Foci were quantified in each cell and designated as γ H2AX-negative (0 foci), low- γ H2AX (1-5 foci/cell), moderate- γ H2AX (6-10 foci/cell), or high- γ H2AX (>10 foci/cell). The percentage of each cell type was calculated as a fraction of the total cells in the images collected for each sample. For each sample, 3-5 images ($n = 30-150$ cells) were collected.

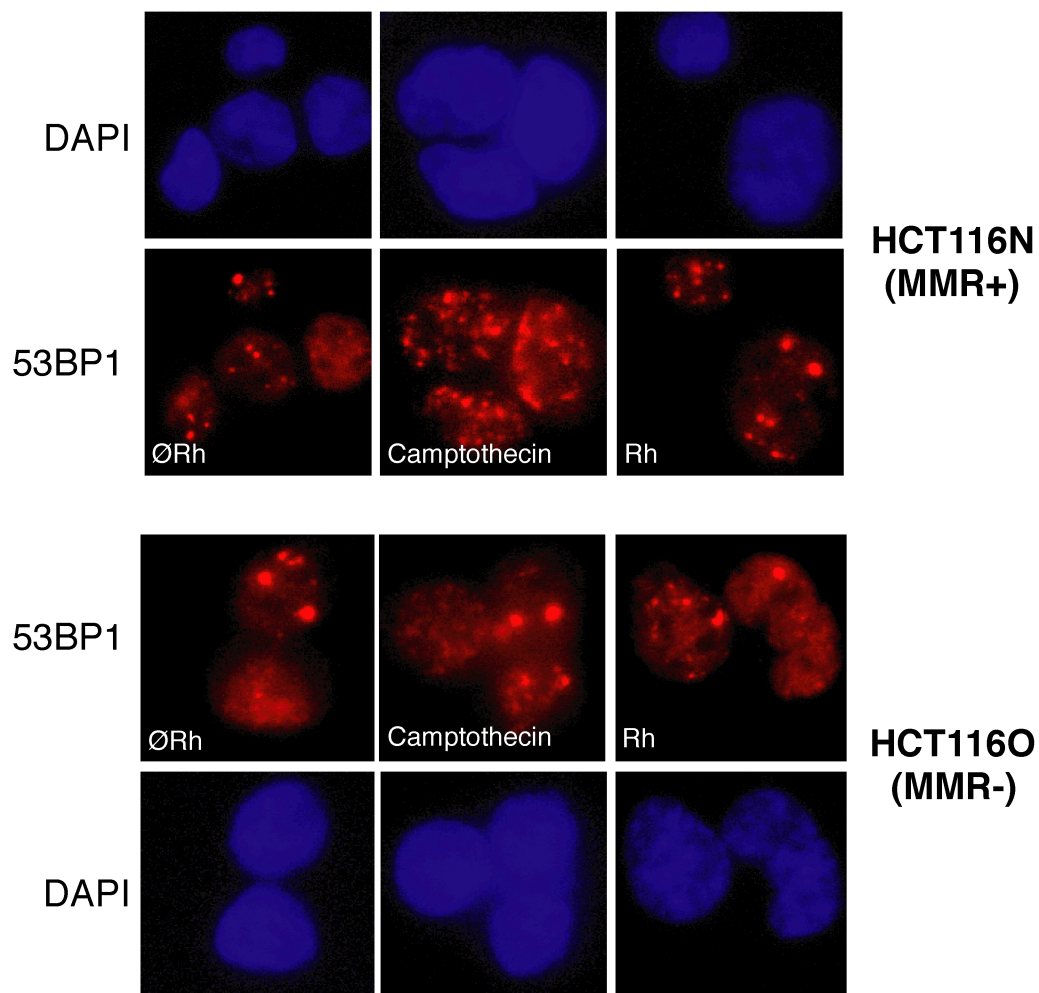


Figure 6.8 Confocal microscopy of immunofluorescence for 53BP1 (red) and nuclear staining with DAPI (blue) in fixed MMR-proficient HCT116N (top) and MMR-deficient HCT116O (bottom) cells after 2h exposure to camptothecin (1 μ M), [Rh(chrysi)(phen)(PPO)]²⁺ (“Rh,” 300 nM), or no treatment (ØRh).

MMR-proficient and MMR-deficient cells under all conditions, including untreated cells, again suggesting that the formation of DSBs may occur spontaneously in HCT116 cells.

Quantitative analysis of 53BP1 staining is shown in **Figure 6.9** and **Figure 6.10**. **Figure 6.9** displays the percentage of cells at each time point designated either as 53BP1-negative (having zero foci), low-53BP1 (1-5 foci per cell), moderate-53BP1 (6-10 foci per cell), or high-53BP1 (>10 foci per cell). Percentages were calculated as a fraction of the total number of cells in the collection of images for each sample. Accumulation of 53BP1 is less pronounced than γ H2AX for both rhodium- and camptothecin-treated cells. The majority of metalloinsertor-treated cells display low-53BP1, with 1 – 5 foci/cell, similar to that of untreated cells. The percentage of moderate- to high-53BP1 cells, i.e., cells containing ≥ 6 foci/cell, was also calculated as a function of time, shown in **Figure 6.10**. The percentage of 53BP1-positive cells treated with rhodium is equal to or lower than that of untreated cells at several time points, especially at 6 and 12h. Moreover, the difference in 53BP1 staining in Rh-treated HCT116N versus HCT116O cells is slight. These results suggest that metalloinsertor treatment has little effect on the induction of 53BP1 in HCT116 cells, signifying that this protein and the BRCA1 pathway are likely not associated with the cellular processing of mismatch recognition.

6.3.2 MTT Cytotoxicity Assay

The cytotoxic effects of $[\text{Rh}(\text{chrysi})(\text{phen})(\text{PPO})]^{2+}$ have been characterized previously in HCT116N and HCT116O cells, but the effects of camptothecin in these matched cell lines has not, to our knowledge, been explored. We performed an MTT cytotoxicity assay (MTT = (3-(4,5-dimethylthiazol-2-yl)-2,5-diphenyltetrazolium bromide) to ascertain the toxicity of camptothecin in the matched cell lines. Cells were

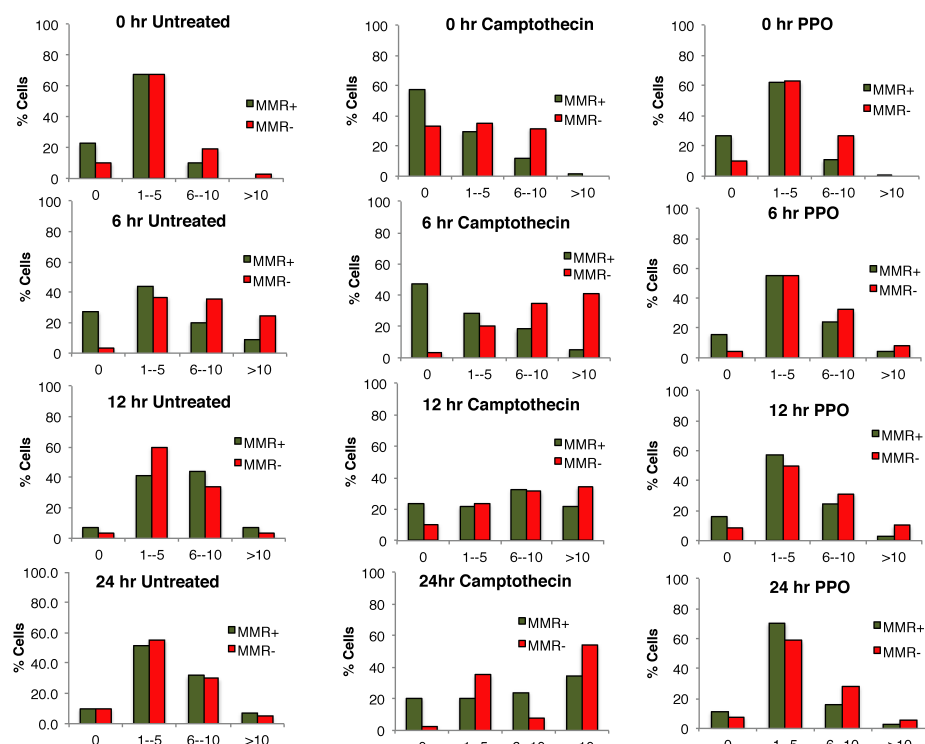


Figure 6.9 Quantitation of 53BP1 foci in HCT116N (MMR+, green) and HCT116O (MMR-, red) cells over time. Cells were either untreated or exposed to camptothecin (1 μ M) or [Rh(chrysi)(phen)(PPO)]²⁺ (300 nM) for 2h. After the treatment period, drug-containing medium was removed, replaced with fresh medium, and allowed to incubate for an additional 6, 12, or 24h. In the case of the 0 hr time point, cells were fixed immediately after treatment. Foci were quantified in each cell and designated as 53BP1-negative (0 foci), low-53BP1 (1-5 foci/cell), moderate-53BP1 (6-10 foci/cell), or high-53BP1 (>10 foci/cell). The percentage of each cell type was calculated as a fraction of the total cells in the images collected for each sample. For each sample, 3-5 images ($n = 30$ -150 cells) were collected.

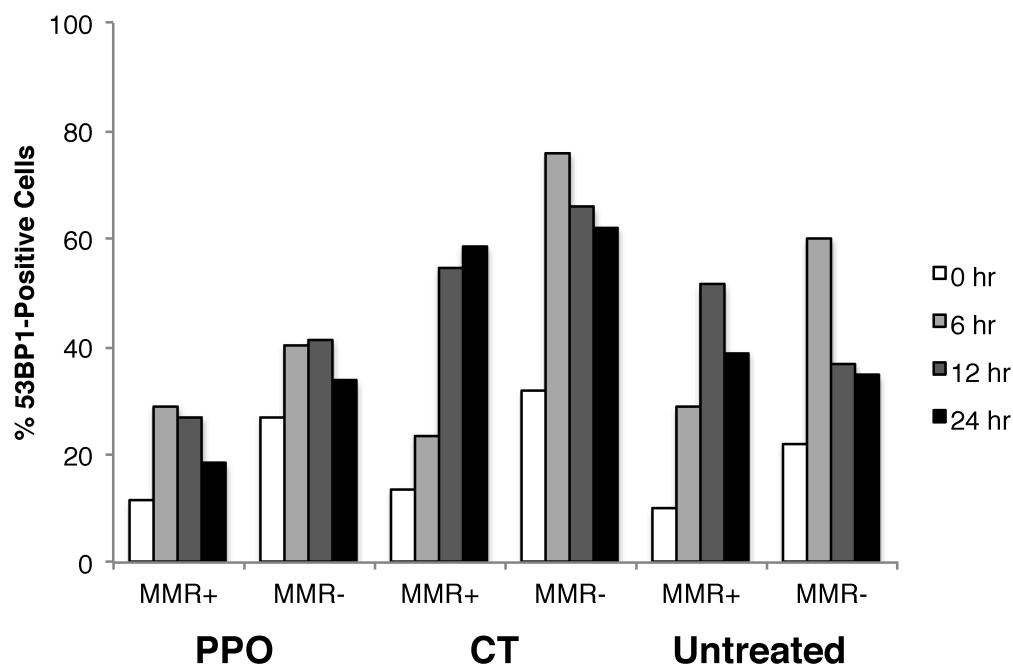


Figure 6.10 Quantitation of 53BP1-positive cells in HCT116N (MMR+) and HCT116O (MMR-) cells treated with $[\text{Rh}(\text{chrysi})(\text{phen})(\text{PPO})]^{2+}$ (PPO, 300 nM) or camptothecin (CT, 1 μM) for 2h followed by growth in media absent of drug for a period of 6, 12, or 24h. For each time point, an untreated control was included, as well as a 0 hr time point in which treated cells were fixed immediately after drug exposure. Cells containing ≥ 6 foci/cell were designated as 53BP1-positive, and the percentage of 53BP1-positive cells was calculated as a fraction of the total cells in the images collected for each sample. For each sample, 3-5 images ($n = 30$ -150 cells) were collected.

plated in 96-well plates at 5.0×10^4 cells/well and treated with varying concentrations of $[\text{Rh}(\text{chrysi})(\text{phen})(\text{PPO})]^{2+}$ or camptothecin, for 72h under humidified atmosphere. Percent viability is defined as the ratio of the amount of formazan in treated cells to that of untreated cells. The cytotoxic effects of the complexes in the HCT116N and HCT116O cell lines are shown in **Figure 6.11**.

The metalloinsertor complex performs as expected, inducing cell-selective death in the HCT116O cell line with a peak differential cytotoxicity (defined as the difference in viability between the two cell lines) of $49 \pm 1.4\%$, occurring at 400 nM. The IC_{50} value (indicating the concentration at which 50% of the cells are viable) in HCT116O cells is approximately 200 nM, consistent with previous reports.²⁹ In contrast, camptothecin displays no preference for either cell line. Camptothecin exhibits moderate potency in both cell lines at the concentrations studied; after 72h at 1 μM exposure, $67 \pm 1.3\%$ of HCT116N cells remained viable, and $58 \pm 8.9\%$ of HCT116O cells were viable. While considerably less potent than $[\text{Rh}(\text{chrysi})(\text{phen})(\text{PPO})]^{2+}$ (which, at 1 μM after 72h, leaves $44 \pm 2.8\%$ and $13 \pm 0.5\%$ viability in HCT116N and HCT116O cells, respectively), camptothecin is clearly capable of inducing cytotoxic effects at the concentrations explored in the immunofluorescence assay. Additionally, the lack of preferential targeting by camptothecin is consistent with the occurrence of γH2AX -positive cells in both cell lines.

6.3.3 Metalloinsertors Induce Double Strand Breaks in the Genome of MMR-deficient Cells: Comet Assay

Immunofluorescence staining of MMR-proficient and MMR-deficient cells revealed that a DNA damage response is rapidly elicited upon exposure to low

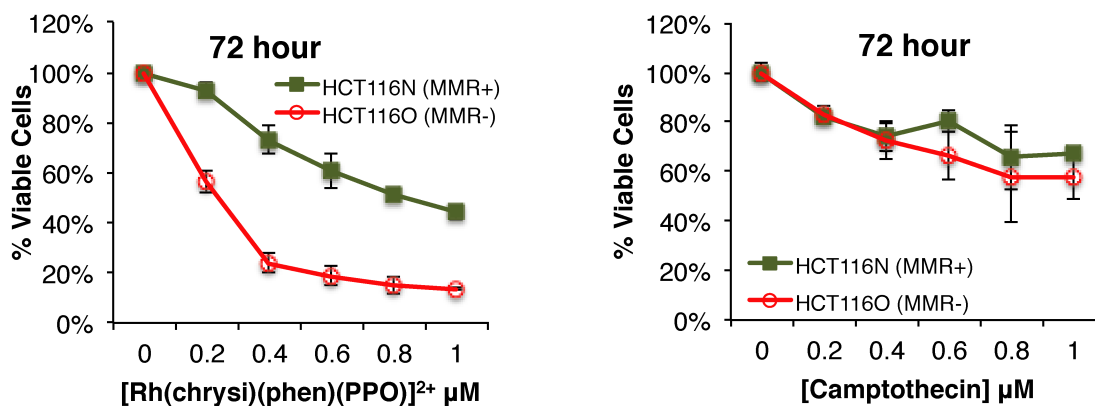


Figure 6.11 MTT cytotoxicity assay of HCT116N (MMR-proficient) and HCT116O (MMR-deficient) cells treated with $[\text{Rh}(\text{chrysi})(\text{phen})(\text{PPO})]^{2+}$ (left), and camptothecin (right). Cells were incubated with each complex at the concentrations indicated for 72h. After the incubation period, cells were treated with the MTT reagent for 4 h, and the resulting formazan crystals were solubilized with acidified SDS. Percent cell viability is defined as the percentage of formazan normalized to that of untreated cells. Standard errors were calculated from 5 replicates.

concentrations of rhodium. However, these assays do not indicate whether metalloinsertors directly damage the DNA themselves. We performed single-cell gel electrophoresis (“comet” assay) on HCT116N and HCT116O cells seeded in 6-well plates at 2×10^5 cells/well and treated with 500 nM $[\text{Rh}(\text{chrysi})(\text{phen})(\text{PPO})]^{2+}$ for 24h. Cells were harvested, washed with PBS, and embedded in low-melting agarose at 37 °C. The cell-agarose mixture was plated onto 3-well microscope slides, lysed with detergent, and electrophoresed under alkaline conditions (300 mM NaOH, 1 mM EDTA, pH >13). Cells were stained with fluorescent DNA-binding dye and analyzed by epifluorescence microscopy ($\lambda_{\text{ex}} = 488$ nm).

The results of the comet assay are depicted in **Figure 6.12**. Lysis conditions involving detergent and high salt concentrations condense undamaged DNA into supercoiled loops in the nucleus, which appear in the image as the heads of the “comet.” DNA containing DSBs becomes uncoiled under the alkaline electrophoresis conditions, thus migrating away from the supercoiled DNA in the gel matrix. Damaged DNA, thus, appears as the “comet tail” in the microscopy image. Remarkably, $[\text{Rh}(\text{chrysi})(\text{phen})(\text{PPO})]^{2+}$ induces DSBs in the DNA of HCT116O cells, but not the HCT116N cells. Comet tails indicating damaged DNA extend away from the supercoiled DNA head, having migrated towards the anodic end of the gel (to the right side of the image). These tails are also observed in cells treated with 500 nM camptothecin. The HCT116N cells containing rhodium largely resemble those of the untreated cells, with little evidence of damage in the form of tails. Untreated samples were run for both HCT116N and HCT116O cells; however, images were only collected for the HCT116O cell line due to photobleaching in the N-cell line.

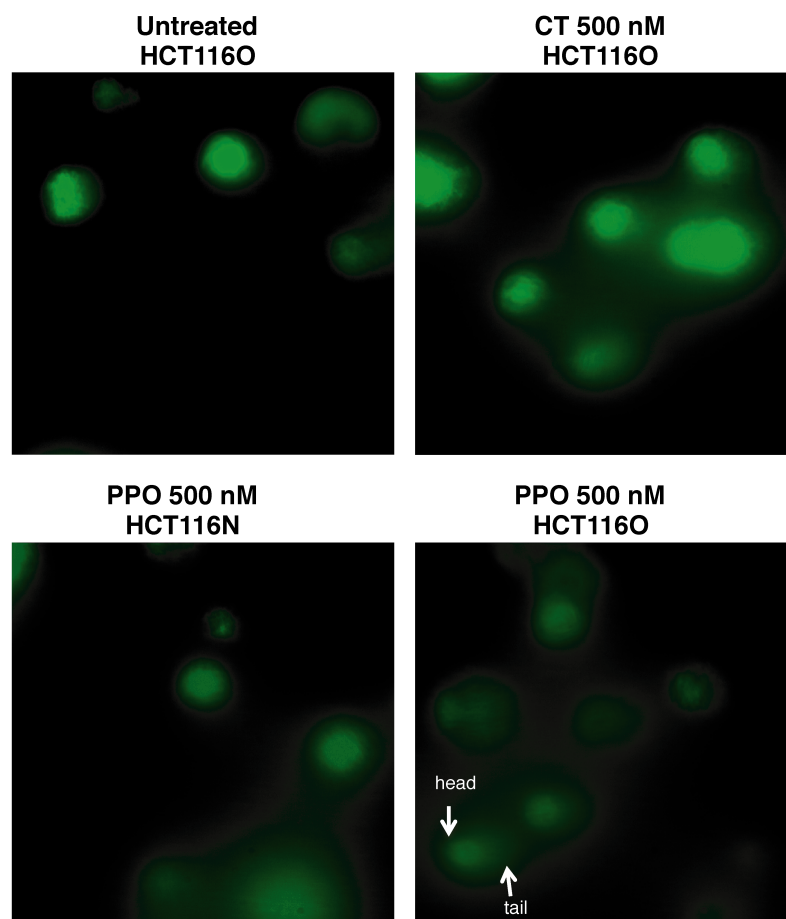


Figure 6.12 Single cell gel electrophoresis of HCT116N (left) and HCT116O (right) cells. Cells were plated at 2×10^5 and treated with 500 nM of either camptothecin or PPO for 24 h. Cells were harvested by trypsinization, washed, and mixed with OxiSelect agarose. Following lysis and alkaline treatment, slides were electrophoresed in alkaline buffer at 20 V (450 mA), stained with VistaGreen DNA dye, and imaged using epifluorescence microscopy, with excitation at 488 nm. Top: Untreated HCT116O cells (“CT,” left), HCT116O cells treated with 500 nM camptothecin. Bottom: HCT116N cells treated with $[\text{Rh}(\text{chrysi})(\text{phen})(\text{PPO})]^{2+}$ (“PPO,” left); HCT116O cells treated with PPO (right). Undamaged DNA is supercoiled to form the comet “head,” while damaged DNA migrates from left to right in the gel matrix, forming the comet “tail” (denoted by white arrows).

The results of the comet assay are consistent with what has been observed in assays of the antiproliferative and cytotoxic effects of metalloinsertors in these cell lines: these complexes would be expected to bind the DNA of the MMR-deficient HCT116O cells as they contain more mismatches than DNA in the corresponding HCT116N line. Yet it is surprising that these complexes are capable of inducing DNA strand breaks, as no evidence of damage has been observed in *in vitro* DNA binding experiments, particularly in the absence of UV light.²⁹ Furthermore, these results are inconsistent with those observed for the immunofluorescence assay, where the localization of DNA damage response proteins such as γ H2AX is observed for both cell lines. Clearly, there are additional response elements at play in the cellular processing of mismatch recognition by metalloinsertors.

6.3.4 Fluorescence Detection of Nascent RNA Synthesis *in Cellulo*

We next examined whether rhodium metalloinsertors inhibit transcription in MMR-deficient cells. HCT116N and HCT116O cells were seeded in 96-well plates at 4,000 cells/well and allowed 24h to adhere. Cells were then treated with either $[\text{Rh}(\text{chrysi})(\text{phen})(\text{PPO})]^{2+}$ (0 – 1 μM) or cisplatin (0 – 10 μM) for 24h. Cisplatin was chosen as a control because it is known to induce apoptosis in cells via inhibition of transcription. Cells were then pulse-chased for 1h with 1 mM ethynyl uridine (EU), which is incorporated into newly synthesized RNA indiscriminately in place of uridine. EU is not incorporated into DNA, so the amount of EU in the cells is reflective of the amount of RNA synthesis relative to untreated controls. After fixation, cells were labeled via copper-catalyzed click reaction with an azide-modified fluorophore. The amount of EU incorporation was quantified by fluorescence detection with excitation at 495 nm and

emission at 519 nm. The extent of transcription is expressed as the ratio of fluorescently labeled EU of cells treated with rhodium or platinum as compared to untreated controls.

As can be seen in **Figure 6.13**, $[\text{Rh}(\text{chrysi})(\text{phen})(\text{PPO})]^{2+}$ selectively inhibits transcription in the HCT116O cell line. The peak differential inhibition, defined as the difference in EU incorporation between the two cell lines, is $49 \pm 3.9\%$, occurring at 800 nM after 24 h. The rhodium complex has little effect on the amount of RNA synthesized in the HCT116N cell line. Cisplatin displays only modest inhibition of transcription ($90 \pm 16\%$ and $82 \pm 4.9\%$ at 10 μM in the HCT116N and HCT116O lines, respectively) and does not preferentially target either cell line. These results imply that the preferential inhibition of transcription by rhodium in MMR-deficient cells is the result of mismatch recognition in genomic DNA.

6.3.5 Rhodium Accumulation in Tumors

Preliminary *in vivo* studies in collaboration with Amgen have begun to explore the effect of metalloinsertor treatment on mice that have been implanted with MMR-deficient HCT116 tumor xenografts. Tumors were harvested from the mice after 24h dosage and nuclear and cytosolic lysates were extracted via differential centrifugation procedures. The soluble fractions were analyzed for rhodium content by inductively coupled plasma mass spectrometry (ICP-MS) and normalized to protein content as determined by bicinchoninic acid (BCA) assay. Rhodium concentration is thus expressed as ng [Rh]/mg [soluble protein]. The insoluble tumor fractions, including membranes and connective tissue, could not be sufficiently solubilized for ICP-MS and thus were not analyzed for rhodium content.

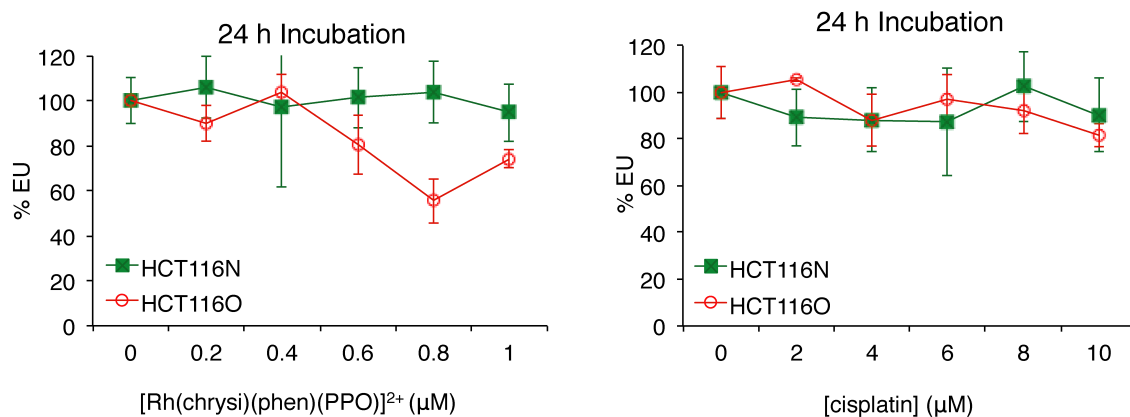


Figure 6.13 Analysis of RNA synthesis in HCT116N (green) and HCT116O (red) cells as a function of $[\text{Rh}(\text{chrysi})(\text{phen})(\text{PPO})]^{2+}$ or cisplatin concentration after 24h. Cells were plated at 4,000 cells/well in 96-well plates. RNA synthesis is expressed as the percentage EU incorporation normalized to the untreated samples. Percent errors are calculated from 5 replicates.

The results are summarized in **Figure 6.14**. Tumor samples for mice treated with 100 mg/kg $[\text{Rh}(\text{HDPa})_2\text{chrysi}]^{3+}$ and $[\text{Rh}(\text{chrysi})(\text{phen})(\text{PPE})]^{2+}$ could not be obtained due to the extreme toxicity of the dosage. Only the controls (PBS only and Cdc7 inhibitor) and the low-dose samples of $[\text{Rh}(\text{chrysi})(\text{phen})(\text{PPE})]^{2+}$ and $[\text{Rh}(\text{chrysi})(\text{phen})(\text{PPO})]^{2+}$ yielded soluble tumor lysate that was suitable for analysis by ICP-MS. High variability was observed within each group of mice. Background rhodium was determined by running samples of 1% $\text{HNO}_{3(\text{aq})}$ through the instrument, which yielded a baseline concentration of 0.11 ± 0.01 ppb Rh. Because the overall rhodium concentrations are low for tumor samples, concentrations are also provided in ppb (**Table 6.2**) to determine whether normalized samples are sufficiently above background.

Unsurprisingly, tumors dosed with only PBS displayed no appreciable rhodium content with < 0.05 ng [Rh]/mg [soluble protein] – well below background. Similarly, mice treated with only Cdc7 inhibitor displayed no rhodium content; one of the replicates appears to display high rhodium content when normalized to protein concentration, but Rh concentration in ppb is below baseline. Two of the three mice treated with 10 mg/kg $[\text{Rh}(\text{chrysi})(\text{phen})(\text{PPE})]^{2+}$ displayed rhodium accumulation well above background, with approximately 0.38 and 0.25 ng [Rh]/mg [soluble protein], while the third mouse in the group displayed rhodium slightly above baseline (0.14 ng [Rh]/mg [soluble protein]). Additionally, all but one of the mice treated with $[\text{Rh}(\text{chrysi})(\text{phen})(\text{PPO})]^{2+}$ showed signs of rhodium uptake into the tumor grafts: dosage at 10 mg/kg $[\text{Rh}(\text{chrysi})(\text{phen})(\text{PPO})]^{2+}$ yielded 0.04 ng [Rh]/mg [soluble protein] (below baseline) and 0.23 ng [Rh]/mg [soluble protein] (above baseline); soluble tumor lysate from the third mouse in this group could not be procured. For the 20 mg/kg dosage of

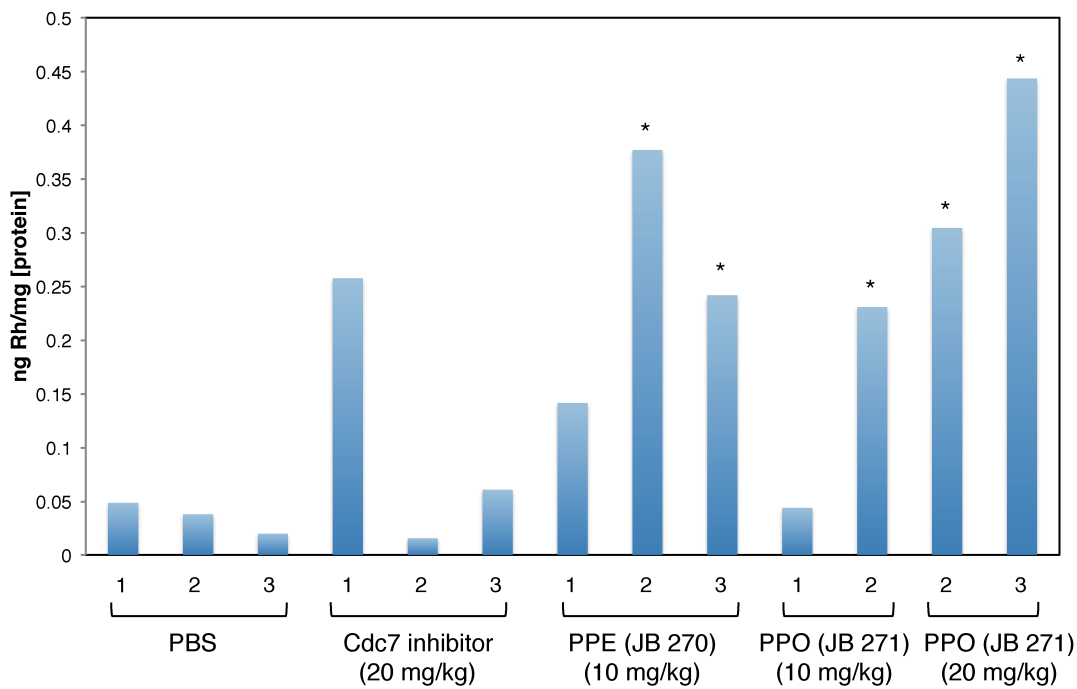


Figure 6.14 Rhodium accumulation in human HCT116 tumors harvested from nude mice. Groups of mice were dosed in triplicate with the indicated compounds for 24h. Tumor samples were lysed, separated from the insoluble content, and the soluble fractions were analyzed for rhodium uptake by ICP-MS. Rhodium content was normalized to protein concentration as determined by BCA analysis, and is expressed as ng Rh/ mg [soluble protein]. Samples containing rhodium determined to be above background are denoted by the asterisks.

[Rh(chrysi)(phen)(PPO)]²⁺ tumor samples were only harvested for two of the three mice in the group. Lysates from both samples, however, displayed some of the highest rhodium accumulation, with 0.30 and 0.44 ng [Rh]/mg [soluble protein]. Additionally, there is evidence for dose-dependent accumulation of [Rh(chrysi)(phen)(PPO)]²⁺ in these tumors.

Overall, HCT116 tumor xenografts implanted in live mice exhibit modest rhodium accumulation, but it is clear that at least some of the metalloinsertor is reaching the tumor in a complex, multicellular environment. However, the accumulation of rhodium in tumors *in vivo* is not sufficient to reach the concentrations required for cellular activity. The development of metalloinsertor conjugates with cell- and tissue-targeting functionalities may assist in improving the biodistribution of metalloinsertors *in vivo*.

Table 6.2 Rhodium Accumulation in HCT116 Tumors^a

Sample ^b	[Rh] ppb	Comparison to Baseline ^a
PBS – 1	0.04	—
PBS – 2	0.02	—
PBS – 3	0.03	—
Cdc7 inhibitor – 1	0.08	—
Cdc7 inhibitor – 2	0.01	—
Cdc7 inhibitor – 3	0.06	—
[Rh(chrysi)(phen)(PPE)] ²⁺ – 1	0.08	—
Rh(chrysi)(phen)(PPE)] ²⁺ – 2	0.30	+
Rh(chrysi)(phen)(PPE)] ²⁺ – 3	0.27	+
Rh(chrysi)(phen)(PPO)] ²⁺ (10 mg/kg) – 1	0.03	—
Rh(chrysi)(phen)(PPO)] ²⁺ (10 mg/kg) – 2	0.24	+
Rh(chrysi)(phen)(PPO)] ²⁺ (20 mg/kg) – 2	0.18	+
Rh(chrysi)(phen)(PPO)] ²⁺ (20 mg/kg) – 3	0.62	+

^aRhodium accumulation in HCT116 tumors expressed in ppb is compared to background rhodium concentration in blank samples (1% HNO_{3(aq)}), determined to be 0.11 ± 0.01 ppb. A “—” indicates that the rhodium concentration measured for each sample lies below the baseline rhodium in blank 1% HNO_{3(aq)} samples. ^bEach dosage was carried out on groups of three mice, denoted by the numbers next to each sample.

6.4 Discussion

6.4.1 Metalloinsertors Damage Genomic DNA

Biological characterization of metalloinsertors in the isogenically matched HCT116N and HCT116O cells has established that these complexes inhibit DNA synthesis, induce cell cycle arrest, and trigger necrosis selectively in cells exhibiting MMR-deficiency – that is, cells with DNA containing approximately 1000 fold more base pair mismatches than the DNA of MMR-proficient cells. Examination of metalloinsertor subcellular localization subsequently revealed that this cell-selectivity is dependent upon uptake into the nucleus, rather than the mitochondria, further supporting the hypothesis that the biological activity of these complexes is derived from mismatch recognition in genomic DNA. However, direct evidence of interaction between metalloinsertors and the genome has not previously been obtained. Immunofluorescence staining of MMR-proficient and MMR-deficient cells revealed that metalloinsertors induce a rapid DNA damage response (2 hours) at low concentrations (300 nM), in the form of focal accumulation of γ H2AX.

The H2AX protein is a component of the H2A histone family and contributes to nucleosome formation. When the genome undergoes DNA damage, particularly in the form of DSBs, H2AX becomes phosphorylated on serine 139 to form γ H2AX, which in turn localizes and recruits DNA repair proteins to points of injury. As such, γ H2AX focal accumulation is an important biomarker for chromosomal damage and could reveal information about the downstream processes associated with rhodium treatment. Immunofluorescence staining of HCT116N and HCT116O cells has revealed that these cells, particularly the HCT116O line, appear to spontaneously induce γ H2AX foci even

in the absence of drug. This could potentially be a result of chromosomal instability arising from the transfection of chromosome 3 (in HCT116N cells) and chromosome 2 (in HCT116O cells); aneuploid cells are highly susceptible to chromosomal aberrations.³⁶ Additionally, the occurrence of DSBs in untreated HCT116O cells may be a result of the lack of MMR, as microsatellite instability can lead to DNA damage and mutations in DNA repair proteins.³⁷

Despite the presence of γ H2AX foci in untreated cells, the addition of $[\text{Rh}(\text{chrysi})(\text{phen})(\text{PPO})]^{2+}$ produces substantially higher γ H2AX staining at sufficient concentrations. At 1 μM rhodium, fluorescence is similar to that of 1 μM camptothecin, indicating that metalloinsertors induce double strand breaks in the genome, possibly via direct interaction with the DNA through mismatch binding (**Figure 6.2**). However, γ H2AX foci also appear in HCT116N cells treated with rhodium, even though the PPO complex is not cytotoxic in the N-cell line.

To explore whether rhodium concentration played a role in incurring nonspecific DNA strand breaks, we carried out the staining with 100 nM and 300 nM $[\text{Rh}(\text{chrysi})(\text{phen})(\text{PPO})]^{2+}$. These concentrations were chosen because 100 nM is the lowest dose at which biological activity occurs, and 300 nM is roughly the concentration at which peak differential cytotoxicity (the difference in viability between the two cell lines) is observed.²⁹ The addition of 100 nM rhodium has little effect on cells, but 300 nM rhodium results in a small but measurable increase in γ H2AX foci compared to untreated cells.

We also examined the possibility that γ H2AX foci may simply occur as an early cellular response to the presence of rhodium, perhaps as it electrostatically associates

with the DNA, searching for a mismatch. If this were the case, foci could potentially appear in both cell lines immediately upon short-term exposure to rhodium, but may clear if cells did not acquire more permanent DNA damage. Cells were consequently treated with complex for 2h, but then allowed a “recovery” period in fresh media without rhodium. It was hypothesized that if γ H2AX was localizing to irreparable damage caused by the metalloinsertor, foci would still be present after the recovery period, but if γ H2AX foci were simply an early “alarm” signal, foci would clear once cells were allowed to grow again in the absence of complex. Indeed, γ H2AX foci do increase over time, and slightly more so in the MMR-deficient cell line than in the MMR-proficient line. For both cell lines, the most dramatic increase in the percentage of γ H2AX-positive cells occurs in the first 6h post-treatment. In the HCT116O cells, the percentage of γ H2AX-positive cells declines over the remainder of the 24h recovery period. One possible explanation is that the metalloinsertor is causing DNA damage that recruits a cellular response in the first 6h, but foci dissipate as the lesions are repaired. It is also possible that the decrease in foci over time is the result of cell cycle arrest and/or cell death – previous work has shown that metalloinsertors inhibit DNA synthesis as early as 6h, and cytotoxicity can be observed at 24h.

In general, the results of the immunofluorescence study exhibited only modest evidence of DNA damage compared to untreated cells as well as a slight preference for the MMR-deficient cell line. Further studies must be carried out to assess whether these current observations hold any significance. Additionally, we examined the effects of metalloinsertor treatment on DNA more directly using single cell gel electrophoresis, which electrophoretically separates damaged DNA from undamaged within a cell. We

observed that $[\text{Rh}(\text{chrysi})(\text{phen})(\text{PPO})]^{2+}$ treatment results in DSBs in HCT116O cells, but not HCT116N cells.

Mismatch repair deficiency appears to correlate with DNA double strand breaks upon treatment with rhodium metalloinsertors, but it is still unclear how metalloinsertion leads to these breaks. *In vitro* DNA binding studies of $[\text{Rh}(\text{chrysi})(\text{phen})(\text{PPO})]^{2+}$ have shown that the complex binds non-covalently and, like most metalloinsertors, do not induce sugar-phosphate backbone cleavage even with irradiation. Even photocleaving metalloinsertors, such as $[\text{Rh}(\text{bpy})_2\text{chrysi}]^{3+}$ and $[\text{Rh}(\text{bpy})_2\text{phzi}]^{3+}$, only lead to scission on one strand, and only at the mismatched sites.

Camptothecin also binds DNA non-covalently and induces DSBs that lead to γH2AX foci and cytotoxicity. This quinolone alkaloid forms highly specific hydrogen bonding contacts between DNA (at cytosine residues) and the DNA binding protein topoisomerase I (topo I). The resulting ternary complex of drug, DNA, and DNA cleavage enzyme results in stalled progression of topo I, leading to accumulation of DSBs in the genome as well as transcription inhibition.³² It is possible that metalloinsertors bound to DNA mismatches are also bound by proteins that recognize and attempt to repair the lesion, leading to an accumulation of DNA strand breaks and inhibition of transcription.

6.4.2 Metalloinsertors Inhibit Transcription in MMR-Deficient Cells

Perhaps more significantly than damaging the genome, metalloinsertors also inhibit RNA synthesis selectively in the HCT116O cell line. Inhibition of transcription is a key step in the anticancer activity of cisplatin: loss of the ability to synthesize messenger RNA prevents cells from entering mitosis, thus leading to cell cycle arrest in

the G2 phase.^{38,39} Early studies of metalloinsertor cytotoxicity revealed that HCT116O cells also undergo cell cycle arrest in the G2/M phase,²³ which could potentially arise from an inability to synthesize the mRNA necessary to pass into mitosis (M phase).

Cisplatin arrests transcription through the formation of covalent DNA adducts, which reduce the binding affinity of RNA polymerases and block elongation.^{40,41} It is remarkable, then, that metalloinsertors also possess such capabilities, given that their interaction with DNA is non-covalent. Previous examples of non-covalent DNA binding compounds have been shown to inhibit transcription. Synthetic polyamides that bind the minor groove of DNA with high sequence specificity block transcription by binding to the transcription factor TFIIIA binding site.⁴² Additionally, a sequence-selective rhodium intercalator complex bearing 4-guanidylmethyl-1,10-phenanthroline ligands blocks transcription factor binding from the major groove.⁴³ In these cases, however, the compounds bound DNA sequences spanning six or more base pairs – comparatively much larger areas than a single base mismatch. In the case of the metallointercalator complex, the DNA helix was also unwound 70°, in addition to steric inhibition of protein binding.⁴³ Metalloinsertors, in contrast, induce no such distortions to the overall structure of the duplex,^{16,19} although extrusion of mismatched bases from the base stack may preclude binding of proteins critical to transcription. Future studies will attempt to further elucidate the specific effects of metalloinsertors and mismatch binding on transcription.

6.4.3 Effects of Rhodium Metalloinsertors *in Vivo*

The development of more potent and more selective metalloinsertor complexes, such as $[\text{Rh}(\text{chrysi})(\text{phen})(\text{PPO})]^{2+}$ and $[\text{Rh}(\text{chrysi})(\text{phen})(\text{PPE})]^{2+}$, have led to efforts to explore the potential efficacy of these compounds *in vivo*. In collaboration with Amgen,

we have discovered that our complexes are stable in plasma and possess pharmacokinetic properties suitable for *in vivo* studies. Here, we examined the effects of metalloinsertor treatment on MMR-deficient tumors implanted in mice, and found tolerable dosages for our most active complexes. While further analysis has revealed that rhodium exposure levels were below the concentrations required for cellular activity, we have also shown that some of the metalloinsertor is in fact reaching the tumor, albeit in concentrations too low to have an effect. With the continued development of bifunctional conjugates, we aim to exert increased control over the biodistribution of these compounds. The appendage of cell- and tissue-specific elements, such as peptides and antibodies, are anticipated to enhance targeting of metalloinsertors in complex biological systems.

6.5 Conclusions

The synthesis of new generations of rhodium metalloinsertors has afforded complexes that target mismatch repair-deficient cells with increasing selectivity and unprecedented potency. With the discovery of metalloinsertors that exhibit cellular EC_{50} activities in the nanomolar range, the development of this class of complexes into clinically viable therapeutics becomes increasingly feasible. Efforts to uncover how the cell responds to mismatch recognition by our complexes in the nucleus have revealed that metalloinsertors selectively inhibit transcription in MMR-deficient cells, and likely cause double strand breaks to the genome. Furthermore, the cellular response to metalloinsertor treatment is rapid, with protein signaling occurring after only 2h. Preliminary *in vivo* mouse studies of rhodium metalloinsertors revealed that these complexes are tolerated at low doses and that the complex can accumulate in MMR-deficient tumors while traversing the complex environment of a multicellular organism. These biological studies,

though preliminary, show great promise for metalloinsertors as targeted chemotherapeutics for mismatch-repair deficient cancers.

6.6 References

- 1 Hoeijmakers, J. H. J. *Nature*. **2001**, *411*, 366-374.
- 2 Watson, J. D.; Baker, T. A.; Bell, S. P.; Gann, A.; Levine, M.; Losick, R. in *Molecular Biology of the Gene*, 5th ed. (Ed: Peason Benjamin Cummings), CSHL Press. **2004**, ch 9-10.
- 3 Wildenberg, J.; Meselson, M. *Proc. Nat. Acad. Sci. USA*. **1975**, *72*, 2202-2206.
- 4 Wagner, Jr., R.; Meselson, M. *Proc. Nat. Acad. Sci. USA*. **1976**, *73*, 4135-4139.
- 5 Iyer, R. R.; Pluciennik, A.; Burdett, V.; Modrich, P. L. *Chem. Rev.* **2006**, *106*, 302-323.
- 6 Parsons, R.; Li, G.-M.; Longley, M.; Modrich, P.; Liu, B.; Berk, T.; Hamilton, S. R.; Kinzler, K. W.; Vogelstein, B. *Science*. **1995**, *268*, 738-740.
- 7 Jiricny, J. *Nat. Rev. Mol. Cell Biol.* **2006**, *7*, 335-346.
- 8 Tzung, T. Y.; Diem, C.; Runger, T. M. *Arch. Dermatol. Res.* **1998**, *290*, 109-112.
- 9 N. Papadopoulos, A. Lindblom, *Hum. Mutat.* **1997**, *10*, 89–99.
- 10 I. I. Arzimanoglou, F. Gilbert, H. R. K. Barber, *Cancer*. **1998**, *82*, 1808–1820.
- 11 D. Fink, S. Aebi, S. B. Howell, *Clin. Cancer Res.* **1998**, *4*, 1-6.
- 12 R. J. Fram, P. S. Cusick, J. M. Wilson, M. G. Marinus, *Mol. Pharmacol.* **1985**, *28*, 51-55.
- 13 Weidmann, A. G.; Komor, A. C.; Barton, J. K. *Comments on Inorganic Chemistry* **2014**, *34*, 114-123.
- 14 Jackson, B. A.; Barton, J. K. *J. Am. Chem. Soc.* **1997**, *119*, 12986–12987.
- 15 Cordier, C.; Pierre, V. C.; Barton, J. K. *J. Am. Chem. Soc.* **2007**, *129*, 12287–12295.

- 16 Zeglis, B. M.; Pierre, V. C.; Kaiser, J. T.; Barton, J. K. *Biochemistry* **2009**, *48*, 4247–4253.
- 17 Jackson, B. A.; Alekseyev, V. Y.; Barton, J. K. *Biochemistry* **1999**, *38*, 4655–4662.
- 18 Jackson, B. A.; Barton, J. K. *Biochemistry* **2000**, *39*, 6176–6182.
- 19 Pierre, V. C.; Kaiser, J. T.; Barton, J. K. *Proc. Natl. Acad. Sci. U.S.A.* **2007**, *104*, 429–434.
- 20 Koi, M.; Umar, A.; Chauhan, D. P.; Cherian, S. P.; Carethers, J. M.; Kunkel, T. A.; Boland, C. R. *Cancer Res.* **1994**, *54*, 4308-4312.
- 21 Hart, J. R.; Glebov, O.; Ernst, R. J.; Kirsch, I. R.; Barton, J. K. *Proc. Natl. Acad. Sci. U.S.A.* **2006**, *103*, 15359–15363.
- 22 Ernst, R. J.; Song, H.; Barton, J. K. *J. Am. Chem. Soc.* **2009**, *131*, 2359–2366.
- 23 Ernst, R. J.; Komor, A. C.; Barton, J. K. *Biochemistry* **2011**, *50*, 10919–10928.
- 24 Komor, A. C.; Schneider, C. J.; Weidmann, A. G.; Barton, J. K. *J. Am. Chem. Soc.* **2012**, *134*, 19223–19233.
- 25 Weidmann, A. G.; Komor, A. C.; Barton, J. K. *Philos. Trans. R. Soc. A.* **2013**, *371*, 20120117.
- 26 Bailis, J. M.; Gordon, M. L.; Gurgel, J. L.; Komor, A. C.; Barton, J. K.; Kirsch, I. R. *PLoS One* **2013**, *8*, e78726.
- 27 Kuo, L. J.; Yang, L. X. *In Vivo* **2008**, *22*, 305-309.
- 28 Murner, H.; Jackson, B. A.; Barton, J. K. *Inorg. Chem.* **1998**, *37*, 3007–3012.

- 29 Komor, A. C.; Barton, J. K. *J. Am. Chem. Soc.* **2014**, *136*, 14160-14172.
- 30 Mosmann, T. *J. Immunol. Methods* **1983**, *65*, 55-63.
- 31 Smith, P. K.; Krohn, R. I.; Hermanson, G. T.; Mallia, A. K.; Gartner, F. H.; Provenzano, M. D.; Fujimoto, E. K.; Goeke, N. M.; Olson, B. J.; Klenk, D. C. *Anal. Biochem.* **1985**, *150*, 76-85.
- 32 Pommier, Y.; Redon, C.; Rao, V.A.; Seiler, J.A.; Sordet, O.; Takemura, H.; Antony, S.; Meng, L.; Liao, Z.; Kohlhagen, G. *Mutat. Res.* **2003**, *532*, 173-203.
- 33 Xuan, L.; Wolf-Dietrich, H. *Cell Res.* **2008**, *18*, 99-113.
- 34 Garcia-Higuera I.; Taniguchi, T.; Ganesan, S.; Meyn, M.S.; Timmers, C.; Hejna, J.; Grompe, M.; D'Andrea, A.D. *Mol. Cell.* **2001**, *7*, 249-262.
- 35 Panier, S.; Boulton, S. J. *Nat. Rev. Mol. Cell Biol.* **2014**, *15*, 7-18.
- 36 McCarthy, N. *Nat. Rev. Cancer* **2011**, *11*, 760.
- 37 Li, H. R.; Shagisultanova, E. I.; Yamashita, K.; Piao, Z.; Perucho, M.; Malkhosyan, S. R. *Cancer Res.* **2004**, *64*, 4760-4767.
- 38 Todd, R. C.; Lippard, S. J. *Metallomics* **2009**, *1*, 290-291.
- 39 Sandman, K. E.; Marla, S. S.; Zlokarnik, G.; Lippard, S. J. *Chem. Biol.* **1999**, *6*, 541-551.
- 40 Tornaletti, S.; Patrick, S. M.; Turchi, J. J.; Hanawalt, P.C. *J. Biol. Chem.* **2003**, *278*, 35791-35797.
- 41 Damsma, G. E.; Alt, A.; Brueckner, F.; Carell, T.; Cramer, P. *Nat. Struct. Mol. Biol.* **2007**, *14*, 1127-1133.
- 42 Gottesfeld, J. M.; Neely, L.; Trauger, J. W.; Baird, E. E.; Dervan, P. B. *Nature* **1997**, *387*, 202-205.

- 43 Odom, D. T.; Parker, C. S.; Barton, J. K. *Biochemistry*, **1999**, 38, 5155-5163.

Chapter 7: Summary and Outlook

The unchecked proliferation of DNA base pair mismatches in the human genome can have severe consequences, leading to mutagenesis. Proliferation of these single base lesions is generally the result of an absent or otherwise defective mismatch repair (MMR) machinery, which is responsible for the recognition and correction of these mutations. Unsurprisingly, deficiencies in the MMR pathway are associated with a variety of cancers, but the consequences of MMR-deficiency continue even further. The resistance that MMR-deficient cancers often exhibit to traditional chemotherapeutic agents renders them largely untreatable, particularly in the later stages of carcinogenesis. Worse, attempted treatment of these malignancies with therapies such as cisplatin or DNA alkylators simply enriches the population of cells exhibiting MMR-deficiency, often resulting in secondary cancers such as leukemia.

The necessity of treatment for MMR-related diseases, combined with the devastating side effects arising from traditional chemotherapeutics targeting healthy cells, has fueled our continued research of rhodium metalloinsertors. These complexes bind DNA mismatches both *in vitro* and in cells with exquisite precision, resulting in highly selective potency in MMR-deficient cancer cells. A significant portion of my doctoral research has been devoted to uncovering *how* this unique biological activity occurs, and employing these discoveries in the development of increasingly complex structures.

In my early work in collaboration with Dr. Alexis Komor and Dr. Curtis Schneider, we uncovered an important structure activity relationship between the non-inserting ancillary ligands of a diverse group of metalloinsertors. These complexes displayed a broad range of biological activities that depended not on their DNA binding

affinities or cellular uptake, but rather their propensity to localize to the nucleus and avoid mitochondria, a characteristic that directly correlated to the lipophilicity of the ancillary ligands. Importantly, we discovered that metalloinsertors localize to the nucleus in concentrations sufficient for mismatch binding, whereas mitochondrial localization is detrimental to cell-selective cytotoxicity, thereby supporting the notion that our rhodium complexes target DNA mismatches in the genome.

Upon gaining a greater understanding of the biological activity of our rhodium complexes, my next goal for my thesis research was to synthesize more complicated structures for enhanced potency. Specifically, I sought to design bifunctional metalloinsertor conjugates, in hopes of conferring their cell-selective activity to another more potent therapeutic cargo, such as a platinum anticancer agent. I synthesized a bimetallic Rh-Pt complex, consisting of a rhodium metalloinsertor tethered to an oxaliplatin derivative. DNA binding studies showed that the complex interacts with DNA through both metalloinsertion at a mismatch and the formation of intrastrand Pt-DNA adducts. While the conjugate was not selective for MMR deficiency *in vitro*, it did exhibit enhanced cytotoxicity compared to cisplatin and oxaliplatin, as well as relative to its unconjugated Rh and Pt subunits.

Further development of additional new generations of metalloinsertor-platinum conjugates did not lead to the cell-selective targeting of platinum to mismatched DNA as we had initially intended. However, we constructed unique and complex structures that nevertheless revealed more information about how metalloinsertors function. I developed the first-generation conjugate derived from our newest family of metalloinsertor complexes – those containing an axial Rh—O bond – that is able to selectively target

platinum to mismatched DNA through the formation of non-classical adducts. I have also synthesized a new inserting ligand with two chelating environments, which has shown that metalloinsertion can place a second metal in the helix in place of the ejected mismatched bases. Most significantly, we discovered that the source of the nonselective toxicity of these conjugates is due to the initiation of apoptosis, rather than necrosis. This implies that the biological pathway leading to necrosis is a general hallmark of the cellular response to DNA mismatch recognition by metalloinsertors.

As we continue to unearth reasons why metalloinsertors do *not* exhibit cell selective cytotoxicity, we are just now beginning to discover why our most potent complexes do. The revelation that metalloinsertors are capable of inducing DNA damage in the genome, as well as selectively inhibiting transcription in MMR-deficient cells, marks an exciting new development in our study of these complexes. As we begin our *in vivo* studies of metalloinsertors, we enter a new frontier: the advancement of these complexes into the clinic as targeted chemotherapeutics.